ISSN 2618-9992

Energy Systems Research

Volume 8, Number 4, 2025

International scientific peer-reviewed journal since 2018

Available online: http://esrj.ru

About the journal

Energy Systems Research is an international peer-reviewed journal addressing all the aspects of energy systems, including their sustainable development and effective use, smart and reliable operation, control and management, integration and interaction in a complex physical, technical, economic and social environment.

Within this broad multi-disciplinary scope, topics of particular interest include strategic energy systems development at the international, regional, national and local levels; energy supply reliability and security; energy markets, regulations and policy; technological innovations with their impacts and future-oriented transformations of energy systems. The journal welcomes papers on advances in heat and electric power industries, energy efficiency and energy saving, renewable energy and clean fossil fuel generation, and other energy technologies.

Energy Systems Research is also concerned with energy systems challenges related to the applications of information and communication technologies, including intelligent control and cyber security, modern approaches of systems analysis, modeling, forecasting, numerical computations and optimization.

The journal is published by Melentiev Energy Systems Institute of Siberian Branch of Russian Academy of Sciences. The journal's ISSN is 2618-9992. There are 4 issues per year (special issues are available). All articles are available online on English as Open access articles.

The journal is indexed in the international database Scopus and included in the Unified Russian List of Scientific Journals ("White List") - level 2. The journal is included in the list of peer-reviewed scientific publications (VAK) in which the main scientific results of dissertations should be published in scientific specialties:
1.2.2. Mathematical modeling, numerical methods and software packages (technical sciences),
2.4.3. Electrical power engineering (technical sciences),
2.4.5. Energy systems and complexes (technical sciences).

Indexed by: Scopus, RSCI, CyberLeninka, Google Scholar, Crossref.

The journal is registered with Roskomnadzor. Certificate Эл № ФС77-84526 January 16, 2023

Topics

- Energy production, conversion, transport and distribution systems
- Integrated energy systems
- Energy complexes
- National, regional, international and global energy systems
- Energy system protection, control and management
- Smart energy systems, smart grids
- Energy systems reliability and energy security
- Electric, gas, oil and heat supply systems
- Energy system development and operation
- System problems of energy consumers
- Energy economics and policy
- Renewable energy and clean fossil fuel-based systems
- Distributed energy systems
- Sustainable energy transitions
- System problems of power and thermal engineering
- Artificial intelligence in energy systems
- Information and communication technologies in energy systems
- Energy system analysis and modelling
- Computational methods and optimization in energy systems

Editor-in-chief

Valery Stennikov,
academician of Russian Academy of Sciences,
director of *Melentiev Energy Systems Institute SB RAS, Russia*

Editorial board

- Sereeter Batmunkh, Mongolian University of Science and Technology, Mongolia
- Vitaly Bushuev, Institute of Energy Strategy, Russia
- Elena Bycova, Institute of Power Engineering of Academy of Sciences of Moldova, Republic of Moldova
- Gary Chang, National Chung Cheng University, Taiwan
- Pang Changwei, China University of Petroleum, China
- Cheng-I Chen, National Central University, Taiwan
- Gianfranco Chicco, Politecnico di Torino, Italy
- Van Binh Doan, lnstitute of Energy Science of VAST, Vietnam
- Petr Ekel, Federal University of Minas Gerais, Pontificial Catholic University of Minas Gerais, Brasil
- Ines Hauer, Otto-von-Guericke-Universität, Magdeburg, Germany
- Marija Ilic, Massachusetts Institute of Technology, Cambridge, USA
- James Kendell,Asian Pacific Energy Research Center, Japan
- Oleg Khamisov, Melentiev Energy Systems Institute SB RAS, Russia
- Alexander Kler, Melentiev Energy Systems Institute SB RAS, Russia
- Przemyslaw Komarnicki, University of Applied Sciences Magdeburg-Stendal, Germany
- Nadejda Komendantova, International Institute for Applied Systems Analysis, Austria
- Yuri Kononov, Melentiev Energy Systems Institute SB RAS, Russia
- Marcel Lamoureux, Policy and Governance Research Institute, USA
- Anatoly Levin, Melentiev Energy Systems Institute SB RAS, Russia
- Yong Li, Hunan University, China
- Faa-Jeng Lin, National Central University, Taiwan
- Alexey Makarov, Energy Research Institute RAS, Russia
- Lyudmila Massel, Melentiev Energy Systems Institute SB RAS, Russia
- Alexey Mastepanov, Oil and Gas Research Institute RAS, Institute of Energy Strategy, Russia
- Alexander Mikhalevich, Institute of Energy, Belarus
- Mikhael Negnevitsky, Tasmania University, Australia
- Takato Ojimi, Asian Pacific Energy Research Center, Japan
- Sergey Philippov, Energy Research Institute RAS, Russia
- Sergey Podkovalnikov, Melentiev Energy Systems Institute SB RAS, Russia
- Waldemar Rebizant, Wroclaw University of Science and Technology, Poland
- Christian Rehtanz, Dortmund Technical University, Germany
- Boris Saneev, Melentiev Energy Systems Institute SB RAS, Russia
- Sergey Senderov, Melentiev Energy Systems Institute SB RAS, Russia
- Zbigniew Styczynski, Otto-von-Guericke University Magdeburg, Germany
- Constantine Vournas, National Technical University of Athens, Greece
- Felix Wu, Hong-Kong University, China
- Ryuichi Yokoyama, Energy and Environment Technology Research Institute, Waseda University,Tokyo, Japan
- Jae-Young Yoon, Korea Electrotechnology Research Institute, Republic of Korea
- Xiao-Ping Zhang, University of Birmingham, United Kingdom

Publishing board

Copyeditors: Marina Ozerova, Eugenia Markova

Contacts

Scientific secretary: Alexey Mikheev, Dr. of Eng.
E-mail: info@esrj.ru
Tel: +7 (914) 8950980 (English, Russian)
Address: 130, Lermontov str., Irkutsk, 664033, Russia

CONTENTS

A Genetic Algorithm for Optimizing the Lifetime of Power Generation Equipment

S.V. Solodusha[1,*], E.V. Markova[1], E.A. Prokofiev[1,2], P.Yu. Solodusha[1,2]

[1] Melentiev Energy Systems Institute of Siberian Branch of Russian Academy of Sciences, Irkutsk, Russia
[2] Irkutsk State University, Irkutsk, Russia

***Abstract* — In this study, we numerically solve an optimization problem of power generation equipment dismantling dynamics. The mathematical modeling aims to make a long-term forecast that determines the most efficient strategy for commissioning new capacities. This approach minimizes total costs, ensuring the required level of electricity demand. The mathematical formulation of the problem is represented through the Volterra integral equation of the first kind with variable limits. A key feature of the problem is determining the required parameter within the integration limits of both the functional and the constraints. The developed approach to finding an approximate solution to this problem relies on a genetic algorithm and factors in the constraints on commissioning capacity during the forecast period and on extending the equipment lifetime. The effectiveness of the proposed approach is illustrated through its comparison with the existing methods.**

***Index Terms* — Electric power system, equipment dismantling problem, Volterra integral equation of the first kind, genetic algorithm.**

I. INTRODUCTION

Mathematical modeling provides the fundamental tools for describing physical processes in energy systems. At present, the dissemination of the Smart Grid concept largely depends on the successful application of systems analysis, facilitating a qualitative transition to energy systems with intelligent infrastructure and the effective use of modern information technologies. The current scientific approach to formalizing metamodels, including both their mathematical descriptions and their “physical meanings” [p. 79, 1], should be complemented by conceptual models based on ontologies [1].

Until recently, the primary tools for systems research in the energy sector were mathematical modeling and forecasting methods, complemented by systems supporting strategic decision-making based on semantic models and visual analytics (including cognitive graphics) [3, 4]. Typically, when substantiating strategic decisions, it is necessary to formalize the integration of software tools and a hierarchical knowledge base (both as a whole and its industry components) of selected energy systems at the same level, achieving horizontal integration. This process also involves the systems at different levels, ensuring vertical integration, which includes internal connections. The emergence of high-performance computing systems and supercomputers, along with the increasing complexity of multifactor models, calls for specialized approaches capable of formalizing modeling methods to enhance their computational efficiency. One such approach is related to metamodeling. The development of metamodels is based on the ideas of machine learning [p. 49, 2], utilizing scientific knowledge about the physical laws governing the processes under study.

In the energy sector facing additional difficulties, such as the hierarchical nature of the processes being modeled, the need for real-time decision-making and data processing, and the complex nature of current problems, there is successful experience in integrating modeling and

---

[*] Corresponding author.
E-mail: solodusha@isem.irk.ru

DOI: 10.25729/esr.2025.04.0001

Received July 16, 2025. Accepted July 24, 2025. Available online December 29, 2025.

forecasting methods with intelligent technologies (including semantic modeling tools, agent-based computing, fuzzy logic methods, and neural networks). The methodological framework of these approaches is detailed in [5–8].

In addition to the methods listed, researchers show sustained interest in algorithms inspired by natural processes, such as genetic and swarm algorithms. These algorithms are often used in conjunction with neural networks as complementary approaches (see, for example, [9]). Genetic algorithms are employed to determine the steady-state conditions of electric networks [10], solve optimization problems [11, 12], and ensure the reliable operation of electrical systems and equipment [13].

As new technologies advance, the complexity of designing the configuration of electrical networks increases. Alternative methods for solving optimization problems to locate equipment and determine electrical parameters are discussed in [14]. An analysis of economic cost characteristics in ensuring reliability revealed the advantages of a heuristic method based on a genetic algorithm compared to an adaptive particle swarm algorithm.

Thus, genetic algorithms, which successfully adapt to various conditions and constraints, are a powerful tool for solving non-standard optimization problems in the energy sector. The purpose of this work is to analyze the effectiveness of a genetic algorithm when used to optimize the replacement of obsolete equipment in a large electric power system (EPS).

II. PROBLEM STATEMENT

Let us consider the problem of forecasting the electric power system (EPS) expansion, which involves formulating a long-term strategy for introducing capacities in a large (combined) system, given the decommissioning of obsolete equipment with a known lifetime. We will assume that all generation capacities have identical characteristics and will write an aggregated model of EPS expansion in the form of a Volterra integral equation of the first kind [15]:

$$\int_{t-c(t)}^{t} \beta(t,s)x(s)ds = p(t),\ t\in[t_0,T], \tag{1}$$

subject to

$$x(t) = x^0(t),\ t\in[t_0-c(t_0),t_0), \tag{2}$$

$$x(t)\geq 0,\ t\in[t_0,T], \tag{3}$$

where $x(t)$ is the desired total generation equipment commissioning in EPS at time t; $\beta(t,s)$ is the coefficient of intensive use at time t of a power unit commissioned previously at time s; $p(t)$ is the expert-defined future dynamics of power consumption (load); $c(t)$ is the lifetime of the oldest power unit in the EPS at time t; $x^0(t)$ is the known dynamics of equipment commissioning within the prehistory $[t_0-c(t_0),t_0)$.

Using models (1)–(3), consider the problem of selecting long-term capacity input strategies $x(t)$ that, given the decommissioning of obsolete equipment, ensure a specified demand $p(t)$, while minimizing the total costs over the forecast period for new capacity installation and operation of power generation units. The problem formulation is as follows:

Find

$$c^*(t) = arg\min_{c(t)\in C} I(x(t),c(t)), \tag{4}$$

where

$$\begin{aligned} I(x(t),c(t)) = \int_{t_0}^{T} a^{t-t_0}\left\{\int_{t-c(t)}^{t} u_1(t-s)u_2(s)x(s)ds\right\}dt + \\ +\int_{t_0}^{T} a^{t-t_0}k(t)x(t)dt, \end{aligned} \tag{5}$$

$$C = \left\{c(t)\,\middle|\, \underline{c}\leq c(t)\leq \bar{c},\ c'(t)\leq 1,\ t\in(t_0,T]\right\}, \tag{6}$$

under the constraints on the phase variable $x(t)$ (1)–(3). The first term in (5) corresponds to operating costs, the second represents the costs of capacity introduction for the entire forecast period. The constraint $c'(t)\leq 1$, which originates from the non-decreasing nature of the function $t-c(t)$, means that the rate of aging for the oldest component cannot exceed the rate of natural aging.

The notation used is as follows: $u_1(t-s)$ is the increase coefficient at time t for the operating costs of equipment commissioned at time s; $u_2(t)$ is the specific (unit) operating costs of equipment commissioned at time t; $k(t)$ is the costs of commissioning a power unit at time t (capital costs); a^{t-t_0} is the costs discount coefficient, $0<a<1$. These functions, as well as $\bar{c}$, $\underline{c}$, $\beta(t,s)$, $p(t)$, and the power units $x^0(t)$ commissioned during the prehistory $[t_0-c(t_0),t_0)$ are considered known (defined by experts).

The assumptions made in the model calculations are as follows. The forecast period is 50 years, from 2000 to

TABLE 1. Dynamics of Equipment Commissioning Within the Prehistory, MW

Year	$x^0(t)$	Year	$x^0(t)$
1963	6 239	1982	4 093
1964	5 437	1983	5 087
1965	4 883	1984	5 515
1966	4 602	1985	8 311
1967	5 149	1986	4 083
1968	5 494	1987	6 662
1969	8 166	1988	5 787
1970	7 556	1989	1 800
1971	6 206	1990	4 000
1972	6 058	1991	2 100
1973	5 649	1992	700
1974	5 719	1993	2 700
1975	7 225	1994	2 400
1976	6 144	1995	1 000
1977	5 062	1996	1 350
1978	4 910	1997	640
1979	8 199	1998	830
1980	9 647	1999	850
1981	5 946	2000	680

2050, $([t_0, T] = [2000, 2050])$. The lifetime $c(t)$ is 38 years (the real mean equipment lifetime in the Russian power industry). Data for equipment commissioning within the prehistory are given in Table 1. Since the system characteristics remain invariable over the forecast period (the system is stationary), the function $\beta(t,s)$ depends only on the difference $t-s$. Therefore, one can assume that $\beta(t,s) \equiv \beta(t-s) \equiv \beta(\tau)$. This function remains at 1 until $\tau = 30$, then drops down to 0.9 over 50 years, vanishing after 70 years. Power consumption $p(t)$ for 2000 is consistent with the reported data (177 907 MW). Between 2001 and 2050, the demand for electricity is expected to grow at a rate of 2% annually at the beginning of the forecast period, declining to 1% by the year 2050.

The data assumed for specific costs are given in Table 2. They reflect the projected increase in specific capital costs and the potential reduction in specific fuel consumption due to the transition to relatively expensive, environmentally friendly power plants. The values of costs are not adjusted for inflation.

The coefficients of growth in operating costs $u_1(t-s) \equiv u_1(\tau)$ as the equipment ages are given as follows:

$$u_1(\tau) = \begin{cases} 1, \ \tau \le 30, \\ 1.03^{\tau-30}, \ \tau > 30. \end{cases}$$

Thus, after the standard equipment lifetime is achieved, an exponential increase in operating costs is expected. The costs discount coefficient a is 0.97.

Solving problems (1)–(6) based on real-life data with various parameter variations is discussed in detail in [15, 16]. These studies utilize a heuristic algorithm to find a long-term generation capacity input strategy. They rely on a class of piecewise linear functions, reducing the problem to a linear programming formulation, which is solved using the General Algebraic Modeling System (GAMS). GAMS is a software environment designed for modeling linear, nonlinear, and mixed-integer optimization problems [17]) with the OSL solver. In this paper, we propose solving the same problem using a genetic algorithm.

III. APPLICATION OF GENETIC ALGORITHM TO PROBLEM (1)–(6)

Genetic algorithms are a type of evolutionary computation that solve optimization problems using natural evolution techniques such as inheritance, mutation, selection, and crossover. The basic operators of genetic algorithms include selection, crossover, and mutation. Crossover (the process of combining two parents to create offspring) plays a central role in genetic algorithms. Due to the flexibility of the algorithm, it can be applied to a wide range of problems.

The stages of the simplest genetic algorithm include:

1) Creation of the initial population;

2) Evaluation of the fitness for each individual in the population;

3) Crossover of the individuals;

4) Mutation of the individuals;

TABLE 2. Specific Operating and Capital Costs, USD/kW

Year	$u_2(t)$	$k(t)$
1960	220	
1970	200	
1985	175	
1995	175	900
2005	170	850
2010	165	800
2020	160	900
2030	150	1 000
2040	140	1 100
2050	130	1 200

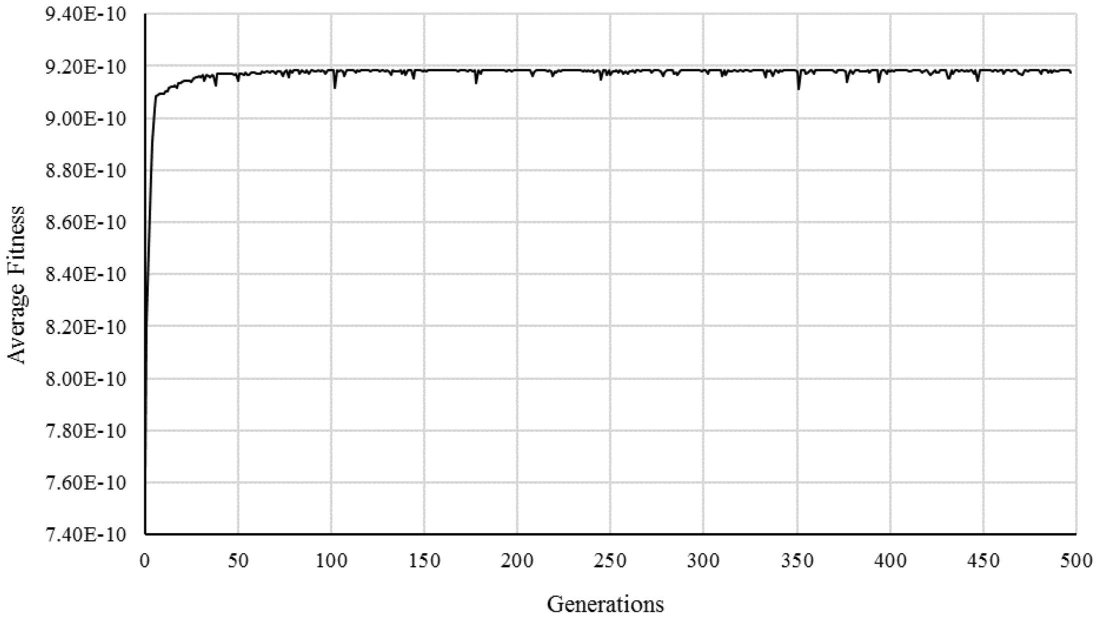

Fig. 1. Dynamics of average fitness.

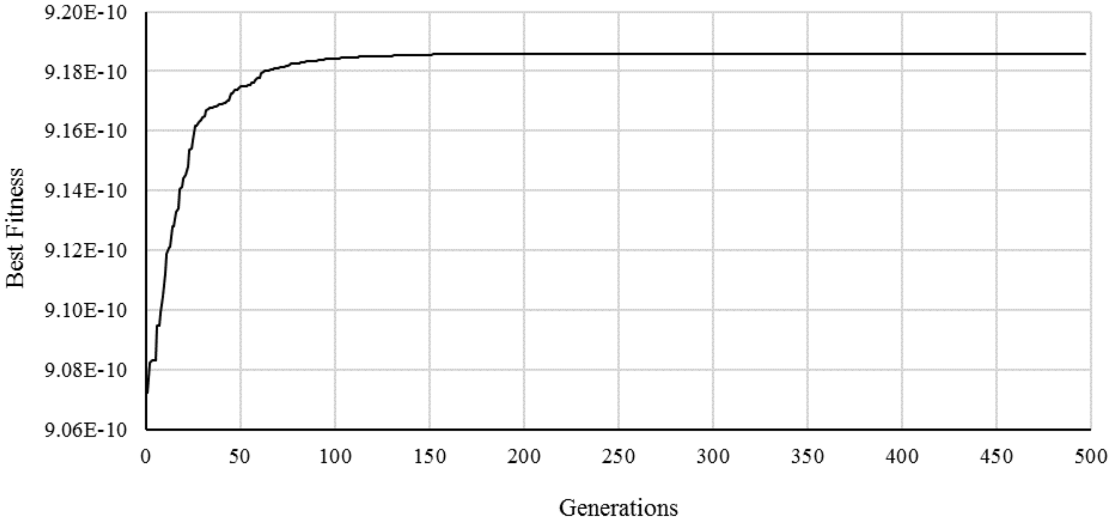

Fig. 2. Dynamics of best fitness.

5) Formation of a new generation.

These steps are repeated until the result meets the specified requirements or until one of the following conditions is satisfied:

- The number of generations (cycles) reaches a predetermined maximum;
- The allotted solving time reaches a predetermined maximum;
- A predefined stopping criterion is met.

Consider the application of a genetic algorithm to problem (1)–(6), using data from [15, 16]. In the first step, an initial population is created. According to the data from [16], the forecast period in the problem spans 50 years, from 2000 to 2050 ($[t_0, T] = [2000, 2050]$), which means that each individual will consist of a set of 50 "genes," i.e., values corresponding to the maximum equipment lifetime in the forecast year. These genes are generated randomly but following the lifetime constraints specified in (6). The number of individuals in a population for problems solved using genetic algorithms is chosen arbitrarily. However, a larger population provides greater genetic diversity and, consequently, the potential for more optimal solutions. In this case, each population consisted of 100 individuals.

After creating the population, it is necessary to calculate the fitness value for each individual. Since the optimization problem aims to minimize equipment operation costs, the fitness of a particular individual is computed as the inverse of the costs associated with the use of that individual's genes in the objective function (5).

Once the fitness of each individual in the population is evaluated, they are ranked from the most to the least fit. Then, random individuals are paired and crossed to create a new population. In this problem, a single-point crossover is employed, where a single random point is selected on both parent gene sequences. The genes are cut at this point, and the segments beyond the point are exchanged between the parents, resulting in two new offspring that inherit genes from both parents. The parent selection operator used is panmixia — both parents are chosen randomly from the population with equal probability. The crossover probability was set to 0.7. After two parents are selected, there is a 70% chance they will produce two offspring that are transferred to the next population, and a 30% chance that the parents themselves will be passed to the next population unchanged. Before crossover, it is necessary to ensure that the constraints specified in (6) are not violated.

To prevent stagnation in local optima and premature convergence of the population in genetic algorithms, the concept of mutation is implemented. Mutation is typically applied after crossover and involves changing an individual's genes to randomly selected values within the specified constraints, with a predetermined probability. Since each gene of an individual can undergo mutation, it should occur with a sufficiently low probability to avoid turning the method into a purely random search. In this problem, mutation was set to occur with a probability of 0.01 and was designed not to violate the lifetime constraints specified in (6).

Next, it is necessary to select individuals that will participate in the next iteration of the algorithm from those resulting from crossover and mutation. To ensure that the new population is at least as good as the previous one and that optimal solutions are not lost during evolution, the concept of elitism is implemented. This involves transferring five individuals with the highest fitness values directly to the next generation without any changes. The remaining members of the population are filled with individuals produced through crossover and selected via tournament selection: a subset of the best solutions is randomly chosen, their fitness values are compared, and the winner is transferred to the new population. The size of one tournament is 2, the individuals are compared pairwise.

The stopping criterion for the algorithm is population degeneration, i.e., a situation where diversity within the candidate solutions decreases to such an extent that most individuals become very similar or even identical. To monitor this, each iteration compares the fitness of the best individual in the current population with that of the best individual in the previous generation. If the difference

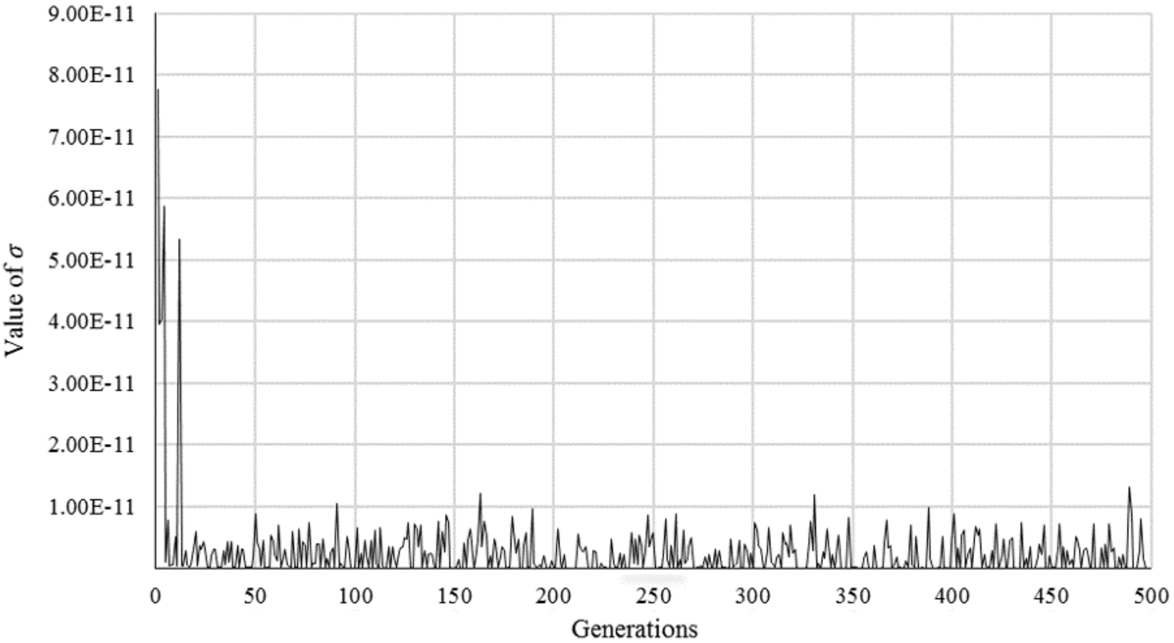

Fig. 3. Dynamics of population diversity σ .

between these fitness values is less than a predefined threshold, the algorithm terminates and outputs the individual with the highest fitness observed throughout the entire cycle. As an additional constraint, the maximum number of generations was 500. Ideally, during degeneration, only one most fit individual and its genetic equivalents remain in the population.

The convergence of the algorithm was assessed using graphs of fitness variation over generations. The best and average fitness values were calculated for each population (see Figs. 1 and 2).

The population diversity metric was defined as the standard deviation of fitness values among individuals:

$$\sigma = \sqrt{\frac{1}{N}\sum_{i=1}^{N}\left(f_i - \bar{f}\right)^2}\,, \tag{7}$$

where f_i is the fitness of the *i*-th individual, $\bar{f}$ is the mean population fitness, and N is the population size. Since the fitness function was defined as the inverse of the cost value, the absolute values of σ were extremely small (on the order of 10^{-11}). Nevertheless, the dynamics of σ across generations allow for the correct assessment of relative diversity and identification of premature convergence tendencies: a drop of σ toward zero indicates population degeneration, while stable values point to the preservation of variability (Fig. 3).

To check for the premature convergence, the population diversity metric σ and the best fitness were monitored. The algorithm was considered prematurely converged if σ approached zero and no improvement in the best fitness was observed over the subsequent 50 generations.

In this study, the fitness reached all-time high values within the first 100 generations, with the most significant improvement occurring around generation 30, where σ also dropped sharply to near-zero. After this point, the best fitness remained stable while diversity fluctuated near zero. This indicates that the algorithm quickly found near-optimal solutions and that further increases in diversity do not improve the performance. Therefore, despite the low σ values, the algorithm demonstrates rapid and correct convergence rather than premature stagnation, which is supported by the fact that the algorithm consistently produced near-optimal solutions after 20 consecutive simulations.

To assess the accuracy of the sample mean, a 95% confidence interval was calculated. The confidence interval for the mean improvement value μ with a sample size of $n = 20$ was determined using the formula:

$$\bar{x} - t_{\alpha/2,n-1}\frac{s}{\sqrt{n}} \le \mu \le \bar{x} + t_{\alpha/2,n-1}\frac{s}{\sqrt{n}}\,, \tag{8}$$

where $\bar{x}$ is the sample mean, s is the sample standard deviation, $t_{\alpha/2,n-1}$ is a critical value of Student's *t*-distribution at a significance level of $\alpha = 0.05$ and $n-1$

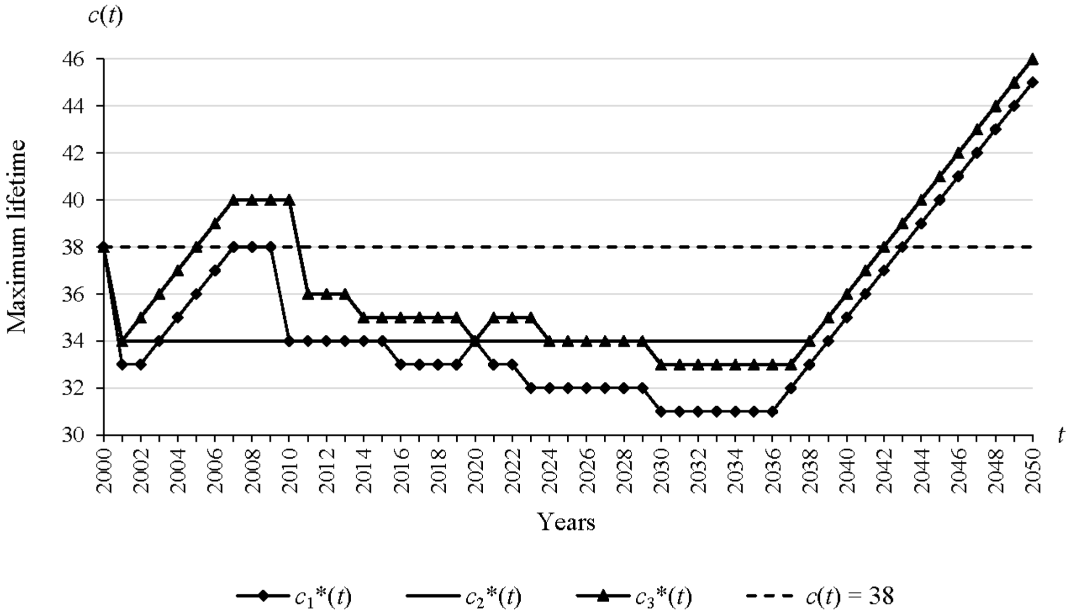

Fig. 4. Dynamics of optimal equipment lifetime.

degrees of freedom.

The statistics obtained for the sample of 20 simulations were the following: the sample mean improvement $\bar{x} = 1.450$ and the standard deviation $s = 0.368$. At a 95% confidence level and 19 degrees of freedom, the critical value of Student's *t*-distribution was $t_{0.975,\,19} = 2.093$.

Thus, the 95% confidence interval for the mean improvement value is $1.450 - 2.093\frac{0.368}{\sqrt{20}} \le \mu \le 1.450 + 2.093\frac{0.368}{\sqrt{20}}$, i.e., $1.277 < \mu < 1.623$. This suggests that with the 95% probability, the true population mean improvement lies within the calculated interval.

IV. RESULTS OF THE COMPUTATIONAL EXPERIMENT

The results of the conducted computational experiment and those obtained earlier [16] were compared in [18]. Figure 4 [18] shows the dynamics of the lifetime $c_1^*(t)$ obtained using the genetic algorithm. This strategy reduces the initial value of the objective function $I(38)$ (the average equipment lifetime assumed in 2000) by 1.72%. The lifetime dynamics $c_2^*(t)$ were determined by a systematic exhaustive search within the class of piecewise linear functions [16]. As a result, the total costs decrease by 1.47%. The lifetime dynamics $c_3^*(t)$ were obtained by reducing the original problem to a linear programming problem and solving it using GAMS [17]. The integral costs for this strategy are lower than $I(38)$ by 1.52%. Thus, the use of the genetic algorithm provides a variation of equipment lifetime $c(t)$, exhibiting the best result among those presented.

V. FURTHER DEVELOPMENT OF THE WORK AND CONCLUSIONS

The modern approach to operating complex dynamic objects is implemented through the concept of digital twins [19]. This concept involves not only the use of mathematical models based on physical laws of operation but also virtual data reflecting the structure, performance, technical condition, and other production characteristics. Thus, digital twins facilitate both creating a virtual prototype of a real-life technical device or technological process and testing control strategies for its lifecycle, considering the specific stage of the dynamic object's evolution. A key feature of today's energy sector is intelligent systems, which are currently defined as the unity of cyber-physical systems, software, and hardware, including those implementing the concept of digital twins.

The relevance of developing a methodological approach to constructing digital twins that relies on ontological engineering of the subject area is undeniable. Systems with a large number of sensors to monitor their operation are susceptible to interference or damage. Adapting semantic modeling techniques for resource-constrained devices can be useful for solving such problems [20]. The availability and performance of ontologies based on semantic modeling, particularly focusing on applications in resource-constrained devices are discussed in [20]. The study highlights the necessity of developing suitable ontologies and importance of their availability for the energy domain [22].

A key challenge in modeling complex systems is managing the combinatorial complexity of operational parameters, configurations, and potential failure conditions. Genetic algorithms offer a powerful approach to address this challenge, enabling the exploration of large solution spaces and the discovery of optimal or near-optimal strategies for system operation and control. In this context, genetic algorithms represent system components, operational decisions, or control parameters as genes within candidate solutions, while chromosomes represent a full configuration or control strategy for the system over a defined period.

For complex dynamic systems, genetic algorithms can interact directly with the digital twin: the twin provides realistic evaluation of each candidate solution, simulating system behavior under physical and operational constraints.

A promising tool for implementing a conceptual approach to modeling complex dynamic systems is high-level Petri nets. A method for interpreting coloured Petri nets is proposed in [23] to design static and dynamic event processing systems within the framework of the Semantic Web based on the SPARQL language [24]. The ontology of coloured Petri nets is considered at the level of TBox (terminological box) and ABox (assertion box). Specifically, a general description such as "There is X such that $P(X)$" contains the subject X and predicate $P(X)$ from the TBox, as well as x_i, $P(x_i)$ from the ABox, where x_i belongs to X, and $P(X)$ is a predicate that performs different functions in both the TBox and ABox. Additional insights from [25] enrich the syntactic description of the Petri net with semantic information by transitioning to categorical attribute statements [26], which are free from ontological assumptions, where an object $Y = P(X)$. This enables the relationship between X and $P(X)$ to be interpreted in terms of logical relations. Integration of Petri nets into digital twin models within the energy sector is explored in numerous studies, with researchers employing varying levels of model complexity and considering the hierarchical structure of energy systems [27]. In particular, [28] presents an aggregation process based on the Unified Modeling Language (UML), illustrated in [Fig. 4, 28] titled “DDHPN Integration in Digital Twin Model.” A dedicated block presented in this Figure suggests the use of empirical methods to optimize operating parameters. This optimization process relies on inputs from two other components: the “Energy Behavior Model” and the “Production Demand Information” blocks. Optimization of operating parameters can be handled through a genetic algorithm. By encoding Petri net states or transition priorities as genes, the genetic algorithm can optimize control strategies dynamically, identifying sequences of events or operational adjustments that maximize system performance or reliability.

Thus, the approach to constructing digital twins using coloured Petri nets and optimizing them with the genetic algorithm ensures a comprehensive framework for simulating, analyzing, and optimizing complex dynamic systems. This approach facilitates iterative exploration of operational strategies, automated adaptation to changing conditions, and the discovery of solutions that might be difficult to identify using conventional methods.

This study numerically solves an optimization problem of the generation equipment dismantling dynamics. The mathematical formulation of the problem is represented though the Volterra integral equation of the first kind with variable integration limits. A genetic algorithm was implemented and tested for solving the problem. The algorithm factors in the constraints on both the commissioning of generation equipment during the forecast period and the extension of the equipment lifetime. The effectiveness of the proposed approach was demonstrated through its comparison with the previously used methods.

ACKNOWLEDGMENT

The research was carried out under the State Assignment Project (no. FWEU-2021-0006) of the Fundamental Research Program of the Russian Federation 2021–2030.

REFERENCES

[1] V. I. Gurianov, “Semantic networks and insufficiency of mathematical description of scientific models,” *Metaphysics*, vol. 2 (52), pp. 67–81, 2024. (In Russian)

[2] M. V. Simonov, A. V. Penigin, A. S. Margarit, A. A. Pustovskikh, N. A. Smirnov, A. N. Sitnikov, “Methodology of surrogate models (metamodels) and their prospects for solving petroleum engineering challenges,” *PROneft. Professionally about Oil*, vol. 2, pp. 48–53, 2019. (In Russian)

[3] A. G. Massel, N. I. Pyatkova, “Application of cognitive modeling methods for energy security threat analysis,” *Information and Mathematical Technologies in Science and Management*, vol. 4 (20), pp. 24–33, 2020. DOI: 10.38028/ESI.2020.20.4.002. (In Russian)

[4] E. A. Yakovleva, I. A. Tolochko, M. M. Kiseleva, I. V. Popov, “Logical and linguistic modeling for enterprise risk management,” *Journal of Economics, Entrepreneurship and Law*, vol. 11, no. 7, pp. 1809–1826, 2021. DOI: 10.18334/epp.11.7.112352. (In Russian)

[5] L. V. Massel, A. G. Massel, “Semantic modeling in the construction of digital twins of energy objects and systems,” *Ontology of Designing*, vol. 13, no. 1, pp. 44–54, 2023. DOI: 10.18287/2223-9537-2023-13-1-44-54. (In Russian)

[6] I. A. Spitsina, K. A. Aksenov, *Method of decision support in the development of information systems based on a multi-agent approach*. Ekaterinburg, Russia: Ural State Pedagogical University Publ., 2018, 156 p. (In Russian)

[7] A. V. Domyshev, E. A. Barakhtenko, P. V. Ilyushin, “Review of state-of-the-art approaches to the design of micro-grid multi-agent control systems,” *Electric Power. Transmission and Distribution*, vol. 3 (78), pp. 46–56, 2023. (In Russian)

[8] N. Simonov, N. Ivenev, “Experience and prospects of using artificial neural networks in electric power industry,” *Electric Power. Transmission and Distribution*, no. S4(15), pp. 42–48, 2019. (In Russian)

[9] A. D. Smorodinov, T. V. Gavrilenko, V. A. Galkin, “Applicability of genetic algorithms for determining the weighting coefficients of an artificial neural network with one hidden layer,” *Bulletin KRASEC. Phys. and Math. Sci.*, vol. 43, no. 2, pp. 69–86, 2023. DOI: 10.26117/2079-6641-2023-43-2-69-86. (In Russian)

[10] R. V. Solopov, A. S. Samulchenkov, “Application of genetic algorithm for electric circuit steady-state response calculation,” *Proceedings of Irkutsk State Technical University*, vol. 22, no. 2, pp. 131–141, 2018. DOI: 10.21285/1814-3520-2018-2-131-141. (In Russian)

[11] A. V. Sobolev, A. S. Gazetdinov, D. S. Samokhin, “Genetic algorithms for nuclear reactor fuel load and reload optimization problems,” *Nuclear Energy and Technology*, vol. 3, no. 3, pp. 231–235, 2017. DOI: 10.1016/j.nucet.2017.07.002.

[12] V. G. Sidorenko, M. A. Zhuo, “Application of genetic algorithms for underground electric trains scheduling problems,” *Electronics and electrical equipment of transport*, no. 6, pp. 13–16, 2016. (In Russian)

[13] N. N. Sergeev, “Program for searching for the optimal location and number of sectioning points of a distribution electric network using evolutionary and swarm algorithms,” Certificate of state registration of a computer program, RU 2024685161, Oct. 25, 2024.

[14] N. N. Sergeev, P. V. Matrenin, “Application of metaheuristic algorithms for optimization of recloser placement in a power supply system with distributed generation,” *Dokl. Math*., vol. 110 (Suppl 1), pp. S87–S94, 2024. DOI: 10.1134/S1064562424602282.

[15] A. S. Apartsyn, V. V. Trufanov, E. V. Markova, *Integral development models of electric power systems*. Irkutsk, Russia: ESI SB RAS, 2002, 36 p. (In Russian)

[16] D. V. Ivanov, I. V. Karaulova, E. V. Markova, V. V. Trufanov, O. V. Khamisov, “Control of power grid development: numerical solutions,” *Autom. Remote Control*, vol. 65, no. 3, pp. 472–482, 2004. DOI: 10.1023/B:AURC.0000019380.88379.d9.

[17] A. Brook, D. Kendrick, A. Meeraus, GAMS Release 2.25. A User's Guide. GAMS Development Corporation, 1996.

[18] E. V. Markova, E. A. Prokofiev, “Application of a genetic algorithm to solving the problem of choosing long-term development strategies,” in *Proc. of the A.S. Apartsyn Seminar with international participation “Unstable problems of computational mathematics,”* Irkutsk, July 29 – August 2, 2024. Irkutsk, Russia: Irkutsk State University, 2024, pp. 48–52. (In Russian)

[19] V. A. Sukhomlin, D. E. Namiot, D. A. Gapanovich, “Analysis of development trends of new generation digital twins,” *International Journal of Open Technologies*, vol. 12, no. 7, pp. 119–130, 2024. (In Russian)

[20] W. Tai, J. Keeney, D. O’Sullivan, “Resource-constrained reasoning using a reasoner composition approach,” *Semantic Web*, no. 6(1), pp. 35–59, 2015. DOI: 10.3233/SW-140142.

[21] J. M. Blanco, B. Rossi, T. Pitner, “A Comparative study of energy domain ontologies,” in *Web Information Systems and Technologies (WEBIST 2020, WEBIST 2021). Lecture Notes in Business Information Processing*, vol. 469, M. Marchiori, F. J. Domínguez Mayo, J. Filipe J., Eds. Springer, Cham, 2023, pp. 43–58. DOI: 10.1007/978-3-031-24197-0_3.

[22] J. M. Blanco, B. Rossi, T. Pitner, “A comparison of smart grids domain ontologies,” in *The 17th International Conference on Web Information Systems and Technologies (WEBIST)*, vol. 1, Oct. 26-28, 2021, pp. 115–123, SciTePress. DOI: 10.5220/0010710000003058.

[23] V. Yu. Kaev, V. N. Dubinin, A. V. Dubinin, L. P. Klimkina, “Modeling of colored Petri nets using semantic web technologies,” *University proceedings. Volga region. Engineering sciences*, no. 1, pp. 62–77, 2022. DOI: 10.21685/2072-3059-2022-1-6. (In Russian)

[24] B. DuCharme, *Learning SPARQL: Querying and Updating with SPARQL 1.1*. Sebastopol, California, USA: O'Reilly Media, Inc., 2013.

[25] V. I. Markin, “Intensional semantics of traditional syllogistic,” *Logical Investigations*, vol. 8, pp. 82–91, 2001. (In Russian)

[26] V. I. Shalack “Syntactic interpretation of categorical attributive propositions,” *Logical Investigations*, vol. 21, no. 1, pp. 60–78, 2015. (In Russian)

[27] A. A. Ardebili, M. Zappatore, A. I. H. A. Ramadan, A. Longo, A. Ficarella, “Digital twins of smart energy systems: a systematic literature review on enablers, design, management and computational challenges,” *Energy Informatics*, vol. 7, Art. no. 94, 2024. DOI: 10.1186/s42162-024-00385-5.

[28] H. Li, D. Yang, H. Cao, W. Ge, E. Chen, X. Wen, C. Li, “Data-driven hybrid petri-net based energy consumption behaviour modelling for digital twin of energy-efficient manufacturing system,” *Energy*, vol. 239, Art. no. 122178, 2022. DOI: 10.1016/j.energy.2021.122178.

Svetlana Vitalievna Solodusha received the Ph.D. degree from Irkutsk State University in 1996. In 2019, she received the D. Sc. degree in mathematical modeling, numerical methods and software packages (engineering) from the Melentiev Energy Systems Institute SB RAS (ESI SB RAS). Currently, she is the head of the Laboratory of Unstable Problems of Computational Mathematics at the ESI SB RAS. Her research interests include mathematical methods for identifying dynamics based on integral models. She has authored and co-authored over 100 scientific papers.

Evgeniia Vladimirovna Markova received the Ph.D. degree from Irkutsk State University in 1999. Currently, she serves as a leading specialist in applied mathematics in the Laboratory of Unstable Problems of Computational Mathematics at the Melentiev Energy Systems Institute SB RAS. Her research interests include mathematical modeling for dynamic systems based on the Volterra integral equations of the first kind. She has authored and co-authored over 50 scientific papers.

Egor Alekseevich Prokofiev is a Master's student at Irkutsk State University. He is an engineer in the Laboratory of Unstable Problems of Computational Mathematics at the Melentiev Energy Systems Institute SB RAS. His research interests include natural algorithms and their applications.

Petr Yurievich Solodusha is a student of Irkutsk State University. His research interests include computational linguistics and formal models of language

Probabilistic Modeling of Steady-State Thermal-Hydraulic Conditions in Tree-Configured Pipeline Networks

N.N. Novitsky[1,*], O.V. Vanteeva[1]

[1] Melentiev Energy Systems Institute of Siberian Branch of Russian Academy of Sciences, Irkutsk, Russia

***Abstract* — This study focuses on a problem of probabilistic modeling of steady-state thermal-hydraulic conditions of a tree-configured pipeline network, which occur under the influence of random external factors. An original algorithm designed to ensure acceptable accuracy and high computational efficiency is proposed to solve the probabilistic modeling problem. Alongside the models introduced in the study, the main tenets of the proposed approach are presented and finite formulas for calculating the main statistical characteristics (means, variances, and covariances) of all operating parameters (flow rates, pressures, and temperatures) are explained. Numerical calculations demonstrate the superior capabilities of the proposed algorithm compared to other alternative methods, including matrix stepwise and statistical testing methods, in terms of both accuracy and speed.**

***Index Terms* — Probabilistic modeling, tree-like configuration, pipeline networks, thermal-hydraulic conditions.**

I. INTRODUCTION

Modeling the operating conditions of pipeline networks of various types and purposes (heat, water, gas, and others) is essential for their design, operation, and dispatch control. This process involves determining pressures, flows, and temperatures of the working medium for all components of the calculated scheme, under their given characteristics and boundary conditions at the points of interaction with the environment. These problems are normally solved to analyze the consequences of changes in the topology, parameters of heat networks, and boundary conditions, to assess the extent to which the consumer loads will be supplied while adhering to technological limitations on equipment operating conditions and other requirements. In real-world environments, however, boundary conditions – which include consumer loads, pressures and temperatures at points of connection to upper-level sources or networks, outdoor air temperatures, and others – are stochastic in nature. Therefore, the operating parameters should be considered as random variables, and the degree to which they satisfy the stated requirements should be assessed probabilistically.

Probabilistic models and methods have recently become increasingly widespread in their application to various types of gas [1–12], heat [12–20], water [15, 21–24], and oil systems [4]; as well as to water disposal [25], integrated energy systems [7–11, 26, 27], and others. These methods and models are also employed when accomplishing various modeling tasks, including 1) reliability analysis of pipeline systems [1–4, 13]; 2) optimization of pipeline systems and their operating parameters [5, 6, 21, 22]; 3) integration with electric power systems and pipeline systems of other types [7–11, 14]; 4) analysis of operating conditions [10–12, 15, 20]; 4) load modeling and forecasting [16, 17, 23, 24]; 5) state identification and estimation [18, 19].

Most researchers rely on the Monte Carlo method (MCM) to obtain probabilistic characteristics [1–5, 17, 22]. In some cases, depending on the objectives, the studies rely on: the Nataf transformation in combination with the point

---

[*] Corresponding author.
E-mail: pipenet@isem.irk.ru

DOI: 10.25729/esr.2025.04.0002

Received July 3, 2025. Revised September 3, 2025. Accepted September 22, 2025. Available online December 29, 2025.

estimation method [9, 10]; Markov random processes [13]; the Poisson spatio-temporal process [24]; the cumulant method [12, 23] using the Gram-Charlier decomposition [11, 14]; the Neumann-Scott rectangular pulse model [24], neural networks [18, 19], and others. Extensive experience has been accumulated in the field of probabilistic modeling of electric power systems [26, 27].

Probabilistic modeling of the pipeline systems using traditional methods, for example, the Monte Carlo method (MCM) [28], is associated with large expenditures of time and computational resources even for small-sized pipeline systems. The Melentiev Energy Systems Institute of the Siberian Branch of the Russian Academy of Sciences (Irkutsk, Russia) has developed analytical models and a matrix stepwise method (MSM) [30–32] for various sets of boundary conditions (specified by their means and variances). These tools can be applied to arbitrarily configured pipeline systems (multi-loop, tree-like, mixed), significantly increasing the calculation speed compared to the MCM. The topological method [33] was proposed [32]for probabilistic modeling of hydraulic conditions of tree-configured pipeline systems. This method is reduced to the use of finite formulas instead of relatively labor-intensive matrix operations, which further boosts the calculation speed. The importance of this case stems from the fact that a great number of pipeline systems of various types and purposes (heat, water, gas, and others), or a significant part (in terms of the number of components or total length) of real-world networks, have a branched (tree-like) configuration.

In this study, we examine the problem of generalizing the topological method to problems of probabilistic modeling of steady-state thermal-hydraulic conditions in branched pipeline systems. These conditions are defined by the distribution of flow rates, pressures, and temperatures.

II. STEADY-STATE THERMO-HYDRAULIC MODEL

The term thermo-hydraulic conditions (specifically as a non-isothermal case) refers to the distribution of flow rates, pressures, and temperatures of the working medium across the components of the calculated scheme when the hydraulic characteristics of the equipment do not depend on temperature, which is typical, for example, of water heating networks, water supply networks, medium- and low-pressure gas networks, and others.

The vector-matrix form of the system of equations for hydraulic and thermal conditions for a system of arbitrary configuration is as follows:

$$Ax = Q\,, \tag{1}$$

$$A^{\mathrm{T}} P = y\,, \tag{2}$$

$$y = f(x)\,, \tag{3}$$

$$A_{\mathrm{s}} X\, t_{\mathrm{s}} + A_{\mathrm{e}} X\, t_{\mathrm{e}} = Q^{+} T^{+} + Q^{-} T\,, \tag{4}$$

$$t_{\mathrm{s}} = A_{\mathrm{s}}^{\mathrm{T}} T\,, \tag{5}$$

$$t_{\mathrm{e}} = g(x, t_{\mathrm{s}}, t_0)\,. \tag{6}$$

Here (1)–(3) are a model of steady-state hydraulic conditions, in which: (1) is the equation of material balance at the nodes of the calculated scheme (Kirchhoff's first law); (2) is the equation of Kirchhoff's second law in a nodal form; (3) is the equation reflecting the laws of pressure drop during the flow of the medium on the branches of the calculated scheme. The thermal conditions model contains the equations of heat balance at nodes (under equal heat capacities of all flows) (4), the condition for complete mixing of flows at the nodes (5), and equation representing the temperature drop as the medium flows through the branches of the calculated scheme (6).

The notation used in these equations is as follows: A is the $m \times n$ incidence matrix of nodes and branches with elements $a_{ji} = 1(-1)$, when node j is the initial (final) for branch i and $a_{ji} = 0$, if branch i is not incident to node j; m, n are the number of nodes and branches in the calculated scheme; Q is the m-dimensional vector of nodal flow rates with elements $Q_j > 0$ for external inflows, $Q_j < 0$ is for sinks, and $Q_j = 0$ for simple junction nodes; P is the m-dimensional vector of nodal pressures; x, y are the n-dimensional vectors of flow rates and pressure drops on the branches; A_{s}, A_{e} are the $(m \times n)$ incidence matrices of outgoing and incoming branches relative to the nodes of the scheme, respectively, so that $A = A_{\mathrm{s}} + A_{\mathrm{e}}$; t_{s}, t_{e} are the n-dimensional vectors of temperature at the start and end of the branches; X is the diagonal matrix with elements x_i, $i = \overline{1,n}$, on the main diagonal; Q^{+}, Q^{-} are the m-dimensional diagonal matrices of nodal inflows and outflows with elements $Q_{jj}^{+} = \max\{Q_j, 0\}$, $Q_{jj}^{-} = \min\{Q_j, 0\}$ on the main diagonal, at $(Q^{+} + Q^{-})e_m = Q$, where e_m is the m-dimensional unit vector; T^{+} is the m-dimensional vector of external inflow temperature; T is the m-dimensional vector of mixed flow temperature at nodes; $f(x)$, $g(x,t_s,t_0)$ are the n-dimensional vector functions with elements $f_i(x_i)$ and $g_i(x_i,t_{s,i},t_0)$, respectively, $i=\overline{1,n}$, that represent the pressure and temperature drop on branches; t_0 is the ambient temperature.

The system of equations (1)–(3) for hydraulic conditions is solvable for unknown flow rates and pressures if the flow rate Q_j or pressure P_j is specified as a boundary condition at each node, with the pressure specified at least at one node. The system of equations (4)–(6) for thermal conditions is solvable for unknown temperatures if the temperatures T^+ of the external inflows at the source and the flow distribution x, Q are specified [34].

Analytical models and methods for probabilistic modeling of hydraulic conditions for the general case of an arbitrarily–configured pipeline system are given in [29, 30], while [31] and [32] focus on thermal conditions. In [33], a topological method is proposed for calculating the means and variances of the hydraulic parameters of a tree-configured pipeline system with one source, when $n=m-1$.

III. INITIAL PREMISES AND STATEMENT OF THE PROBLEM

Figure 1 shows the actual graphs of the time distribution for the frequencies of nodal flow (Fig. 1a) and nodal pressure (Fig. 1b). The first graph serves as a representation of a disturbance (a boundary condition), while the second illustrates a response (an operating parameter). Analysis of these processes shows [29] that the frequency distribution in any cross-section of both processes is quite satisfactorily approximated by normal distribution, their variance remains relatively constant over time, and the autocorrelation function stabilizes fairly quickly at zero. The hypothesis of the normal distribution law is not refuted by the goodness-of-fit test χ^2 at a 10% significance level. Thus, the problem of probabilistic

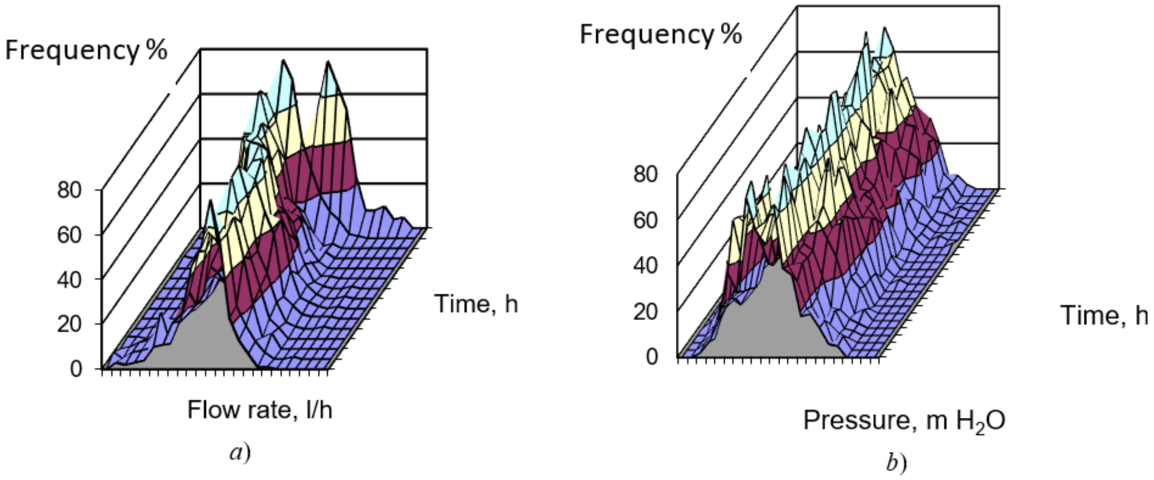

a) *b)*

Fig. 1. Change in the frequency distribution of operating parameters during the day: a) for nodal flow; b) for nodal pressure.

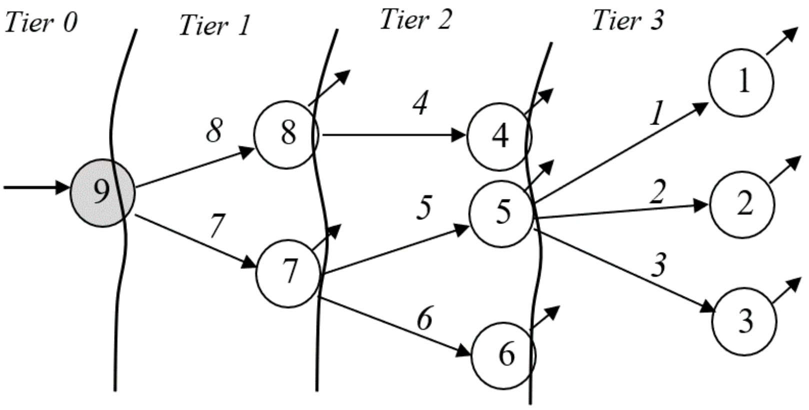

$i(e_i)$	s_i	k
1	5	3
2	5	3
3	5	3
4	8	2
5	7	2
6	7	2
7	9	1
8	9	1

Fig. 2. An example of a tree diagram numbered for calculation using the topological method.

modeling of steady-state thermal-hydraulic conditions can be reduced to finding the parameters of a normal distribution for a random vector of the conditions based on the known parameters of normally distributed boundary conditions, as random variables, and consists of the following.

The given parameters include a scheme of a tree-like pipeline network; hydraulic and thermophysical characteristics of all its components ($i=\overline{1,n}$ branches) accurate to coefficients; means and variances of nodal pressure (P_m) and temperature (T_m) at the source with node index *m*, nodal loads (Q_j) at the remaining nodes ($j=\overline{1,m-1}$), and ambient air temperature t_0. It is necessary to determine means and variances of the remaining operating parameters, i.e., flow rates at branches (x_i, $i=\overline{1,n}$), nodal pressures (P_j) and temperatures (T_j) for $j=\overline{1,m-1}$, as well as temperatures at the start $(t_{\mathrm{s},i})$ and end $(t_{\mathrm{e},i})$ of the branches, $i=\overline{1,n}$.

IV. Basic Principles of the Topological Method and Its Application in Probabilistic Hydraulic Calculation

Figure 2 shows an example of a tree diagram numbered in accordance with the following principles [33]: 1) the nodes and branches are numbered sequentially from the last tier of nodes to the root of the tree with the source of flow (*k* is the tier number); 2) the root of the tree has the number *m*, while the nodes most distant (by the number of branches) from the root have the first numbers; 3) the branch index is assigned to coincide with the index of its end node; 4) in this case, $i=\mathrm{e}_i=j$, and $\mathrm{s}_i>\mathrm{e}_i$, $i=\overline{1,n}$, where s_i, e_i are the indices of the start and end nodes of the *i*-th branch.

Let us illustrate the use of the topological method by an example of probabilistic calculation of the hydraulic parameters for a tree-configured network, under the following conditions: the specified parameters at the root node (source) are the mean $(\bar{P}_m)$ and the variance $(D(P_m))$ of the nodal pressure, and at the remaining nodes, these are the corresponding characteristics of the nodal flow rates $\bar{Q}_j$, $D(Q_j)$, $j=\overline{1,n}$. It is necessary to determine the means and the variance-covariances of the operating parameters x_i, y_i, P, $i=\overline{1,n}$, and Q_m.

By virtue of the introduced numbering of the calculated scheme components, the means of flow rates on the branches can be calculated sequentially using the formula

$$\bar{x}_i=\sum_{z\in I_i^-}\bar{x}_z+\bar{Q}_i,\ i=\overline{1,n}, \tag{7}$$

where I_i^- is the set of branches outgoing from node *i* and the condition $i>z\in I_i^-$ is satisfied, thus, by the time of calculation $\bar{x}_i$, all $\bar{x}_z$, $z\in I_j^-$ are already known. The mean of the nodal inflow from the source is determined as

$$\bar{Q}_m=\sum_{z\in I_m^-}\bar{x}_z\,. \tag{8}$$

The mean of pressure losses and nodal pressures are calculated using the formulas

$$\bar{y}_i\approx f_i(\bar{x}_i)\,,\ i=\overline{1,n}\,. \tag{9}$$

$$\bar{P}_i=\bar{P}_{\mathrm{s},i}-\bar{y}_i\,,\ i=\overline{n,1}\,. \tag{10}$$

In (10), the calculation begins for the nodes of tier $k=1$ when $\mathrm{s}_i=m$ and $\bar{P}_m$ is known. When calculating $\bar{P}_i$ for $k>1$, the values of $\bar{P}_{\mathrm{s},i}$ are also known, since $\mathrm{s}_i>i$.

Thus, the calculation of unknown means of operating parameters is reduced to two passes through the tree: 1) the forward pass ($i=\overline{1,n}$) to determine vectors $\bar{x}$, $\bar{y}$ and means of the nodal flow rate at the root of the tree $\bar{Q}_m$ using relations (7)–(9); 2) the backward pass ($i=\overline{n,1}$) to calculate $\bar{P}_1,...,\bar{P}_{m-1}$ using relation (10).

Variances and covariances can also be calculated using the finite formulas, relying on the fact that in the case of the tree-configured network at issue, matrix *A*, after deleting row *m*, acquires a triangular structure.

Variances of flow rates and pressure losses on the branches are determined from the formulas

$$D(x_i)=D(Q_i)+\sum_{z\in I_i^-}D(x_z)\,,i=\overline{1,n}. \tag{11}$$

$$D(y_i)\approx(f_{x,i}^{'})^2D(x_i),\ \ i=\overline{1,n}\,, \tag{12}$$

where $f_{x,i}^{'}=\partial f_i^{'}/\partial x_i$ is the derivative at point $\bar{x}_i$.

Variances of nodal pressures are determined from the relation

$$D(P_i)=D(P_{\mathrm{s},i})+D(y_i)+2f_{x,i}^{'}D(x_i)\,f_{\Sigma,i},\ \ i=\overline{n,1}\,, \tag{13}$$

where the value of $f_{\Sigma,i}$ accumulates recursively –

$$f_{\Sigma,m}=0,\ \ f_{\Sigma,i}=f_{\Sigma,\mathrm{s}i}+f_{x,i}^{'}\,,\ i=\overline{n,1}\,. \tag{14}$$

Variance of the flow rate at node *m* is determined as

$$D\left(Q_m\right)=\sum_{z\in I_m^-} D\left(x_z\right) . \tag{15}$$

As shown in [33], covariances can be simultaneously calculated

$$\operatorname{cov}(x_i, x_z)=\operatorname{cov}(x_z, x_i)=D\left(x_i\right),\ \ i<z\in R_i , \tag{16}$$

$$\begin{gathered}\operatorname{cov}(y_i, y_z)\approx f'_{x,i}\, f'_{x,z} \operatorname{cov}(x_i, x_z),\\ i\neq z,\ i,\ z=\overline{1,n-1},\ i<z\in R_i ,\end{gathered}\ , \tag{17}$$

where R_i is the set of branches belonging to the path from the root of the tree to node *i*.

V. PROBABILISTIC MODELING OF THERMAL CONDITIONS BY THE TOPOLOGICAL METHOD

Equations (4)–(6) of the thermal conditions for a hydraulically connected circuit with the root of the tree at node *m* can be written in the following index form:

$$\sum_{i\in I_m^-} x_i t_{\mathrm{s},i}-T_m^+ Q_m=0, \tag{18}$$

$$\sum_{i\in I_j^-} x_i t_{\mathrm{s},i}-x_j t_{\mathrm{e},j}-T_j Q_j=0,\quad j=\overline{1,m-1}, \tag{19}$$

$$t_{\mathrm{s},i}=T_j,\ \ j=\mathrm{s}_i,\ \ i=\overline{1,n}, \tag{20}$$

$$t_{\mathrm{e},i}=g_i(t_{\mathrm{s},i}, x_i, t_0),\ i=\overline{1,n}. \tag{21}$$

Given (20), it follows from (18) that $T_m\sum_{i\in I_m^-} x_i-T_m^+ Q_m=0$, and since $\sum_{i\in I_m^-} x_i=Q_m$, then $\bar{T}_m=\bar{T}_m^+,\ D(T_m)=D(T_m^+)$. It also follows from (20) that the means and variances of temperature at the beginning of all branches are calculated as

$$\bar{t}_{\mathrm{s},i}=\bar{T}_j,\quad D(t_{\mathrm{s},i})=D(T_j),\quad j=\mathrm{s}_i . \tag{22}$$

Statistical characteristics for $\bar{t}_{\mathrm{e},i}$ can be obtained from (21). Neglecting the nonlinear distortion of the function, we have

$$\bar{t}_{\mathrm{e},i}\approx g_i(\bar{t}_{\mathrm{s},i}, \bar{x}_i, \bar{t}_0)\ ,\ i=\overline{1,n} . \tag{23}$$

The expression for the variance $D(t_{\mathrm{e},i})=E(\xi_{t\mathrm{e},i}^2)=E[(t_{\mathrm{e},i}-\bar{t}_{\mathrm{e},i})^2]$, where E denotes the mean, is obtained on the basis of the linearized approximation of (21) $\xi_{t\mathrm{e},i}\approx g'_{t\mathrm{s},i}\,\xi_{t\mathrm{s},i}+g'_{t0}\xi_{t0}+g'_{x,i}\,\xi_{x,i}$, where $g'_{t\mathrm{s},i}=\dfrac{\partial g_i}{\partial t_{\mathrm{s},i}},\quad g'_{t0}=\dfrac{\partial g_i}{\partial t_0},\quad g'_{x,i}=\dfrac{\partial g_i}{\partial x_i}$. In this case,

$$\begin{gathered}D(t_{\mathrm{e},i})\approx\left(g'_{t\mathrm{s},i}\right)^2 D(t_{\mathrm{s},i})+\left(g'_{t0}\right)^2 D(t_0)+\\ +\left(g'_{x,i}\right)^2 D(x_i)+2g'_{t\mathrm{s},i}\, g'_{x,i} \operatorname{cov}(t_{\mathrm{s},i}, x_i),\end{gathered} \tag{24}$$

since random values of t_0 do not depend on the operating parameters and $\operatorname{cov}(t_0, t_{\mathrm{s},i})=\operatorname{cov}(t_0, x_i)=0$. In addition, $\operatorname{cov}(t_{\mathrm{s},i}, x_z)=0$ for $i\in I_m^-$ and $z=\overline{1,n}$, since $t_{\mathrm{s},i}=T_m$, $i\in I_m^-$, and the quantity T_m is statistically independent.

Now the means and variances of temperature of the inflows to the nodes of the next (first) tier are known $j\in I_m^-$. From (19), given (20), it follows that $T_j\left(\sum_{i\in I_j^-} x_i-Q_j\right)-x_j t_{\mathrm{e},j}=0$ and $x_j=\sum_{i\in I_j^-} x_i-Q_j$. In this case, we have $\bar{T}_j=\bar{t}_{\mathrm{e},j}$, $D(T_j)=D(t_{\mathrm{e},j})$.

For the branches of the second tier $i\in I_j^-$, where $j\in I_m^-$, according to (22), we have $\bar{t}_{\mathrm{s},i}=\bar{T}_j$, $D(t_{\mathrm{s},i})=D(T_j)$. The variances $D(t_{\mathrm{e},i})$, $i\in I_j^-$ are determined in accordance with (24). However, here, $\operatorname{cov}(t_{\mathrm{s},i}, x_i)\neq 0$ already. Given that $t_{\mathrm{s},i}=T_j=t_{\mathrm{e},j}$, we have $\operatorname{cov}(t_{\mathrm{s},i}, x_i)=\operatorname{cov}(T_j, x_i)=\operatorname{cov}(t_{\mathrm{e},j}, x_i)$, $i\in I_j^-$. In this case, $\operatorname{cov}(t_{\mathrm{e},j}, x_i)=E(\xi_{t\mathrm{e},j}\xi_{x,i})\approx E[(g'_{t\mathrm{s},j}\xi_{t\mathrm{s},j}+g'_{t0}\xi_{t0}+g'_{x,j}\xi_{x,j})\xi_{x,i}]$, $i\in I_j^-$, from where

$$\begin{gathered}\operatorname{cov}(t_{\mathrm{s},i}, x_i)=g'_{t\mathrm{s},j} \operatorname{cov}(t_{\mathrm{s},j}, x_i)+\\ +g'_{x,j} \operatorname{cov}(x_j, x_i),\ \ i\in I_j^-,\end{gathered}$$

or, given (16), we have

$$\operatorname{cov}(t_{\mathrm{s},i}, x_i)=g'_{t\mathrm{s},j} \operatorname{cov}(t_{\mathrm{s},j}, x_i)+g'_{x,j} D(x_i),\ \ i\in I_j^- , \tag{25}$$

since we assume $\operatorname{cov}(t_0, x_i)=0$, j is the index of the node from which the *i*-th branch originates. Therefore, for the second and subsequent tiers, the value $\operatorname{cov}(t_{\mathrm{s},i}, x_i)$ must be calculated in advance.

Thus, the calculation of the probabilistic parameters of temperature distribution for a hydraulically connected tree-like scheme is reduced to a single pass through its components, starting from the root of the tree downstream.

VI. TOPOLOGICAL ALGORITHM FOR PROBABILISTIC CALCULATION OF THERMAL-HYDRAULIC CONDITIONS

Based on the aforementioned, we propose the following topological algorithm for integrated probabilistic modeling of the hydraulic and thermal conditions of a tree-configured network with one source, which is reduced to two passes through the tree of the calculated scheme.

1. Forward pass (from consumers to a source). For $i=\overline{1,n}$, calculate $\bar{x}_i$, $D\left(x_i\right)$ using (7), (11) and $\bar{y}_i$,

$D(y_i)$ using (9), (12); for $t=\overline{1,n-1}$, $t \neq i$, calculate $\text{cov}(x_i, x_t)$ and $\text{cov}(y_i, y_t)$ using (16) and (17); determine $\bar{Q}_m$, $D(Q_m)$ using (8), (15).

2. Backward pass (from a source to consumers). Assume $f_{\Sigma,m}=0$, $\bar{T}_m=\bar{T}_m^+$, $D(T_m)=D(T_m^+)$. For each $i=\overline{n,1}$, determine $\bar{P}_i$, $D(P_i)$ using (10) and (13), having previously calculated $f_{\Sigma,i}$ by (14); determine $\bar{t}_{\mathrm{s},i}=\bar{T}_{\mathrm{s},i}$, $D(t_{\mathrm{s},i})=D(T_{\mathrm{s},i})$, $\bar{t}_{\mathrm{e},i} \approx g_i(\bar{t}_{\mathrm{s},i}, \bar{x}_i, \bar{t}_0)$ using (23), and $D(t_{\mathrm{e},i})$ using (24), having previously calculated $\text{cov}(t_{\mathrm{s},i}, x_i)$ by (25).

VII. A NUMERICAL CASE STUDY

Let us present the calculation results for the distribution parameters of thermal-hydraulic conditions for the calculated scheme shown in Fig. 1. The hydraulic characteristics of the branches have the form $f_i(x_i)=s_{h,i}\,|\,x_i\,|\,x_i$, $i=\overline{1,n}$, where $s_{h,i}$ is the hydraulic resistance of the *i*-th branch, and the thermal characteristics are $t_{\mathrm{e},i}=t_0+\left(t_{\mathrm{s},i}-t_0\right)\exp\left(-r_i/x_i\right)$, $i=\overline{1,n}$, where $r_i=\left(\pi d_i l_i K_i\right)/c$ is the thermal resistance; d_i, l_i, K_i are the diameter, length, and heat transfer coefficient for the *i*-th branch; π is the pi number; c = 1 kcal/(kg ° C) is the specific heat capacity of the coolant (water). The expressions for the derivatives are $f'_{x,i}=2s_{h,i}x_i$; $g'_{\mathrm{ts},i}=e^{-r_i/x_i}$; $g'_{t0,i}=1-e^{-r_i/x_i}$; and $g'_{x,i}=(t_{\mathrm{s},i}-t_0)(r_i/x_i^2)e^{-r_i/x_i}$, respectively.

The values of boundary conditions are $\bar{t}_0=-20$ ºC, $D(t_0)=1$, $\bar{P}_9=60$ m H_2O, $D(P_9)=0.04$, $\bar{T}_9=105$ ºC, $D(T_9^+)=6.4$, $\bar{Q}=\{20;\ 35;\ 27;\ 18;\ 25;\ 35;\ 40;\ 80\}$ and

TABLE 1. Means and Variances of Nodal Pressures and Temperatures, Calculated Using Different Methods

j	Topological method				Monte-Carlo method			
	$\bar{P}_j$, m	$D(P_j)$	$\bar{T}_j$, ºC	$D(T_j)$	$\bar{P}_j$, m	$D(P_j)$	$\bar{T}_j$, ºC	$D(T_j)$
1	46.20	0.91	97.22	5.83	46.24	0.95	97.13	5.33
2	42.67	1.43	98.08	5.80	42.73	1.54	98.01	5.38
3	45.47	1.34	98.85	5.99	45.50	1.37	98.76	5.65
4	49.95	1.36	95.38	7.89	49.88	1.39	95.04	8.03
5	47.20	0.80	102.77	6.18	47.24	0.83	102.73	5.74
6	53.43	0.20	102.24	6.14	53.44	0.21	102.19	5.71
7	53.76	0.18	103.99	6.29	53.77	0.18	103.96	5.86
8	50.93	0.64	102.79	6.18	50.91	0.65	102.76	5.76

TABLE 2. Means and Variances of Flow Rates and Temperatures at the End of Branches, Calculated Using Different Methods

i	Topological method				Monte Carlo method			
	$\bar{x}_i$, m^3/h	$D(x_i)$	$\overline{tk}_i$, ºC	$D(tk_i)$	$\bar{x}_i$, m^3/h	$D(x_i)$	$\overline{tk}_i$, ºC	$D(tk_i)$
1	20	2.37	97.2	5.83	19.94	2.35	97.1	5.33
2	35	3.80	98.0	5.80	34.87	4.13	98.0	5.38
3	27	8.23	98.8	5.99	26.93	7.95	98.7	5.65
4	18	13.83	95.3	7.89	18.03	13.90	95.0	8.53
5	107	19.56	102.7	6.18	106.66	19.98	102.7	5.74
6	35	8.17	102.2	6.14	34.95	7.83	102.1	5.71
7	182	30.11	103.9	6.29	181.64	31.42	103.9	5.86
8	98	17.64	102.7	6.18	98.01	18.07	102.7	5.76

$D(Q) = \{2.37;\ 3.8;\ 8.23;\ 13.83;\ 5.15;\ 8.17;\ 2.37;\ 3.8\}$. Hydraulic and thermal resistances of the branches are $s_h =$ {0.0025; 0.0036; 0.0023; 0.003; 0.0005; 0.0002; 0.0001; 0.0009} and $r = \{0.33;\ 0.48;\ 0.31;\ 0.4;\ 0.38;\ 0.18;\ 0.53;\ 0.62\}$, respectively.

The results of calculations by the topological and matrix stepwise methods completely coincide. Tables 1 and 2 show the results of comparison for the topological and Monte-Carlo methods (with the number of realizations of random values of boundary conditions $N = 1\,000$), when used to calculate means and variances of the thermal-hydraulic parameters.

The Tables indicate that the variances and means of all operating parameters remain below 1%, with discrepancies in the variances of these parameters not exceeding 10%. With an increase in the number of realizations of random values of the boundary conditions in the Monte Carlo method by an order of magnitude ($N = 10\,000$), the discrepancies according to the calculation results for means and variances remain within the same limits (1% and 10%, respectively), while the calculation time increases by more than an order of magnitude, which is in full agreement with the theory [28].

Figure 3 shows graphs of the computation time for different methods (topological, matrix stepwise, and Monte Carlo methods) as a function of the network dimension (the number of nodes) under comparable algorithmic conditions in the Maple mathematical software. As seen in the Figure, as the number of network nodes rises, the computation time increases proportionally for all methods. However, the topological method requires several times less computation time than the matrix stepwise method and several orders of magnitude less time than Monte-Carlo method, even for $N = 1\,000$, and this gap expands as the network dimension grows.

The obtained results enable the construction of intervals, or confidence regions, that contain operating parameters with a given probability, as well as the assessment of the probabilities of violating the required or permissible operating parameters. For example, let the minimum permissible pressure (under the condition that connected consumers are provided with a specified flow rate) be $\underline{P} = 50$ m H_2O. In this case, the probability that the pressure at node 4 will be less than this value is $p(P_4 < \underline{P}) \approx 0.52$, and at node 8 – $p(P_8 < \underline{P}) \approx 0.12$. This means that for a consumer at node 4, the probability of not receiving the target product is significantly greater than for a consumer at node 8. The probabilities of compliance with regulatory or contractual requirements can be similarly analyzed for other operating parameters or their combinations. For example, for the minimum required temperature at consumption nodes $\underline{T} = 100\,^{\circ}$C, adjacent nodes on the third branch have different probabilities of meeting this requirement, $p(T_3 < \underline{T}) \approx 0.68$ and $p(T_5 < \underline{T}) \approx 0.13$.

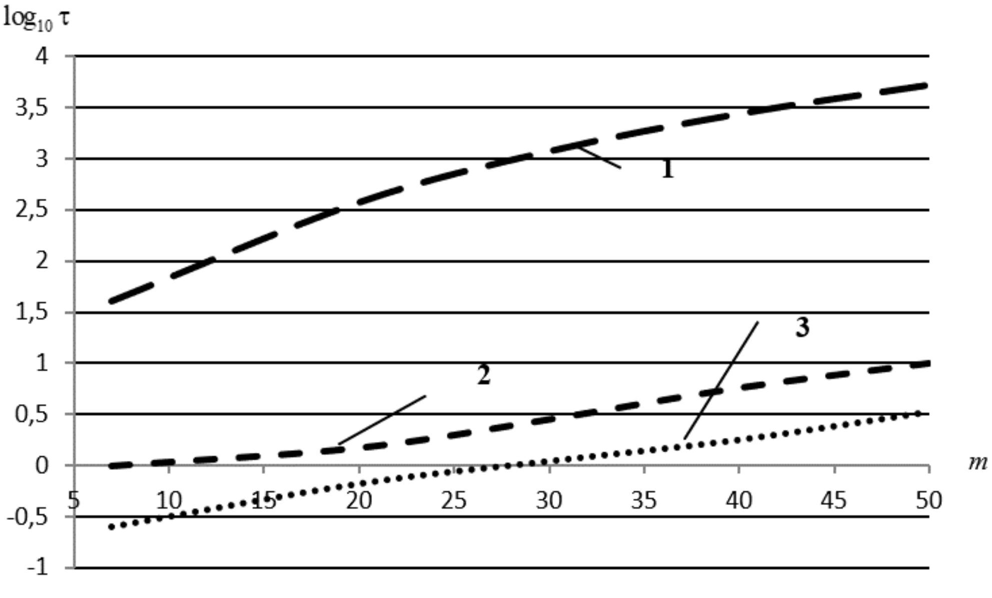

Fig. 3. Illustration of comparative calculation efficiency for different methods: 1 – Monte Carlo method (N = 1 000), 2 – Matrix stepwise method, 3 – Topological method; t – calculation time, s; m – the number of nodes in the calculated scheme.

VIII. CONCLUSIONS

In this study, the independent problem of probabilistic modeling of steady-state thermal-hydraulic conditions of a tree-configured pipeline system has been formulated for the first time. A new algorithm has been developed to solve this problem through the combined calculation of all statistical parameters of the hydraulic and thermal conditions within a single computational process. This algorithm involves traversing the components of the calculated scheme and using finite formulas instead of labor-intensive matrix operations in the general case of an arbitrarily configured pipeline system. The numerical example demonstrates the acceptable accuracy of the results obtained by the proposed method, highlighting its superior computational efficiency compared to other alternative methods.

REFERENCES

[1] V. I. Kucheryavyi, S. N. Mil'kov, “Statistical modeling of the remaining life of a section of a main gas pipeline by low-cycle loading,” *Journal of Machinery Manufacture and Reliability*, vol. 37, no. 3. pp. 305–310, 2008.

[2] F. Chen, C. Wu, “A novel methodology for forecasting gas supply reliability of natural gas pipeline systems,” *Front. Energy*, vol. 14, no. 2, pp. 213–223, 2020.

[3] P. Praks et al., “Probabilistic modeling of security of supply in gas networks and evaluation of new infrastructure,” *Reliability Engineering and System Safety*, no. 144, pp. 254–264, 2015.

[4] M. D. Pandey, “Probabilistic models for condition assessment of oil and gas pipelines,” *NDT&E International*, vol. 1, no. 5, pp. 349–358, 1998.

[5] L. Wu, M. Shahidehpour, “Optimal coordination of stochastic hydro and natural gas supplies in midterm operation of power systems,” *IET Gen. Transm. Distrib.*, vol. 5, no. 5, pp. 577–587, 2011.

[6] X. Wu, C. Li, Y. He, W. Jia, “Operation optimization of natural gas transmission pipelines based on stochastic optimization algorithms: A review,” *Mathematical Problems in Engineering*, vol. 2018, no. 6, Art. no. 1267045, 2018. DOI: 10.1155/2018/1267045.

[7] X. Zhang, M. Shahidehpour, A. Alabdulwahab, A. Abusorrah, “Hourly electricity demand response in the stochastic day-ahead scheduling of coordinated electricity and natural gas networks,” *IEEE Transactions on Power Systems*, vol. 31, no. 1, pp. 592–601, 2016.

[8] L. Bai, F. Li, H. Cui et al., “Interval optimization based operating strategy for gas-electricity integrated energy systems considering demand response and wind uncertainty,” *Applied Energy*, no. 167, pp. 270–279, 2016.

[9] S. Balaei-sani, F. Jabari, B. Mohammadi-Ivatloo, “Stochastic analysis of gas-electricity hybrid grid using Nataf transformation combined with point estimation method,” in *Integration of Clean and Sustainable Energy Resources and Storage in Multi-Generation Systems*, Springer, Cham, 2020, pp. 259–281.

[10] L. Yang, X. Zhao, X. Li, W. Yan, “Probabilistic steady-state operation and interaction analysis of integrated electricity, gas and heating systems,” *Energies*, vol. 11, no. 4, Art. no. 917, 2018. DOI: 10.3390/en11040917.

[11] Y. Hu, H. Lian, Z. Bie, B. Zhou, “Unified probabilistic gas and power flow,” *Journal of Modern Power Systems and Clean Energy*, vol. 5, pp. 400–411, 2017.

[12] J. H. Zheng, W. Xiao, C. Q. Wu, et al., “A gradient descent direction based cumulants method for probabilistic energy flow analysis of individual based integrated energy systems,” Energy, Vol. 265, 2023. ID: 126290.

[13] I. Postnikov, V. Stennikov, “Modifications of probabilistic models of evolutionary states for reliability analysis of district heating systems,” *Energy Reports*, no. 6, pp. 293–298, 2020.

[14] M. Salehimaleh, A. Akbarimajd, K. Valipour, A. Dejamkhooy, “Uncertainty modeling in operation of multi-carrier energy networks,” in *Planning and Operation of Multi-Carrier Energy Networks*, M. Nazari-Heris, S. Asadi, B. Mohammadi-Ivatloo, Eds. Springer, Cham, 2021, pp. 257–338. DOI: 10.1007/978-3-030-60086-0_12.

[15] M. Fayzul, K. Pasha, K. Lansey, “Strategies to develop warm solutions for real-time pump scheduling for water distribution systems,” *Water Resource Management*, vol. 28, pp. 3975–3987, 2014.

[16] E. L. Segarra, G. R. Ruiz, C. F. Bandera, “Probabilistic load forecasting for building energy models,” *Sensors*, vol. 20, no. 22, Art. no. 6525, 2020. DOI: 10.3390/s20226525.

[17] M. J. Ritchie, J. A. A. Engelbrecht, M. J. Booysen, “A probabilistic hot water usage model and simulator for use in residential energy management,” *Energy & Buildings*, vol. 235, Art. no. 110727, 2021.

[18] G. Yi, X. Zhuang, Y. Li, “Probabilistic state estimation in district heating grids using deep neural network,” *Sustainable Energy, Grids and Networks*, vol. 38, Art. no. 101353, 2024. DOI: 10.1016/j.segan.2024.101353.

[19] A. Bott, T. Janke, F. Steinke, “Deep learning-enabled MCMC for probabilistic state estimation in district heating grids,” *Applied Energy*, vol. 336, Art. no. 120837, 2023.

[20] G. Sun, W. Wang, Y. Wu, et al., “A nonlinear analytical algorithm for predicting the probabilistic mass flow of a radial district heating network,” *Energies*, vol. 12, no. 7, Art. no. 1215, 2019. DOI: 10.3390/en12071215.

[21] A. V. Babayan, Z. Kapelan, D. A. Savic, G. A. Walters, “Least-cost design of water distribution networks under demand,” *J. Water Resour. Plann. Management*, vol. 131, no. 5, pp. 375–382, 2005.

[22] Z. Kapelan, A. V. Babayan, D. A. Savic, G. A. Walters, S. T. Khu, “Two new approaches for the stochastic least cost design of water distribution systems,” *Water Science and Technology: Water Supply*, vol. 4, no. 5–6, pp. 355–363, 2004.

[23] R. Gargano, C. Tricarico, F. Granata, et al., “Probabilistic models for the peak residential water demand,” *Water*, vol. 9, no. 6, Art. no. 417, 2017.

[24] V. H. Alcocer-Yamanaka, V. G. Tzatchkov, F. I. Arreguin-Cortes, “Modeling of drinking water distribution networks using stochastic demand,” *Water Resource Management*, vol. 26, pp. 1779–1792, 2012.

[25] A. Gabriele, F. Di Palma, E. Todini, R. Gargano, “Probabilistic forecast for real-time control of rainwater pollutant loads in urban environments,” *Hydrology*, vol. 12, no. 11, Art. no. 289, 2025. DOI: 10.3390/hydrology12110289.

[26] A. Z. Gamm, *Probability models of electric power system operation*. Novosibirsk, Russia: Nauka, Siberian Publishing Company, 1993, 133 p. (In Russian)

[27] E. V. Boloev, I. I. Golub, “Use the probabilistic load flow methods for solution of problems in electric power systems,” *Bulletin of SSTU*, vol. 1, no. 2(64), pp. 110–119, 2012. (In Russian)

[28] I. M. Sobol, Numerical *Monte Carlo Methods*. Moscow, Russia: Nauka, 1973, 311 p. (In Russian)

[29] N. N. Novitsky, O. V. Vanteeva, “Problems and methods of probabilistic modeling of hydraulic conditions in pipeline systems,” *Scientific and Technical Bulletin of SPbSTU*, no. 1(53), pp. 68–75, 2008. (In Russian)

[30] N. N. Novitsky, O. V. Vanteeva, “Modeling the stochastics of flow distribution in hydraulic circuits,” *Proceedings of the Russian Academy of Sciences. Power Engineering*, no. 2, pp. 145–154, 2011. (In Russian)

[31] O. V. Vanteeva, N. N. Novitsky, “Study on problems of probabilistic modeling of temperature conditions in hydraulic circuits,” in *Energy Pipeline Systems: Mathematical and Computer Technologies of Intelligentization*, N. N. Novitsky, Ed. Novosibirsk, Russia: Nauka, 2017, pp. 60–71.

[32] N. N. Novitsky, O. V. Vanteeva, “Analysis of hydraulic conditions of pipeline systems under probabilistic nodal boundary conditions,” *Proceedings of ISTU*, vol. 21, no.8 (127), pp. 130–142, 2017. (In Russian)

[33] N. N. Novitsky, O. V. Vanteeva, “Probabilistic modeling of hydraulic conditions of tree-structured pipeline networks using a topological method,” *Proceedings of the Russian Academy of Sciences. Power Engineering*, no. 6, pp. 12–23, 2017. (In Russian)

[34] A. P. Merenkov, V. Ya. Khasilev, *Theory of hydraulic circuits*. Moscow, Russia: Nauka, 1985, 280 p. (In Russian)

N.N. Novitsky, D.Eng., is presently the Head of the Laboratory of Pipeline and Hydraulic Systems at the L.A. Melentiev Energy Systems Institute of the Siberian Branch of the Russian Academy of Sciences. N.N. Novitsky has authored and co-authored over 250 scientific publications. His research interests include the theory of hydraulic circuits; theory and methods of analysis, control, optimization and identification of pipeline systems; mathematical modeling; computer modeling; information technology; software and computing systems.

O.V. Vanteeva, Ph.D., is a Research Associate in the Laboratory of Pipeline and Hydraulic Systems at the L.A. Melentiev Energy Systems Institute of the Siberian Branch of the Russian Academy of Sciences. O.V. Vanteeva has authored and co-authored over 40 scientific publications. Her research interests include advancing approaches and methods for probabilistic modeling of pipeline systems, enabling effective analysis of their performance.

An Approach to Load Balancing in Power Distribution Networks Based on Electric Revenue Metering Data

T.T. Omorov[1,*], K.E. Zakiriaev[2], B.K. Takyrbashev[1], T.M. Zholdoshev[3]

[1] Institute of Mechanical Engineering and Automation, National Academy of Sciences of the Kyrgyz Republic, Bishkek, Kyrgyzstan
[2] K. Tynystanov Issyk-Kul State University, Karakol, Kyrgyzstan
[3] Osh State University, Osh, Kyrgyzstan

Abstract **— The study focuses on unbalanced power distribution networks operating within integrated hardware and software solutions in Automated Systems of Electric Revenue Metering (ASERM) designed to automate and digitalize electricity monitoring and metering processes. Unbalanced load flows in power distribution networks cause significant active power loss and, consequently, compromise the efficiency and techno-economic performance of these networks. This study seeks to minimize technical power loss in power distribution networks through the development of an Automatic Control System (ACS) within the ASERM structure for balancing the three-phase network. Previous studies show that modern ASERM implementations lack technologies capable of solving the problem. We propose a method for designing a digital ACS controller whose primary function is to maintain the required phase power levels in specific sections of the network in real time. Conceptually, the method is based on the idea of redistributing load flows between power distribution network phases by appropriately switching single-phase customers to minimize deviations of phase powers from their set values. To achieve the effective control, criterion functions are built to serve as quality metrics of ACS performance and algorithms are designed to govern the operation of the digital controller and generate controls to be applied to the controlled object. The controls are represented as a digital code containing data on the coordinates of electricity meters of three-phase network customers that are to be switched to another phase. The findings from the study aim at improving the automation and digitalization of power distribution networks (PDN) and enhancing their reliability.**

Index Terms **— Power distribution system, network balancing, digital controller.**

I. INTRODUCTION

It is well known that current and voltage unbalance in power distribution systems causes significant electricity loss [1–3]. According to the published research, in networks with distributed loads, deviations (unbalances) of phase currents from their average value result in substantially increased technical loss. Experimental evidence from power supply systems shows that technical loss in power transmission lines and their feeding transformer substations (TS) accounts for more than 6% of the total amount of electricity fed into power distribution networks [1]. Furthermore, power quality deteriorates, increasing the likelihood of failure of household appliances and industrial equipment. Various methods and devices are proposed for load balancing in power distribution networks [4–9]. Their practical application, however, is hindered by the technical complexity of creating automated balancing systems for three-phase distribution networks with a large

---

[*] Corresponding author.
E-mail: omorovtt@mail.ru

DOI: 10.25729/esr.2025.04.0003

Received September 25, 2025. Revised October 29, 2025. Accepted December 11, 2025. Available online December 29, 2025.

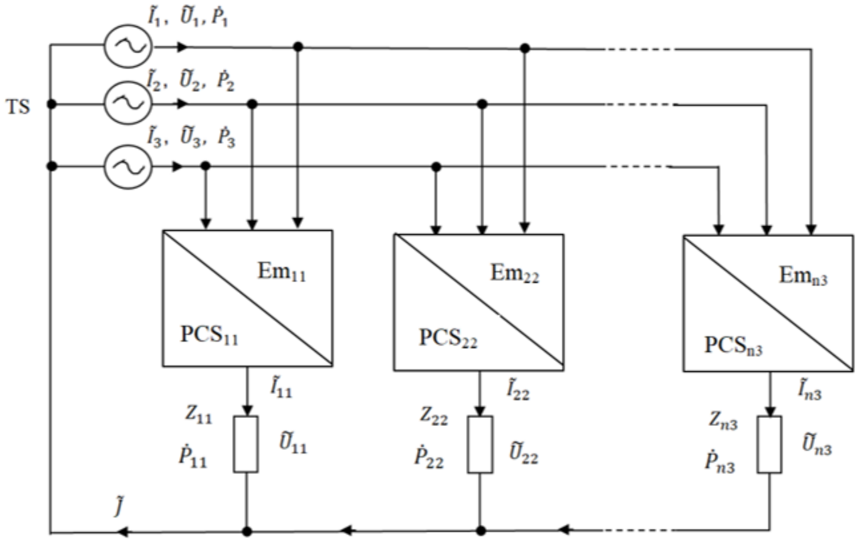

Fig. 1. Schematic diagram of a power distribution network with $Em_{k\nu}$ and $PCS_{k\nu}$.

number of electricity consumers. The technical implementation of these solutions requires the creation of separate local subsystems at the points where loads are connected to network phases. These subsystems must include individual units for performing measurement, parameter monitoring, and data processing. The design of such subsystems involves rather complex processing algorithms based on measurements of a set of data-driven parameters. For example, the technique reported in [4] requires measuring the active power of the neutral conductor of the line, as well as voltage and current signals of the neutral conductor at the points where loads are connected to the network. The reactive power control system in [4] uses the positive-, negative-, and zero-sequence currents of the loads. Modern electricity meters [10, 11] operating within the Automated System for Electric Revenue Metering (ASERM) lack such measurement capabilities, which makes it problematic to use the above technologies in modern ASERM systems. The studies [12, 13] contribute a possible solution to the problem through the creation of a digital automated control system for load balancing within the data concentrator (DC) of the ASERM.

This paper aims to further advance the approaches proposed in [12, 13].

II. PROBLEM STATEMENT

We consider a three-phase four-wire power distribution network connected to a feeding transformer substation (TS) and a group of n electricity meters $\{Em_{k\nu}\}$ installed at single-phase consumers. Its schematic diagram is shown in Fig. 1, where k and ν are index variables denoting, respectively, the phase numbers A, B, C ($k=\overline{1,3}$) and the load (electrical appliance) numbers of the PDN customers ($\nu=\overline{1,n}$); $\tilde{I}_k$ and $\tilde{U}_k$ are the sinusoidal instantaneous current and voltage at the input of the k-th phase; $\dot{Z}_{k\nu}$ is the load impedance with coordinates (k,ν); $\tilde{I}_{k\nu}$ and $\tilde{U}_{k\nu}$ are the instantaneous current and voltage of the load $\dot{Z}_{k\nu}$; $\tilde{J}_\nu$ is the instantaneous current in the ν-th section of the neutral conductor; $\dot{S}_k$ is the complex power of the k-th phase; $\dot{S}_{k\nu}$ is the complex power consumed by the load of the customer with coordinates (k,ν); $PCS_{k\nu}$ is the phase-current switch of meter $Em_{k\nu}$.

The following assumptions are made:

1) The three-phase PDN operates under current and voltage unbalance;

2) The electricity meters ($Em_{k\nu}$) are equipped with phase-current switches ($PCS_{k\nu}$);

3) The data concentrator (DC) polls the main three-phase electricity meter (Em^{TS}) and the groups of customer meters connected to phases A, B, C at discrete time instants $t=t_\xi$ ($\xi=1,2,\dots$), recording the following quantities in the ASERM database:

- Active powers $p_{k\nu}$ and reactive powers $q_{k\nu}$ consumed by customer loads with coordinates (k, ν);
- Active powers p_k and reactive powers q_k consumed by the corresponding phases at the input of the three-phase network.

The technical power loss in the TS and the network are largely determined by the effective (root mean square, RMS) currents $J_1, J_2, \ldots, J_n$ flowing in the corresponding sections of the neutral conductor. The smaller these currents, the higher the level of network unbalance and the lower the power losses. Therefore, the quality and efficiency of the PDN can be evaluated by the following objective function:

$$E = \sum_{\nu=1}^{n} J_\nu . \tag{1}$$

Minimizing the efficiency index E is equivalent to optimizing the load flow of an unbalanced PDN, in which the unbalance of the total power consumed by each network phase is reduced to a minimum. To this end, it is advisable to design a power loss control system based on the balancing of phase loads and relying on criterion functions [12] and computational methods [14, 15].

In our earlier studies [12, 13], due to the complexity of controlling technical power loss, we implement the balancing process only for the initial section of the PDN, since a large share of load unbalance-related loss occurs in the transformer substation. In an unbalanced load flow, the effective values of the above currents can become significant due to the phase-current unbalance. The smaller these values, the higher the balancing level of the network and the lower the active power loss. Thus, the sum of the effective currents in the neutral conductor of a three-phase network can serve as an objective (criterion) function, i.e., a metric of the quality and efficiency of the distribution system. By minimizing this criterion, it is possible to optimize the load flow of the PDN. To this end, we propose using an automatic control system for technical losses in the distribution network, whose main functional component is a microprocessor-based digital controller. The primary function of the digital controller is to process load-state data to determine the coordinates of those customers whose loads must be switched from more heavily loaded phases to less loaded ones [12, 13] to minimize the criterion function. Consequently, control u is generated for the facility, which includes a group of loads with electronic electricity meters $\{Em_{k\nu}\}$ installed at the customers of the three-phase network. Control signal u is the digital code of a command containing information on the coordinates of the corresponding customer meters and the phases of the three-phase network where the required switching operations must be performed. This control information is transmitted via a communication channel to the customer meters, which must be equipped with special devices — phase-current switches (PCS). The practical implementation of this principle of redistributing load flows between network phases is feasible, since phase-current switches have already been designed and tested [7, 8]. It should be noted that modern ASERM systems can use microprocessor-based electricity meters that allow synchronized real-time measurements of the required data with accuracy of up to 2% [10, 11]. The meter readings are recorded at the moments of their remote polling.

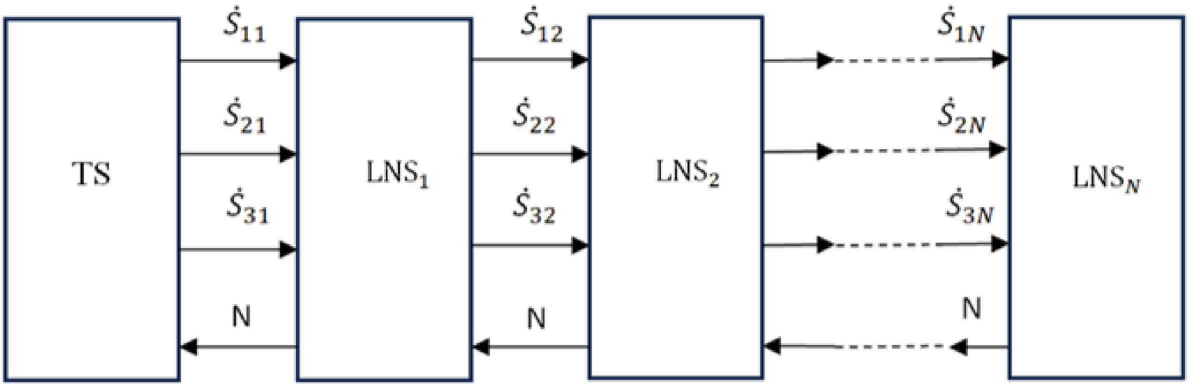

Fig. 2. Schematic of a power distribution system divided into N modules.

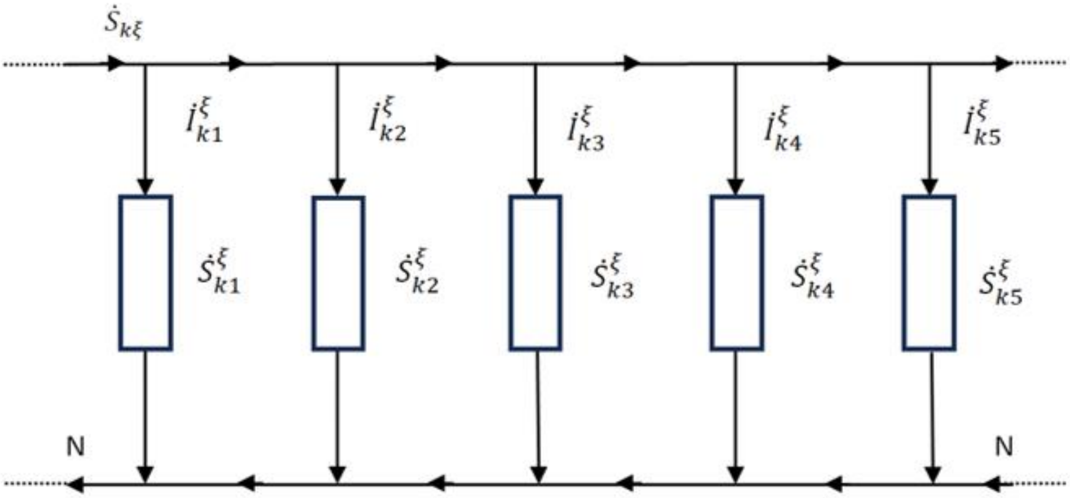

Fig. 3. Schematic of a local network section LNS_{ξ}.

The task is to determine the structure and operating algorithm of the digital controller that ensures the minimization of technical power losses in the PDN based on ASERM data.

III. CONCEPT OF POWER LOSS CONTROL IN THE NETWORK

Further research reveals that a more effective method for controlling technical loss is based on the decomposition of the PDN into a number of local network sections (LNS), each combining a group of adjacent loads (customers) that are invariant (independent) with respect to certain electrical variables of the PDN. Such variables may include the total power consumed by the local PDN sections, as well as the total currents of the customer loads connected to the phases of the LNS. Selecting the composition of an LNS, it is essential to ensure the presence of at least one single-phase customer electricity meter. Figure 2 shows a schematic of a PDN divided into LNSs.

Here, $\dot{S}_{k\xi}$ is the total complex power of the network module with coordinates (k,ξ), where ξ is the serial number of the module.

Figure 3 illustrates the concept of the local network section (LNS_{ξ}) for a subsection of the k-th phase.

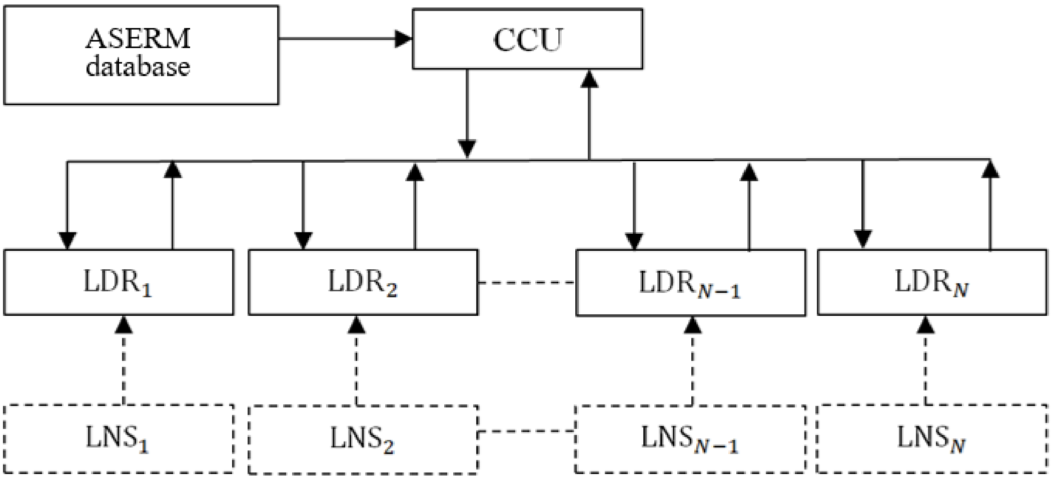

Fig. 4. Schematic of the digital controller system.

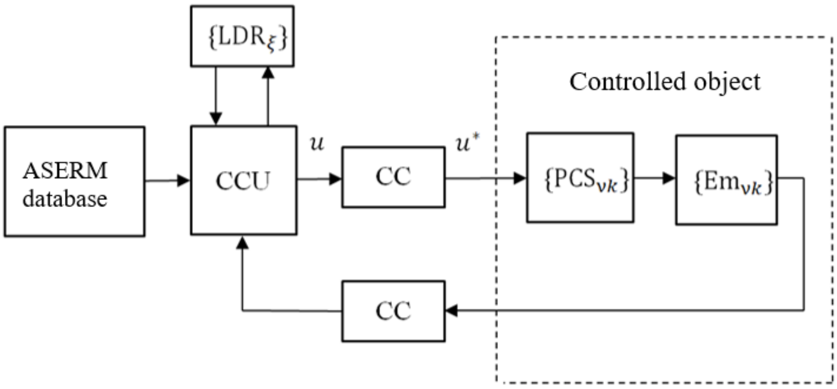

Fig. 5. The functional structure of the power loss control system.

Here, $\dot{S}^{\xi}_{k\nu}$ is the complex power of the load of a customer in LNS_ξ with coordinates (k,ν). The total power consumed by LNS_ξ is

$$\dot{S}^{\xi}_{k\xi} = \sum_{\nu=1}^{N_\xi} S^{\xi}_{k\nu}\ , \tag{2}$$

where N_ξ is the number of loads in the ξ -th local network section.

This approach enables the study on the operation of each local section independently of the others. Moreover, it facilitates designing an individual local digital controller (LDC) for each section, whose main function is to ensure the balancing process of the corresponding LNS. Local controllers allow for parallel data processing, which significantly speeds up computations. The independent LDCs are coordinated by a central control unit (CCU) relying on information from all LDCs and the ASERM database (Fig. 4).

Based on the preliminary processing of data obtained from customer electricity meters, the CCU:

- Determines the composition of the LNS in the PDN;
- Calculates setpoints for all digital controllers;
- Generates controls (u) for the controlled object, consisting of a group of phase-current switches { $PCS_{k\nu}$ } and customer meters { $Em_{k\nu}$ }, using the results of the LDCs' operation. Control commands can be transmitted via a communication channel (CC) using PLC or GSM technologies. Figure 5 shows the functional structure of the power loss control system.

In our earlier studies [12, 13], due to the complexity of controlling technical power loss, we implement the balancing process only for the initial section of the PDN, since a large share of load unbalance- related loss occurs in the transformer substation.

Based on the preliminary processing of data obtained from customer electricity meters, the CCU:

- Determines the composition of the LNS in the PDN;
- Calculates setpoints for all digital controllers;
- Generates controls (u) for the controlled object, consisting of a group of phase-current switches { $PCS_{k\nu}$ } and customer meters { $Em_{k\nu}$ }, using the results of the LDCs' operation. Control commands can be transmitted via a communication channel (CC) using PLC or GSM technologies. Figure 5 shows the functional structure of the power loss control system.

In our earlier studies [12, 13], due to the complexity of controlling technical power loss, we implement the balancing process only for the initial section of the PDN, since a large share of load unbalance- related loss occurs in the transformer substation.

The technical implementation of the CCU and the LDCs can be carried out using a microprocessor-based controller.

IV. Scenario Analysis of the Controlled Object

The balancing process for each local network section (LNS_ξ) is carried out as follows. The input data for the problem are the measured active powers $p^{\xi}_{k\nu}$ and reactive powers $q^{\xi}_{k\nu}$ consumed by the loads of LNS_ξ. The total complex power of LNS_ξ can be calculated as

$$\dot{S}_{k\xi} = \sum_{\nu=1}^{N_\xi}\left(p^{\xi}_{k\nu} + jq^{\xi}_{k\nu}\right) = S_{k\xi}e^{j\varphi_{k\xi}}\ , \tag{3}$$

where $S_{k\xi}$ and $\varphi_{k\xi}$ are the magnitude and phase of the complex power $S_{k\xi}$, respectively, and $j=\sqrt{-1}$ is the imaginary unit. Next, the average power S_ξ over the phases of the considered LNS_ξ is determined as

$$S_\xi = \frac{S_{1\xi}+S_{2\xi}+S_{3\xi}}{3}. \tag{4}$$

The deviations from the average value S_ξ, i.e., the phase mismatches for the local network section, are then calculated as

$$\begin{aligned} e_{1\xi} &= S_{1\xi}-S_\xi, \\ e_{2\xi} &= S_{2\xi}-S_\xi, \\ e_{3\xi} &= S_{3\xi}-S_\xi, \end{aligned} \tag{5}$$

which forms the mismatch vector $e_\xi=\left[e_{1\xi},e_{2\xi},e_{3\xi}\right]$. It is important to note that the quantities $e_{1\xi}$, $e_{2\xi}$ and $e_{3\xi}$, as defined by (5), essentially represent control errors (mismatches) that should tend toward zero during the control process. Based on the computed entries of vector e_ξ, the following cases can be distinguished:

Case 1. One entry of the control error vector $e_\xi=\left[e_{1\xi},e_{2\xi},e_{3\xi}\right]$ is positive, another is negative, and the third is zero. For example, $e_{1\xi}>0$, $e_{2\xi}<0$, $e_{3\xi}=0$ (Fig. 6a). In this case, phase A is overloaded. Therefore, its loads should be switched to phase B (denoted as A → B). Phase C remains unchanged, since $e_{3\xi}=0$.

Case 2. Two entries of the control error vector e_ξ are positive, and the third is negative. For example, $e_{1\xi}>0$, $e_{2\xi}>0$, $e_{3\xi}<0$ (Fig. 6b). In this case, phase A is overloaded, while phases B and C are underloaded. To balance the loads, switching should be performed as A → B and A → C.

Case 3. One entry of the mismatch vector e_ξ is positive, and the other two are negative. For example, $e_{1\xi}>0$, $e_{2\xi}<0$, $e_{3\xi}<0$ (Fig. 6c). Here, phases A and B are overloaded, and phase C is underloaded. Therefore, loads from phases A and B should be reassigned to phase C (denoted as A → C and B → C).

Thus, the identification of the required phase-switching operations in the power distribution network requires a scenario analysis of the signs of the quantities $e_{k\xi}$, $k=\overline{1,3}$. Loads from phases with positive control errors $e_{k\xi}$ should be switched to phases with negative control errors.

V. CRITERIA FOR OPTIMIZATION OF THE CONTROL PROCESS

There is evidence to suggest that identifying (evaluating) the quality metrics of processes in the power distribution network, as defined by expression (1), poses major computational challenges. Therefore, the criterion (penalty) function used for balancing all local network sections is as follows:

$$f_\xi = \left|e_{1\xi}\right|+\left|e_{2\xi}\right|+\left|e_{3\xi}\right|, \tag{6}$$

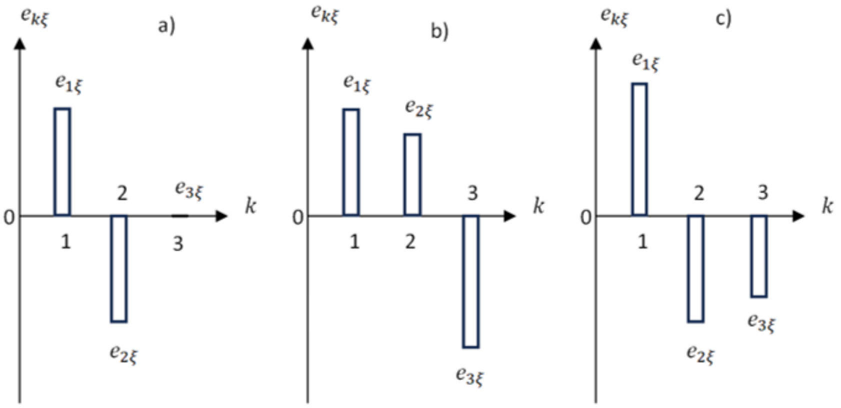

Fig. 6. Possible control error e_ξ scenarios.

the parameters of this function are the magnitudes of the powers consumed by network users equipped with single-phase electricity meters. The penalty function f_ξ characterizes the level of symmetry of the local network section LNS_ξ.

The minimization problem is then formulated as

$$\min f_\xi = f_\xi^*, \tag{7}$$

where f_ξ^* is the optimal value of the criterion function with respect to the above-mentioned parameters.

It is important to note that solving the extreme-value problem (7) ensures a reduction in the value of metric *E*. Issues related to formulating the criterion functions and solving the extreme-value problem are addressed in [12, 13].

The value of the criterion f_ξ^* determines the quality of control for LNS_ξ, i.e., the level of load balance in this local section. To assess the quality of power loss control for the entire PDN, we introduce a generalized (global) objective function *F* defined as

$$F = \sum_{\xi=1}^{N} f_\xi . \tag{8}$$

Analysis shows that a sufficiently high level of balancing, i.e., the desired quality of power loss control, is achieved by solving the minimization problem

$$\min F = F^*, \tag{9}$$

where F^* is the optimal value of the global criterion *F*, which reflects the overall symmetry of the entire distribution network formed by local network sections.

VI. FUNCTIONAL TASKS OF DIGITAL CONTROLLERS

The above considerations make it possible to specify the functional tasks of the digital controllers. The main functions of the local digital controllers (LDCs) are as follows:

1) Receiving data on the complex powers $\dot{S}_{k\xi}$ consumed by the corresponding customer loads of LNS_ξ;

2) Calculating the magnitudes of powers $S_{k\xi}$ and their average value S_ξ by equations (3) and (4), respectively;

3) Evaluating the entries of the control error vector $e_{k\xi} = \left[e_{1\xi}, e_{2\xi}, e_{3\xi}\right]$ and the value of the criterion function f_ξ by equations (5) and (6), respectively;

4) Solving the minimization problem (7) for the criterion function f_ξ;

5) Proposing actions for controlling the electricity meters of LNS_ξ based on the solution of the minimization problem;

6) Transmitting the quality metrics (balancing level) determined by the value f_ξ^* and controls proposed for the object to the central control unit (CCU).

The main functions of the CCU include:

1) Forming the input data for the control problem based on ASERM data for network balancing;

2) Determining the composition of the local network sections (LNS) according to a specified algorithm based on the input data analysis;

3) Setting the setpoints for the LDCs and transmitting the necessary data to them;

4) Receiving the relevant control data for the group of objects (phase-current switches, PCS, and meters, Em) from the LDCs;

5) Analyzing the data of the vector $f = \left[f_1^*, f_2^*, \ldots, f_N^*\right]$ obtained from all LDCs and evaluating the generalized objective function *F* by expression (8);

6) Generating control commands for the object to switch selected customers from one phase to another based on the analysis of the data received from the LDCs.

The control commands are selected based on the following condition:

$$f_\xi^* \geq f_\xi^{\max}, \ \xi = \overline{1, N}, \tag{10}$$

where $f_\xi^{\max}$ is the maximum allowable value of f_ξ^*. Control commands to the object are issued only for those LNSs where condition (10) holds.

VII. CONCLUSION

This study proposes a method for automatic control of technical power loss in 0.4 kV power distribution networks. The method leverages phase-load balancing based on ASERM data. To solve the control problem, a three-phase network is arbitrarily divided (decomposed) into local network sections (LNSs) that are invariant with respect to the currents and powers consumed by the network customers. The extent to which load is balanced in an LNS is assessed by a criterion function introduced as a function of the unbalance in the current phase powers, which are determined as the sums of the powers consumed by the customers of the local sections. The coordinates of the customer electricity meters are identified by minimizing the criterion function. The required computational procedures employ a group of local digital controllers (LDCs) whose operation is coordinated by a central control unit (CCU). Based on the results obtained from the LDCs, the CCU generates and transmits control commands to the controlled object in order to carry out the required operations for switching customer electricity meters from one phase to another. The findings of the study may prove instrumental in the design of an ASERM subsystem for power loss control in power distribution networks.

REFERENCES

[1] M. A. Averbukh, E. V. Zhilin, “On power loss in power supply systems for individual housing construction,” *Energetik*, no. 6, pp. 54–56, 2016. (In Russian)

[2] F. D. Kosoukhob, N. V. Vasilev, A. O. Filipov, “Reducing losses from current unbalance and improving power quality in 0.38-kV networks with municipal loads,” *Russian Electrical Engineering*, no. 85 (6), pp. 350–353, 2014.

[3] T. T. Omorov, B. K. Takyrbashev, T. Zh. Koibagarov, R. Ch. Osmonova, Zh. S. Imanakunova, T. O. Zhanybaev, A. T. Asiev, “A novel technique for technical and non-technical power loss control and monitoring in power distribution systems as based on the data from the automated system for electricity revenue metering,” *Energy Systems Research*, vol. 6, no. 4, pp. 25–33, 2023.

[4] I. V. Naumov, D. A. Ivanov, S. V. Pod’yachikh, G. Damdinsuren, “A load balancer for three-phase networks with a neutral conductor,” RU Patent 2490768, Aug. 20, 2013. (In Russian)

[5] V. V. Samokish, “A balancing technique for phase currents in a three-phase four-wire line and a device for its implementation,” RU Patent 2548656, Dec. 27, 2013. (In Russian)

[6] M. G. Kiselev, M. G. Lepanov, “Current balancing in power supply networks using a power regulator of reactive power,” *Electrical Engineering*, no. 11, pp. 63–70, 2018. (In Russian)

[7] E. Zevelev, “An innovative approach to managing 0.4 kV networks,” Electric *Power. Transmission and Control*, no. 4(19), pp. 39–41, 2013. (In Russian)

[8] A. I. Orlov, S. V. Volkov, A. A. Savel’ev, “Control Algorithms for a three-phase load balancing device of an electric network,” *Bulletin of Chuvash State University*, no. 1, pp. 162–172, 2017. (In Russian)

[9] T. T. Omorov, B. K. Takyrbashev, K. E. Zakiriaev, T. D. Koibagarov, “Synthesis of control algorithms for technical losses of electricity in distribution networks,” in *Proc. 2021 4th International Conference on Control in Technical Systems (CTS)*, Saint Petersburg, Russian Federation, 2021, pp. 7–10.

[10] Energomera Official Website. [Online]. Available: http://www.energomera.ru/en. Accessed on: Aug. 31, 2025.

[11] Mir-Omsk Official Website. [Online]. Available: http://www.mir-omsk.ru/stuff/career/vacancies. Accessed on: Aug. 31, 2025. (In Russian)

[12] T. T. Omorov, B. K. Takyrbashev, T. D. Koibagarov, “Electricy losses management in distribution network as a composition of automated meter reading and control system,” *Mekhatronika, Avtomatizatsiya, Upravlenie*, vol. 22, no. 4, pp. 191–199, 2021. (In Russian)

[13] T. T. Omorov, B. K. Takyrbashev, K. E. Zakiryaev, Zh. S. Imanakunova, T. Zh. Koibagarov, A. T. Asiev, “New approaches and digital technology automation tasks processes of control and accounting of electricity in distribution networks,” *E3S Web of Conf.*, vol. 384, Art. no. 01016, 2023.

[14] T. T. Omorov, B. K. Takyrbashev, T. D. Koibagarov, R. Ch. Osmonova, Zh. S. Imanakunova, T. O. Zhanybaev, A. T. Asiev, “Algorithmic foundations of automated monitoring of commercial and technical power losses in distribution,” *E3S Web of Conf.*, vol. 461, Art. no. 01040, 2023.

[15] T. T. Omorov, K. E. Zakiriaev, B. K. Takyrbashev, Zh. S. Imanakunova, “Automated control of unauthorized power take-offs in a distributed electrical network,” *Mechatronics, Automation, Control*, vol. 24, no. 1, pp. 24–32, 2023.

Turatbek Omorov currently holds the position of the Head of the Laboratory of Adaptive and Intelligent Systems of the National Academy of Sciences of the Kyrgyz Republic (NAS KR), Bishkek, and is a Corresponding Member of the NAS KR. A graduate of the Department of Automation and Computer Engineering of the Leningrad Electrotechnical Institute (1975), T. Omorov earned his degrees of Ph.D. in Engineering from the Bauman Moscow State Technical University in 1981 and D. Eng. from the Research, Development, and Production Facility ‘Cybernetics’ under the Academy of Sciences of the Republic of Uzbekistan in 1997. He directed the Institute of Automation from 2000 to 2008 and then served as Vice-President of the National Academy of Sciences of the Kyrgyz Republic from 2008 to 2013. His research interests include automatic control, informatization and optimization of management processes, automation of power systems.

Kubanychbek Zakiriaev is a Senior Lecturer at Issyk-Kul State University, Karakol, the Kyrgyz Republic. He graduated from the Department of Automation and Computer Engineering of Tomsk Polytechnic University in 1992. He is engaged in the design of microprocessor-based automatic control systems.

Beishenaly Takyrbashev, Ph.D., is currently a Senior Researcher in the Laboratory of Adaptive and Intelligent Systems of the National Academy of Sciences of the Kyrgyz Republic (NAS KR), Bishkek. He graduated from Frunze Polytechnic Institute (1973) with a degree in Automation and Telemechanics. B. Takyrbashev headed the Protective Relay and Automatic Controls Service at Severelectro JSC. His research interests inlcude automation and informatization of processes in power distribution systems.

Tolkunbek Zholdoshov, Ph.D., currently serves as the Head of the Department of Applied Mathematics, Computer Science, and Graphic Design at Osh State University. He graduated from Osh State University with a degree in Applied Mathematics and Computer Science in 2004. His research interests include automatic control, informatization and optimization of control processes.

An Investigation of Soil Radiation Levels in the Territory of Ulaanbaatar City

S. Batmunkh[1,*], Z. Battogtokh[1], B. Erdev[1]

[1] Institute of Thermal Engineering and Industrial Ecology, Mongolian University of Science and Technology, Ulaanbaatar, Mongolia

***Abstract* — This study focuses on the gamma spectrometry analysis of soil samples collected from 180 locations across every kilometer in the densely populated areas of Ulaanbaatar city to determine the activity concentrations of natural radioactive isotopes, including radium-226, thorium-232, potassium-40, and the man-made radioactive isotope cesium-137. Following the analysis, the radium equivalent activity was calculated, and the equivalent dose rate of the soil was measured with a dosimeter at the locations, thereby revealing the background radiation level of the city's soil. The objective of the study was to establish the external and internal hazard indices, outdoor external dose rate, indoor external dose rate, annual outdoor effective dose rate, annual indoor effective dose rate, and excess lifetime cancer risk at selected locations across every kilometer within the densely populated areas of Ulaanbaatar city. It is important to note that the gamma spectrometry analysis of the samples was conducted by the accredited laboratory of the Nuclear Physics Research Center (NPRC) at the National University of Mongolia (NUM). The findings were processed, plotted on a map of Ulaanbaatar city, and published for each soil in Ulaanbaatar, indicating that the activity and content of the isotopes are generally within the permissible limits. In the future, this study will be expanded to create an ecological atlas of soil radiation in the capital city of Ulaanbaatar. This investigation will be an important baseline for future monitoring of soil radiation levels.**

***Index Terms* — Absorbed dose rate, equivalent dose rate, radiation hazard indices, radium equivalent activity.**

I. INTRODUCTION

Numerous studies assessed soil radiation levels in Mongolia, focusing on the concentrations of natural radioactive isotopes such as uranium-238 (^{238}U), thorium-232 (^{232}Th), and potassium-40 (^{40}K) [1–3]. However, these investigations were geographically restricted. For example, measurements in the “Southern-Central zone” near Ulaanbaatar were limited to a few roadside locations and were not synthesized into comprehensive radiation maps [1–3]. Although soil geochemical maps for elements like As, Pb, Zn, and Mo exist for Ulaanbaatar, these datasets lack data on radioactive elements [4]. Furthermore, the studies conducted in 2001–2007 to measure gamma dose rates and soil radioactivity in Western Mongolia, Zuunmod (Central region of Mongolia), and Ulaanbaatar were also limited in scope and could not be regarded as a systematic survey [3, 5, 6]. Consequently, there is a significant lack of a comprehensive, multi-point radiation pollution map for the Ulaanbaatar area.

To address this gap, we propose a systematic study of previously un-surveyed areas within Ulaanbaatar, including the Songinokhairkhan and Nalaikh districts, as well as the surrounding ger areas [1–3, 6–9]. The methodology involves collecting multiple soil samples from various locations, with precise geolocation data

---

[*] Corresponding author.
E-mail: batmunkh_acad@yahoo.com

DOI: 10.25729/esr.2025.04.0004

Received September 17, 2025. Accepted October 26, 2025. Available online December 29, 2025.

recorded using GPS. These samples are analyzed by gamma spectrometry to determine the activity concentrations of ^{238}U, ^{232}Th, ^{40}K, and the anthropogenic isotope ^{137}Cs [3, 10, 11]. Gamma spectrometry is a crucial and well-established technique for environmental radiation monitoring, which facilitates the direct quantification of specific radioactive isotopes in soil and ensures accurate assessment of environmental radiation levels [1, 7, 8, 15–19, 24]. This method is already extensively applied in Mongolia for geophysical and environmental research, utilizing equipment with specifications tailored to the specific application.

This methodology provides reliable and sensitive detection of γ-emitting radio nuclides found in soil [7]. Its high sensitivity and precision, along with compliance with international standards, such as ISO 18589-3, make it the preferred technique for environmental monitoring, post-accident assessment, and evaluation of the impact of nuclear facilities [7, 8]. Crucially, the accurate radiation dose assessments offered by this method are fundamental for evaluating potential health risks to the human population.

Previous applications of this methodology in Ulaanbaatar involved measuring isotopes, including ^{226}Ra, ^{232}Th, ^{40}K, and ^{137}Cs, in soil samples [3, 11–14]. Key findings revealed that the activity concentration of ^{40}K in landfill areas was twice the global average. The radium equivalent activity (Ra_{eq}) ranged from 69 to 183 Bq/kg overall, reaching 338.3 Bq/kg at specific landfill sites. Associated hazard indices were reported as 0.2 for the external hazard index (H_{ex}) and 0.5 for the internal hazard index (H_{in}), with an estimated long-term cancer risk ranging from 0.8×10^{-3} to 1.58×10^{-3} [11]. These results underscore the necessity of systematic and repeated studies across multiple locations in Ulaanbaatar to thoroughly assess the effects on public health.

A critical area for such monitoring is the Songinokhairkhan district, particularly the soil near its ash ponds and landfills. While the Narangiin Enger landfill is studied, more detailed measurements are needed to analyze the soil around ash ponds and thermal power plants, focusing on multiple sampling sites within adjacent residential areas. In Mongolia, these activities are guided by national standards, including:

- **MNS 5626:2006:** A standard for the detection of radioactive isotopes in soil, ash, coal, and construction materials using gamma spectrometry [20].
- **MNS 5840:2008:** A standard for the calibration of ionizing radiation survey meters used for environmental monitoring [21].
- **MNS 5246:2003:** A standard for the of radon concentration assessment in air, applicable to traditional and modern dwellings [22].

The existing studies on soil radioactivity in Mongolia, which measure isotopes such as ^{238}U, ^{232}Th, and ^{40}K, are predominantly limited to the southern and western regions of the country. These investigations often focus on specific sites like uranium deposits or waste sites, relying on a limited number of samples, which leads to inadequate statistical analysis and constrained environmental assessment. Consequently, there is currently no integrated, spatially detailed radiation map for Ulaanbaatar city as existing knowledge is based solely on small-scale studies with limited sampling points [1–3, 6, 9–11].

Generating a reliable radiation map of Ulaanbaatar requires a substantially larger and more representative dataset. In response to this gap, the Institute of Thermal Engineering and Industrial Ecology (ITEIE) at the Mongolian University of Science and Technology (MUST) initiated a systematic research program in 2014 [12–14]. This ongoing effort involves multi-point sampling, repeated measurements, and strict adherence to national and international standards [8, 20–23]. In line with this initiative, our study collected and analyzed samples according to IAEA recommendations, implementing rigorous quality control protocols. A key priority was to utilize the resulting data for assessing a social risk and evaluating the long-term health effects on the local population.

Radioactivity is a natural phenomenon originating from terrestrial radio nuclides found in rocks, soil, sediments, and construction materials. The naturally occurring radioactive materials (NORMs), such as radium decay products, are typically long-lived and contribute significantly to the overall radioactivity of soil, which is primarily determined by the parent rock composition. The concentration of radioactive isotopes in soil serves as a key indicator of environmental radioactivity, which has direct implications for the health of humans, flora, and fauna. Ulaanbaatar presents a unique environmental landscape. In the ger districts of the city, raw coal is the primary source of thermal energy, producing a significant amount of waste ash. Estimates reveal that less than 50% of this ash is disposed of in designated containers. The remainder is often indiscriminately dumped in streets and ravines,

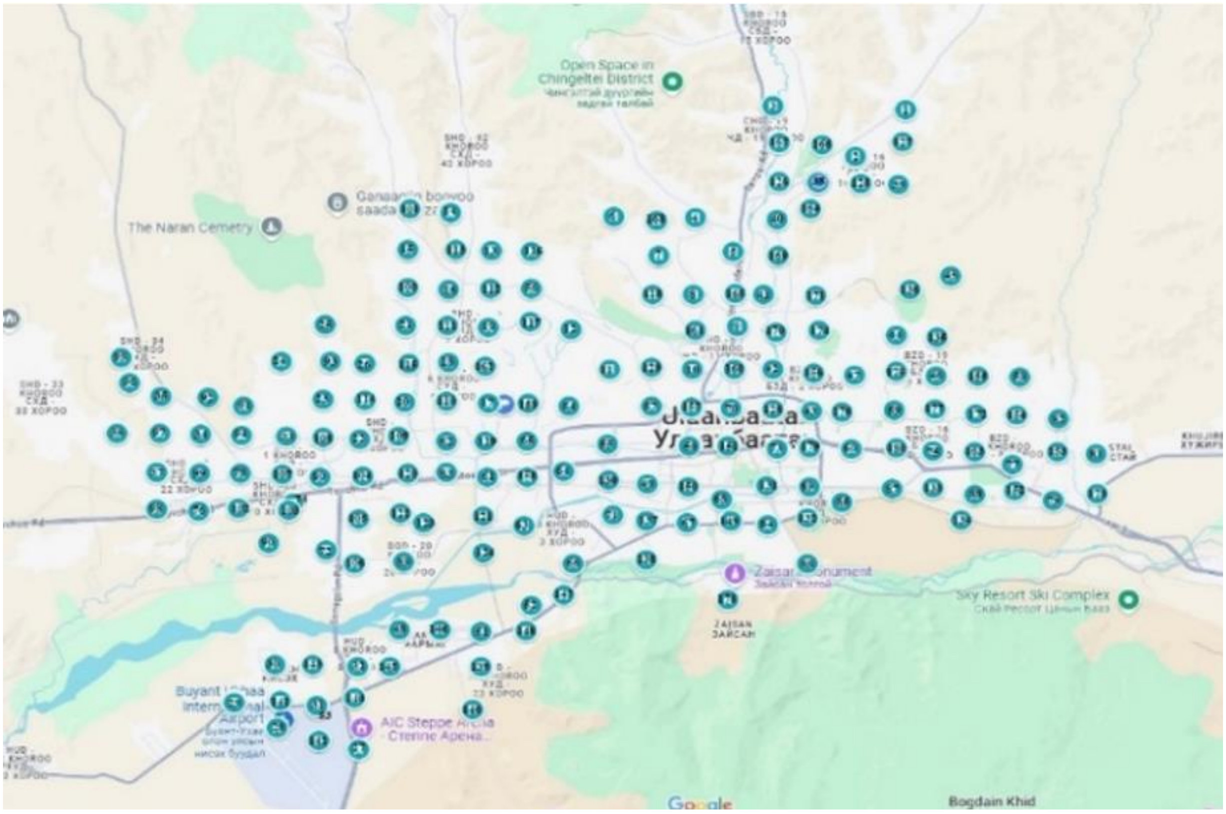

Fig. 1. Sampling locations for soil radiation measurement in the densely populated areas of Ulaanbaatar city.

creating potential point sources of contamination, which is a result of insufficient public awareness of the consequences. In this study, the activity concentrations of ^{226}Ra, ^{232}Th, ^{40}K, and ^{137}Cs in soil samples are measured using gamma-ray spectrometry with a high-purity germanium coaxial detector (HPGe). The mean values of specific activities are estimated at 24.7 ± 8.2 Bq/kg (with a range of 13 to 79) for ^{226}Ra, 18.5 ± 3.9 Bq/kg (with a range of 2 to 40) for ^{232}Th, and 720.2 ± 88.1 Bq/kg (with a range of 422 to 966) for ^{40}K. These results indicate that the mean activities of ^{226}Ra and ^{232}Th are below the world average of 35 Bq/kg and 30 Bq/kg, respectively. The presence of the anthropogenic isotope ^{137}Cs was found to be low in most locations.

II. Methods, Sample Collection and Preparation

1. *Gamma Spectrometry Analysis*

Soil radioactive isotopes were analyzed in the accredited gamma spectrometry laboratory of the Nuclear Physics Research Center (NPRC) at the National University of Mongolia (NUM). The method involves detecting gamma quanta emitted from natural and man-made radioactive isotopes using a gamma spectrometer equipped with a high-resolution semiconductor detector, and determining the activity concentration of the isotope by the number of impulses recorded by the detector of these gamma lines, using the detector's absolute detection efficiency. The study aimed to assess the radiation level at selected points across every kilometer within the densely populated areas of Ulaanbaatar city. This involved measuring the gamma radiation dose and the specific activity of the isotopes, including ^{226}Ra, ^{232}Th, ^{40}K, and ^{137}Cs. The analysis also included assessing the content of uranium and thorium per tonne and potassium per percentage at 180 points across each kilometer. The samples were analyzed using gamma spectrometry, with the results processed, plotted on a map of Ulaanbaatar city, and published for each element. For each sample, the precise location of collection was established by GPS. The points selected for sampling are shown in Fig. 1 [12–14].

2. *Sample Collection and Preparation*

In the 180 locations selected for sampling, 1–2 kg of samples, were excavated from a 0.15×0.15 m^2 area, removing large rocks from the surface, and from a depth of 5 cm of soil. To reduce gamma radiation scattering, the samples were ground to a diameter of less than 1 mm,

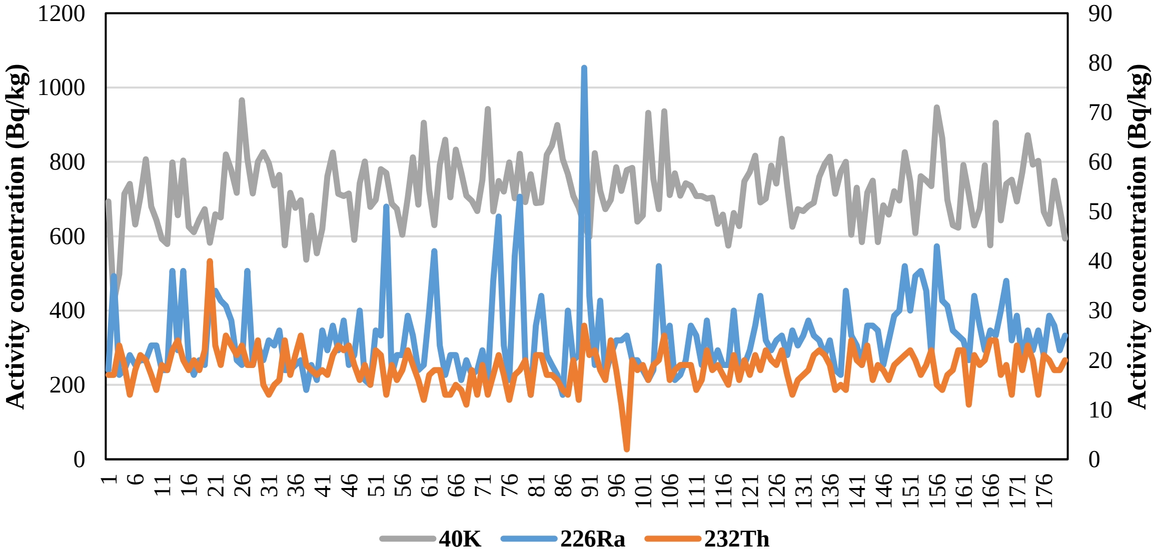

Fig. 2 Activity concentrations of 226Ra, 232Th, and 40K in the soil of Ulaanbaatar city.

dried, placed in a Marinella container, weighed, and prepared for measurement in a germanium detector [23].

III. RESULTS AND DISCUSSION

1. *Activity concentrations of ^{226}Ra, ^{232}Th, and ^{40}K in the soil of Ulaanbaatar*

The activity concentrations of ^{226}Ra, ^{232}Th, ^{40}K, along with their values for the 180 soil samples, are shown in Fig. 2. The activity concentration of ^{40}K is shown using the left-hand axis, while the activity concentrations of ^{226}Ra and ^{232}Th are plotted using the right-hand (secondary) axis. This was done to make the graph easier to read because their values differ greatly. All values are given in Bq/kg. The mean values and ranges of the activities for ^{226}Ra, ^{232}Th, and ^{40}K, respectively, are 24.7 ± 8.2 Bq/kg (with a range of 13 to 79 Bq/kg), 18.5 ± 3.9 Bq/kg (with a range of 2 to 40 Bq/kg) and 720.2 ± 88.1 Bq/kg (with a range of 422 to 966 Bq/kg). The highest value of ^{226}Ra activity concentration was observed in the southeastern part of the ash pond of power plant No. 4, located at 47.53’43.7” N latitude and 106.53’43.7” longitude in the territory of the 20th Khoroo of Songinokhairkhan district (point 90, sample 5180). The man-made radioactive isotope ^{137}Cs was almost absent in the soil samples, and at some

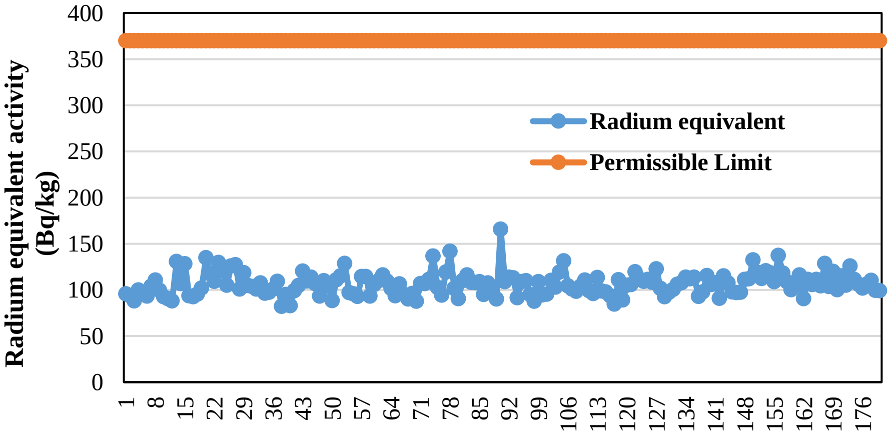

Fig. 3 Radium equivalent activity of soil in Ulaanbaatar city.

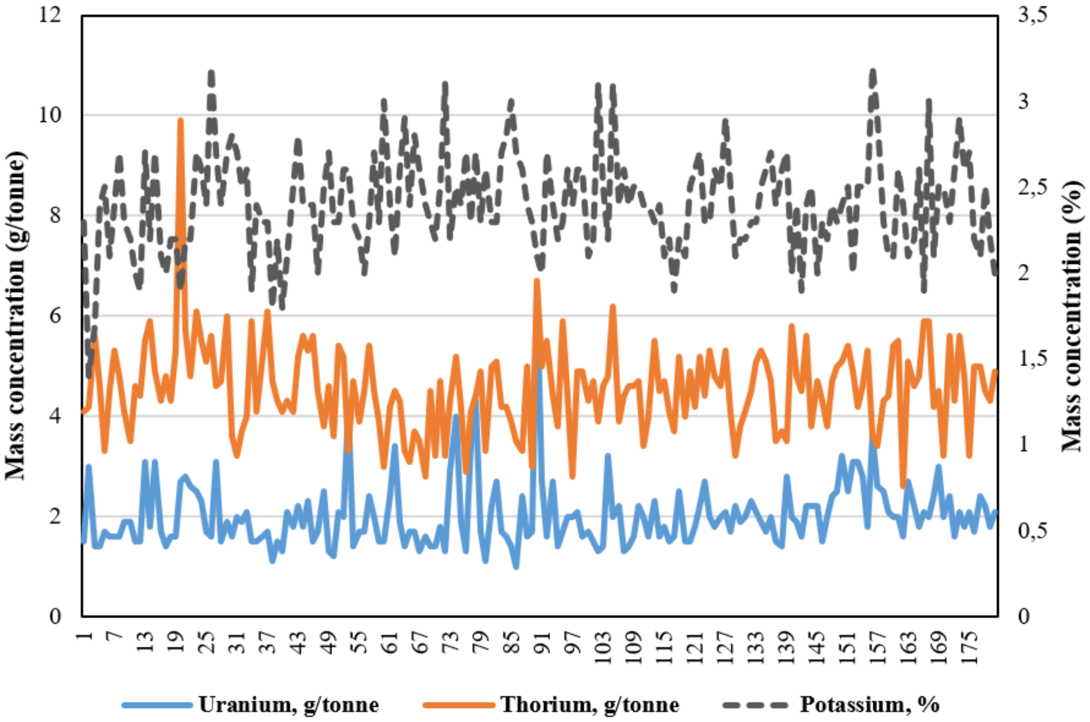

Fig. 4. Mass concentrations of uranium, thorium, and potassium in the soil of Ulaanbaatar city.

locations, it was very low, which is why it is not discussed further.

2. *Radium Equivalent Activity*

The method of calculating the activity of natural radioactive nuclei based on radium equivalent activity, which was proposed by Beretka and Matthew [15], is widely used to assess radiation hazards.

Radium equivalent activity is defined by the following formula:

$$Ra_{eq} = A_{\mathrm{Ra}} + 1.43A_{\mathrm{Th}} + 0.077A_{\mathrm{K}}, \qquad (1)$$

where A_{Ra}, A_{Th}, and A_{K} are the activity concentrations of ^{226}Ra, ^{232}Th, ^{40}K in Bq/kg, respectively [15–17, 19, 24]. Radium equivalent activity is the sum of the activities of naturally radioactive ^{226}Ra, ^{232}Th, and ^{40}K isotopes converted to radium activity and is the main measure for assessing radiation levels. The maximum permissible level of radium equivalent activity is 370 Bq/kg. The mean radium equivalent activity is 106.6 ± 12.3 Bq/kg ranging from 82.5 to 166.0 Bq/kg, which is 2.2 times lower than the permissible level [12–14]. This value corresponds to a dose rate of 1.5 mGy/year at about 1 m above the ground level. The assessment results for radium equivalent activity are shown in Fig. 3.

Figure 3 shows that the mean radium equivalent activity is 106.6 ± 12.3 Bq/kg, ranging from 82.5 to 166.0 Bq/kg. The highest value of radium equivalent activity (166.0 Bq/kg) was observed in the southeastern part of the ash pond of power plant No. 4 (point 90, sample 5180). This high level is due to the radioactive contamination of coal ash in the environment, while radium equivalent activity is normal compared to the maximum permissible level. This investigation provides crucial information for future monitoring of the soil radiation level.

3. *Mass Concentrations of Uranium, Thorium, and Potassium*

The following equation is used to calculate the mass concentration of naturally occurring radioactive elements (Fig. 4) in a sample based on the specific activity concentration of their isotopes [20]:

$$\begin{gathered} 1\%\ (\mathrm{K}) = 310\ \mathrm{Bq/kg\ of\ }^{40}\mathrm{K}, \\ 1\ \mathrm{g/tonne\ (U)} = 12.35\ \mathrm{Bq/kg\ of\ }^{226}\mathrm{Ra}, \\ 1\mathrm{g/tonne\ (Th)} = 4.06\mathrm{Bq/kg\ of\ }^{232}\mathrm{Th}. \end{gathered} \qquad (2)$$

Figure 4 displays the mass concentrations of uranium and thorium in g/tonne on the primary (left) axis, while the mass concentration of potassium, expressed in percent, is shown on the secondary (right) axis. The uranium mass concentration varies from 0.7 to 6.4 g/tonne, with the mean value of 2.0 ± 0.7 g/tonne. The thorium mass concentration is in the range of 0.5 to 9.9g/tonne, with the mean value of

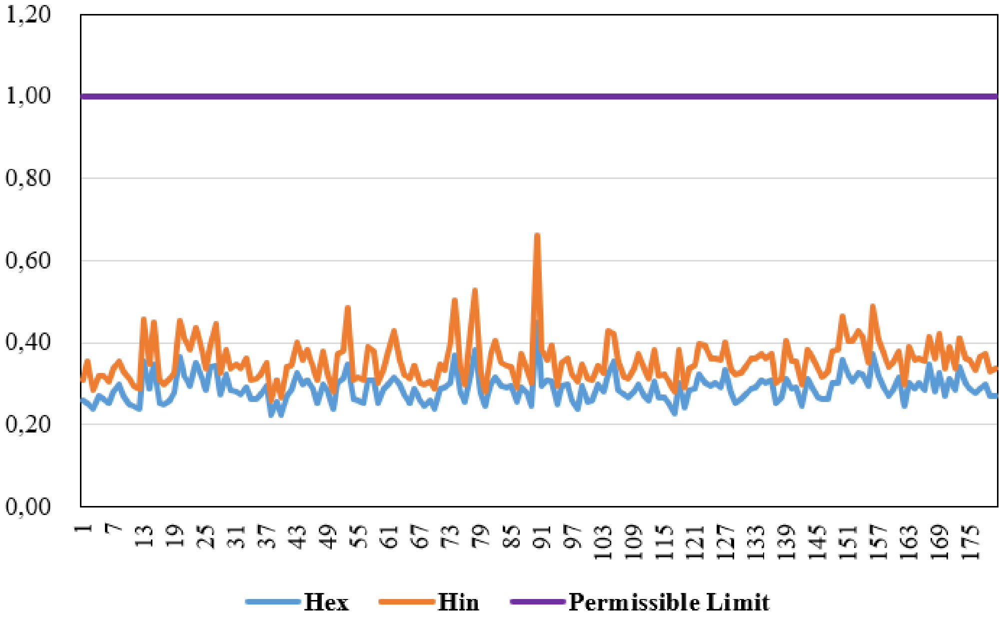

Fig. 5 External (H_{ex}) and internal (H_{in}) radiation hazard indices in Ulaanbaatar city.

4.6 ± 1.0 g/tonne, and the potassium mass concentration lies within the range of 0.3 to 3.1 %, with the mean value of 2.3 ± 0.3 %.

4. *External and Internal Indices*

Radiation resulting from decay is absorbed by the human body, producing external radiation, while radioactive dust penetrates the body through the respiratory and digestive systems, where it decomposes, causing internal radiation. Directly dependent on the amount of external and internal radiation, ionization processes that occur in body tissues change human biochemical and functional processes, increasing the probability of various diseases. Additionally, radiation sickness leads to genetic changes and lifelong infertility. The effects on humans when the dose rate is less than 1.00 mSv/year were calculated using the equation derived by Krieger [18]. He proposed the model for calculation of external hazard index H_{ex} based on infinitely thick walls without windows and doors to serve as a criterion. The external hazard index due to gamma radiation was calculated using following formula [15]:

$$H_{ex} = \frac{A_{\mathrm{Ra}}}{370} + \frac{A_{\mathrm{Th}}}{259} + \frac{A_{\mathrm{K}}}{4810} \leq 1, \qquad (3)$$

where 370 Bq/kg of ^{226}Ra, or 259 Bq/kg of ^{232}Th, or 4 810 Bq/kg of ^{40}K produce the same gamma dose rate, Ra_{eq} is related to the external γ-dose and internal dose due to radon and its daughters [8, 19]. The assessment results for external (H_{ex}) and internal (H_{in}) radiation hazard indices in Ulaanbaatar city for the soil samples are demonstrated in Fig. 5.

The mean value of the external hazard index obtained in the study is 0.29 ± 0.03 mSv/y, ranging from 0.22 to 0.44 mSv/yr, which is 2.3 times lower than the permissible limit [12–14, 19].

The maximum permissible activity concentration of ^{226}Ra is 185 Bq/kg. When studying the possibility of developing cancer in internal organs, the internal hazard index is calculated. The index is assessed to reduce the maximum permissible concentration of ^{226}Ra to half the values appropriate for the external exposure alone. The gaseous short-lived decay product of ^{226}Ra, called Radon (^{222}Rn), poses a threat to the respiratory organs. In addition to the external hazard index, internal exposure to radon and its products is quantified by estimating the H_{in}. If the maximum concentration of ^{226}Ra is half that of the permissible limit, then H_{in} is less than unity. The H_{in} due to the radio nuclides was estimated using the formula proposed by Beretka and Matthew [15]. The internal hazard is expressed by the following formula:

$$H_{in} = \frac{A_{\mathrm{Ra}}}{185} + \frac{A_{\mathrm{Th}}}{259} + \frac{A_{\mathrm{K}}}{4810} \leq 1. \qquad (4)$$

The internal radiation hazard index in Ulaanbaatar city is

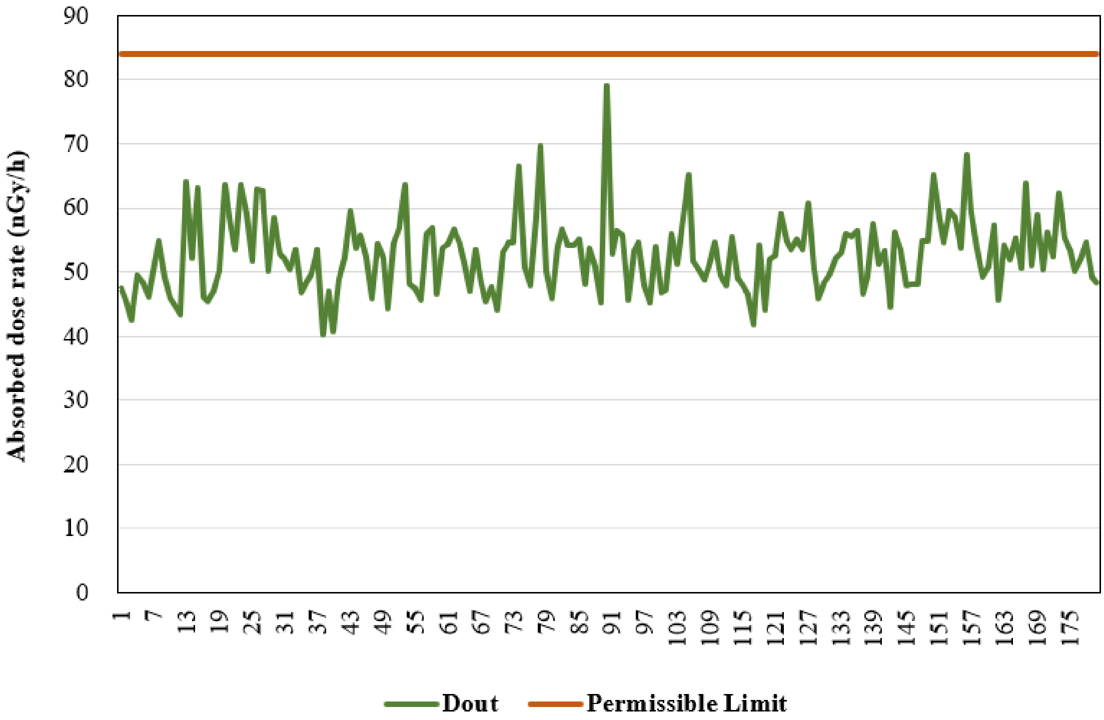

Fig. 6. Outdoor absorbed dose rate compared to permissible limit.

shown in Fig. 5. Our findings indicate that the internal radiation hazard index stands at a mean value of 0.34 ± 0.05 mSv/year (ranging from 0.19 to 0.43 mSv/yr), which is 2.3 times lower than the permissible limit.

5. *Absorbed Dose Rate*

The contribution of natural radio nuclides to the absorbed dose rate (D_{out}, D_{in}) in air depends on the natural specific activity concentrations of ^{238}U, ^{232}Th, and ^{40}K. The greatest part of the gamma radiation comes from terrestrial radio nuclides. There is a direct connection between terrestrial gamma radiation and radionuclide concentrations. If a radionuclide activity is known then its exposure dose rate in the air at 1 m above the ground can be calculated [19, 25]. The conversion factors used to compute the absorbed gamma dose rate (D_{out}, D_{in}) in air per unit activity concentration in Bq/kg corresponds to 0.462 nGy/h for ^{226}Ra, 0.604 nGy/h for ^{232}Th, and 0.0417 nGy/h for ^{40}K.

The dose rate absorbed in the air can be determined by the radioactivity in the soil. It was calculated for a height of 1 m above the ground surface. A computer program employed was based on the volume integral method using the following conversion factors:

$$D_{out} = (4.62A_{\text{Ra}} + 6.04A_{\text{Th}} + 0.417A_{\text{K}}) \times 10^{-1}, \quad (5)$$

where D_{out} is the absorbed dose rate in the outdoor air, nGy/h; A_{Ra}, A_{Th}, A_{K} are activity concentrations of ^{226}Ra, ^{232}Th, and ^{40}K, Bq/kg,

$$D_{in} = (9.2A_{\text{Ra}} + 11A_{\text{Th}} + 0.8A_{\text{K}}) \times 10^{-1}, \quad (6)$$

where D_{in} is the absorbed dose rate in the indoor air, nGy/h. The absorbed dose rate (D_{out}) values range between 40.3 nGy/h and 79.0 nGy/h with a mean value of 52.6±5.9 nGy/h. This mean value is lower than the value of the world average absorbed dose rate of 84 nGy/h [8, 24]. The results of the D_{out} comparison with the permissible limit are shown in Fig. 6.

6. *Annual Effective Dose Rate, E_{eff}*

The United Nations Scientific Committee on the Effects of Atomic Radiation (UNSCEAR) (2000) used the annual effective dose, E_{eff} (E_{out}, E_{in}), of 0.7 Sv/Gy for the conversion coefficient from absorbed dose in the air to effective dose received by adults, and 0.8 for the outdoor occupancy factor [25]. The annual effective dose in mSv/y, resulting from the absorbed dose values (D_{out}, D_{in}), was calculated using the following formulas [19, 25]:

$$E_{out} = 1.4 \times 10^{-3} D_{out}. \quad (7)$$

The annual effective dose obtained (Fig. 7) ranges between 0.07 mSv/y and 0.11 mSv/y with a mean value of 0.07 ± 0.01 mSv/y [13]:

$$E_{in} = 3.068 \times 10^{-3} D_{in} . \qquad (8)$$

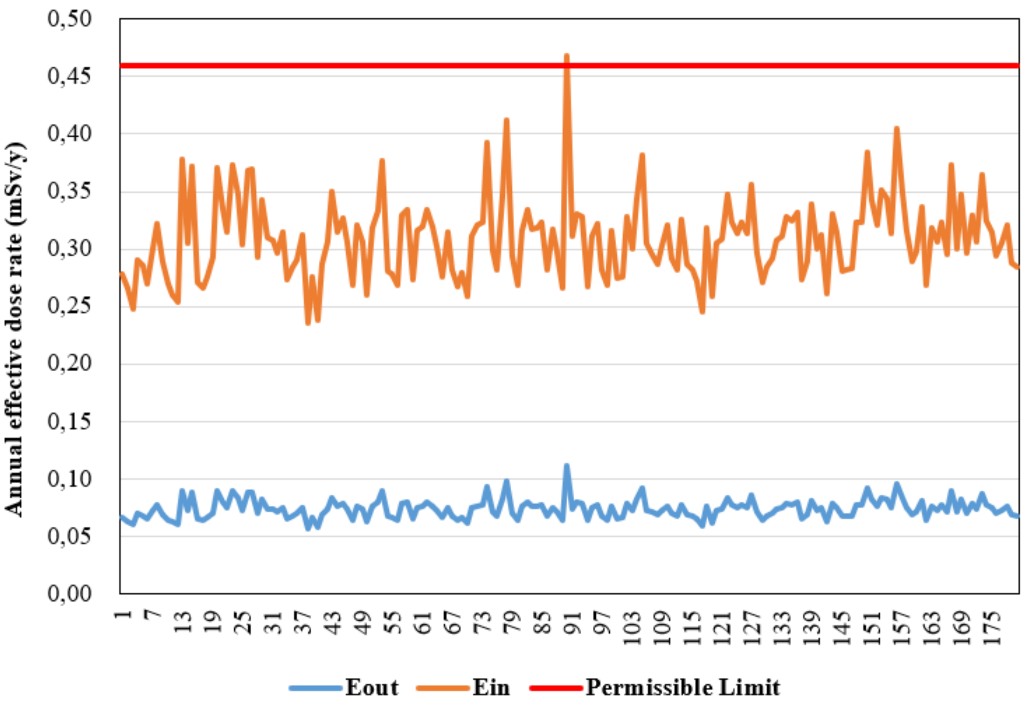

Fig. 7. Annual effective dose rate in different locations of Ulaanbaatar.

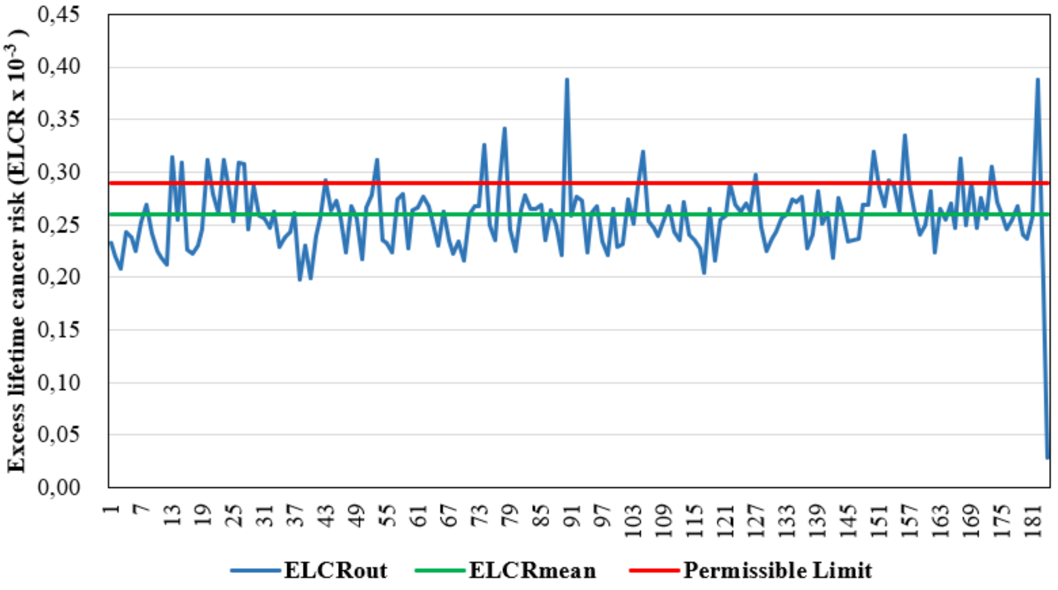

Fig.8. Excess lifetime cancer risk (ELCR) in Ulaanbaatar, Mongolia.

In normal background areas, the average annual indoor effective dose from terrestrial radio nuclides is 0.46 mSv/y [8, 25]. Therefore, the obtained mean value from this study area, 0.31 ± 0.04 mSv/y, ranging from 0.24 to 0.47 mSv/y, is lower than the world average value [8, 12–14]. The high value of E_{in} was observed in the southeastern part of the ash pond of power plant No. 4 (point 90, sample 5180). Figure 7 shows variations in annual effective dose rate at different points of Ulaanbaatar and the permissible limit.

7. *Health Effects of Radiation*

Radiation can damage human cells, causing skin burns, hair loss, and cancer. Pregnant women are particularly

TABLE 1. Comparative Results of Radiation Studies Conducted on Soil Samples from Ulaanbaatar City in 2014 and 2024

Parameters	Mean values		Range	
	2014	2024	2014	2024
1. Activity concentration of isotopes, Bq/kg				
^{226}Ra	21.2±5.9	24.7±8.2	11–40	13–79
^{232}Th	20.2±5.0	18.5±3.9	10–49	2–40
^{40}K	708.4±117.8	720.2±88.1	277-1002	422–966
Ra_{eq}	104.5±12.6	106.6±12.3	58–129	82–166
2. Content of elements				
U, g/ton	1.7±0.5	2.0±0.7	0.9–3.2	0.7–6.4
Th, g/ton	5.0±1.2	4.6±1.0	2.4–12.0	0.5–9.9
K, %	2.3±0.4	2.3±0.3	0.9–3.1	0.3–3.1
3. Radiation hazard indicies – H				
H_{ex}	0.28±0.03	0.29±0.03	0.16–0.35	0.22–0.44
H_{in}	0.34±0.05	0.36±0.05	0.19–0.43	0.26–0.66
4. Absorbed dose rate – D, nGy/h				
D_{out}	51.4±6.1	52.6±5.9	28–64	40.3–79.0
D_{in}	98.4±11.8	100.7±11.4	52.8–123	77–153
5. Annual effective dose rate – $E_{eff,}$ mSv/y				
E_{out}	0.07±0.01	0.07±0.01	0.04–0.09	0.07–0.11
E_{in}	0.30±0.03	0.31±0.04	0.16–0.38	0.24–0.47
6. Excess lifetime cancer risk ($ELCR$)				
$ELCR$, 10^{-3}	0.25±0.03	0.26±0.03	0.13–0.31	0.20–0.39

vulnerable to radiation, as fetuses are sensitive to radiation. The additional or extra risk of devloping cancer stems from exposure to a toxic substance incurred over the lifetime of an individual. Excess lifetime cancer risk (*ELCR*) is calculated using the following formula:

$$ELCR = E_{out} \times DL \times RF\ , \tag{9}$$

where E_{out}, DL, and RF are respectively the annual effective dose, duration of life (70 years), and risk factor (0.05 Sv^{-1} for public exposure, ICRP-2007 [27]), i.e., fatal cancer risk per Sievert. The calculated range of *ELCR* is 0.20×10^{-3} to $0.39x10^{-3}$ with a mean value of $(0.26 \pm 0.03)\times10^{-3}$. The mean value of *ELCR* in the study area is lower than the world average of 0.29×10^{-3} [24, 26]. Figure 8 shows the sampling points, excess lifetime cancer risk (*ELCR*), the permissible limit (*PL*), and the mean value determined in our study.

Table 1 presents a comparison between the findings from our study conducted across 180 locations in Ulaanbaatar in 2024 and the results from our earlier study carried out in 2014 [12–14].

The 2024 radiation survey at 180 sites in Ulaanbaatar showed generally slightly higher levels than the 2014 survey, all of the above figures as well as the average, minimum, and maximum values in the text, are presented using the 2024 survey data.

IV. CONCLUSION

1. This study can be used as a baseline for future investigations while the data obtained in this study may be instrumental in natural radioactivity mapping. These findings can also be employed as reference data for future monitoring possible radioactive pollution. The activity levels of natural terrestrial radionuclides – ^{238}U, ^{232}Th, and ^{40}K – were measured using gamma-ray spectrometry system. The soil samples were collected from selected locations of Ulaanbaatar city.

2. The mean radium equivalent activity stands at 106.6 ± 12.3 Bq/kg, ranging from 82.5 to 165.9 Bq/kg. Its maximum value is 2.2 times lower than the maximum permissible level. The uranium mass concentration lies in the range of 0.9 to 3.2 g/tonne, with the mean value of 1.7.5 ± 0.5 g/tonne. The thorium mass concentration falls within the range of 2.4 to 12 g/tonne, with the mean value of 5.0 ± 1.2 g/tonne. The potassium mass concentration ranges between 0.9% and 3.1%, with the mean value of 2.4 ± 0.4 %. The activity concentrations and the content of

uranium, thorium, and potassium in the studied soils are found to be normal.

3. The highest value of radium equivalent activity (165.96 Bq/kg) was observed in the southeastern part of the ash pond of power plant No. 4, located at 47.53’43.7” latitude and 106.53’43.7” longitude in the territory of the 20th Khoroo of Songinokhairkhan district (point 90, sample 5180). This high level is due to the radioactive contamination of coal ash found in the environment. However, the radium equivalent activity remains within normal limits compared to the permissible level.

4. Our study shows that the mean value of the external hazard index is 0.28 ± 0.03, varying between 0.16 and 0.35, which is 2.8 times lower than the permissible limit. The mean annual indoor effective dose obtained is 0.30 ± 0.03 mSv/y, ranging from 016 to 0.38 mSv/y, which is 1.2 times lower than the permissible limit.

5. The calculated range of *ELCR* is 0.20×10^{-3} to 0.39×10^{-3} with a mean value of $(0.26 \pm 0.03)\times10^{-3}$. The mean value of *ELCR* in the study area is lower than the world average of 0.29×10^{-3}.

6. All measured radiological parameters are below the permissible limit. Hence the natural radioactivity of soil does not pose any harmful radiation risks to residents or tourists.

References

[1] B. Dalkhsuren, B. Erdev, “Detection of some elements in fallout and radioactivity in soil,” *INIS ATOMINDEX*, vol. 24, no. 18, Art. no. 059194, Sep. 1993.

[2] B. Erdev, Z. Battogtokh, R. Maakhuu, “Determination of radioactivity in environment (monitoring environmental pollution depending on main sources),” *Mongolian Scientific Transactions, Physics*, no. 225(12), pp. 46–49, 2005.

[3] B. Dalkhsuren, Ts. Tserengombo, Ts. Namchinsuren, Sh. Gerbish, *Study of Radioactivity in the Soil of Western Mongolia*, JINR-R-18-2006-140, Ulaanbaatar, Mongolia, 2006. (In Russian)

[4] J. Garidkhuu, S. Batmunkh, G. Bayarsaikhan, B. Erdev, G. Ariuntuul, “Ecological map of Ulaanbaatar City,” in *Ecology and Sustainable Development*, Ulaanbaatar, Mongolia, May 2001, pp. 211–213. (In Mongolian)

[5] Ts. Erkhembayar, N. Norov, G. Khuukhenkhuu, “The study of soil radioactivity around Central Region of Mongolia,” *Scientific Transaction of the National University of Mongolia, Physics*, no. 8(159), Ulaanbaatar, 2001. (In Mongolian)

[6] S. Batmunkh, S. Enkhbat, B. Erdev, Z. Battogtokh, Ts. Batbuyan, “Activity concentrations of natural radionuclides in soil near TPP-4 of Ulaanbaatar,” in *Proc. IFOST 2007 – Second Int. Forum on Strategic Technology*, Oct. 3–5, 2007, pp. 628–630.

[7] G. F. Knoll, *Radiation Detection and Measurement*, 4th ed., IAEA Tech. Rep. Ser. No. 295, 1989.

[8] ISO 18589-3:2023, *Measurement of Radioactivity in the Environment—Soil—Part 3: Gamma Spectrometry for the Determination of Radionuclides*, 2023.

[9] B. Dalkhsuren, B. Erdev, “Investigations of radioactivity and microelements in air by nuclear techniques,” in *Environmental Conditions, History and Culture of West Mongolia and Adjacent Region*, Proc. 7th Int. Conf., Kizil, Russia, Sep. 19–23, 2005, pp. 97–102.

[10] Ch. Sonomdagva, Ch. Byambatsruren, D. Davaadorj, “Some results of soil pollution study in the settlement area of Ulaanbaatar City,” *Proceedings of the Mongolian Academy of Sciences*, vol. 56, no. 1, 2016 (in Mongolian).

[11] B. Dorjsuren et al., “Radioactive levels and human health effects in a dumpsite on Ulaanbaatar City, Mongolia,” *Journal of Hazardous, Toxic, and Radioactive Waste*, vol. 26, no. 4.

[12] S. Batmunkh, Z. Battogtokh, B. Erdev, M. Davaasambuu, “Study of the radium equivalent activity of soil in Ulaanbaatar City,” in *Proc. Int. Conf. Energy Transition: Technology and Ecology (ICETTE-2025)*, Jun. 12–13, 2025.

[13] Institute of Thermal Engineering and Industrial Ecology, MUST, “Project for the new development of the ecological Atlas of Ulaanbaatar City: Field survey report on soil pollution in the residential area of Ulaanbaatar City—Section on radioactive contamination,” Ulaanbaatar, Mongolia, 2024. (In Mongolian)

[14] B. Jargalsaikhan et al., “Radioactivity level survey to be conducted in the area of Ulaanbaatar City,” Scientific Research Report, Institute of Thermal Engineering and Industrial Ecology, Ulaanbaatar, Mongolia, 2014. (In Mongolian)

[15] J. Beretka, P. J. Mathew, “Natural radioactivity of Australian building materials, industrial wastes and by-products,” *Health Phys.*, vol. 48, no. 1, pp. 87–95, 1985.

[16] M. Faheem, S. A. Mujahid, S. Matiullah, “Assessment of radiological hazards due to natural radioactivity in soil and building material samples collected from six districts of Punjab province, Pakistan,” *Radiation Measurement*, vol. 43, pp. 1443–1447, 2008.

[17] UNSCEAR, *Sources and Effects of Ionizing Radiation*, United Nations Scientific Committee on the Effects of Atomic Radiation, Annex A & B, United Nations, New York, 2011.

[18] R. Krieger, “Radioactivity of construction materials,” *Betonwerk und Fertigteil-Technik*, vol. 47, pp. 468–473, 1981.

[19] Kurnaz et al., “Determination of radioactivity levels and hazards of soil and sediment samples in Fırtına Valley (Rize, Turkey),” *Applied Radiation and Isotopes*, pp. 1281–1289, 2007.

[20] MNS 5626:2006, *Method for Determination of Radioactive Isotopes in Soil, Ash, Coal, and Building Materials Using Gamma Spectrometry*, Agency for Standardization and Metrology, Ulaanbaatar, Mongolia, 2006 (in Mongolian).

[21] MNS 5840:2008, *Method for Calibration of Instruments Measuring Environmental Radiation Levels (Ionizing Radiation Survey Meters)*, Agency for Standardization and Metrology, Ulaanbaatar, Mongolia, 2008 (in Mongolian).

[22] MNS 5246: 2003 – Method for Determination of Radon Concentration in Atmospheric Air, Agency for Standardization and Metrology, Ulaanbaatar, Mongolia, 2003 (in Mongolian).

[23] IAEA, *Guidelines on Soil and Vegetation Sampling for Radiological Monitoring*, 2019.

[24] R. Ravisankar et al., "Natural radioactivity in soil samples of Yelagiri Hills, Tamil Nadu, India and the associated radiation hazards," *Radiation Physics and Chemistry*, vol. 81, no. 12, pp. 1789–1795, 2012.

[25] UNSCEAR, *Sources, Effects and Risks of Ionizing Radiation*, United Nations, New York, 1988, 1993, 2000.

[26] S. Dizman, F. K. Görür, R. Keser, "Determination of radioactivity levels of soil samples and the excess of lifetime cancer risk in Rize province, Turkey," *International Journal of Radiation Research*, vol. 14, no. 3, pp. 237–244, 2016.

[27] International Commission on Radiological Protection (ICRP), *The 2007 Recommendations of the International Commission on Radiological Protection*, ICRP Publ. 103, *Ann. ICRP*, vol. 37, no. 2–4, 2007.

Academician **Batmunkh Sereeter** was born in Mongolia on July 1, 1947. He received the B.S. degree in Industrial Thermal Engineering from the Ural Polytechnic Institute in Sverdlovsk, Russia; the Ph.D. degree in Technical Thermodynamics from the Physics-Technical Institute of the Academy of Sciences in Ashgabat, and the D.Sc. degree in Energy Systems and Complexes from the Melentiev Energy Systems Institute of the Siberian Branch of the Russian Academy of Sciences, Irkutsk, Russia. He served as a Professor, Scientific Worker, and Senior Academic Leader at major institutions, including the Mongolian University of Science and Technology, and was affiliated with key scientific bodies such as the Mongolian Academy of Sciences, where he is an Academician. He is currently a Consulting Professor and Scientific Project Leader at the Institute of Thermal Engineering and Industrial Ecology, Mongolian University of Science and Technology (MUST), Ulaanbaatar, Mongolia. His research interests include thermal engineering, solar energy utilization, energy system modeling, environmental pollution, and the development of Mongolia's electric power systems.

Battogtokh Zagdaa was born in Mongolia on May 26, 1962. She received the B.S., M.S., and Ph.D. degrees in Thermal Engineering and Thermal Process Automation from the Mongolian University of Science and Technology, Ulaanbaatar. She served as an engineer in thermal process automation and later as a Lecturer and Associate Professor at the School of Energy Engineering, MUST. She is currently a Scientific Worker and Head of a Department at the Institute of Thermal Engineering and Industrial Ecology, MUST, Ulaanbaatar, Mongolia. Her research interests include thermal process automation, energy ecology, and radionuclide-based environmental assessment.

Batjargal Erdev was born in Mongolia on March 26, 1956. She received the B.S., M.S., and Ph.D. degrees in nuclear physics from the National University of Mongolia, Ulaanbaatar. Serving as a Professor and Scientist at the National University of Mongolia, she was also affiliated with the Nuclear Energy Agency of Mongolia. She has authored over 120 scientific publications. Currently, Batjargal Erdev holds the position of a Scientist at the Institute of Thermal Engineering and Industrial Ecology, MUST, Ulaanbaatar, Mongolia, where she remains committed to contributing to academic and applied research. Her research interests include nuclear physics, environmental radioactivity, gamma spectrometry, and radiation protection.

Scientometric Review of the 3D Energy Transition: Decarbonization, Digitalization, and Decentralization in Energy Systems

A.V. Mikheev[1,*], N.E. Karimov [1]

[1] Melentiev Energy Systems Institute of Siberian Branch of Russian Academy of Sciences, Irkutsk, Russia

***Abstract* — This article presents a scientometric review that quantifies the contribution of the three-dimensional energy transition, that is decarbonization, digitalization, and decentralization, to the research field of energy systems over the period 2001 to 2025. Records were retrieved from Scopus using a two-level query that first captured the general energy systems domain and then stratified it into the three components. Standardized preprocessing, cleaning, and keyword harmonization were applied. Descriptive indicators trace publication growth and portfolio shares, and network mapping with VOSviewer visualizes keyword co-occurrence and topic evolution. Results show substantial expansion of the field and a shift of the research mainstream toward the 3D topics. Decarbonization accounts for approximately half of the corpus, digitalization for about one fifth, and decentralization for a smaller but persistent share. Integration between energy transition components increases over time, with the strongest coupling along the decarbonization and digitalization axes, and a compact but growing 3D core emerges. Topic maps indicate an early policy and renewables nucleus, followed by acceleration in storage, hydrogen, power electronics and control, data-driven operations, cyber security, and market mechanisms for local flexibility.**

***Keywords* — energy transition; energy systems; decarbonization; digitalization; decentralization; bibliometrics; scientometrics; Scopus; VOSviewer.**

I. INTRODUCTION

The transformation of energy systems in the early twenty-first century is increasingly described as the convergence of three interrelated directions: decarbonization, digitalization, and decentralization (hereafter, the 3D paradigm) [1, 2]. Decarbonization entails reducing the carbon intensity of energy supply through the large-scale deployment of renewable energy sources, improvements in efficiency, and the implementation of carbon capture, utilization, and storage (CCUS) technologies. Digitalization establishes a technological layer, spanning sensors, the Internet of Things (IoT), artificial intelligence and machine learning (AI/ML), digital twins, and distributed ledgers, that enables enhanced observability, forecasting, and automated control [3]. Decentralization reconfigures system architecture and governance by expanding distributed energy resources (DER), microgrids, and energy communities, thereby broadening prosumer participation and facilitating local market mechanisms. At the intersection of these three dimensions arises a complex agenda involving the integration of high shares of renewables, the provision of flexibility and cyber-resilience, and the development of new regulatory and market frameworks, rendering a system-level account of the energy transition a subject of intensive scholarly inquiry. In parallel, a broad socio-technical literature on energy transitions has matured, refining conceptual categories and temporal scales of change and emphasizing the roles of institutions, practices, and justice in transition trajectories [4, 5].

The salience of this topic is driven both by the

---

[*] Corresponding author.
E-mail: mikheev@isem.irk.ru

DOI: 10.25729/esr.2025.04.0005

Received November 22, 2025. Revised December 10, 2025. Accepted December 22, 2025. Available online December 29, 2025.

acceleration of climate policy and international Net-Zero targets and by the rapid diffusion of digital technologies for power-system operation alongside the growth of distributed generation. These processes position the 3D paradigm not as a set of isolated trends but as an interdependent framework in which digitalization acts as a horizontal enabler of operational control and integration of renewables/DER, while decentralization imposes new requirements on digital infrastructure, flexibility markets, and data protection [3, 6]. In this configuration, the contribution of the scientific community (its publication scale, thematic clusters, dynamics, and geography) becomes an indicator of the conceptual and technological readiness of the energy transition as well as a source of evidence for policy and industry [7, 8].

At the same time, existing reviews and bibliometric studies tend to focus either on the general field of the energy transition and its associated trajectories, including issues of renewable integration and market design [9], or on specific subsectors. The latter reveals thematic fragmentation: energy storage is examined through the lens of resource management under renewable uncertainty [10]; microgrids and hybrid architectures constitute a rapidly evolving domain with its own clusters and trends [11]; and energy communities are analyzed as an institutional and socio-technical form of decentralization with an emerging conceptual and empirical core [12]. Concurrently, the literature records an acceleration of digital themes in power systems—smart grids, forecasting algorithms, and data-driven optimization—together with a reframing of market and tariff design [13]. Regional studies identify pronounced asymmetries of attention and capability and underscore the need for normalized comparisons and methodologically comparable approaches, for example, for Sub-Saharan Africa [14]. Taken together, this evidence suggests that, despite the breadth of the literature and the rapid development of digitalization and decentralization themes, there remain few integrated studies in which the scientific contribution across all three components of the 3D paradigm is assessed comparatively within a single, reproducible bibliometric framework.

The energy transition within the development of energy systems has been examined using scientometric methods [15, 16]. By constructing publication co-citation networks, these studies visualize the evolution of scientific knowledge in the energy-systems domain and identify the research and technology development front.

In light of the above, the aim of the present study is to assess and compare the scientific contribution to each component of the 3D paradigm - decarbonization, digitalization, and decentralization - based on a bibliometric analysis of the international publication corpus for 2001–2025. The objectives are: (1) to quantify the scale and dynamics of research across the three components; (2) to construct and interpret keyword-based thematic maps and clusters; (3) to identify zones of thematic integration at the interfaces among the 3D components, together with associated research gaps. This design leverages established bibliometric methods while situating the inquiry within the socio-technical theoretical perspective on energy transitions.

II. DATA AND METHODS

The empirical basis for the analysis is a Scopus-derived dataset spanning 2001–2025. The temporal scope captures the early emergence of the transition discourse and its subsequent consolidation. To ensure comparability, the corpus is restricted to English-language publications and standard scholarly document types (journal articles, conference papers, reviews, and book chapters). Records include bibliographic metadata, abstracts, author and index keywords, citation counts, and source information.

The query design follows a two-level logic. At the first level, which is intended to capture the general field, we employ a set of terms that reflect standard disciplinary vocabulary and the principal levels of analysis in energy studies: “energy system,” “power system,” “energy transition,” “power industry” or “power grid,” “energy sector” or “power sector,” “energy policy” or “energy planning,” and “energy transformation.” This umbrella layer is designed to ensure that the search retrieves the core literature on energy systems while remaining neutral with respect to specific technologies or policy instruments.

At the second level, the corpus is structured by the three components of the 3D paradigm. This follows the established interpretation of decarbonization, digitalization, and decentralization as three interrelated drivers of energy system transformation [1]. For the decarbonization block, the keyword set includes “global warming,” “carbon neutral,” “greenhouse gas,” “climate change,” (“carbon dioxide” OR “CO2”) AND emission, “zero carbon,” “low carbon,” hydrogen, renewable, and “clean energy.” These expressions represent canonical markers of the climate mitigation agenda as codified in IPCC assessments and widely applied in bibliometric and policy analysis [17]. The inclusion of both policy-oriented

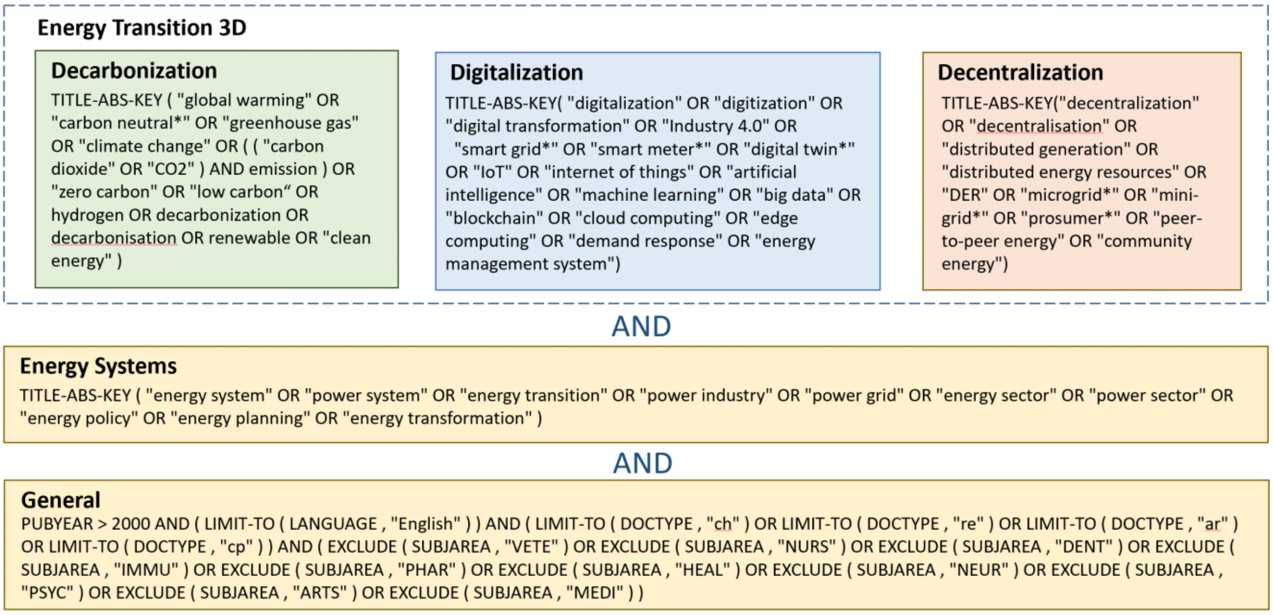

Energy Transition 3D

Decarbonization
TITLE-ABS-KEY ("global warming" OR "carbon neutral*" OR "greenhouse gas" OR "climate change" OR (("carbon dioxide" OR "CO2") AND emission) OR "zero carbon" OR "low carbon" OR hydrogen OR decarbonization OR decarbonisation OR renewable OR "clean energy")

Digitalization
TITLE-ABS-KEY("digitalization" OR "digitization" OR "digital transformation" OR "Industry 4.0" OR "smart grid*" OR "smart meter*" OR "digital twin*" OR "IoT" OR "internet of things" OR "artificial intelligence" OR "machine learning" OR "big data" OR "blockchain" OR "cloud computing" OR "edge computing" OR "demand response" OR "energy management system")

Decentralization
TITLE-ABS-KEY("decentralization" OR "decentralisation" OR "distributed generation" OR "distributed energy resources" OR "DER" OR "microgrid*" OR "mini-grid*" OR "prosumer*" OR "peer-to-peer energy" OR "community energy")

AND

Energy Systems
TITLE-ABS-KEY ("energy system" OR "power system" OR "energy transition" OR "power industry" OR "power grid" OR "energy sector" OR "power sector" OR "energy policy" OR "energy planning" OR "energy transformation")

AND

General
PUBYEAR > 2000 AND (LIMIT-TO (LANGUAGE , "English")) AND (LIMIT-TO (DOCTYPE , "ch") OR LIMIT-TO (DOCTYPE , "re") OR LIMIT-TO (DOCTYPE , "ar") OR LIMIT-TO (DOCTYPE , "cp")) AND (EXCLUDE (SUBJAREA , "VETE") OR EXCLUDE (SUBJAREA , "NURS") OR EXCLUDE (SUBJAREA , "DENT") OR EXCLUDE (SUBJAREA , "IMMU") OR EXCLUDE (SUBJAREA , "PHAR") OR EXCLUDE (SUBJAREA , "HEAL") OR EXCLUDE (SUBJAREA , "NEUR") OR EXCLUDE (SUBJAREA , "PSYC") OR EXCLUDE (SUBJAREA , "ARTS") OR EXCLUDE (SUBJAREA , "MEDI"))

Fig. 1. Structure of search queries in the Scopus international database of peer-reviewed scientific literature.

labels (for example, net zero and low carbon) and technology terms (for example, hydrogen and renewables) increases the likelihood of capturing documents that discuss mitigation pathways, technology deployment, and emissions outcomes within the same analytical frame.

For the digitalization block, the keywords are "digitalization," "digitization," "digital transformation," "Industry 4.0," "smart grid*," "smart meter*," "digital twin*," "IoT" or "internet of things," "artificial intelligence" or "machine learning," "big data," "blockchain," "cloud computing," "edge computing," "demand response," and "energy management system." This set covers both infrastructural layers of digital energy systems and algorithmic or data-centric approaches, aligning with the IEA's framework and survey literature on smart grids and digital energy [18], [19]. The use of truncation where appropriate (for example, "smart grid*," "digital twin*") allows for terminological variants while preserving specificity.

For the decentralization block, the terms are "decentralization" or "decentralisation," "distributed generation," "distributed energy resources," "DER," "microgrid*," "mini-grid*," "prosumer*," "peer-to-peer energy," and "community energy*." This vocabulary captures the architectural and organizational shift toward distributed resources, local markets, and energy communities, and it is grounded in foundational microgrid literature together with recent reviews of community-based energy models [20 - 22]. The combination of technical descriptors (for example, microgrids and DER) with socio-institutional concepts (for example, prosumers and energy communities) enables the retrieval of both engineering-centric and governance-oriented strands of the decentralization discourse.

Taken together, this two-level dictionary balances recall and precision. The first level secures comprehensive coverage of the energy systems domain, while the second level supports a reproducible stratification of the corpus into thematic clusters aligned with the 3D paradigm of the energy transition. The explicit linkage to established reports and reviews provides conceptual legitimacy and facilitates comparability with prior bibliometric studies.

All terms are searched in TITLE-ABS-KEY fields. Global filters harmonize the selection across blocks: publication year greater than 2000, English language, and exclusion of non-energy biomedical areas not germane to the present inquiry. The detailed query structure in the international database of peer reviewed scientific literature Scopus is shown in Figure 1.

Retrieved records are exported in standardized formats and subjected to a consistent preprocessing pipeline. Normalization includes lowercasing and harmonization of British and American spellings (e.g., decarbonization / decarbonisation) followed by lemmatization. Abbreviations such as RES or DER are unified and connected to the related terms (e.g. RES = renewable energy resources). Document duplicates are removed primarily via DOI matching; in the absence of

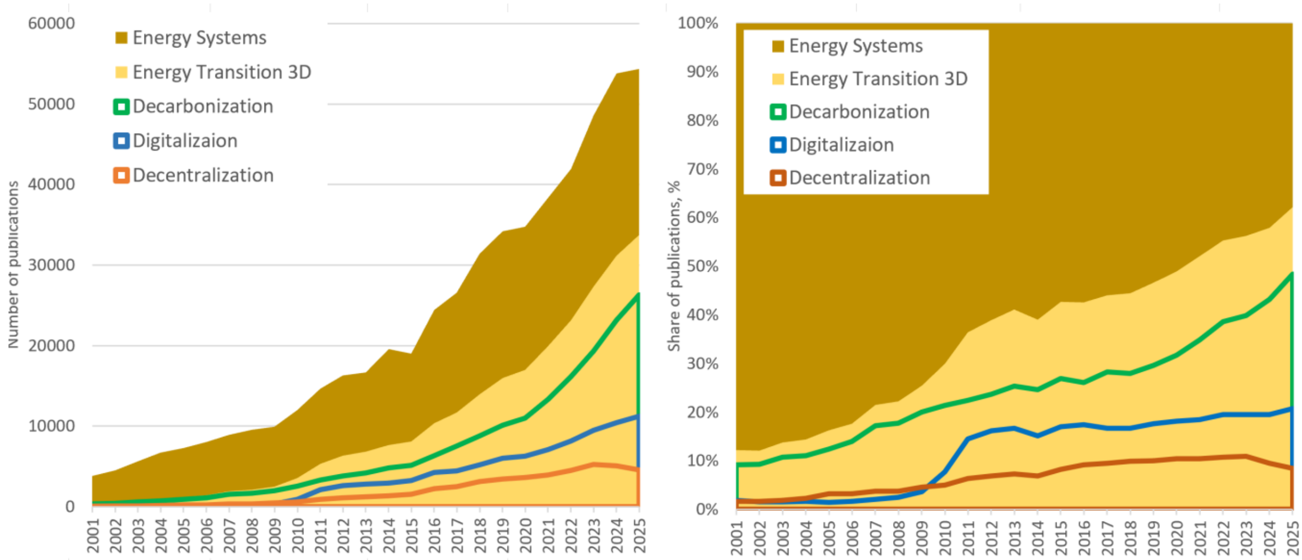

Fig. 2. Annual publication counts and relative shares on energy-transition research in energy systems together with 3D components (decarbonization, digitalization, and decentralization) over 2001–2025.

DOIs, fuzzy title matching with year and source tie-breakers is applied. Subject-area filters are verified to reduce contamination from adjacent but out-of-scope fields.

The descriptive component comprises annual publication counts and citations, which collectively trace phases of emergence, consolidation, and accelerated growth. To compare the three components, records are tagged by block after de-duplication, allowing computation of portfolio shares within the transition-themed corpus. Headline proportions from the working dataset indicate that decarbonization accounts for approximately half of the output, digitalization for roughly one fifth, and decentralization for a smaller, though steadily expanding, share. Country-level contributions are summarized through publication counts and a simple impact proxy (citations per publication), acknowledging that more refined field-normalized indicators would strengthen cross-national comparisons.

III. Results and Discussion

Using the query structure outlined in the previous section, bibliographic records were retrieved from the Scopus database for the period 2001 to 2025. The corpus reflects the state of indexing as of 10 December 2025; consequently, data for 2025 remain slightly incomplete. Figure 2 shows quantitative publication growth and relative shares on energy-transition research in energy systems together with 3D components (decarbonization, digitalization, and decentralization).

The analysis indicates a pronounced expansion of publication activity in energy research overall and a sharp intensification of the Energy Transition 3D strand within that corpus. Total publications in the energy systems domain increased from 3,849 to 54,330, while the Energy Transition 3D subset grew from 469 to 33,761. The share of 3D in the overall corpus rose steadily: from 12% in 2001 to 30% in 2010, approximately 43 to 49% in 2016 to 2020, surpassing one half in 2021 (52%), and reaching 62% by 2025. These figures point not only to quantitative growth but also to a qualitative shift in the center of gravity of research agendas toward decarbonization, digitalization, and decentralization within energy systems.

The internal structure of energy transition research shows asymmetric yet coordinated growth across all three components. Publications on decarbonization increased from 354 to 26,280, and its share within Energy Systems rose from 9% to 48% by 2025, with a sustained acceleration after 2018. Digitalization is the fastest growing component in relative terms: from 72 to 11,245 publications and from 2% in 2001 to 21% in 2025. A key inflection occurred around 2010 to 2012, when the share rose from 8% to 15 to 16%, followed by stabilization at 18 to 21% during 2019 to 2025. This inflection marks the point at which the digitalization concept entered broad circulation in the research literature. Decentralization rose from 63 to 4,601 publications, with its share increasing from 2% to a peak of 10 to 11% in 2018 to 2023, then moderating to 9% in 2024 and 8% in 2025. This pattern may reflect both a reorientation of research effort toward decarbonization and digitalization and potential lags in the indexing of 2024 to 2025 work on distributed energy and community models.

A phase-based representation is also observed on Fig. 2. Phase 1 (2001 - 2009) shows a gradual rise in the 3D share from 12% to 25% at modest absolute volumes. Phase 2 (2010 - 2016) exhibits a structural break: the 3D share increases to about 43%, digitalization moves rapidly from the periphery toward the quasi-core (from 8% to 17%), and decarbonization consolidates its dominance (21 to 26%). Phase 3 (2017 - 2021) is characterized by consolidation, with Energy Transition 3D occupying 44 to 52% of the total corpus and all three components growing in tandem. Phase 4 (2022 - 2025) features a deepening of decarbonization’s dominance (share rising from 39% to 48%), a persistently high contribution from digitalization (19 to 21%), and a plateau in decentralization, including a modest decline from 11% to 8%. Taken together, these results indicate that by the mid-2020s the energy transition had shifted from a discrete thematic niche to the principal research mainstream within energy systems, with decarbonization setting the overall scale, digitalization providing speed and controllability, and decentralization driving architectural transformation and institutional innovation.

Dividing the Energy Transition 3D corpus into mutually exclusive subsets: single-component publications (decarbonization only, digitalization only, decentralization only), pairwise intersections (decarbonization–digitalization, decarbonization–decentralization, digitalization–decentralization), and the three-way core itself we quantify the extent of thematic integration by year. The results indicate a marked rise in integrative work. Aggregating by periods, the share of publications that engage at least two components grows from 6.5% in 2001–2009 to 17.8% in 2010–2016 and 20.8% in 2017–2025; within this, the three-way core increases in absolute terms from 44 to 1,279 to 5,996 records and reaches about 3.1% of the 3D corpus in the latest period. Pairwise overlaps are led by decarbonization–digitalization (rising to 8.9% in 2017–2025), followed by decarbonization–decentralization (6.1%) and digitalization–decentralization (2.7%). Despite this consolidation, single-component contributions remain the majority: decarbonization-only accounts for roughly 52.0% of the 2017–2025 3D corpus, digitalization-only for 20.6%, and decentralization-only for 6.7%. Taken together, the evidence points to a progressive coupling of research agendas across the 3D paradigm, with the strongest integration occurring along the decarbonization–digitalization axis and a smaller, but

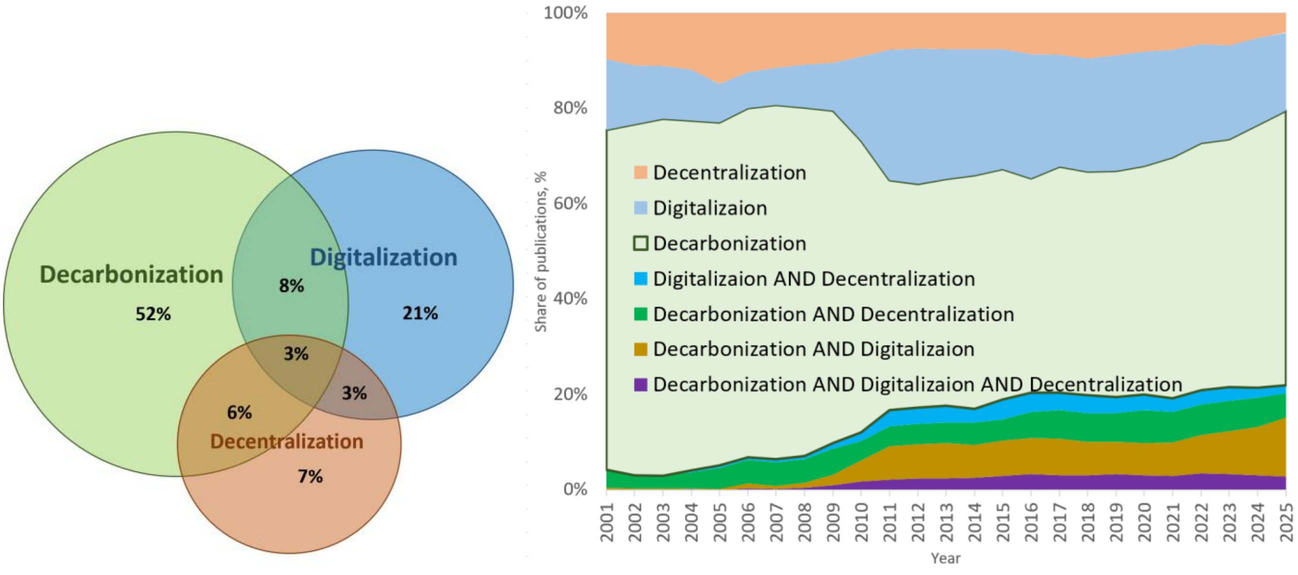

a) b)

Fig. 3. Overlaps among the 3D components in the Energy Transition 3D corpus in energy systems, 2001–2025: (a) Venn diagram showing total publication shares; (b) yearly share distribution.

growing, three-way core.

Figure 3 (a) illustrates that decarbonization remains the system-forming strand, accounting for just over half of the 3D corpus in singleton form. Integration occurs primarily along the decarbonization–digitalization axis (8%), with smaller but nontrivial overlaps for decarbonization–decentralization (6%) and digitalization–decentralization (3%). The three-way core is compact (3%), suggesting that genuinely triadic studies are still a minority relative to single-component contributions. Taken together, the composition points to a field where decarbonization sets the dominant research baseline, digitalization acts as the principal transversal enabler, and decentralization contributes a focused but more specialized body of work interfacing with the other two components.

Using VOSviewer [23], thematic maps for each component of the 3D energy transition (decarbonization, digitalization, and decentralization) were generated from the top 1,000 keywords drawn from the component-specific article subsets, applying a publication citation threshold greater than 20 (see Fig. 4–6). The color scale encodes the average publication year over 2001–2025, where blue indicates earlier years and yellow indicates later years, which allows the temporal evolution of macrotopics to be assessed. Node size reflects keyword frequency rather than importance, and the average-year metric is sensitive to recent surges; both factors should be considered when interpreting the maps.

The decarbonization map in Figure 4 exhibits a core–periphery structure with a pronounced temporal gradient. At the center lies an earlier cluster around renewable energy source, energy policy, climate change, carbon dioxide, fossil fuel, and alternative energy. The blue and turquoise hues indicate that during the 2000s and early 2010s the discourse shifted from a climate policy frame toward the scaling of renewables and their system integration.

By the mid-2010s the core becomes more technology oriented. Adjacent, relatively larger nodes include solar energy, photovoltaics, solar power generation, energy storage, electric battery, smart grid, demand response, and microgrid. Their green coloration signals continued growth through the 2010s, while the size of the PV and storage nodes confirms sustained high frequency across the entire 2001–2025 period.

A later wave is visible in yellow clusters along two fronts. First, electrochemistry and hydrogen: hydrogen production, electrolysis, fuel cell, electrocatalyst, and

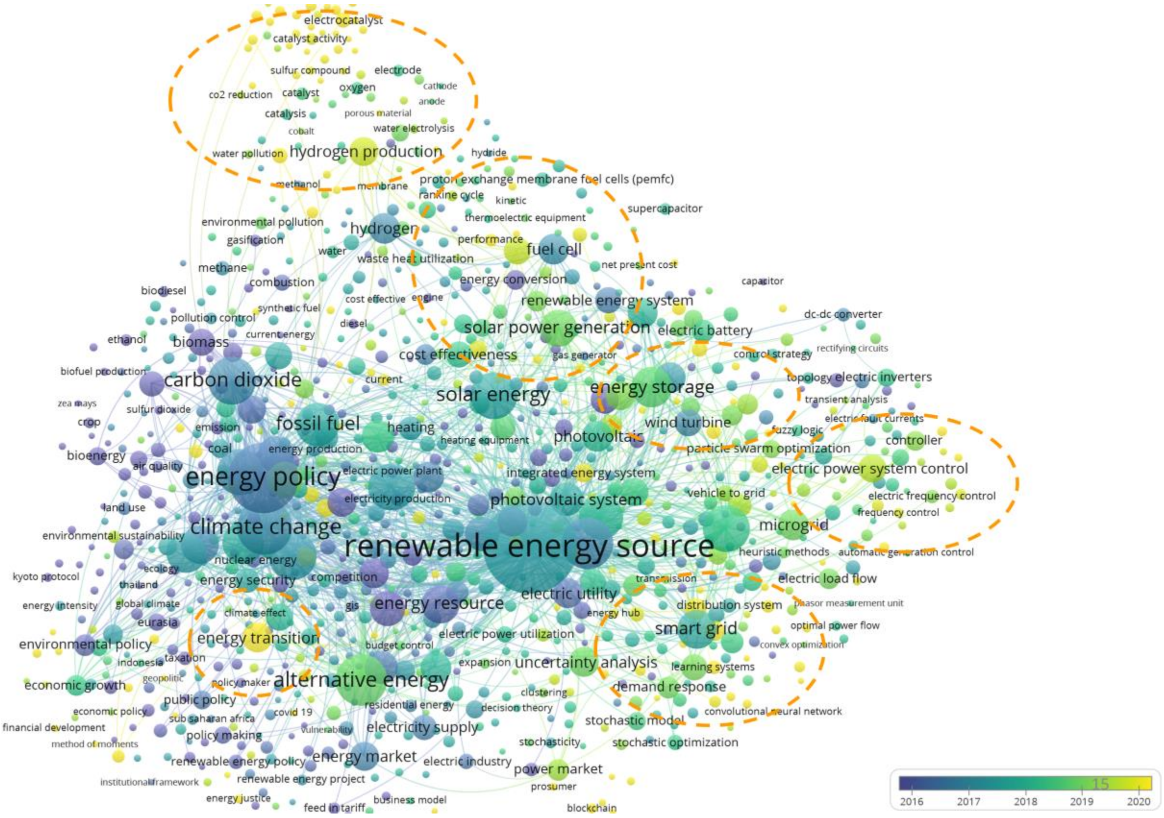

Fig. 4. Decarbonization: keyword co-occurrence map within energy-systems research, 2001-2025.

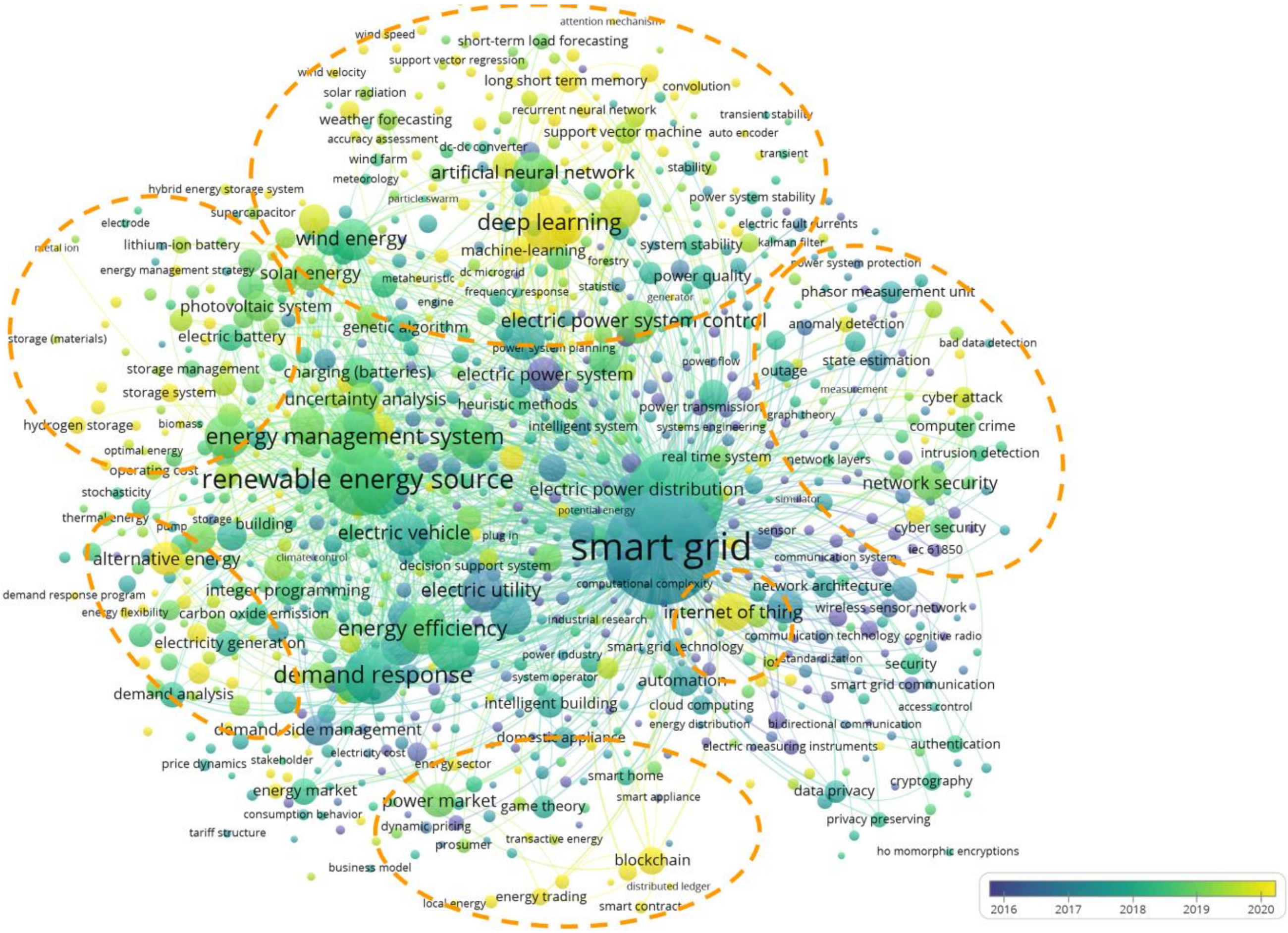

Fig. 5. Digitalization: keyword co-occurrence map within energy-systems research, 2001-2025.

related materials represent comparatively recent and fast-growing subfields. Second, power electronics and system control: electric power system control, inverters, dc-dc converter, controller, frequency control, together with algorithmic methods such as particle swarm optimization, stochastic models, and neural networks. These areas reflect a transition from simply adding renewables to actively managing flexibility and power quality at high variable renewable shares.

Bridging topics include integrated energy system, vehicle-to-grid, uncertainty analysis, and cost effectiveness. Their relatively late average year suggests strengthening attention after 2018 at the interface of engineering and economics.

Figure 5 shows the “Digitalization” thematic map, which exhibits a clear core-periphery structure and a pronounced temporal gradient. At the center are early, high-frequency nodes such as smart grid, demand response, energy management system, renewable energy source, energy efficiency, internet of things, and links to electric power distribution and electric utility.

From the mid-2010s onward the core becomes increasingly technology and algorithm oriented. Larger, later clusters appear around deep learning, artificial neural network, internet of thing, support vector machine, and forecasting, including short-term load, wind, and solar, together with uncertainty analysis and optimization. This pattern reflects a shift toward data-driven methods for prediction and operational planning. In parallel, a cyber-resilience contour strengthens, centered on network security, cyber-attack, intrusion detection, anomaly detection, state estimation, and phasor measurement unit, with yellowish hues signaling acceleration in 2018–2025. At the interface of markets and ICT, clusters on blockchain, smart contract, energy trading, transactive energy, and demand-side management trend later, indicating the institutionalization of digital transactions and local flexibility markets. Connections to electric vehicle, charging, electric battery, and storage management point to the integration of DER within the

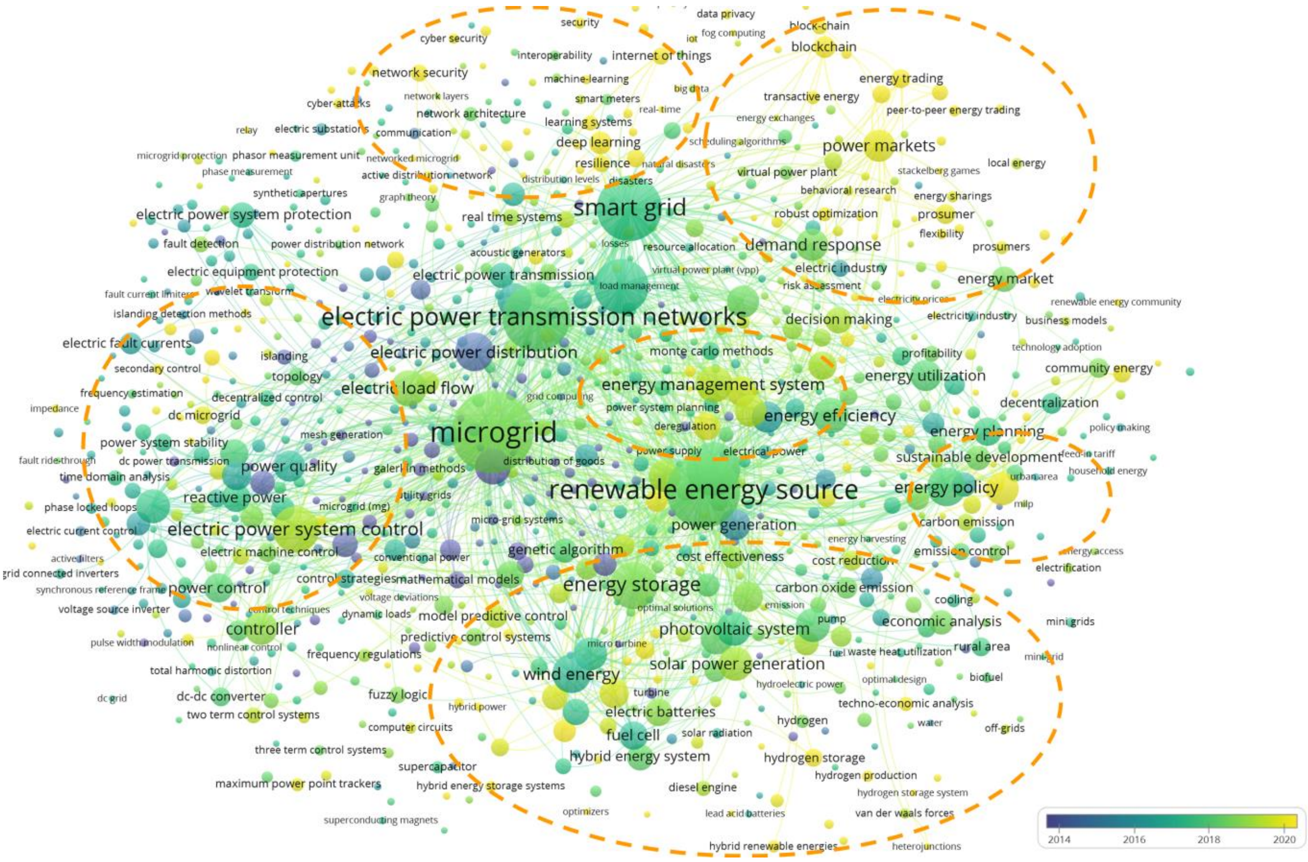

Fig. 6. Decentralization: keyword co-occurrence map within energy-systems research, 2001-2025.

digital control layer. Overall, the evolution proceeds from the classical smart-grid and demand-response paradigm to a mature digital ecosystem in which machine-learning methods, cybersecurity, platform solutions, and transaction mechanisms are central.

Figure 6 represents the decentralization topic map as a compact technical core with a clear temporal gradient from engineering-focused foundations toward market and community themes. Early, high-frequency nodes cluster around microgrid, renewable energy source, energy storage, photovoltaic system, wind energy, and electric power transmission networks, together with control and protection topics such as electric power system control, controller, reactive power, fault detection, stability, dc microgrid, and dc-dc converter. This pattern reflects the initial emphasis on distributed architectures, power electronics, and operational reliability for integrating variable renewables. From the mid-2010s the map broadens toward system operation and planning, with energy management system, demand response, decision making, uncertainty analysis, and techno-economic analysis gaining prominence. Later-year clusters concentrate on power markets, transactive energy, energy trading, blockchain, prosumers, and community energy, indicating a shift toward market design, participation models, and institutional arrangements for local energy systems. A parallel strand in the upper left highlights network security and cyber-attack detection, signaling growing attention to cyber-resilience of distributed infrastructures. Taken together, the evolution moves from hardware and control of microgrids to socio-technical integration through markets, communities, and cybersecurity.

To aid interpretation, the decentralization map can be read in conjunction with the decarbonization and digitalization maps (cf. Fig. 4–5). Several high-frequency constructs recur across figures and anchor the triad: energy storage, photovoltaic system and wind energy link decarbonization to decentralization; smart grid, demand response, and energy management system connect decentralization with digitalization; microgrid appears in all three as the canonical distributed architecture. The temporal gradients are also coherent: the 2016–2020 window marks a shared inflection where data-driven forecasting and control (Fig. 5) intersect with large-scale VRE deployment and storage build-out (Fig. 4) and with the maturation of microgrid operation and protection (Fig. 6). At the same time, each map retains distinctive late-emerging contours: hydrogen and electrocatalysis in decarbonization; machine-learning methods and cybersecurity in digitalization; and market and community constructs such as transactive energy, energy trading, and community energy in decentralization. Together these correspondences and divergences indicate progressive coupling of the three components around a common operational stack, while preserving domain-specific frontiers.

IV. CONCLUSION

This scientometric assessment shows that research on energy system transformation has moved from a peripheral niche to the principal mainstream, with the three-dimensional framework now structuring the field. Decarbonization functions as the system forming axis, digitalization has matured into a transversal enabler of forecasting, control, and market participation, and decentralization advances through distributed energy resources, microgrids, and energy community architectures. The internal composition of the literature displays increasing pairwise integration and a small but expanding triadic core, which indicates convergence of technological, digital, and institutional trajectories. Thematic maps show a temporal shift from policy and resource framing to technology intensive fronts, including storage and hydrogen, power electronics and system control, machine learning methods, cyber security, and transactive energy, consistent with the operational challenges of high shares of variable renewables. Given the secular growth of global publishing and uneven country contributions, future work should incorporate field normalized impact indicators, country level baselines, and analyses of collaboration networks, and should triangulate bibliometric evidence with patent and demonstration datasets. The study has limitations related to a single database, an English language focus, and indexing latency for 2025, and it outlines a reproducible path for future comparative analyses.

ACKNOWLEDGMENT

The research was carried out under State Assignment Project (no. FWEU-2021-0007) of the Fundamental Research Program of Russian Federation 2021-2030 using the resources of the High-Temperature Circuit Multi-Access Research Center (Ministry of Science and Higher Education of the Russian Federation, project no 13.CKP.21.0038). The results were preliminary presented and discussed on the international conference “Energy Systems Research - 2025”, September 5-11, 2025, Irkutsk, Russia.

REFERENCES

[1] M. L. Di Silvestre, S. Favuzza, E. R. Sanseverino, and G. Zizzo, “How decarbonization, digitalization and decentralization are changing key power infrastructures,” *Renewable and Sustainable Energy Reviews*, vol. 93, pp. 483–498, 2018, doi: 10.1016/j.rser.2018.05.068.

[2] N. Morell-Dameto, J. P. Chaves-Ávila, and T. Gómez San Román, “Revisiting electricity network tariffs in a context of decarbonization, digitalization and decentralization,” *Energies*, vol. 13, no. 12, 3111, 2020, doi: 10.3390/en13123111.

[3] F. Heymann, T. Milojevic, A. Covatariu, and P. Verma, “Digitalization in decarbonizing electricity systems: Phenomena, regional aspects, stakeholders, use cases, challenges and policy options,” *Energy*, vol. 262, art. 125521, 2023, doi: 10.1016/j.energy.2022.125521.

[4] F.W. Geels, “Socio-technical transitions to sustainability: A review of criticisms and elaborations of the multi-level perspective,” *Current Opinion in Environmental Sustainability*, vol. 39, pp. 187–201, 2019, doi: 10.1016/j.cosust.2019.06.009.

[5] B.K. Sovacool, D. J. Hess, and R. Cantoni, “Energy transitions from the cradle to the grave: A meta-theoretical framework integrating responsible innovation, social practices, and energy justice,” *Energy Research and Social Science*, vol. 75, art. 102027, 2021, doi: 10.1016/j.erss.2021.102027.

[6] M. Mahmood, P. Chowdhury, R. Yeassin, M. Hasan, T. Ahmad, and N.-U.-R. Chowdhury, “Impacts of digitalization on smart grids, renewable energy, and demand response: An updated review of current applications,” *Energy Conversion and Management: X*, vol. 24, 100790, 2024, doi: 10.1016/j.ecmx.2024.100790.

[7] S. Harichandan, S. K. Kar, R. Bansal, S. K. Mishra, M. S. Balathanigaimani, and M. Dash, “Energy transition research: A bibliometric mapping of current findings and direction for future research,” *Cleaner Production Letters*, vol. 3, art. 100026, 2022, doi: 10.1016/j.clpl.2022.100026.

[8] M. Diaconescu, L. E. Marinas, A. M. Marinoiu, M.-F. Popescu, and M. Diaconescu, “Towards renewable energy transition: Insights from bibliometric analysis on scholar discourse to policy actions,” *Energies*, vol. 17, no. 18, 4719, 2024, doi: 10.3390/en17184719.

[9] E. Hache and A. Palle, “Renewable energy source integration into power networks, research trends and policy implications: A bibliometric and research actors survey analysis,” *Energy Policy*, vol. 124, pp. 23–35, 2019, doi: 10.1016/j.enpol.2018.09.036.

[10] Z. Li, Han Pu, and Tiezhi Li, “Knowledge mapping and evolutionary analysis of energy storage resource management under renewable energy uncertainty: A bibliometric study,” *Frontiers in Energy Research*, vol. 12, 1394318, 2024, doi: 10.3389/fenrg.2024.1394318.

[11] K. A. Tahir, J. Ordóñez, and J. Nieto, “Exploring evolution and trends: A bibliometric analysis and thematic quantification of hybrid microgrid systems,” *Sustainability*, vol. 16, no. 12, 5156, 2024, doi: 10.3390/su16125156.

[12] C. Delcea, S.-V. Oprea, A. M. Dima, A. Domenteanu, A. Bara, and L.-A. Cotfas, “Energy communities: Insights from scientific publications,” *Oeconomia Copernicana*, vol. 15, no. 3, pp. 1101–1155, 2024, doi: 10.24136/oc.3137.

[13] A. H. H. Mohamad and R. Ab-Rahim, “Mapping the research landscape of energy market and renewable energy: A bibliometric analysis,” *International Journal of Renewable Energy Development*, vol. 14, no. 4, pp. 703–716, 2025, doi: 10.61435/ijred.2025.61058.

[14] E. I. Obanor, J. O. Dirisu, O. O. Kilanko, O. S. Ohunakin, O. O. Ajayi, and S. O. Oyedepo, “Bibliometric analysis of sustainable energy transition and climate action in sub-Saharan Africa with a focus on Nigeria,” *Discover Energy*, vol. 5, 19, 2025, doi: 10.1007/s43937-025-00084-6.

[15] A. V. Mikheev, “Scientometric analysis of research trends and frontiers on global energy transition,” *AIP Conference Proceedings*, vol. 2552, 080017, 2023, doi: 10.1063/5.0111238.

[16] A. V. Mikheev, “Evolution of energy systems research: Analysis of documents co-citation network,” *Energy Systems Research*, vol. 5, no. 3, pp. 57–66, 2022, doi: 10.38028/esr.2022.03.0008.

[17] IPCC, Climate Change 2022: Mitigation of Climate Change. Summary for Policymakers. Geneva, Switzerland: Intergovernmental Panel on Climate Change, 2022. [Online]. Available: https://www.ipcc.ch/report/ar6/wg3/ Accessed on: Nov. 21, 2025.

[18] International Energy Agency, Digitalization and Energy. Paris, France: IEA, 2017. [Online]. Available: https://www.iea.org/reports/digitalisation-and-energy Accessed on: Nov. 21, 2025.

[19] X. Fang, S. Misra, G. Xue, and D. Yang, “Smart Grid — The New and Improved Power Grid: A Survey,” *IEEE Communications Surveys & Tutorials*, vol. 14, no. 4, pp. 944–980, 2012, doi: 10.1109/SURV.2011.101911.00087.

[20] International Energy Agency, Unlocking the Potential of Distributed Energy Resources: Power System Opportunities and Best Practices. Paris, France: IEA, 2022. [Online]. Available: https://www.iea.org/reports/unlocking-the-potential-of-distributed-energy-resources Accessed on: Nov. 21, 2025.

[21] International Renewable Energy Agency, Innovation Landscape for a Renewable Powered Future: Solutions to Integrate Variable Renewables. Abu Dhabi, UAE: IRENA, 2019. [Online]. Available: https://www.irena.org/-/media/Files/IRENA/Agency/Publication/2019/Feb/IRENA_Innovation_Landscape_2019_report.pdf Accessed on: Nov. 21, 2025.

[22] International Renewable Energy Agency, Quality Infrastructure for Smart Mini Grids. Abu Dhabi, UAE: IRENA, 2020. [Online]. Available: https://www.irena.org/publications/2020/Dec/Quality-infrastructure-for-smart-mini-grids Accessed on: Nov. 21, 2025.

[23] N. J. van Eck and L. Waltman, “Software survey: VOSviewer, a computer program for bibliometric mapping,” *Scientometrics*, vol. 84, no. 2, pp. 523–538, 2010, doi: 10.1007/s11192-009-0146-3.

Alexey V. Mikheev is a Doctor of Engineering and Head of the Research and Analytical Center at the Melentiev Energy Systems Institute, Siberian Branch of the Russian Academy of Sciences (SB RAS). His research interests include mathematical modeling and optimization of energy systems and power units; energy technology assessment; scientometric and bibliometric analysis; image processing; optical measurements; flow visualization; and software development.

Nikolai E. Karimov is a doctoral student specializing in the development of tools for monitoring and analyzing directions of scientific research and science-and-technology development in the energy sector and related fields, with a focus on assessing their innovation potential and building predictive models.

Machine Learning for Identifying Characteristics of Isolated, Clustered, and Pulsed Vapor Bubbles on a Heated Surface under Non-Stationary Boiling Conditions

P.V. Khan[1,2*], A.A. Levin[1,2], I.I. Chupin[1,2], A.S. Safarov[2]

[1] Novosibirsk State University, Novosibirsk, Russia
[2] Melentiev Energy Systems Institute of Siberian Branch of Russian Academy of Sciences, Irkutsk, Russia

Abstract **— This paper presents an automated system for analyzing high-speed video of non-stationary nucleate boiling on an opaque steel surface. The method leverages the DenoiSeg deep learning network for robust bubble segmentation under challenging conditions (reflected light, optical distortions) and introduces an algorithm for tracking bubbles and calculating time-dependent characteristics.**

The system identifies and classifies bubbles into three types (isolated, clustered, and pulsating) to extract the essential boiling parameters, including nucleation site density, surface area fraction, maximum diameter, and nucleation frequency. Validation against manual key frame analysis confirms the system's accuracy. The results not only verify the significant prevalence of clustered and pulsating bubbles but also, thanks to extensive data processing, reveal trends hidden by stochastic noise, such as the growth of the maximum diameter of clusters with increasing surface temperature. The developed tool provides a reliable foundation for building predictive heat transfer models for non-stationary boiling regimes.

Index Terms **— Nucleate boiling, machine learning, image segmentation, time-averaging, nucleation site density, maximum bubble diameter, nucleation frequency.**

I. INTRODUCTION

Nucleate boiling in a flow of subcooled liquid is one of the most effective heat removal methods, with widespread applications in power engineering, electronics cooling, and other fields **used three CNN models to segment overlapping bubbles, followed by a generative adversarial network (GAN) for hidden bubble part reconstruction** [1]. However, boiling properties under non-stationary regimes involving rapid heater temperature changes remain insufficiently studied [2–4].

In recent decades, high-speed videography has been increasingly used to investigate nucleate boiling characteristics. It is impossible to extract parameters of individual bubbles and statistical boiling characteristics from the resulting large volumes of video data without modern automated image and video processing tools [5–10].

The objective of this work is to develop an automated system for identifying bubbles on the heater surface in high-speed video frames captured in reflected light under non-stationary heating conditions, and to obtain characteristics of isolated, clustered, and pulsating bubbles.

II. LITERATURE REVIEW

Numerical modeling of heat and mass transfer during boiling is a powerful tool for understanding underlying mechanisms [4, 11–13]. Boiling heat flux correlations rely

---

[*] Corresponding author.
E-mail: polinakhan@isem.irk.ru

DOI: 10.25729/esr.2025.04.0006

Received November 14, 2025. Revised November 15, 2025. Accepted December 9, 2025. Available online December 29, 2025.

on experimentally determined characteristics such as nucleation site density, bubble diameter, and frequency [14, 15]. Generalizing these correlations for non-stationary, high-temperature-rise-rate regimes remains a significant challenge.

When acquiring new experimental data, it is essential to account for the stochastic nature of vapor generation and the extremely wide parameter scatter of individual bubbles coexisting under identical conditions [16–19]. Measuring the lifetime and dimensions of individual bubbles with sufficient accuracy, while simultaneously gathering statistical data on a sufficiently large number of bubbles, requires processing tens of thousands of bubble images across thousands of frames. Consequently, it is not surprising that with the widespread adoption of high-speed videography in nucleate boiling experiments, methods for machine-assisted processing of video frames have been actively developed.

Heuristic algorithms based on threshold binarization, edge detection, or background subtraction have in some cases allowed for the automation of nucleate boiling video processing [5, 20, 21]. Dark bubbles on a light background are typically obtained when filming in transmitted light using a transparent heater [22, 23]. However, it is well-established that the surface roughness and wettability of the heater, as well as its thickness, heat capacity, and thermal conductivity, have a profound influence on boiling characteristics and the removed heat flux. Therefore, it is essential to obtain experimental data with heater properties that closely approximate those of the heat-transferring surfaces in industrial heat exchangers. Bubbles on a steel heater surface in reflected light are visible to the human eye because they create glares and refract light; however, they do not differ from the background in intensity level and often lack distinct boundaries.

In some cases, algorithms based on correlating video frames with pre-selected bubble templates have shown sufficient effectiveness [24, 25]. The method for cross-correlation of successive video frames is used in the PIV (Particle Image Velocimetry) method for studying the motion of bubbles with more or less constant sizes and shapes [26]. However, cross-correlation is computationally expensive. More importantly, it is poorly suited for bubble clusters, which exhibit immense diversity in forms and structures.

More flexible methods for bubble identification are machine learning techniques implemented in various neural network models. Convolutional Neural Networks (CNNs) have demonstrated strong performance [6, 7, 9, 10]. Compared to a multilayer perceptron, a CNN contains far fewer weights, making it less resource-demanding and less prone to overfitting. There are several recent works on application of models based on You Only Look Once (YOLO) architecture to detection of bubbles in bubbly flows [8, 27]. Hessenkemper et al. [28] used three CNN models to segment overlapping bubbles, followed by a generative adversarial network (GAN) for hidden bubble part reconstruction.

Nevertheless, preparing a sufficient amount of labeled data for training a deep neural network from scratch is a task as labor-intensive as manually processing a series of experiments. One way to overcome this obstacle is to use pre-trained neural networks, which may require only a few dozen images specific to a given experiment for fine-tuning. This approach is proposed by the authors of the VideoSAM model for segmenting the vapor phase in high-speed video frames [29, 30]. Another approach is unsupervised learning. It is used, in particular, in the DenoiSeg (Denoising & Segmentation) model [31], where the same network is trained to produce both a segmented image and an image denoised from random noise at different outputs. The segmentation output is trained in a supervised manner, while the denoising output is trained unsupervised. There are also examples of successful training of a neural network model designed for recognizing individual bubbles in bubbly flow on generated images [7].

Most existing heat transfer models for nucleate boiling assume that bubble interaction is negligible until at least one-third of the heater surface is covered and can therefore be disregarded. However, several studies [32, 33] have demonstrated that bubbles can activate nearby nucleation sites, meaning bubble clusters can form at the very early stages of boiling. The shape of clustered bubbles is far from spherical, and their size may not correspond to the amount of heat withdrawn from the heater for a given bubble, as heat and vapor transfer occurs between bubbles. In addition to isolated and clustered bubbles, the authors of [33] identified pulsating bubbles. Once formed, these bubbles remain on the surface for 10 to 100 times longer than ordinary bubbles, periodically growing and shrinking in size.

This work tests the hypothesis of the suitability of available neural network architectures, particularly DenoiSeg, for automating the processing of non-stationary boiling videos on an opaque heater. The developed automated system is validated by comparison with manual processing results. In doing so, it verifies previous conclusions based on manual processing results, regarding the significant proportion of clustered and pulsating bubbles at all stages of nucleate boiling.

III. METHODOLOGY

A. Process Outline

During the experiment on non-stationary boiling, high-speed videography of vapor structures on the heater surface was performed. Each experimental run was defined by two key parameters: the flow subcooling (ΔT_{sub}) and the heater temperature rise rate. The temperature rise rate, which reaches up to 16 000 K/s in this study, was determined relying on the average power generated by the electric current passing through the heater.

The entire processing pipeline for the video frame sequence from a single experiment consisted of three stages:

1. Neural network-based segmentation to define two classes (background and vapor phase).
2. Bubble detection and cataloging.
3. Calculation of time-dependent, averaged boiling characteristics.

In this process, bubbles were accounted for separately according to three types: isolated, clustered, and pulsating.

B. Experimental Setup

The experimental data were obtained at the “High-Temperature Circuit” Multi-Access Research Center. A description of the facility and the results of processing individual experiments are provided in [33, 34]. The automated high-speed video frame processing system developed in this study was tested using experimental data for water bubble boiling, characterized by a subcooling of 23–103 K at a pressure of 0.29 MPa, on a technically smooth (machined) steel surface with a maximum roughness of 4 μm, and at an average flow velocity of 0.52 m/s.

Videography of the vapor structures on the heater surface was performed through the opposite transparent channel wall and a 3 mm layer of water. One or two high-power LED lamps were used for illumination. The light passed through the same transparent wall from above and below the camera at an angle of approximately 45° to the heater surface. This configuration created one or two glares on each isolated bubble and, due to the scattered light component, made it possible to distinguish the overall structure of the background and vapor cavities.

A Phantom V2012 high-speed camera was used for filming, with a resolution of 5.5 μm per pixel. This setup allowed for the recording of bubbles with a size of approximately 10 μm and larger. Frame rates of up to 350 000 Hz were available at a resolution of 128×128 pixels. However, preliminary video analysis established that no bubbles with a lifetime of less than 10 μs were observed; it was therefore decided to reduce the frame rate to 180 000 Hz. This allowed for capturing frames with a size of 256×256 pixels, corresponding to a 1.4 mm × 1.4 mm area on the heater surface plane. The size of individual bubbles on the surface did not exceed 0.3 mm.

For subsequent image segmentation and vapor structure identification, frames were extracted from the video of each experiment, covering the period from the appearance of the first bubble, τ_{ONB} (Onset of Nucleate Boiling) until the moment when vapor agglomerates detached from the surface, moved out of the depth of field, and began to obscure other bubbles nucleating on the surface.

C. Neural Network-Based Segmentation

The identification system was based on the DenoiSeg neural network architecture [31], which exists in two forms: as a plugin for ImageJ and as a Python module. This work utilized the ImageJ plugin, extended with a macro for batch processing of video frames. The DenoiSeg neural network is a U-Net architecture with four outputs, three of which are dedicated to segmentation, and the fourth to denoising. The target output for the denoising branch is generated automatically, and this output is used for training on unlabeled images. This process adjusts the network's weights that constitute the feature maps, ultimately improving the segmentation results as well.

Our analysis, based on training the network on diverse experimental video datasets, indicates that a segmentation accuracy of ≥95% requires a model specialized for a single surface type. For a given surface, the training data can encompass variations in key parameters such as flow subcooling, heater temperature rise rate, and video capture settings (illumination, focus, exposure, framing). The total training dataset comprised 491 images, of which 68 were annotated. Another 35 annotated images were used for validation and to prevent network overfitting.

When tested on boiling frames from a structured surface, the model trained on data from a technically smooth surface detected approximately 70% of bubbles. While the Python implementation of the DenoiSeg model allows for adaptation or fine-tuning to address this, the ImageJ plugin version lacks this functionality. Training a new model from scratch for the structured surface is therefore a viable alternative, especially since the process required less than 10 hours on a PC equipped with a single NVIDIA GeForce RTX 4060 Ti GPU.

Figure 1 provides an example of the visual validation of the trained model, showing a comparison of the original frames with their corresponding manually labeled frames and the frames obtained via segmentation by the trained neural network. Although noticeable differences exist between the manual labeling and the results of the automatic segmentation, the statistical characteristics of the bubbles do not exhibit significant distortion.

Furthermore, in the frames marked with numbers 1, 2, and 3, the neural network detected even small bubbles. In the left part of the original frame 3, optical distortions are present, caused by the movement of fluid layers at different temperatures, which had developed during the slow heating process. This did not hinder the automatic identification of bubbles in this area. Frame 4 features large bubbles with a pronounced dry spot area, where the heater surface is visible without any distortion. The neural network misidentified these areas as background. Nevertheless, the overall error rate across various conditions ranged from 0.5 to 5%.

D. Bubble detection and cataloging

The next step after image segmentation was to compile, for each experiment, a list of all bubbles that existed from the onset of vapor generation until the detachment of large vapor agglomerates. The characteristics determined for each bubble included its type, the coordinates of the center of mass of its two-dimensional image at the moment of nucleation, the initial and final frames, the maximum achieved size, lifetime, and nucleation frequency.

The maximum achieved size (effective diameter) D_j of an individual bubble was determined based on the maximum area A_j reached during its lifetime:

$$D_j = \sqrt{\frac{4A_j}{\pi}}\,. \quad (1)$$

The bubble lifetime, in seconds, was calculated as the lifetime in frames divided by the frame rate. Since bubble interactions made re-nucleation at the same site infrequent, determining the waiting time for each individual bubble was not feasible. Therefore, the nucleation frequency f_j of an individual bubble was defined as the reciprocal of its lifetime.

These individual characteristics were determined by analyzing the intersections of regions (objects) marked as vapor (white) across consecutive frames, starting from the frame preceding the appearance of the first bubble. Three bubble types were identified: isolated (also referred to as single), clustered, and pulsating.

An isolated bubble is the most common type considered in the majority of boiling models. It refers to a bubble that nucleates in an area not occupied by other bubbles due to the accumulation of sufficient surface superheat near an active site, undergoes phases of hydrodynamic and thermal expansion, then shrinks and either condenses on the surface or detaches.

In image processing, an isolated bubble is algorithmically defined as a continuous sequence of segmented objects that do not undergo merging or splitting. The sequence must satisfy two criteria: 1) the intersection between two consecutive objects is non-empty, and 2) the displacement of their centroids does not exceed 5 pixels. This threshold, corresponding to a velocity of approximately 5 m/s, was determined through visual inspection of the video dataset. The first object in such a sequence has no intersection with any object in the preceding frame.

Clustered bubbles are defined by their participation in interactions such as merging, splitting, or rapid displacement. These processes enable vapor and heat exchange between bubbles, so a bubble's size may no longer directly reflect the energy received from the heater alone. While touching yet distinct bubbles can be identified during manual frame-by-frame analysis, they appear as a single, irregularly shaped region in a segmented binary image, representing a bubble cluster.

Unlike an isolated bubble, a cluster exhibits three critical features that affect its contribution to heat transfer models: 1) internal vapor and heat transfer, 2) a complex, non-spherical shape with a thickness significantly smaller than its in-plane diameter, and 3) a shortened effective lifetime, typically confined to the interval between interactions.

A pulsating bubble is defined by its resumption of growth after beginning to shrink, undergoing multiple such cycles until it is displaced or absorbed by a cluster. It typically attains a smaller maximum size and exhibits a lower growth rate compared to an isolated bubble at the same nucleation site. This is because, lacking a dormant phase for energy accumulation, it cannot initiate the rapid hydrodynamic growth and micro-layer evaporation characteristic of an isolated bubble. Consequently, an individual pulsating bubble transfers less heat. Despite this, the collective contribution of pulsating bubbles to the total heat flux can be significant, as their small and stable sizes allow for high surface packing density.

In automated processing, a pulsating bubble is identified similarly to an isolated one, with a key distinction: the sequence starts from an object intersecting a single, shrinking bubble from the previous frame. Consequently, each growth-shrinkage cycle was logged as a separate "bubble" entry in the dataset.

E. Calculation of Time-Dependent, Averaged Boiling Characteristics

Surface cavities contribute to the population of active nucleation sites as the increasing surface temperature expands the range of permissible curvature radii [35]. However, they can be activated earlier upon contact with another bubble. On the other hand, once the required surface temperature is reached, a bubble might be absent from a nucleation site for a stochastic waiting period. Furthermore, on an engineered surface, the spatial distribution of cavities with different curvature radii is random. For these reasons, even the most precise bubble count on a single frame from a small surface area does not provide reliable data on the overall nucleation site density on the heater at a given temperature. Further increasing the camera's field of view is only possible by reducing the frame rate. Therefore, the hypothesis of equivalence between spatial and temporal averaging with a certain time step was adopted; that is, the ergodicity of the bubble system on the heater surface was assumed. The temporal averaging window, Δt, must exceed the average bubble lifetime (approximately 0.03 ms) and be less than the time required for the surface temperature to increase by 10 K (0.5 ms at a surface temperature rise rate of 20 K/ms).

The boiling characteristics in each individual experiment were calculated for time instances $t \in \left[\tau_{ONB}+\frac{\Delta t}{2}, \tau_{ONB}+\Delta t_1, \tau_{ONB}+\frac{\Delta t}{2}+2\Delta t_1, \tau_{ONB}+\frac{\Delta t}{2}+3\Delta t_1, \ldots, \tau_{OSV}-\frac{\Delta t}{2}\right]$, where $\Delta t_1 \le \Delta t$. This study used values of $\Delta t = 0.55$ ms and $\Delta t_1 = 0.16$ ms. Statistical processing was performed for four bubble categories: S – single (isolated), C – cluster, P – pulsating, A – all. The last category is the union of the first three. The processing yielded the following time-dependent functions: nucleation site density, $N_{a,l}(t)$, maximum diameter, $D_{m,l}(t)$, nucleation frequency, $f_{b,l}(t)$ and fraction of surface area occupied by bubbles, $F_{v,l}(t)$, where $l \in \{S, C, P, A\}$. The values of these functions for each bubble category l and time t were determined based on a sublist $J_l(t)$, comprising all bubbles of category l present in at least one frame from $i_0(t) = \left(t - \frac{\Delta t}{2}\right) f_c$ to $i_1(t) = \left(t + \frac{\Delta t}{2}\right) f_c - 1$, where f_c is the frame rate. Henceforth in this subsection, the index l is omitted for brevity, as the processing was performed identically and independently for each category.

When compiling the sublist of bubbles for the category under consideration, the value $p_j(t)$ – the fraction of frames within the interval $[i_0(t), i_1(t)]$, in which the bubble with index j was present – was calculated for each j-th bubble. Note that $0 < p_j(t) \le 1$. The nucleation site density at time t is simply the sum of $p_j(t)$, divided by the frame area A_c:

$$N_a(t) = \frac{1}{A_c} \sum_{j=1}^{J(t)} p_j(t). \tag{2}$$

In particular, if all $J(t)$ bubbles existed throughout the entire considered interval, then $N_a(t) = \frac{J(t)}{A_c}$. If all $J(t)$ bubbles appeared strictly sequentially from a single nucleation site, then $N_a(t) = \frac{1}{A_c}$.

When calculating the averaged maximum diameter values, the maximum diameter of each bubble was multiplied by a weighting factor equal to $p_j(t) D_j^3$, because the amount of heat transferred from the heater surface to the liquid during the formation and subsequent condensation of a given bubble is approximately proportional to its volume. Thus,

$$D_m(t) = \frac{\sum_{j=1}^{J(t)} p_j(t) D_j^4}{\sum_{j=1}^{J(t)} p_j(t) D_j^3}. \tag{3}$$

The nucleation frequency, as a characteristic of an individual bubble, was also averaged using a weight proportional to its volume and presence fraction $p_j(t)$:

$$f_b(t) = \frac{\sum_{j=1}^{J(t)} p_j(t) f_j D_j^3}{\sum_{j=1}^{J(t)} p_j(t) D_j^3}. \tag{4}$$

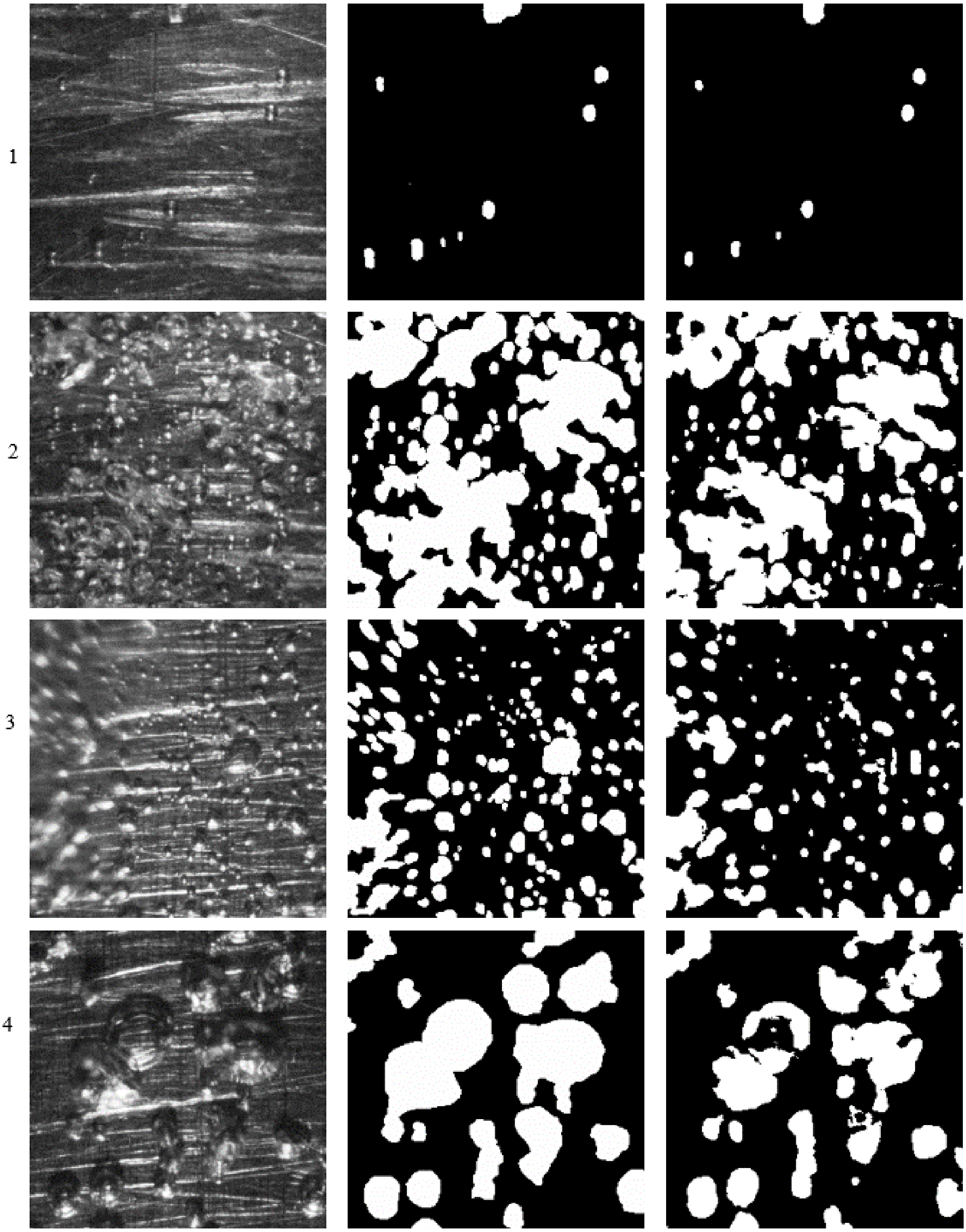

Fig. 1. Validation of individual video frame segmentation results. Raw: original frames, gt: manually labeled ground truth, NN-result: neural network segmentation result. Experimental conditions: 1, 2 – ΔT_{sub} = 53 K, dT/dt = 3600 K/s; 3 – ΔT_{sub} = 103 K, dT/dt = 330 K/s; 4 – ΔT_{sub} = 23 K, dT/dt = 9900 K/s.

The areas occupied by individual bubbles in a single frame are non-intersecting segments. However, when determining the surface area involved in the heat transfer process due to boiling, each bubble was considered with the maximum area it achieved during its lifetime. At the stage of statistical processing of the bubble list, information about the shape of the region covered by the bubble at that moment was unavailable, and it was approximated as a circle with a diameter D_j. Such circles with maximum diameters for different bubbles can overlap, and this must be accounted for.

To estimate the fraction of area occupied by bubbles as accurately as possible, a two-dimensional array corresponding to all pixels in the frame was created. The array was initialized with zeros. Then, for each bubble from $J(t)$ the value $p_j(t)$ was added to all array elements corresponding to pixels within the circle of diameter D_j centered at the bubble's center of mass, with the constraint that no element value could exceed 1. Subsequently, $F_v(t)$ was calculated as the sum of all elements in this array, divided by the total frame area in pixels.

IV. RESULTS

To validate the developed automated video data processing system, its results were compared with those previously obtained through manual processing. For comparison, two experiments with a high surface temperature rise rate (12 000–16 000 K/s) and flow subcooling of ΔT_{sub} = 23 K and 103 K were selected.

The manual processing was conducted as follows. In each experiment, approximately 10 key frames (KF) were selected during the initial phase of nucleate boiling. For each key frame, a list of bubbles present in it was compiled. For each bubble, its lifetime, maximum diameter, and type (isolated, clustered, or pulsating) were determined by reviewing the video forward and backward from the key frame. The values of nucleation site density, maximum diameter, nucleation frequency, and the fraction of surface area occupied by bubbles of each type and the generalized “All” category were determined using formulas analogous to those in the previous section, with $p_j(t) = 1$.

As is seen in Fig. 2(a, b), the total number of bubbles of all types aligns almost exactly between the automated and manual processing methods. An exception is the N_a values for $\tau - \tau_{ONB} > 0.8$ ms at $\Delta T_{sub} = 103$ K, where manual processing yields higher values. This discrepancy is associated with differences in handling clustered bubbles: during automated processing, an entire cluster of touching bubbles was counted as a single bubble, whereas during manual processing, bubbles distinguishable in the original frame were counted as separate bubbles of the clustered type. The results of the automated processing, covering a longer time period, allow for determining the limiting value of nucleation site density at which saturation occurs. For both experiments considered, this value was approximately 90 mm^{-2}.

The fraction of the heater surface area occupied by bubbles of all types (Fig. 2 (c, d)), and particularly by clustered bubbles, is on average higher in the manual processing results compared to the automated results. The total area occupied by a bubble cluster might have been overestimated during manual processing because the area of each bubble within the cluster was calculated as the area of a circle with a diameter equal to the bubble's largest visible dimension. Although the overlap of these circles was accounted for, the actual overlap might have been greater. Furthermore, as seen in Fig. 2 (a, b, c, d), the automated processing attributes a higher relative contribution to pulsating bubbles and a lower one to single bubbles compared to the manual processing. This is because bubbles that did not fully condense but underwent a sharp change in size or structure during the transition from shrinking to growing were classified as single in the manual processing, whereas in the automated processing they were identified as pulsating.

The averaged maximum bubble diameter (Fig. 2 (e, f)) shows close agreement between the manual and automated processing results, especially for the combined category of all bubble types. Clustered bubbles in the automated processing reach larger sizes within the same time interval, which is associated with the distinction between treating an entire cluster as a single entity versus individual bubbles within a cluster. The discrepancy between these two approaches could have been significantly more pronounced if D_m represented a simple arithmetic mean. The use of a weighting function proportional to the bubble volume during averaging renders small bubbles within a cluster negligible compared to the single bubble that absorbed them upon merging. The differences in D_m values for isolated and pulsating bubbles obtained manually and via neural networks are not unidirectional, as they are linked to the differences in bubble type classification.

The most significant discrepancies between the manual and automated processing are observed in the nucleation frequency values (Fig. 2 (g, h)). In principle, a close match

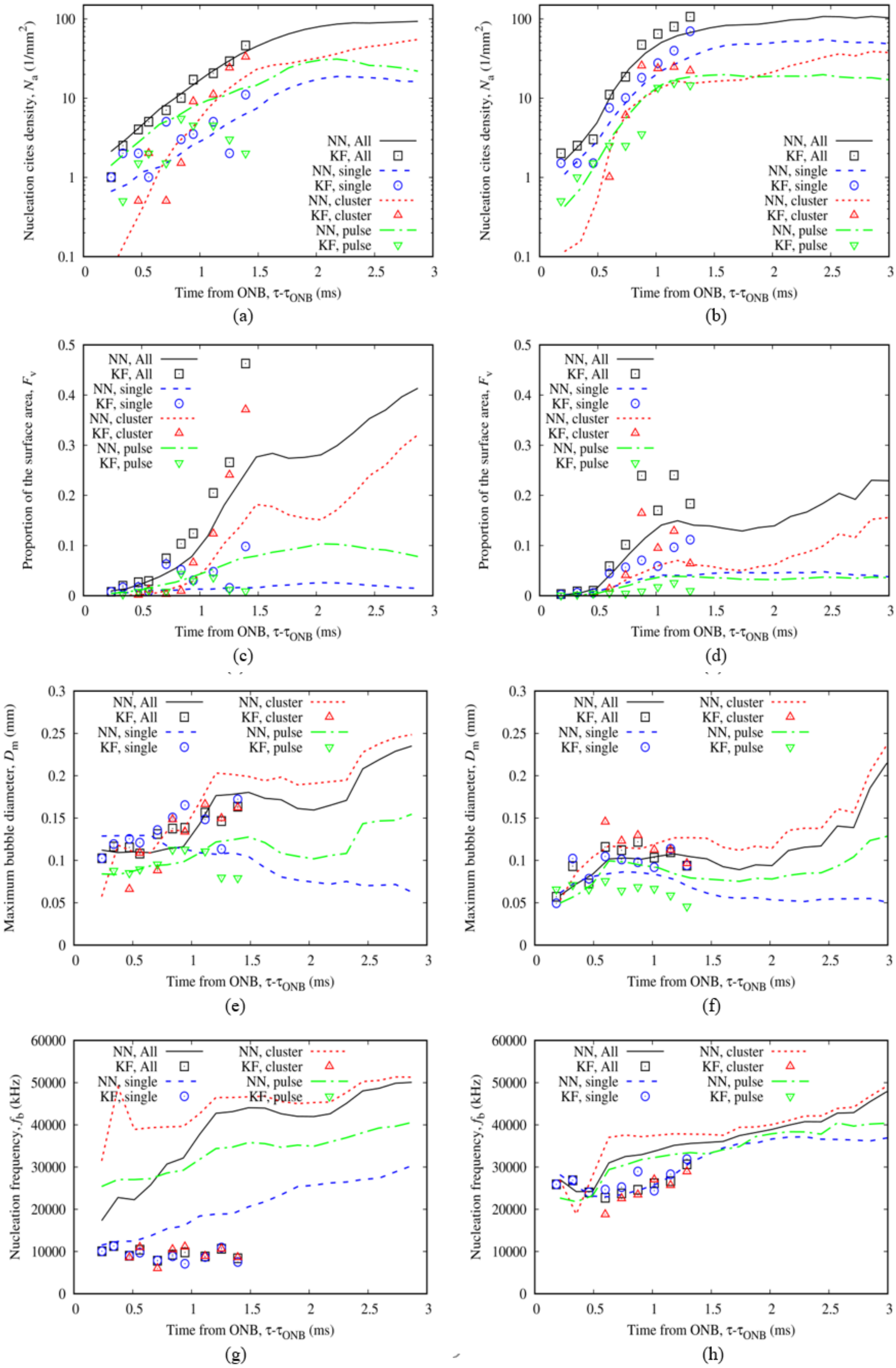

(a) (b)

(c) (d)

(e) (f)

(g) (h)

Fig. 2. Verification of neural network (NN) results against manual key frame (KF) analysis for bubble statistics at flow subcoolings of 23 K (a, c, e, g) and 103 K (b, d, f, h). Compared parameters: (a, b) nucleation site density, N_a ; (c, d) surface area fraction, F_v ; (e, f) maximum diameter, D_m ; (g, h) nucleation frequency, f_b .

for this parameter could only be expected for isolated bubbles. For clustered bubbles, the manual processing yields the lifetime of individual bubbles within a cluster, which characteristically shows little difference from the lifetime of single bubbles. In contrast, the automated processing for clustered bubbles essentially provides not the nucleation frequency, but the frequency of interactions. The lifetime and nucleation frequency of pulsating bubbles were not determined in the manual processing. In the automated processing, this value corresponds to the pulsation frequency.

Thus, the observed discrepancies are minor and largely attributable to differences in the definition of clustered and pulsating bubbles. It should also be noted that, due to the use of temporal averaging over the interval Δt and the presence fraction $p_j(t)$ for each bubble within this interval in the automated processing, the values of the flow characteristics at the specific time t, corresponding to a key frame could not exactly match the characteristics derived solely from that key frame, even if the characteristics of individual bubbles had been identified identically. Owing to this temporal averaging, the results of the automated processing provide a more accurate representation of the boiling characteristics averaged over the entire heater surface than the results of the manual processing.

V. DISCUSSION AND CONCLUSIONS

This study has developed and validated an automated system for quantifying bubble dynamics in non-stationary nucleate boiling on an opaque surface. By integrating the DenoiSeg convolutional neural network for robust segmentation in reflected light with a novel tracking algorithm, the system reliably extracts time-dependent characteristics (nucleation site density, area fraction, maximum diameter, and nucleation frequency), while classifying bubbles into isolated, clustered, and pulsating types.

Methodological Validation: Comparison with manual key frame analysis confirmed the system's accuracy. The principal discrepancies are attributed to the more consistent and physically-grounded definitions of bubble interactions within the automated algorithm. Its primary advantage is the ability to process large datasets, yielding statistically robust results and enabling trend analysis that is infeasible manually.

Physical Insights: The analysis confirms the significant prevalence of clustered and pulsating bubbles across all tested conditions. Crucially, the automated processing revealed previously obscured trends, such as the distinct evolution of bubble diameters: while the maximum diameter of clustered and pulsating bubbles increases with surface heating, that of isolated bubbles decreases due to heightened nucleation site density. This underscores the necessity of accounting for bubble type in heat transfer models.

Method Extendibility: The developed framework is inherently adaptable. By training the model on new or augmented datasets, it can be applied to segment boiling on structured surfaces or under different system conditions, such as pressure, flow velocity, heater temperature rise rate, and flow subcooling. The subsequent feature extraction would follow the same validated pipeline, ensuring consistency. Applying this methodology to large-scale data collection will enable the systematic identification of key differences in boiling behavior across various surfaces and conditions, distinguishing fundamental trends from stochastic fluctuations.

In conclusion, we have developed and validated an automated tool that enables detailed, physics-based analysis of non-stationary boiling. This methodology paves the way for creating the large, consistent datasets required to refine heat transfer correlations for complex boiling regimes.

ACKNOWLEDGMENT

The research was funded by the Russian Science Foundation, Grant No. 22-19-00092-П.

REFERENCES

[1] C. S. Brooks, T. Hibiki, “Wall nucleation modeling in subcooled boiling flow,” *Int. J. Heat Mass Transf.*, vol. 86, pp. 183–196, 2015. DOI: 10.1016/j.ijheatmasstransfer.2015.03.005.

[2] M. C. Duluc, B. Stutz, M. Lallemand, “Transient nucleate boiling under stepwise heat generation for highly wetting fluids,” *Int. J. Heat Mass Transf.*, vol. 47, no. 25, pp. 5541–5553, 2004. DOI: 10.1016/j.ijheatmasstransfer.2004.04.038.

[3] A. N. Pavlenko, E. A. Tairov, V. E. Zhukov, A. A. Levin, A. N. Tsoi, “Investigation of transient processes at liquid boiling under nonstationary heat generation conditions,” *J. Eng. Thermophys.*, vol. 20, no. 4, pp. 380–406, 2011. DOI: 10.1134/S1810232811040060.

[4] A. Levin, P. Khan, “Intensification of non-stationary nucleate boiling at increasing flow velocity,” *Heat Transf. Eng.*, vol. 43, no. 3–5, pp. 388–396, 2022. DOI: 10.1080/01457632.2021.1874682.

[5] V. Serdyukov, I. Malakhov, A. Surtaev, “High-speed visualization and image processing of sub-atmospheric water boiling on a transparent heater,” *J. Vis*., vol. 23, no. 5, pp. 873–884, 2020. DOI: 10.1007/s12650-020-00660-z.

[6] T. Haas, C. Schubert, M. Eickhoff, H. Pfeifer, “BubCNN: Bubble detection using Faster RCNN and shape regression network*,” Chem. Eng. Sci.*, vol. 216, Art. no. 115467, 2020. DOI: 10.1016/j.ces.2019.115467.

[7] I. Poletaev, M. P. Tokarev, K. S. Pervunin, “Bubble patterns recognition using neural networks: Application to the analysis of a two-phase bubbly jet,” *Int. J. Multiph. Flow*, vol. 126, Art. no. 103194, 2020. DOI: 10.1016/j.ijmultiphaseflow.2019.103194.

[8] L. Lentz, D. Hüne, S. Handrich, C. Niems, T. Gimpel, “Bubble Evolution Detector B.E.D. – A neural network-based approach to accurately detect, classify, and evaluate gas bubbles captured by a high-speed camera on textured surfaces,” *J. Open Res. Softw*., vol. 13, no. 1, Art.no. 5, 2025. DOI: 10.5334/jors.505.

[9] A. Seredkin et al., “Pattern recognition for bubbly flows with vapor or gas-liquid interfaces using U-Net architecture,” in *Proceedings - 2020 Science and Artificial Intelligence Conference, S.A.I.ence 2020*, Novosibirsk, Russia, 2020, pp. 5–8. DOI: 10.1109/S.A.I.ence50533.2020.9303175.

[10] J. H. Seong, M. Ravichandran, G. Su, B. Phillips, M. Bucci, “Automated bubble analysis of high-speed subcooled flow boiling images using U-Net transfer learning and global optical flow,” *Int. J. Multiph. Flow*, vol. 159, Art. no. 104336, 2023. DOI: 10.1016/j.ijmultiphaseflow.2022.104336.

[11] S. P. Aktershev, A. A. Levin, I. V. Mesentsev, N. N. Mesentseva, “Self-oscillatory regime of boiling of a highly subcooled liquid in a flow-passage annular duct,” *Thermophys. Aeromechanics*, vol. 25, no. 6, pp. 875–887, 2018. DOI: 10.1134/S0869864318060082.

[12] A. A. Levin, A. S. Safarov, V. M. Chudnovskii, A. A. Chernov, “Modeling of non-stationary temperature field in the neighborhood of the optical fiber end under laser pulse heating,” *Interfacial Phenom. Heat Transf*., vol. 8, no. 1, pp. 25–32, 2020. DOI: 10.1615/InterfacPhenomHeatTransfer.2020032806.

[13] A. A. Levin, V. F. Chistyakov, E. A. Tairov, “On application of the structure of the nonlinear equations system, describing hydraulic circuits of power plants, in computations,” *Bull. South Ural State Univ. Ser. Math. Model. Program. Comput. Softw*., vol. 9, no. 4, pp. 53–62, 2016. DOI: 10.14529/mmp160405.

[14] R. L. Mohanty, M. K. Das, “A critical review on bubble dynamics parameters influencing boiling heat transfer,” *Renew. Sustain. Energy Rev*., vol. 78, pp. 466–494, 2017. DOI: 10.1016/j.rser.2017.04.092.

[15] G. Yang, W. Zhang, M. Binama, Q. Li, W. Cai, “Review on bubble dynamic of subcooled flow boiling-part b: Behavior and models,” *Int. J. Therm. Sci*., vol. 184, Art. no. 108026, 2023. DOI: 10.1016/j.ijthermalsci.2022.108026.

[16] S. S. Kutateladze, *Fundamentals of heat transfer*. London, UK: Edward Arnold, 1963.

[17] N. V. Vasiliev, A. Y. Varaksin, Y. A. Zeigarnik, K. A. Khodakov, A. V Epelfeld, “Characteristics of subcooled water boiling on structured surfaces,” *High Temp*., vol. 55, no. 6, pp. 880–886, 2017. DOI: 10.1134/S0018151X17060189.

[18] A. A. Levin, P. V. Khan, “Experimental observation of the maximum bubble diameter in non-stationary temperature field of subcooled boiling water flow,” *Int. J. Heat Mass Transf.*, vol. 124, pp. 876–883, 2018. DOI: 10.1016/j.ijheatmasstransfer.2018.03.078.

[19] A. A. Levin, P. V Khan, “Effect of micro-sized vapor bubbles on heat transfer at different heater temperature rise rate,” *Tech. Phys. Lett*., vol. 50, no. 2, pp. 58–61, 2024. DOI: 10.61011/TPL.2024.02.57987.19762.

[20] N. Agarwal, M. Lee, H. Kim, “A non-invasive method for measuring bubble column hydrodynamics based on an image analysis technique,” *Processes*, vol. 10, no. 8, art. no. 1660, 2022. DOI: 10.3390/pr10081660.

[21] B. A. Phillips, “Experimental investigation of subcooled flow boiling using synchronized high speed video, infrared thermography, and particle image velocimetry,” Ph. D. dissertation, Department of Nuclear Science and Engineering, Massachusetts Institute of Technology, Cambridge, MA, USA, 2014.

[22] J. Kim, B. Do Oh, M. H. Kim, “Experimental study of pool temperature effects on nucleate pool boiling,” *Int. J. Multiph. Flow*, vol. 32, no. 2, pp. 208–231, 2006. DOI: 10.1016/j.ijmultiphaseflow.2005.09.005.

[23] S. Narayan, A. Srivastava, S. Singh, “Rainbow schlieren-based direct visualization of thermal gradients around single vapor bubble during nucleate boiling phenomena of water,” *Int. J. Multiph. Flow*, vol. 110, pp. 82–95, 2019. DOI: 10.1016/j.ijmultiphaseflow.2018.08.012.

[24] X. Zabulis, M. Papara, A. Chatziargyriou, T. D. Karapantsios, “Detection of densely dispersed spherical bubbles in digital images based on a template matching technique. Application to wet foams,” *Colloids Surfaces A: Physicochem. Eng. Asp*., vol. 309, no. 1–3, pp. 96–106, 2007. DOI: 10.1016/j.colsurfa.2007.01.007.

[25] P. Zhevnev, P. Khan, A. Mikheev, “Image processing for identification of vapor phase on a heating surface under the nonstationary boiling conditions,” *E3S Web of Conferences*, 2019, vol. 114, Art. no. 07006. DOI: 10.1051/e3sconf/201911407006.

[26] E. Teodori, A. S. Moita, A. L. N. Moreira, “Characterization of pool boiling mechanisms over micro-patterned surfaces using PIV,” *Int. J. Heat Mass Transf*., vol. 66, pp. 261–270, 2013. DOI: 10.1016/j.ijheatmasstransfer.2013.07.033.

[27] T. Chen, Q. Zeng, “Research on bubble detection based on improved YOLOv8n,” *IEEE Access*, vol. 12, pp. 9659–9668, 2024. DOI: 10.1109/ACCESS.2024.3353196.

[28] H. Hessenkemper, S. Starke, Y. Atassi, T. Ziegenhein, D. Lucas, “Bubble identification from images with machine learning methods,” *Int. J. Multiph. Flow*, vol. 155, Art. no. 104169, 2022. DOI: 10.1016/j.ijmultiphaseflow.2022.104169.

[29] A. Kirillov et al., “Segment Anything,” *arXiv:2304.02643*, 2023. DOI: 10.48550/arXiv.2304.02643.

[30] C. Maduabuchi, E. Jossou, M. Bucci, “VideoSAM: A large vision foundation model for high-speed video segmentation,” 2024. DOI: 10.48550/arXiv.2410.21304.

[31] T. O. Buchholz, M. Prakash, D. Schmidt, A. Krull, F. Jug, “DenoiSeg: Joint denoising and segmentation,” in *Computer Vision – ECCV 2020 Workshops. Glasgow, UK, August 23–28, 2020, Proceedings, Part I. Lecture Notes in Computer Science Series*, 1st ed., vol. 12535, A. Bartoli, A. Fusiello, Eds. Springer Cham, 2020, pp. 324–337. DOI: 10.1007/978-3-030-66415-2_21.

[32] R. L. Judd, A. Chopra, “Interaction of the nucleation processes occurring at adjacent nucleation sites,” *J. Heat Transfer*, vol. 115, no. 4, pp. 955–962, 1993. DOI: 10.1115/1.2911392.

[33] P. V. Khan, A. A. Levin, “Experimental study of the influence of bubble interaction on their characteristics during transient boiling in a flow of subcooled liquid,” *Thermophys. Aeromechanics*, vol. 31, no. 2, pp. 313–319, 2024. DOI: 10.1134/S0869864324020100.

[34] A. A. Levin, P. V. Khan, “Characteristics of nucleate boiling under conditions of pulsed heat release at the heater surface,” *Appl. Therm. Eng.*, vol. 149, pp. 1215–1222, 2019. DOI: 10.1016/j.applthermaleng.2018.12.126.

[35] Y. Y. Hsu, “On the size range of active nucleation cavities on a heating surface,” *J. Heat Transfer*, vol. 84, no. 3, pp. 207–213, 1962. DOI: 10.1115/1.3684339.

Polina V. Khan is a senior researcher at the Laboratory for Dynamic of Steam-generating systems at Melentiev Energy Systems Institute, Russia. She received her Ph.D. from Yeungnam University, School of Mechanical Engineering, in 2006. Her research interests include nucleate boiling, unsteady heat transfer, and multiphase flow.

Anatoliy A. Levin is a head of the Laboratory for Dynamic of Steam-generating systems at Melentiev Energy Systems Institute, Russia. He received his Ph.D. from Melentiev Energy Systems Institute in 2008 and D.Sc. in Engineering from Melentiev Energy Systems Institute in 2024. His research interests include nucleate boiling, unsteady heat transfer, and mathematical modeling of thermal plants equipment. He is an elected member of the Scientific Council of the International Centre for Heat and Mass Transfer (ICHMT).

Ilya I. Chupin is a research assistant at the Laboratory for Dynamic of Steam-generating systems at Melentiev Energy Systems Institute, Russia.

Alexey S. Safarov is a junior researcher at the Laboratory for Dynamic of Steam-generating systems at Melentiev Energy Systems Institute, Russia.

Production of Refuse-Derived Fuel Pellets from Wood and Agricultural Waste: Technological Solutions and Economic Efficiency

E.V. Gubiy[1], M.V. Penzik[1], V.V. Badenko[1,*], A.N. Kozlov[1]

[1] Melentiev Energy Systems Institute of the Siberian Branch of the Russian Academy of Sciences, Irkutsk, Russia

Abstract **— The study assesses the potential of Russia's wood and agricultural waste for bioenergy. A technology for producing composite refuse-derived fuel (RDF) pellets from this feedstock is proposed, along with an economic evaluation. Optimal blend ratios are identified to ensure the pellets comply with the state standard (GOST) 33103.2-2017 and exhibit high mechanical durability (≥ 93%). Economically viable production is achievable when lignin is sourced as a zero-cost by-product and raw material prices remain below specific thresholds. Pellets with higher lignin content demonstrate the best economic performance. The results highlight that feedstock composition and preparation are critical factors influencing pellet quality, energy value, and cost-effectiveness, which are essential for advancing sustainable bioenergy in Russia.**

Index Terms **— Bioenergy, composite fuel, economic efficiency, energy potential, mechanical durability, RDF pellets, torrefaction, wood and agricultural waste.**

I. INTRODUCTION

At present, the depletion of natural resources represents one of the most serious threats facing society. Rapid population growth intensifies demand for water, energy, and food, exacerbating this challenge and stimulating the search for sustainable solutions. Biomass utilization emerges as a promising avenue for mitigating both the energy crisis and environmental degradation [1]. As a renewable feedstock, biomass possesses significant potential, low environmental impact, and a high degree of versatility in application. At the international level, biomass is recognized as a carbon-neutral energy source and a renewable fuel [2]. Rather than being regarded merely as waste or unused material, biomass should be valued as a resource capable of yielding various products and energy with minimal environmental footprint. A circular economy approach enables maximization of resource efficiency while promoting the sustainable use of biomass [3]. The feedstock base for biomass-derived fuels consists primarily of waste streams from the forestry and agricultural sectors [4]. These wastes are actively employed in the production of pelletized fuel, which is subsequently utilized for heating and cooking in Scandinavian countries, Canada, Russia, and many other regions worldwide [5].

Pelletization of such feedstock is a complex process accompanied by several technical challenges related both to inherent biomass properties and to granulation technology. Biomass materials – such as sawdust, straw, and husks, –typically exhibit low bulk density and heterogeneous moisture content, necessitating preliminary preparation and drying [6]. Furthermore, biomass particles demonstrate low natural adhesion; insufficient heating during pelletization may therefore lead to pellet disintegration. When processing herbaceous biomass (e.g., straw, hay), material adhesion to die walls can occur, hindering continuous operation. To overcome these issues, various binders are commonly employed [7–9]. Pelletization is an energy-intensive process, consuming approximately 50–100 kWh per tonne of product [10].

Notably, wood and agricultural residues impose significant environmental burdens; yet simultaneously, they constitute a largely underutilized energy resource that

---

[*] Corresponding author.
E-mail: badenko@isem.irk.ru

DOI: 10.25729/esr.2025.04.0007

Received October 21, 2025. Revised November 15, 2025. Accepted December 2, 2025. Available online December 29, 2025.

can be valorized via refuse-derived fuel (RDF) technologies. RDF pellets have found widespread application in co-firing with coal at large-scale thermal power plants [11]. The quality of such pellets is governed by the technical standards EN ISO 17225 – Solid Biofuels. RDF pellets produced from agricultural residues (e.g., straw, miscanthus, rice husk, olive pomace, etc.) must meet specific requirements, including mechanical durability (>90%), ash content (<8%), and limited chlorine and sulfur levels to prevent slagging and corrosion during combustion.

Despite the progress achieved, the formulations of RDF pellets from wood and agricultural waste remain insufficiently optimized, which limits their integration into sustainable energy systems [12]. This is attributed to the need for various preparatory procedures for different types of waste and the use of different binders, such as torrefaction [13]. The use of RDF is expanding in Russia and globally, yet it is still constrained by limitations in the waste-to-energy sector.

The main challenges in biomass pelleting are associated with feedstock characteristics and equipment settings. It is important to note that optimizing blends with local biomass is crucial and highly relevant for Russia, which faces significant obstacles – limited resource availability and economic feasibility.

In this context, this paper implements a regionally-oriented approach with three interconnected objectives: 1) assessment of the extractable energy potential of wood and agricultural waste for bioenergy needs; 2) development of a technology for producing composite RDF pellets from locally available waste with an optimal ratio ensuring compliance with quality standards; 3) a techno-economic assessment aimed at determining the maximum acceptable feedstock prices and waste integration scenarios under which RDF pellet production becomes commercially viable in current Russian market conditions.

II. ASSESSMENT OF THE POTENTIAL OF WOOD AND AGRICULTURAL WASTE FOR BIOENERGY APPLICATIONS

According to data from Rospotrebnadzor (the Federal Service for Surveillance on Consumer Rights Protection and Human Wellbeing), in 2022, Russia generated 5.94 million tonnes of wood waste and 2.97 million tonnes of crop production residues [14].

Figure 1a illustrates the regional distribution of wood waste across federal districts in Russia for 2022. These values were estimated based on national statistics on total waste from the forest processing industry (FPI) [14] combined with regional data on timber harvesting volumes [15, 16]. The largest volumes of wood waste originated in the most forested federal districts—namely, the Siberian Federal District (SFD), accounting for 30.3% of the national total, and the Northwestern Federal District (NWFD), contributing 26.3%. In contrast, wood waste generation in the Southern (StFD) and North Caucasian (NCFD) Federal Districts was negligible (<1% each).

Crop production is a sector characterized by a high waste-to-product ratio: the yield of the primary (marketable) product typically constitutes no more than 30% of the initial biomass input. Figure 1b presents the regional distribution of crop residues in Russia for 2022, calculated using national data on agricultural waste volumes [14] and regional data on cultivated areas for major crops in 2022 [17]. The largest quantities of crop

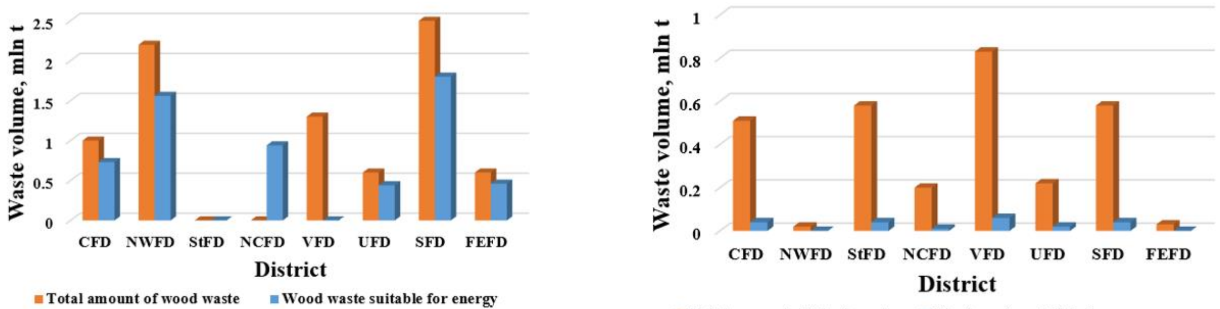

a) b)

Fig. 1. Volumes of wood waste (a) and crop residues (b) in Russia in 2022, by Federal District.

TABLE 1. Energy Potential of Wood Waste and Crop Residues

Federal District	Fuel consumption, Mtoe	Energy potential, Mtoe		Potential share of total fuel demand, %		
		Wood	Ag-waste	Wood	Ag-waste	Total
CFD	99.60	0.26	0.01	0.26	0.01	0.28
NWFD	63.36	0.56	0.00	0.89	0.00	0.89
StFD	27.18	0.00	0.01	0.02	0.05	0.06
NCFD	10.86	0.00	0.00	0.01	0.03	0.04
VFD	99.29	0.34	0.02	0.34	0.02	0.36
UFD	121.45	0.16	0.01	0.13	0.01	0.14
SFD	71.82	0.65	0.01	0.90	0.02	0.92
FEFD	36.72	0.16	0.00	0.45	0.00	0.45
RF	530.28	2.14	0.07	0.40	0.01	0.42

residues in 2022 were generated in the Volga Federal District (VFD), representing 28.6% of the national total, followed by the Siberian (SFD), Central (CFD), and Southern Federal Districts – each contributing approximately 19.1%. Notably, residues from cereal and grain-legume crops – which are among the most promising feedstocks for bioenergy applications accounted for 55–70% of total crop residues in 2022 [14].

Depending on the specific economic activities prevailing in different regions of Russia, the ratios of both generated and utilized waste vary significantly. For instance, the Southern Federal District (StFD) is characterized by a well-developed agricultural sector, utilizing on average 64% of Russian agricultural waste, whereas the Siberian (SFD) and Northwestern (NWFD) Federal Districts are primarily oriented towards forestry. According to official statistics, these regions utilized 82.5% of wood waste in 2022 [18].

Despite the substantial total volume of wood and crop residues – 11.2 million tonnes – their combined energy potential remains relatively low. Due to economic and technological constraints, only up to 6 million tonnes are currently considered feasible for energy recovery. Consequently, in 2022 the energy potential of wood and crop residues amounted to just 0.42% of Russia's total fuel consumption [19].

It should be noted that the highest energy potential from these two waste streams is concentrated in the Siberian Federal District (SFD: 0.66 million tonnes of oil equivalent, Mtoe) and the Northwestern Federal District (NWFD: 0.56 Mtoe), owing to their dominant share of wood waste generation. The Volga Federal District (VFD) ranks third (0.36 Mtoe), with a less developed forest processing industry but a more advanced agro-industrial complex (Table 1).

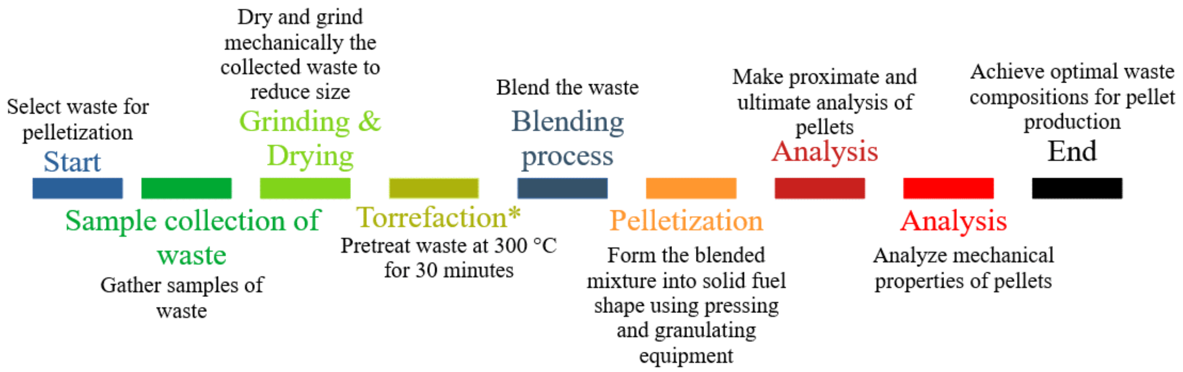

Fig. 2. The procedure to produce RDF.

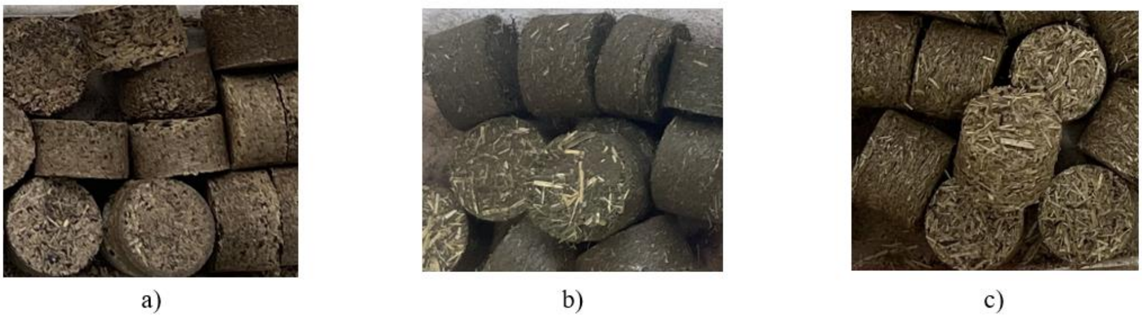

Fig. 3. The appearance of RDF pellets: a) pine sawdust-to-lignin ratio of 58% / 42%; b) straw-to-mixed-grasses ratio of 25% / 75%; c) torrefied sunflower husk-to-straw ratio of 15% / 85%.

III. PELLETIZATION OF WOOD AND AGRICULTURAL WASTE

Despite the relatively modest energy potential of wood and crop waste, the pellet production market demonstrates a stable growth trend. Among the principal wood-derived feedstocks are by-products of the forest industry – primarily sawdust and lignin, the latter being a residue from hydrolysis and pulp-and-paper production. Promising agricultural waste in the Russian context include sunflower husk, straw (both individually and in combination with mixed grasses), and mixed grasses commonly harvested as livestock fodder.

The experimental study focused on producing composite pellets from the selected wood and agricultural residues: pine sawdust, lignin (supplied as waste from the Baikal Pulp and Paper Mill), sunflower husk, straw, and mixed grasses. These raw materials underwent preliminary preparation – including drying, size reduction, and conditioning – to enable granulation into dense, solid pellets suitable for subsequent physicochemical characterization.

Figure 2 illustrates the step-by-step process for RDF pellet production, encompassing raw material collection, size reduction, drying, torrefaction (* – if necessary for a specific material), granulation (pelletizing), proximate and ultimate analysis, and analysis of mechanical properties, and finally the determination of optimal waste ratios in composite RDF pellets.

It should be noted that feedstock pretreatment prior to pelletization varies depending on the waste type. Straw comprising dried stems and leaves of cereal crops remaining after threshing can reach lengths of 60 cm to 1.5 m, with considerable variation in stalk thickness; therefore, it was milled, and the 3–6 mm fraction was selected for further study. Mixed grasses were freshly cut and exhibited high initial moisture content (~60%); they were air-dried to an equilibrium moisture level of ~6%. Pine sawdust was dried in a ventilated room to air-dry condition and sieved, after which the 3–6 mm fraction was retained. Lignin from the Baikalsk Pulp-and-Paper Mill (BPPM) is a plastic, clay-like, finely dispersed material with moisture content up to 85%; samples were oven-dried at 105 °C to near-absolute dryness (3% moisture). Sunflower husk, the outer shell of sunflower seeds (6–8 mm long, 4–5 mm wide), is difficult to mill in its raw state, and unprocessed husk yields mechanically unstable pellets. Hence, sunflower husk was first torrefied in a screw reactor at 300 °C for 30 minutes and subsequently ground using a high-speed laboratory mill.

Following pretreatment, composite mixtures were prepared in varying proportions for RDF pellet production, targeting combinations with high utilization potential:

- Pine sawdust – lignin: 100% / 0%, 95% / 5%, 88% / 12%, 77% / 23%, 58% / 42%, 40% / 60%;
- Torrefied sunflower husk – straw: 10% / 90%, 15% / 85%, 25% / 75%, 100% / 0%;
- Straw – mixed grasses: 100% / 0%, 75% / 25%, 70% / 30%, 50% / 50%, 0% / 100%.

Pelletization was performed using a standard hydraulic press operating at 5 tonnes of force (scale-up to screw or flat-die pelletizers is planned for future work). The resulting pellets had a diameter of 20.5 mm and heights ranging from 12.5 to 14.5 mm. Figure 3 shows the

TABLE 2. Ultimate Analysis of Waste

Name	C, %	H, %	O, %	S, %
Pine sawdust	46.6	6.3	47.1	–
Lignin	54.2	4.5	39.7	0.12
Straw	46.5	5.4	48.1	–
Mixed grasses	43.3	6.1	50.2	0.37
Sunflower husks	39.7	5.8	53.4	1.10
Sunflower husks (torrefied)	47.5	4.7	47.2	0.63

TABLE 3. Proximate Analysis and Analysis of Mechanical Properties of Pellets

No.	Composition of RDF pellets	Volatile matter, %	Ash content, %	Low calorific value, MJ/kg	Bulk density, g/ml	Mechanical durability, %
Pine sawdust (%)/lignin (%)						
1	**100/0**	**87±0.96**	**1.52±0.03**	**17.91±0.45**	**0.38±0.02**	**96.1±0.72**
2	**95/5**	**80±0.88**	**3.20±0.06**	**18.28±0.46**	**0.43±0.02**	**96.3±0.72**
3	**88/12**	**78±0.86**	**4.00±0.08**	**18.17±0.45**	**0.46±0.02**	**95.7±0.72**
4	**77/23**	**72±0.79**	**7.00±0.13**	**17.56±0.44**	**0.50±0.02**	**92.3±0.69**
5	58/42	66±0.73	8.50±0.16	17.08±0.43	0.45±0.02	87.3±0.65
6	40/60	63±0.69	10.50±0.20	16.00±0.40	0.53±0.02	79.3±0.59
Torrefied sunflower husks (%)/straw (%)						
7	100/0	63±0.69	6.97±0.13	22.07±0.55	0.57±0.03	30.2±0.23
8	25/75	73±0.80	5.65±0.11	19.20±0.48	0.42±0.02	91.7±0.69
9	**15/85**	**75±0.83**	**4.65±0.09**	**17.18±0.43**	**0.44±0.02**	**93.2±0.70**
10	**10/90**	**77±0.85**	**5.01±0.10**	**16.88±0.42**	**0.40±0.02**	**95.7±0.72**
Straw (%)/mixed grasses (%)						
11	**100/0**	**80±0.88**	**5.44±0.10**	**16.85±0.42**	**0.33±0.02**	**95.9±0.72**
12	**50/50**	**80±0.88**	**7.80±0.15**	**16.89±0.42**	**0.55±0.03**	**93.0±0.70**
13	30/70	79±0.87	14.70±0.28	15.79±0.39	0.59±0.03	91.6±0.69
14	25/75	75±0.83	17.60±0.33	15.30±0.38	0.54±0.03	90.3±0.68
15	0/100	73±0.80	13.20±0.25	16.85±0.42	0.49±0.02	87.1±0.65

appearance of the produced RDF pellets.

The proximate analysis, ultimate analysis, and analysis of mechanical properties of the produced composite RDF pellets were performed using the resources of the High-Temperature Circuit Multi-Access Research Center (MESI SB RAS): a macro-thermogravimetric analyzer (TGA 801), an AC 500 calorimeter, and elemental analyzers for carbon (C), hydrogen (H), and sulfur (S). Bulk density was measured in accordance with State Standard (GOST) 54191–2010, and mechanical durability was assessed following GOST R 55110–2012. The moisture content of all pellet samples was maintained within 3–5%. Table 2 presents the ultimate analysis of the main RDF pellet components, normalized to a dry, ash-free basis.

Table 3 presents the proximate analysis and analysis of mechanical properties of 15 different composite formulations of the produced RDF pellets.

Analysis of Table 3 reveals several trends.

For RDF pellets produced from pine sawdust and lignin, an increase in lignin content leads to a systematic decrease in volatile matter yield (from 87% to 63%) and lower heating value (LHV) (from 18 to 16 MJ/kg), while ash content and bulk density rise. Mechanical durability declines from 96.1% to 79.3% as the lignin proportion increases. Therefore, the optimal lignin content should not exceed 23%, since higher shares substantially impair pellet integrity.

Pellets produced from torrefied sunflower husks and straw show an increase in volatile matter yield as the straw content increases, accompanied by a reduction in heating value and ash content. Notably, pellets composed solely of sunflower husk exhibit the lowest mechanical durability among all tested formulations – only 30.2%. However, incorporation of straw markedly improves durability, reaching 95.7% at 90% straw content. Consequently, the minimum recommended sunflower husk content is no more than 10% to ensure adequate binding and structural stability while preserving the benefits of husk inclusion (e.g., ash composition modulation, waste valorization).

In the case of straw-mixed grass blends, an increase in the proportion of mixed grasses reduces volatile matter yield and raises ash content, whereas the LHV remains relatively constant (~15–16 MJ/kg) across all blend ratios. Mechanical durability shows a linear decline with rising grass content. Hence, to ensure acceptable pellet quality, the straw content should be at least 50%, as this composition delivers the best overall balance of mechanical strength and combustion properties.

Only 7 RDF pellet options – highlighted in black in Table 3 – achieve mechanical durability ≥ 93%, thereby meeting the requirements of GOST 33103.2-2017 (Solid biofuels – Technical specifications and fuel classes – Part 2: Classification of wood pellets) and qualifying for use as solid biofuel.

IV. ECONOMIC EFFICIENCY OF PELLET PRODUCTION

Since pellets, as a fuel, are typically not consumed at the production site but rather transported over long distances [20–22], mechanical durability was selected as the primary criterion for evaluating economic feasibility: high durability ensures minimal degradation (dust formation, breakage) during handling, storage, and transport, thus preserving fuel quality and calorific value. Within this study, RDF pellets exhibiting mechanical durability above 93% were considered promising for commercial production.

Additionally, pellets composed of 23% lignin and 77% sawdust, though marginally below the 93% threshold (92.3% durability), were also considered in the economic assessment. Their inclusion is justified by the significant advantage of enabling industrial-scale lignin valorization, thereby transforming a costly waste stream (e.g., from pulp mills) into a valuable co-feedstock.

Accordingly, the economic assessment presented herein covers eight pellet formulations identified in Table 3 as technically viable candidates (including the 23% lignin option). This analysis considers raw material costs, processing requirements, and market conditions to determine production feasibility in the Russian economic landscape.

A. *Methods and Input Data for the Economic Assessment*

To evaluate the economic viability of producing fuel pellets from wood and agro-industrial waste, this study employs three standard investment appraisal indicators: Net Present Value (NPV), Discounted Payback Period (DPP), and Internal Rate of Return (IRR) [23].

The Net Present Value (NPV) is calculated using equation

$$NPV = \sum_{t=0}^{n} \frac{NCF_t}{(1+r)^t} - \sum_{t=0}^{n} I_t \, , \qquad (1)$$

where NCF_t is the net effective cash flow in year *t*, million RUB; r is the discount rate, I_t is the investment expenditure in year *t*, million RUB/year; n is the project lifetime, years.

Based on (1), the Discounted Payback Period (DPP) is

TABLE 4. Input Economic Parameters Used in the Calculations

Parameter	Unit of measurement	Value	
Capital costs			
A plant for the production of fuel pellets, with a capacity of		from wood	from ag-waste
500 kg/h	mln RUB	10	8
700 kg/h		12	10
1 000 kg/h		14	12
1 500 kg/h		17	15
2 000 kg/h		20	18
Warehouse construction	million RUB/m²	0.004	
Operating costs			
Payroll fund	million RUB/person per year	0.8	
Electricity	RUB/kWh	5.0	
Other expenses	% of equipment cost	3	
Pine sawdust	RUB/t	1 000	
Straw	RUB/t	5 000	
Mixed grasses	RUB/t	5 000	
Torrefied sunflower husk	RUB/t	4 500	
Lignin (BPPM waste)	RUB/t	0	
Other indicators			
Discount rate	%	10	
Project lifetime	years	15	
Property tax	%	2	

TABLE 5. Change in Project Investment Indicators for Pellets with Different Compositions Depending on Raw Material Prices

Pellet composition	NPV at different raw material prices (% of current price), million RUB			DPP at different raw material prices (% of current price), years			IRR at different raw material prices (% of current price), %		
	0	50	100	0	50	100	0	50	100
Pine sawdust (%) / lignin (%)									
100/0	129.7	57.4	-14.8	2.0	3.8	62.9	100.64	51.79	–
95/5	129.7	61.0	-7.6	2.0	3.6	24.6	100.64	54.24	2.39
88/12	129.7	66.1	2.5	2.0	3.4	13.3	100.64	57.68	12.20
77/23	129.7	74.0	18.4	2.0	3.1	7.7	100.64	63.06	24.62
Straw (%) / mixed grasses (%)									
100/0	138.7	18.3	-102.2	1.8	7.5	–	112.02	25.27	–
50/50	138.7	-282.8	-704.3	1.8	–	–	112.02	–	–
Torrefied sunflower husks (%) / straw (%)									
15/85	138.7	-33.3	-205.3	1.8	–	–	112.02	51.79	–
10/90	138.7	-16.3	-171.3	1.8	130.0	–	112.02	–	–

determined as the smallest integer for which the cumulative discounted cash flows become non-negative:

$$\sum_{t=0}^{DPP} \frac{NCF_t}{(1+r)^t} = \sum_{t=0}^{n} I_t \;, \tag{2}$$

and the internal rate of return (IRR):

$$\sum_{t=0}^{n} \frac{NCF_t}{(1+IRR)^t} - \sum_{t=0}^{n} I_t = 0 \,. \tag{3}$$

Furthermore, to assess the cost of thermal energy derived from the pellets, the Levelized Cost of Pellets (LCOP) is calculated, following the methodology [24]:

$$LCOP = \frac{\sum_{t=1}^{n} (C_t + I_t)(1+r)^{-t}}{\sum_{t=1}^{n} P_t (1+r)^{-t}} \,, \tag{4}$$

where C_t is the annual operating and maintenance costs in year t, million RUB/year; I_t is the annual capital investment t, million RUB/year; P_t is the annual pellet output, tonnes/year.

The economic calculations were performed using the baseline parameters provided in Table 4.

B. Results of the Economic Assessment of Fuel Production

Assessment of the investment attractiveness for a pellet plant with a capacity of 1 000 kg/h and examination of current raw material prices (Table 4) reveal that NPV values are negative for all pellet compositions under base-case pricing except for pellets made from 88% sawdust and 12% lignin and from 77% sawdust and 23% lignin. For these compositions, the NPV amounts to RUB 2.5 million and RUB 18.4 million, respectively.

However, given the tightening of Russian waste management regulations in recent years (e.g., Federal Law

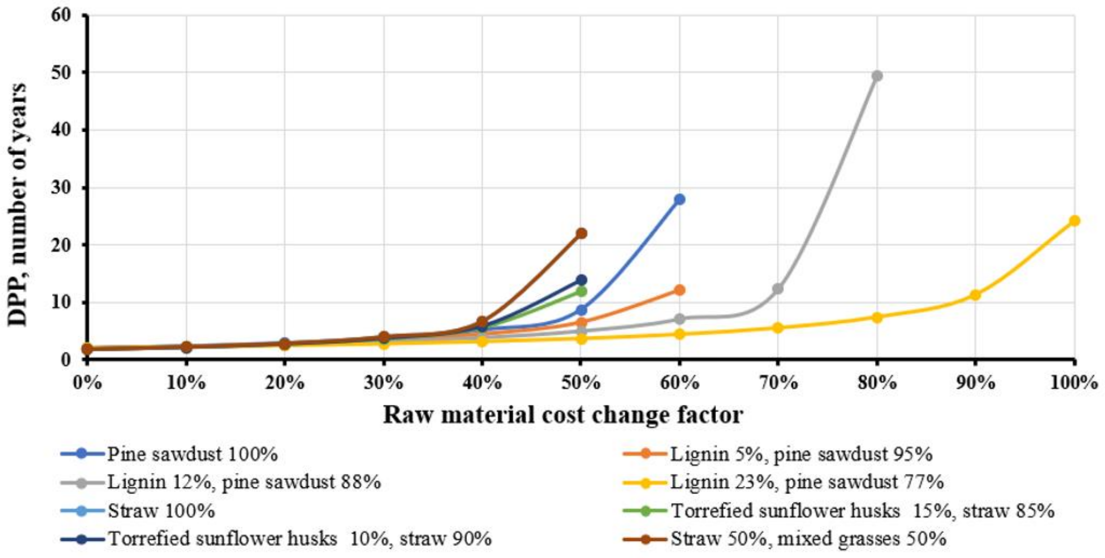

Fig. 4. Change in DPP for pellets with different compositions depending on raw material prices.

No. 89-FZ amendments, extended producer responsibility), it is reasonable to assume that certain biomass residues, particularly industrial by-products such as lignin or sawdust from integrated mills, may become effectively free or even incentivized (negative-cost) feedstocks, as enterprises seek to avoid disposal fees or environmental penalties.

Under the “zero-cost feedstock” scenario (i.e., raw material cost = 0% of values in Table 4), the project economics improve dramatically:

- DPP ≤ 2 years for all 8 technically viable formulations;
- NPV (15-year horizon) ranges from RUB 129.7 million to RUB 138.7 million;
- IRR reaches 100.6 % to 112.0 %, indicating extremely high profitability.

Under a 50% raw material cost scenario (midway between base case and zero-cost):

- NPV improves from – RUB 282.8 million to +74.0 million RUB (i.e., 5 of 8 blends become NPV-positive);
- DPP ranges from 3.1 to 130.0 years (only 5 blends remain uneconomical within 15 years);
- IRR rises from 25.3 to 63.1%, with higher-lignin blends again outperforming others.

Table 5 summarizes how key investment indicators (NPV, DPP, IRR) vary with raw material cost levels (expressed as % of base-case prices in Table 4), across the 8 RDF pellet formulations.

Figure 4 shows the change in the Discounted Payback Period (DPP) of the RDF pellet production facility for different raw material prices.

The study demonstrates that pellet production becomes economically viable, achieving payback within 15 years under the following conditions:

- Pellets composed of 95–100% sawdust and 0–5% lignin: feasible when raw material costs are reduced to 90% of the base-case values (Table 4);
- Pellets composed of 77–88% sawdust and 12–23% lignin: feasible when raw material costs are 100% of the base-case values;
- Pellets composed of 15% torrefied sunflower husks and 85% straw: feasible when raw material costs are reduced to 30% of the base-case values;
- Pellets composed of 10% torrefied sunflower husks and 90% straw: feasible when raw material costs are reduced to 40% of the base-case values;
- Pellets composed of 100% straw: feasible when raw material costs are reduced to 50% of the base-case values;
- Pellets composed of 50% mixed grass and 50% straw: feasible when raw material costs are reduced to 10% of the base-case values.

The analysis of LCOP (Levelized Cost of Pellets) and

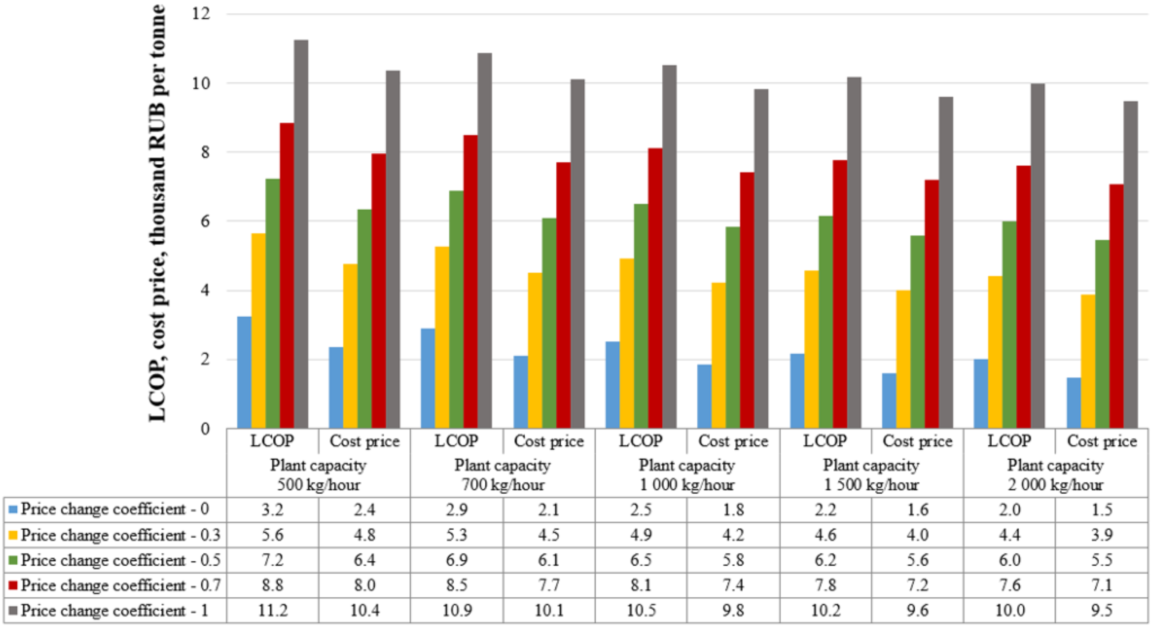

	Plant capacity 500 kg/hour		Plant capacity 700 kg/hour		Plant capacity 1 000 kg/hour		Plant capacity 1 500 kg/hour		Plant capacity 2 000 kg/hour	
	LCOP	Cost price	LCOP	Cost price	LCOP	Cost price	LCOP	Cost price	LCOP	Cost price
🟦 Price change coefficient - 0	3.2	2.4	2.9	2.1	2.5	1.8	2.2	1.6	2.0	1.5
🟨 Price change coefficient - 0.3	5.6	4.8	5.3	4.5	4.9	4.2	4.6	4.0	4.4	3.9
🟩 Price change coefficient - 0.5	7.2	6.4	6.9	6.1	6.5	5.8	6.2	5.6	6.0	5.5
🟥 Price change coefficient - 0.7	8.8	8.0	8.5	7.7	8.1	7.4	7.8	7.2	7.6	7.1
■ Price change coefficient - 1	11.2	10.4	10.9	10.1	10.5	9.8	10.2	9.6	10.0	9.5

Fig. 5. Change in LCOP and production cost of pellets made from 100% sawdust depending on raw material prices and plant capacity.

unit production cost confirms a pronounced economies-of-scale effect: both metrics decline significantly as plant capacity increases (Figures 5–9). The breakeven threshold (i.e., minimum pellet selling price for $NPV = 0$) shifts downward with scale, though the magnitude depends on formulation.

Specifically, when production capacity rises from 500 kg/h to 2 000 kg/h (i.e., 4× scale-up), unit production costs decrease as follows (Table 6).

The wide cost-reduction range (e.g., 14.2–37.5%)

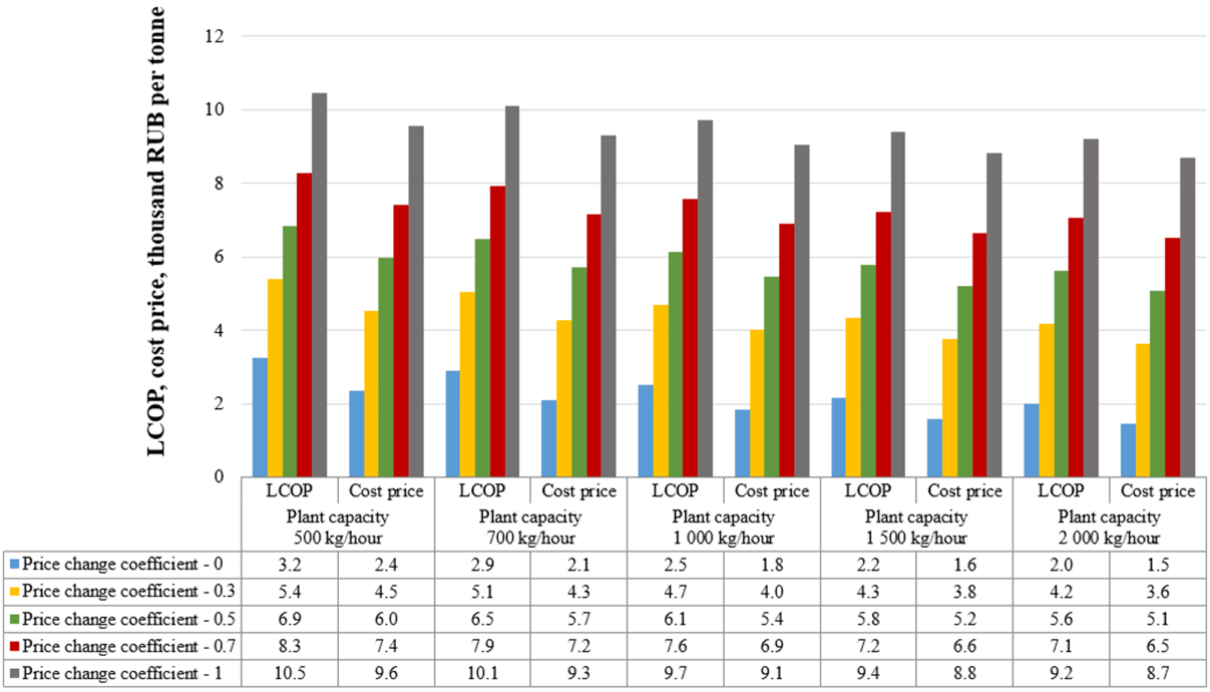

	Plant capacity 500 kg/hour		Plant capacity 700 kg/hour		Plant capacity 1 000 kg/hour		Plant capacity 1 500 kg/hour		Plant capacity 2 000 kg/hour	
	LCOP	Cost price	LCOP	Cost price	LCOP	Cost price	LCOP	Cost price	LCOP	Cost price
🟦 Price change coefficient - 0	3.2	2.4	2.9	2.1	2.5	1.8	2.2	1.6	2.0	1.5
🟨 Price change coefficient - 0.3	5.4	4.5	5.1	4.3	4.7	4.0	4.3	3.8	4.2	3.6
🟩 Price change coefficient - 0.5	6.9	6.0	6.5	5.7	6.1	5.4	5.8	5.2	5.6	5.1
🟥 Price change coefficient - 0.7	8.3	7.4	7.9	7.2	7.6	6.9	7.2	6.6	7.1	6.5
⬛ Price change coefficient - 1	10.5	9.6	10.1	9.3	9.7	9.1	9.4	8.8	9.2	8.7

Fig. 6. Change in LCOP and production cost of pellets consisting of 95% sawdust and 5% lignin depending on raw material prices and plant capacity.

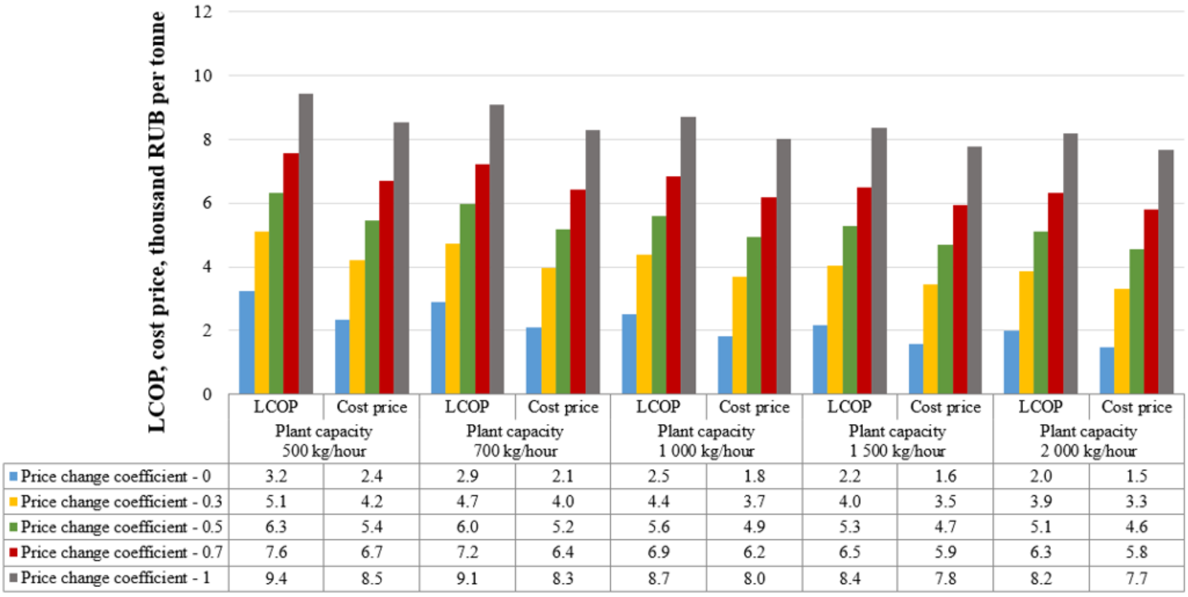

	Plant capacity 500 kg/hour		Plant capacity 700 kg/hour		Plant capacity 1 000 kg/hour		Plant capacity 1 500 kg/hour		Plant capacity 2 000 kg/hour	
	LCOP	Cost price	LCOP	Cost price	LCOP	Cost price	LCOP	Cost price	LCOP	Cost price
🟦 Price change coefficient - 0	3.2	2.4	2.9	2.1	2.5	1.8	2.2	1.6	2.0	1.5
🟨 Price change coefficient - 0.3	5.1	4.2	4.7	4.0	4.4	3.7	4.0	3.5	3.9	3.3
🟩 Price change coefficient - 0.5	6.3	5.4	6.0	5.2	5.6	4.9	5.3	4.7	5.1	4.6
🟥 Price change coefficient - 0.7	7.6	6.7	7.2	6.4	6.9	6.2	6.5	5.9	6.3	5.8
⬛ Price change coefficient - 1	9.4	8.5	9.1	8.3	8.7	8.0	8.4	7.8	8.2	7.7

Fig. 7. Change in LCOP and production cost of pellets consisting of 88% sawdust and 12% lignin depending on raw material prices and plant capacity.

reflects varying assumptions in operating hours, labor efficiency, and maintenance intensity at different scales.

Across all formulations, economies of scale significantly reduce production costs, but the magnitude of this benefit is strongly formulation-dependent. Pine sawdust/lignin blends, particularly those containing ≥23% lignin, demonstrate the steepest cost reduction (up to 37.5%) with scale-up, consolidating their status as the most economically resilient and scalable option. This advantage stems not only from lignin's binding properties reducing reliance on external additives but, crucially, from its potential to serve as a negative-cost or zero-cost waste stream, transforming a disposal liability feedstock into a value-added one.

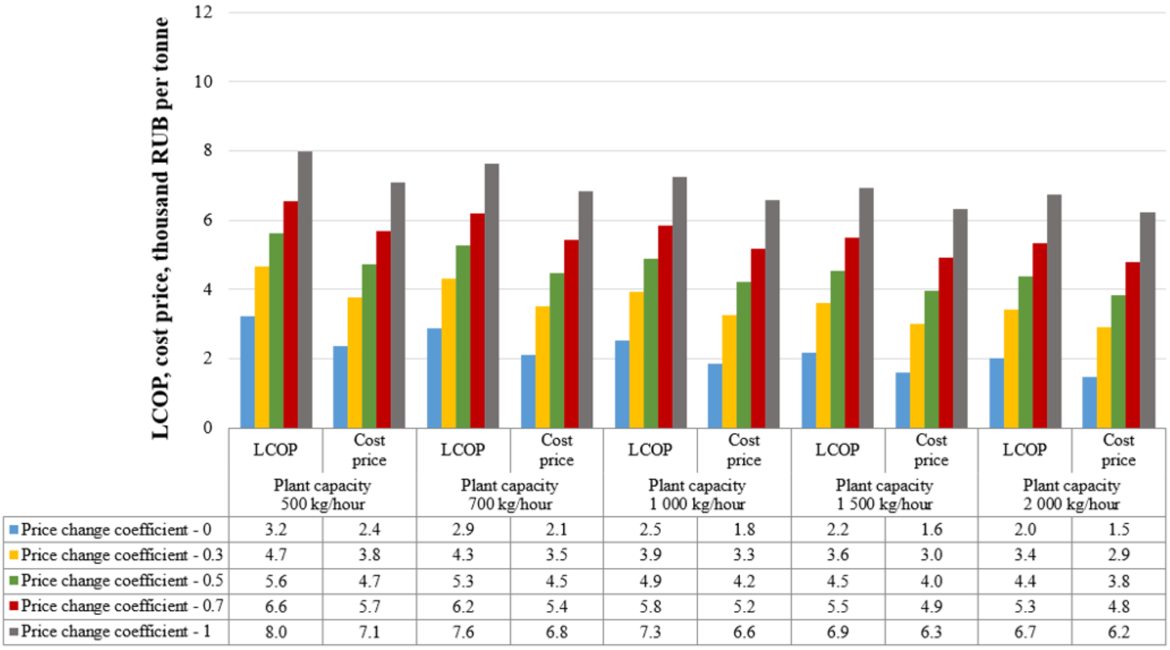

	LCOP Plant capacity 500 kg/hour	Cost price Plant capacity 500 kg/hour	LCOP Plant capacity 700 kg/hour	Cost price Plant capacity 700 kg/hour	LCOP Plant capacity 1 000 kg/hour	Cost price Plant capacity 1 000 kg/hour	LCOP Plant capacity 1 500 kg/hour	Cost price Plant capacity 1 500 kg/hour	LCOP Plant capacity 2 000 kg/hour	Cost price Plant capacity 2 000 kg/hour
🟦 Price change coefficient - 0	3.2	2.4	2.9	2.1	2.5	1.8	2.2	1.6	2.0	1.5
🟨 Price change coefficient - 0.3	4.7	3.8	4.3	3.5	3.9	3.3	3.6	3.0	3.4	2.9
🟩 Price change coefficient - 0.5	5.6	4.7	5.3	4.5	4.9	4.2	4.5	4.0	4.4	3.8
🟥 Price change coefficient - 0.7	6.6	5.7	6.2	5.4	5.8	5.2	5.5	4.9	5.3	4.8
⬛ Price change coefficient - 1	8.0	7.1	7.6	6.8	7.3	6.6	6.9	6.3	6.7	6.2

Fig. 8. Change in LCOP and production cost of pellets consisting of 77% sawdust and 23% lignin depending on raw material prices and plant capacity.

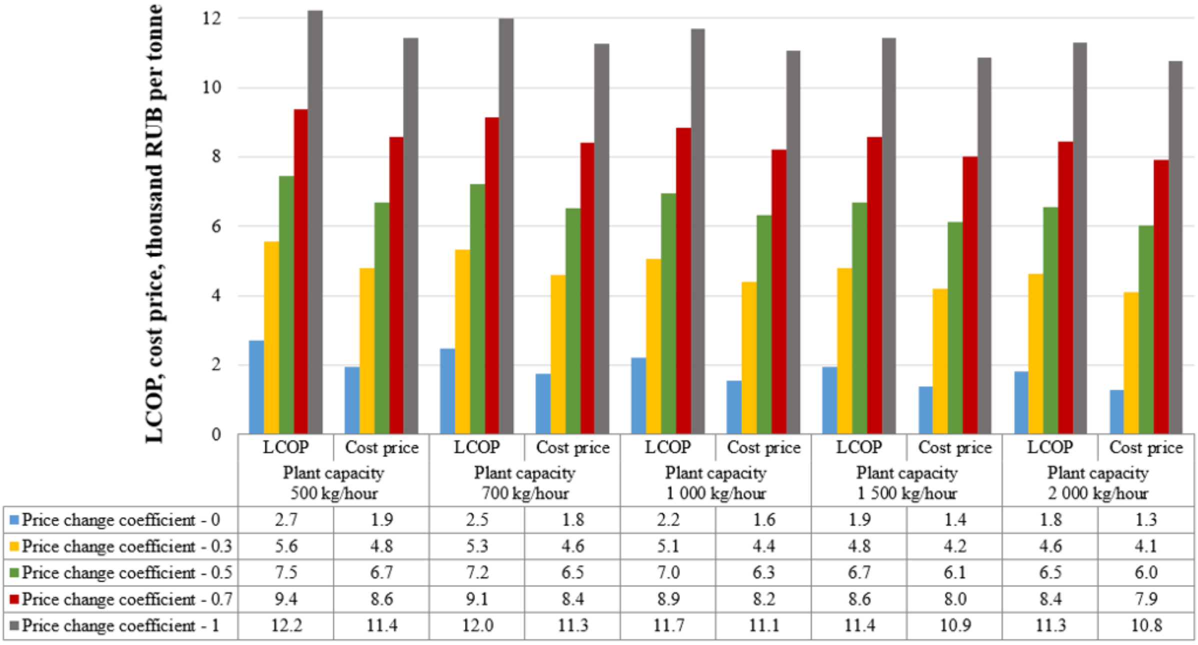

	LCOP Plant capacity 500 kg/hour	Cost price Plant capacity 500 kg/hour	LCOP Plant capacity 700 kg/hour	Cost price Plant capacity 700 kg/hour	LCOP Plant capacity 1 000 kg/hour	Cost price Plant capacity 1 000 kg/hour	LCOP Plant capacity 1 500 kg/hour	Cost price Plant capacity 1 500 kg/hour	LCOP Plant capacity 2 000 kg/hour	Cost price Plant capacity 2 000 kg/hour
🟦 Price change coefficient - 0	2.7	1.9	2.5	1.8	2.2	1.6	1.9	1.4	1.8	1.3
🟨 Price change coefficient - 0.3	5.6	4.8	5.3	4.6	5.1	4.4	4.8	4.2	4.6	4.1
🟩 Price change coefficient - 0.5	7.5	6.7	7.2	6.5	7.0	6.3	6.7	6.1	6.5	6.0
🟥 Price change coefficient - 0.7	9.4	8.6	9.1	8.4	8.9	8.2	8.6	8.0	8.4	7.9
⬛ Price change coefficient - 1	12.2	11.4	12.0	11.3	11.7	11.1	11.4	10.9	11.3	10.8

Fig. 9. Change in LCOP and production cost of pellets consisting of 90% straw and 10% mixed grasses depending on raw material prices and plant capacity.

TABLE 6. Range of Cost Reduction Depending on Production Capacity and RDF Pellet Composition

Pellet composition	Cost reduction range, %
Pine sawdust (%) / lignin (%)	
100/0	12.0–37.5
95/5	12.4–37.5
88/12	13.1–37.5
77/23	14.2–37.5*
Straw (%) / mixed grasses (%)	
100/0	6.5–34.4
50/50	2.1–34.4
Torrefied sunflower husks (%) / straw (%)	
15/85	4.8–34.4
10/90	5.2–34.4

*Largest benefit reflecting lignin’s dual role as a low-cost binder and a waste valorization driver

In contrast, agro-pellets (straw-, grass-, and husk-based blends) exhibit markedly smaller cost savings (2.1–34.4%), even at larger capacities. Their economic viability remains highly vulnerable to volatile raw material prices and logistical constraints, highlighting the necessity of targeted policy interventions, such as subsidies for agricultural residue collection, waste-to-energy premiums, or integration into existing agro-logistics and co-firing schemes to enhance competitiveness.

Critically, the analysis reveals that feedstock cost structure and plant scale are dominant determinants of commercial feasibility, far outweighing the influence of marginal variations in pellet durability (e.g., 92.3% vs. 96.1%) or heating value (±1–2 MJ/kg). Economic performance is extremely sensitive to raw material pricing: even modest reductions (e.g., to 50–60% of current levels) can shift NPV from deeply negative to highly positive and reduce DPP from >20 years to <2 years.

Therefore, strategic policy measures aimed at de-risking feedstock supply, such as incentivizing industrial lignin valorization, enforcing landfill diversion for biomass residues, introducing carbon pricing, or establishing regional waste-exchange platforms, are not merely beneficial but essential for unlocking the large-scale deployment of RDF pellet technologies in Russia. Without such enablers, even technically sound formulations risk remaining confined to pilot-scale demonstrations.

V. CONCLUSION

This study assessed the regional bioenergy potential of wood and crop residues across Russia, revealing that despite their large annual availability (~11.2 million tonnes in 2022), only a small fraction (0.42% of national fuel use) is currently recoverable due to economic and technological barriers. The highest potential lies in the Siberian and Northwestern Federal Districts, where forest residues could offset up to 0.66% and 0.56% of local fuel demand, respectively highlighting the need for region-specific strategies and supportive policies.

Composite RDF pellets made from sawdust, lignin, sunflower husk, straw, and grasses were successfully developed and tested. Formulations meeting a mechanical durability threshold of ≥93% comply with GOST 33103.2–2017 and are suitable for commercial use. Optimal blends include up to 23% lignin in sawdust-based pellets, at least 50% straw in grass mixtures, and limited sunflower husk (≤10%) to maintain quality.

Economic viability hinges primarily on feedstock costs. Sawdust – lignin pellets are feasible only if lignin is sourced as a zero-cost by-product. Agro-pellets require significantly lower raw material prices than current market levels (straw ≤ RUB 2 500/t, grass ≤ RUB 450/t, and sunflower husk ≤ RUB 1 500/t). Overall, integrating waste streams and optimizing composition are key to advancing cost-effective, sustainable bioenergy in Russia.

ACKNOWLEDGMENT

The research was funded by the Russian Science Foundation, Grant No. 24-29-00596 (https://rscf.ru/project/24-29-00596/).

REFERENCES

[1] S. B. Issa-zadeh, A. Jahanbakhsh Mashhadi, M. C. Garcia Gonzalez, “The contribution of biomass energy on urban sustainable development: Opportunities and challenges,” *Environmental Research and Technology*, vol. 8, no. 3, pp. 770–783, 2025. DOI: 10.35208/ert.1563758.

[2] V. M. Markova, V. N. Churashev, “Energy decentralization: Integration and innovation,” *ECO*, vol. 4, pp. 8–27, 2020. DOI: 10.30680/ECO0131-7652-2020-4-8-27. (In Russian)

[3] N. F. Islam, B. Gogoi, R. Saikia, B. Yousaf, M. Narayan, H. Sarma, “Encouraging circular economy and sustainable environmental practices by addressing waste management and biomass energy production,” *Regional Sustainability*, vol. 5, no. 4, Art. no. 100174, 2024. DOI: 10.1016/j.regsus.2024.100174.

[4] A. Thakur, A. Kumar, A. Somya, “Forestry and agricultural residues-based wastes: Fundamentals, classification, properties, and applications,” in *Biomass Wastes for Sustainable Industrial Applications*. CRC Press, 2024, pp. 95–139.

[5] H. Mortadha, H. B. Kerrouchi, A. Al-Othman, M. Tawalbeh, “A comprehensive review of biomass pellets and their role in sustainable energy: Production, properties, environment, economics, and logistics,” *Waste and Biomass Valorization*, vol. 16, no. 9, pp. 4507–4539, 2025. DOI: 10.1007/s12649-024-02873-x.

[6] D. S. Bajwa, T. Peterson, N. Sharma, J. Shojaeiarani, S. G. Bajwa, “A review of densified solid biomass for energy production,” *Renewable and Sustainable Energy Reviews*, vol. 96, pp. 296–305, 2018. DOI: 10.1016/j.rser.2018.07.040.

[7] J. W. Butler, W. Skrivan, S. Lotfi, “Identification of optimal binders for torrefied biomass pellets,” *Energies*, vol. 16, no. 8, Art. no. 3390, 2023. DOI: 10.3390/en16083390.

[8] T. Olugbade, O. Ojo, T. Mohammed, “Influence of binders on combustion properties of biomass briquettes: A recent review,” *BioEnergy Research*, vol. 12, no. 2, pp. 241–259, 2019. DOI: 10.1007/s12155-019-09973-w.

[9] K. Y. Vershinina, V. V. Dorokhov, G. S. Nyashina, D. S. Romanov, “Influence of binders on the properties of pellets based on wood waste,” *Coke and Chemistry*, vol. 67, no. 2, pp. 104–111, 2024. DOI: 10.3103/S1068364X24701291.

[10] N. P. K. Nielsen, D. Gardner, T. Poulsen, C. Felby, “Importance of temperature, moisture content, and species for the conversion process of wood residues into fuel pellets,” *Wood and Fiber Science*, vol. 41, pp. 414–425, 2009.

[11] L. Liu, M.Z. Memon, Y. Xie, S. Gao, Y. Guo, J. Dong, Y. Gao, A. Li, G. Ji, “Recent advances of research in coal and biomass co-firing for electricity and heat generation,” *Circular Economy*, vol. 2(4), Art. no. 100063, 2023. DOI: 10.1016/j.cec.2023.100063.

[12] N. Y. Abd Halim, N. I. S. Muhammad, F. Z. Mansur, N. Ahmad, “Sustainable fuel from agricultural waste: Mixture design optimization of refuse-derived fuel for enhanced energy output,” *Next Sustainability*, vol. 6, Art. no. 100196, 2025. DOI: 10.1016/j.nxsust.2025.100196.

[13] D. A. Agar, M. Rudolfsson, S. Lavergne, T. Melkior, D. Da Silva Perez, C. Dupont, M. Campargue, G. Kalén, S. H. Larsson, “Pelleting torrefied biomass at pilot-scale – Quality and implications for co-firing”, *Renewable Energy*, vol. 178, pp. 766–774, 2021. DOI: 10.1016/j.renene.2021.06.094.

[14] “Russian Federal Service for Surveillance on Consumer Rights Protection and Human Wellbeing. Information on the generation, processing, recycling, disposal, and disposal of production and consumption waste according to Form 2-TP (waste) for 2022, classified by waste type (Federal Classification Catalog of Waste).” [Online]. Available: https://rpn.gov.ru/upload/iblock/eab/scszkj8sefdf9vrk0l6wj98ueax3kf1b/2TP-_otkhody_-_-Razdel-1-_-Po-vidam-otkhodov-FKKO.xlsx. Accessed on: Nov. 01, 2025. (In Russian)

[15] “UIISS. Volume of harvested timber.” [Online]. Available: https://fedstat.ru/indicator/37848. Accessed on: Nov. 04, 2025. (In Russian)

[16] “Federal State Statistics Service. On industrial production in 2022.” [Online]. Available: https://rosstat.gov.ru/storage/mediabank/prom-december_2022.xlsx. Accessed on: Nov. 06, 2025. (In Russian)

[17] “Federal State Statistics Service. Agriculture in Russia. 2023. Supplement to the collection (information by constituent entity of the Russian Federation).” [Online]. Available: https://rosstat.gov.ru/storage/mediabank/Pril_sb_S-x_2023.xlsx. Accessed on: Nov. 03, 2025. (In Russian)

[18] “Russian Federal Service for Surveillance on Consumer Rights Protection and Human Wellbeing. Information on the formation, processing, recycling, disposal, and placement of production and consumption waste in form 2-TP (waste) for 2022, systematized for federal districts and constituent entities of the Russian Federation.” [Online]. Available: https://rpn.gov.ru/open-service/analytic-data/statistic-reports/production-consumption-waste/. Accessed on: Nov. 07, 2025. (In Russian)

[19] E. Gubiy, A. Kozlov, M. Penzik, “Recycling production and consumption waste for bioenergy purposes: Status and prospects,” *Ecology and Industry of Russia*, vol. 28, no. 10, pp. 30–36, 2024. DOI: 10.18412/1816-0395-2024-10-30-36. (In Russian)

[20] J. S. Tumuluru, C. Igathinathane, D. Archer, R. McCulloch, “Energy-based break-even transportation distance of biomass feedstocks,” *Frontiers in Energy Research*, vol. 12, Art. no. 1347581, 2024. DOI: 10.3389/fenrg.2024.1347581.

[21] T. T. Matheus, A. C. Farrapo, R. M. Lagunes, R. Filleti, D. P. Garcia, D. A. Lopes Silva, “The effect of transportation choices for mitigating climate-related impacts: The case of solid biofuels exported to Europe produced by Latin American countries,” *Sustainable Production and Consumption*, vol. 45, pp. 551–566, 2024. DOI: 10.1016/j.spc.2024.01.022.

[22] Y. Deng, X. Ran, H. Elshareef, R. Dong, Y. Zhou, "Emergy, Environmental and Economic (3E) Assessment of Biomass Pellets from Agricultural Waste," Agriculture, vol. 15, no. 6, 2025.

[23] M. P. Loginov, D. G. Sandler, *Investment analysis in project* management. Ekaterinburg, Russia: UFU Publ., 112 p., 2024 (In Russian)

[24] J. Friedmann, Z. Fan, Z. Byrum, E. Ochu, A. Bhardwaj, H. Sheerazi, “Levelized cost of carbon abatement: An improved cost-assessment methodology for a net-zero emissions world,” Columbia University SIPA Center on Global Energy Policy, 2020. [Online] Available: https://www.energypolicy.columbia.edu/wp-content/uploads/2020/10/LCCA_CGEP-Report_111522.pdf. Accessed on: Nov. 21, 2025.

Elena Gubiy, Ph.D., is a Research Associate in the Department for Complex and Regional Energy Problems at the Melentiev Energy Systems Institute of the Siberian Branch of the Russian Academy of Sciences (ESI SB RAS). Her research interests include the analysis of the efficiency of biofuels and the assessment of the bioenergy expansion potential.

Maxim Penzik, Ph.D., is a Senior Researcher in the Department of Thermal Power Systems at the ESI SB RAS. Since 2022, he has been an Associate Professor at the Faculty of Chemistry at Irkutsk State University. His research interests include the study on the processes of thermal decomposition of biomass, polymers, and organic compounds using the TG-MS method.

Vladislav Badenko is a Junior Researcher in the Department of Thermal Power Systems at the ESI SB RAS. His research interests include thermochemical conversion of biomass, numerical modeling of combustion processes, and combined energy facilities for biomass decomposition.

Alexander Kozlov, Ph.D., is a Senior Researcher in the Department of Thermal Power Systems at the ESI SB RAS. His research interests include the combustion of heterogeneous solid fuels (biomass, coal) and the development of simple engineering techniques for calculating gasification processes.

Grid Stability Assessment of Emerging Power Systems with DFIG Wind Integration

I.O. Ozioko[1], N.S. Ugwuanyi[2,*], A.O. Ekwue[3]

[1] Electrical Engineering Department, University of Nigeria, Nsukka, Nigeria
[2] Electrical and Electronics Engineering Department, Alex Ekwueme Federal University, Abakaliki, Nigeria
[3]Africa Center of Excellence/Electrical Engineering Department, University of Nigeria, Nsukka, Nigeria

***Abstract* — Most electricity-generating plants today rely on fossil fuels that emit greenhouse gases and are a major contributor to global warming. Renewable energy sources such as wind power offer a sustainable alternative but can impact power system stability—particularly in developing grids. This study relies on a detailed case study model to investigate the impact of Doubly-Fed Induction Generator (DFIG)-based wind turbine generators (WTGs) on the transient stability of the Nigerian power system. Two scenarios were evaluated: (1) supplementing existing conventional generators with WTGs, and (2) replacing gas-fired generators (GFGs) entirely with WTGs. The most suitable connection points for each scenario were identified. Case study results indicate a 9% improvement in transient stability when WTGs supplement conventional generators, while replacing GFGs with WTGs led to a 9% reduction in stability. These findings underscore the need for appropriate inertial support or alternative stabilization measures during the transition to a high penetration of renewable energy in the Nigerian grid.**

***Index Terms* — Renewable energy, greenhouse gas emission, wind energy penetration, transient stability, power system.**

I. INTRODUCTION

Fossil fuel combustion contributes 83% of global energy consumption, causing climate change [1]. Renewable energy sources, like hydro, wind, and solar, account for 12.6% [2]. Rapid development and population growth increase fossil fuel consumption, necessitating an eightfold increase in renewable energy generation for 100% CO_2 reduction [2]. Recent technological advancements in renewable energy have made it possible to integrate it into the existing grid.

Currently, several power systems rely on generators that produce high CO_2 emissions [3]. Consequently, the integration of carbon-free renewable energy is necessary, but it poses challenges to the existing grid [4, 5]. Research efforts are underway to identify these challenges and improve the performance of the grid-connected renewable energy (RE).

Renewable energy (RE), despite its numerous positive contributions, raises a number of economic, environmental, and engineering issues that have been a major subject of research in recent years [4, 6]. Environmental impacts and the unpredictable nature of RE are the focus of the authors in [7]. Erdiwansyah et al. [8] highlight the voltage stability as one of the critical issues associated with integrating various types of RE into an electrical grid. They propose a voltage management scheme to address this issue. Impram et al.'s [9] survey on the impact of RE sources on voltage, frequency, and small-signal stability reveals that the effect depends on the level of penetration, which is consistent with the findings in [10]. They recommend implementing demand and supply management techniques to ensure adequate stability control. Studies [11] and [12] report an improved voltage of a power system with wind energy integration. Kuri and Brackenhammer [13] discuss harmonics, forecasting, and

---

[*] Corresponding author.
E-mail: ugwuanyi.nnaemeka@funai.edu.ng

DOI: 10.25729/esr.2025.04.0008

Received June 27, 2025. Revised October 5, 2025. Accepted October 10, 2025. Available online December 29, 2025.

time scheduling as challenges of integrating RE into a power system. The authors in [13] design a Power Plant Controller for energy forecasting and time scheduling, while intelligent techniques are reported in [6] and [14] for accurate control of the grid with RE.

Furthermore, numerous studies highlight power quality as one of the most challenging aspects of grid-connected RE and suggest certain solutions that could remedy such conditions. Study [15] proposes an Adaptive Neuro-fuzzy Inference System (ANFIS) controller and a conventional controller to improve power quality. Ozioko et al. [16] analyze the impact of wind energy on the real power flow and conclude that optimal integration can reduce power losses, while high penetration increases active power losses. Similarly, Mastoi et al. [17] utilize a DFIG-WTG to reduce power losses in a power system. Other studies focus on improving the loadability of the grid-connected wind turbines using FACTS devices [18]. However, some researchers [19, 20] argue that integrating both FACTS devices and RE sources into an existing grid to enhance system performance may increase energy generation costs and reliability concerns.

The impact of RE penetration on the small-signal stability (SSS) of a grid has been studied by different researchers. Study [21] indicates that wind-solar energy integration favors the SSS of a power system compared to the performance of the grid with power electronics-based converter control. Moreover, He et al. [22] show that the participation of wind-solar energy systems in frequency regulation can improve the SSS of a grid. Modal analysis, Newton-Raphson power flow, and time-domain simulations are applied in [23] to assess SPV integration effects on voltage profiles, active power loss, and system stability in IEEE 4-machine and Nigerian 50-bus power systems. The findings point to varied impacts, stressing the need for a comprehensive approach considering voltage stability, power losses, and stability constraints. The effects of replacing conventional synchronous generators with inverter-based renewable (IBR) energy sources on the electromechanical oscillation are examined by Chen et al. [24] and Agrawal et al. [25]. According to [24], the SSS improves when the replaced states have higher participation factors in the electromechanical modes. Conversely, the replacement may worsen the SSS if participation factors are low. The authors of [25] note that a single trend could not be identified to correlate the impact of increased RES penetration levels with system's damping ratios.

The reviewed works primarily focus on integrating wind, solar, or both energy sources into the electrical grid and their impact on voltage, harmonics, and frequency. Some studies also explore grid small-signal stability when RE generators supplement conventional ones. However, more analysis is needed, especially regarding transient stability when replacing gas-fired generators (GFGs) and supplementing the GFGs with wind energy to cut down CO_2 emissions. Moreover, given the context-dependent nature of RE-research, it is necessary to explore the implication of replacing or supplementing conventional generators with DFIG-based wind turbines, especially in a developing grid, which is inherently weak. Our study fills these gaps, analyzing how DFIG-WTG impacts system stability, focusing on Nigeria's power system. This paper's primary contribution is that it examines how DFIG-WTG affects power system transient stability, viewing DFIG-WTG as both a supplement and a substitute for conventional synchronous generators within the same system. This holistic approach provides comprehensive insights into DFIG-WTG's impact on power system stability.

The remainder of the paper is organized as follows. Section 2 discusses the methodology, outlining the challenges faced by power supply, assessing the potential of renewable energy in Nigeria and identifying the CO_2 emission-affected area, with a focus on wind energy integration. Section 3 presents and discusses the findings obtained under different scenarios. Finally, section 4 concludes the study by stating limitations and recommendations.

II. METHODOLOGY

This section details the challenges faced by Nigeria's power system and the methodology we applied in this study.

A. The Power Supply Problem of the Nigeria Electricity Grid

Nigeria, Africa's most populous nation and largest economy in sub-Saharan Africa, faces severe power sector limitations that impede its economic growth [26]. Despite 26 operational grid-connected plants with 12 199 MW installed capacity, only about 4 000 MW is dispatched daily [27], which is insufficient. Even after government restructuring of the power sector into generation, transmission, and distribution companies for improved operation [26], electricity supply significantly lags behind demand, making Nigeria one of the world's most underpowered countries [27].

Nigeria's power system relies on 330 KV and 132 KV high-voltage transmission lines, alongside 33 KV, 11 KV, and 415 V sub-distribution lines, covering over 20 000 km high-voltage transmission lines [27]. However, the network faces constant technical challenges such as high losses, voltage degradation, and frequent collapses, preventing the utilization of at least 7 500 MW of its capacity [27]. Furthermore, most generators are GFGs suffering from inadequate gas supply that reduces generation. Even when gas supply is sufficient, these GFGs, however, contribute to high CO_2 emissions. On the other hand, Nigeria is endowed with abundant renewable energy resources, like wind and solar, with a wind farm under construction in Katsina State and several operational solar plants [28], though none are yet grid-connected.

B. *Wind Energy-Grid Integration*

This subsection represents the theoretical background of wind energy-grid integration.

1) Power Flow with WTGs

Wind energy conversion systems (WECS) can be integrated into the grid either at the load or generator buses. In either case, the power flow model will depend on whether the WTG is PV-controlled or PQ-controlled. The PQ-controlled model is usually adopted when the WTG is used to supplement the GFGs. In this case, the integration is done at a specified power factor, often unity, and the WTG power is modelled as a negative load [29, 30]. When the WTG is used to replace existing GFGs, it is common to model it as a PV-generator, much like the GFGs being replaced, while respecting the reactive power limits.

In a conventional load flow, real and reactive power on bus *i* can be expressed as

$$P_i = P_{gi} - P_{di}\,, \tag{1}$$

and

$$Q_i = Q_{gi} - Q_{di}\,, \tag{2}$$

where P_{gi}, P_{di}, Q_{gi}, and Q_{di} are the real power supply, real power demand, reactive power supply, and reactive power demand, respectively, on bus *i*.

For an *n*-bus system, total losses can be calculated by adding up the individual losses on the lines as

$$P_{realpowerloss} = \sum_{i=1}^{n} \left(\frac{P_i + Q_i}{V_i} \right)^2 R_i\,, \tag{3}$$

where R_i and V_i are resistance and voltage drop, respectively, on the *i*-th line.

For PQ-controlled WTG, equations (1) and (2) become

$$P_i = -P_{gi} + P_{di}\,, \tag{4}$$

and

$$Q_i = -Q_{gi} + Q_{di}\,. \tag{5}$$

Adopting the unity power factor for the PQ-controlled model leads to rewriting equation (3) as

$$P_{realpowerloss} = \sum_{i=1}^{n} \left(\frac{P_i}{V_i} \right)^2 R_i\,. \tag{6}$$

The power flow between the wind generator and the grid is driven by the mechanical power, P_m, expressed as

$$P_m = \frac{1}{2} C_p(\lambda, \alpha) \rho A V_{ws}^3\,, \tag{7}$$

where C_p is the turbine performance coefficient, λ is the tip speed ratio, α is the pitch angle of the blade, ρ is the density of the air (kg·m^{-3}), *A* is the swept area of the turbine (m^2), V_{ws} is the wind speed (m·s^{-1}). Equation (7) indicates how the wind energy is converted to mechanical power. This mechanical power is later converted to electrical power through DFIG electrical dynamics. The conversion system is summarized in Figure 1.

When WTGs replace conventional generators, the power flow remains unchanged. However, due to different dynamic characteristics, stability will not be the same. For instance, synchronous generators contribute more to inertia

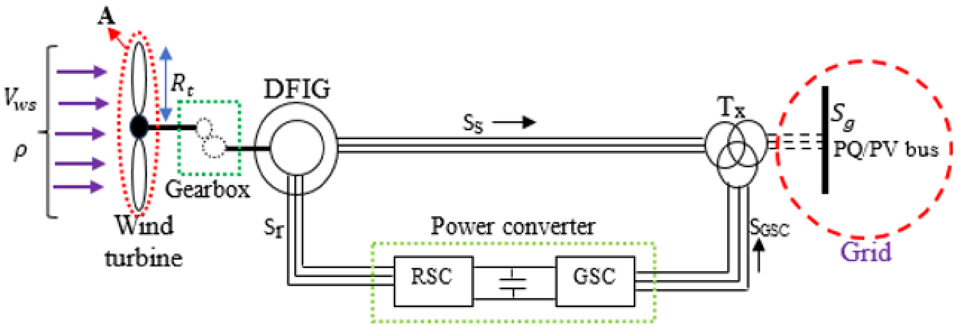

Fig. 1. DFIG-Based wind energy conversion system.

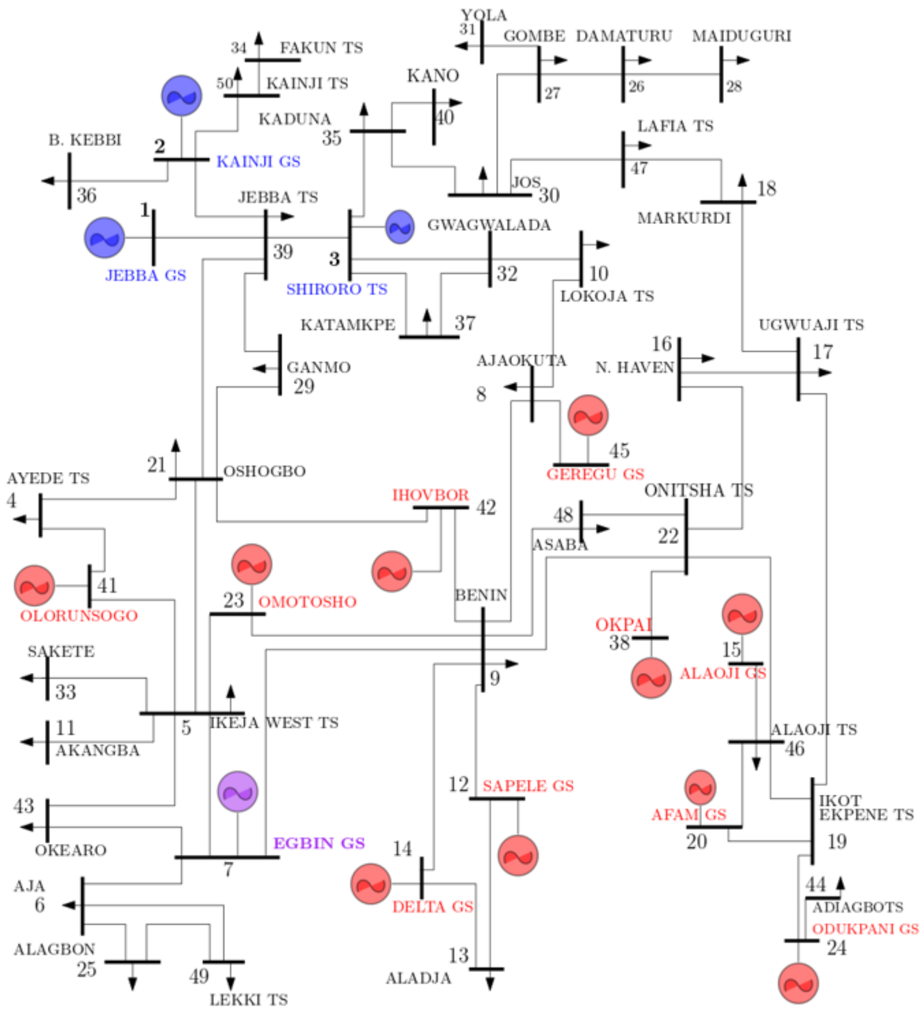

Fig. 2. The Nigerian 330 kV, 50-bus system [33].

than WTGs. In the stability analysis of DFIG wind turbines, the drive-train model is crucial. It is assumed that converter control can handle the shaft dynamics. Therefore, both mechanical dynamics resulting from wind speed variability and electrical dynamics resulting from wind turbine interactions with the grid are given by equation

$$\dot{\omega}_m = \frac{(T_m - T_e)}{2H_m}, \qquad (8)$$

where ω_m is the tip speed of the rotor (rad/s), T_e is the electromagnetic torque expressed as $T_e = X_m i_{qr} i_{ds} - X_m i_{dr} i_{qs}$, H_m is the inertial constant (kW s/kVA), and T_m is the mechanical power input. In the expression for the electromagnetic torque, X_m is the magnetization reactance (Ohm), i_{qr} and i_{dr} are q- and d-axis rotor current, respectively, i_{ds} and i_{qs} are d- and q-axis stator current, respectively. The comprehensive DFIG-based WECS model parameters used in this analysis are as shown in Table 1. Equation (8) indicates that the wind turbine will introduce oscillation to the power system due to the imbalance between the mechanical and electrical torques. An ideal case is when these two torques are equal, which is the objective of the WTG control strategies.

2) Calculation of WTGs Penetration

In this study, we define wind energy penetration as the ratio of the wind energy injected to the total generation in the system. The percentage penetration is expressed formally as shown in equation

$$P_{\%windpenetration} = \left[\frac{P_{wind}}{\sum \left(P_{gen.(i)} + P_{wind} \right)} \right] \times 100, \qquad (9)$$

where $P_{\%windpenetration}$ is the percentage of wind power

TABLE 1. The DFIG-Based WECS Model Parameters

Parameter	Value	Parameter	Value
Number of blades	3.0	ρ (kg/m^3)	1.225
The length of blade (m)	75.0	Gear box ratio	1/89
Frequency (Hz)	50.0	Number of poles, P	4.0
Power rating (MW)	2.0	Inertia constants, H_m (KWs/KVA)	3.0
Number of turbines in the farm	900	Magnetization reactance, X_m (p.u)	3.0
Wind speed (m/s)	7.7	Rotor reactance (p.u)	0.08
Voltage rating (kV)	330	Rotor resistance (p.u)	0.01
Coefficient of Power (Cp)	0.40	Stator reactance (p.u)	0.10
Capacity factor	40%	Stator resistance (p.u)	0.01
Pitch control gain (p.u)	10.0	Time constants (s)	3.0
Voltage control gain, Kv (p.u)	10.0	Power control time constants, T_e (s)	0.01

penetration in the system; P_{wind} is the wind energy generator capacity in the system, p.u.; $P_{gen.(i)}$ is the *i*-th conventional generator's capacity, p.u. For every additional wind power generator in the grid, the contribution of each of the other existing generators is adjusted proportionately. However, the power of the already existing RE generators remains unchanged.

3) Selection of the Wind Farm Connection Bus

Figure 2 shows a schematic of the Nigerian power system, operating at 330 kV. The network consists of two primary types of generators: hydro plants and gas-fired generators, located in the northern and southern regions of the country, respectively. Notably, almost all GFGs are concentrated in the southern part of the country, resulting in substantial gas emissions in the region. However, this area also has significant wind energy potential, as identified in [31]. Replacing GFGs with WTGs could significantly enhance Nigeria's electricity supply and mitigate its current shortage, as reported by the International Renewable Energy Agency (IRENA) in 2023 [32].

To integrate WTGs and reduce the share of GFGs, we identified suitable connection points in the southern region following a two-stage process. First, we screened for strong buses, defined as those that maintain a voltage profile within the ±5% grid code tolerance under normal operation. Second, from this pool of strong buses, we identified the optimal candidates by simulating incremental wind energy injection to find the buses that yielded the minimal active power loss, adopting a loss minimization approach. This ensures that the chosen connection points are both robust and efficient.

When replacing GFGs with WTGs, we conduct a sequential replacement process, allowing for priority-based replacement order to prevent any deterioration of system stability. This approach enables the identification of the most suitable replacement strategy, ensuring the efficient integration of WTGs and minimizing potential disruptions to the power system.

4) Considered Cases

The study examines the impact of DFIG-based wind turbine generators (WTG) on Nigeria's grid stability. We consider three cases. **Case 1**: the base case that assumes no use of wind energy. **Case 2**: WTGs supplement the GFG output. **Case 3**: the power system has gas-fired generators replaced by the equivalent capacity of wind turbines. The presentation and discussion of results relies onPSAT®, a MATLAB® toolbox for electric power system analysis and simulation.

III. RESULTS AND DISCUSSION

This section presents and discusses the findings of our analysis as detailed in the following subsections.

A. Analysis of Cases 1 and 2

The base case power flow analysis revealed a real power loss of 70 MW. Additionally, five key buses in southern Nigeria, namely Akamgba, Okearo, Sakete, Ajah, and Alagbon, were identified as strong buses. The best WTG connection point was deemed the bus that exhibited the lowest real power loss as wind energy penetration levels increased on the strong buses. Figure 3a shows the real power loss evolution on selected buses with increased wind energy penetration (base case: 0%). Akamgba, Okearo, and Ajah had minimum losses (51.70, 52.10, and 55 MW,

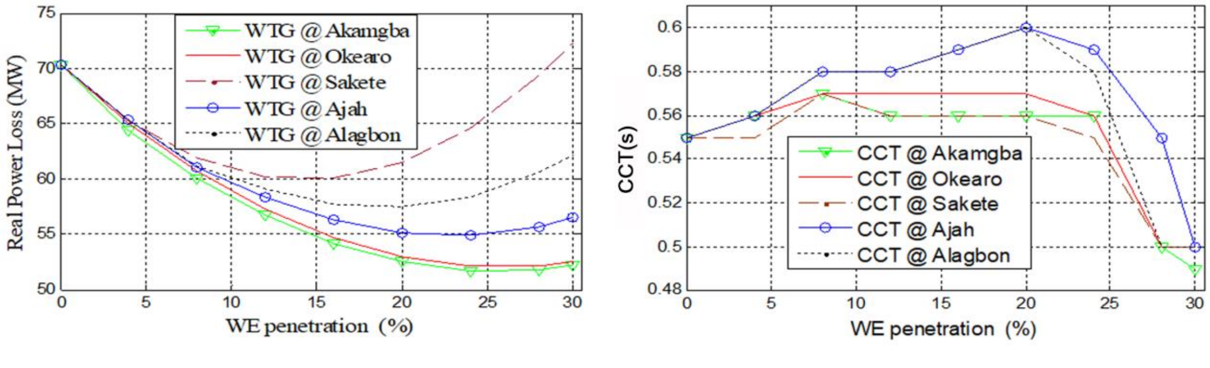

(a) (b)

Fig. 3. (a) Evolution of real power loss against the penetration on the selected load buses, (b) Critical clearing time (CCT) against the penetration on the selected load buses

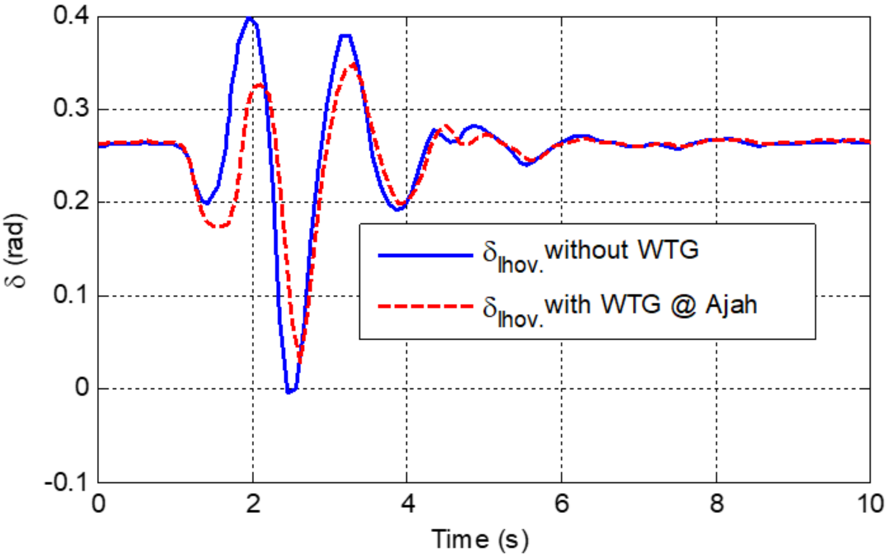

Fig. 4. Oscillation of the base case versus WEI at Ajah.

respectively) at 24% penetration. Sakete and Alagbon had minimum losses (60.10 and 58 MW) at 16% and 20% penetration, respectively. This shows that buses handle renewable energy differently. Akamgba is the preferred candidate for Wind Energy Integration (WEI) due to its lowest minimum real power loss compared to the base case, with Okearo and Ajah considered as viable alternatives. While Akamgba excels in loss minimization, this does not guarantee stability, so each bus will undergo further stability testing.

Focusing on the severe inter-area oscillation, a three-phase fault was simulated at the Ihovbor generator bus, which is known for the system's slowest oscillation (0.67 Hz) [34, 35]. We then determined the critical clearing time (CCT); a higher CCT indicates improved transient stability and greater wind energy integration. CCT with increasing wind penetration is shown in Figure 3b. In the base case (0% penetration), the system records a CCT of 0.55 s. At low penetration levels, wind integration enhances transient stability across all candidate buses. However, stability declines beyond certain levels — after 7.5% for Sakete and Akamgba (both with CCT = 0.57 s), and after 20% for Okearo (CCT = 0.57 s), Alagbon (CCT = 0.60 s), and Ajah (CCT = 0.60 s). In contrast, the loss-based analysis (Fig. 3a) indicates that Sakete can accommodate up to 12.5% wind penetration and Akamgba up to 24%, underscoring the trade-off between minimizing real power losses and maintaining transient stability. Ajah and Alagbon exhibit the best stability performance, each achieving a maximum CCT of 0.60 s at 20% penetration (a 9% improvement over the base case). When both stability and loss reduction are considered, Ajah emerges as the most favorable site, having the lower real power loss (55 MW) compared to Alagbon (58 MW).

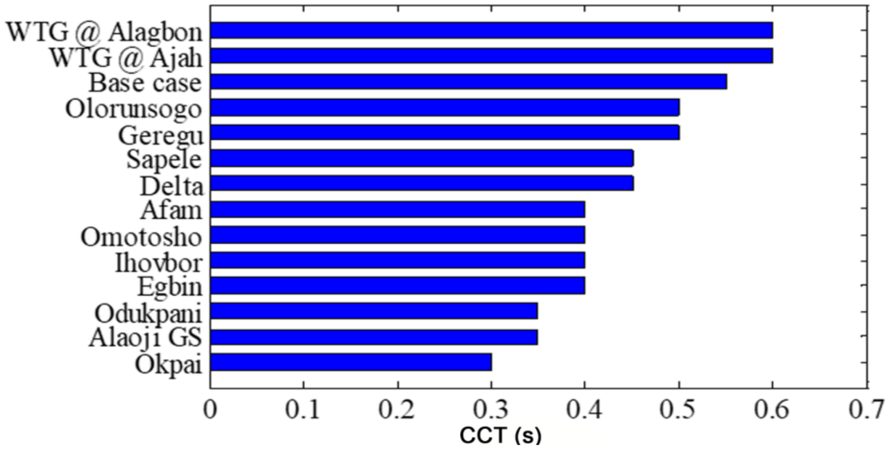

Fig. 5. CCT of GFGs replacement compared to the base case and best load buses.

Figure 4 displays the rotor oscillation of the WTG at Ajah at 20% penetration. The reduced amplitude in Case 2 compared to Case 1 confirms enhanced stability when Wind Turbine Generators (WTG) supplement Gas Fired Generators (GFGs). This demonstrates grid stability at 20% penetration (626 MW), as the system with WEI exhibits faster oscillation damping than in the base case.

B. Analysis of Case 3

In this case, we analyzed the impact of replacing GFGs with WTGs of equivalent capacity. The methodology involved a sequential, one-by-one replacement of each GFG in the southern part of the grid. For each replacement, a transient stability analysis was performed to calculate the CCT, with the fault located, similarly to Cases 1 and 2, at the Ihovbor bus. This systematic process allowed us to identify which GFG replacements were the least detrimental to system stability. The CCT results for each replacement scenario are presented in Figure 5.

For comparison, the Figure also includes cases where WTGs are connected at the Alagbon and Ajah load buses, allowing assessment of stability improvements from supplementing generation at load buses versus replacing GFGs. The results indicate that replacing GFGs with DFIG-WTGs reduces transient stability due to the associated loss of rotational inertia, underscoring the need for alternative mechanisms to compensate for this unbalance. Among the replacement cases, substituting Olurunsogo and Geregu generators provided the best outcome, though the CCT still declined from 0.55 to 0.50 s — a 9% reduction in stability. Overall, Figure 5 demonstrates that WTGs enhance system stability more effectively when supplementing existing generation at load buses than when replacing conventional GFGs.

Figure 6 displays the Ihovbor generator's rotor angle

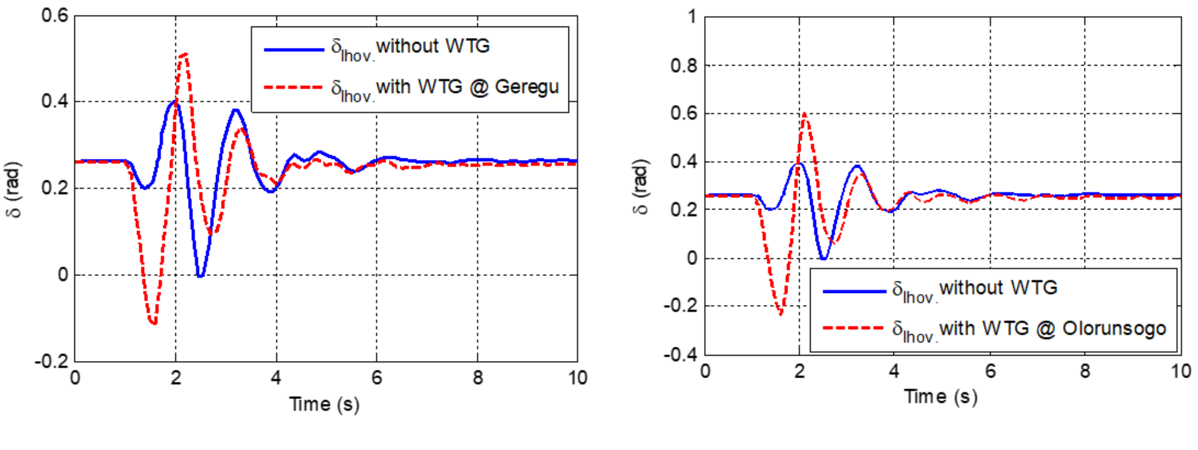

(a) (b)

Fig. 6. (a) Comparing rotor angle oscillation in the base case against the WTG at Geregu, (b) Comparing rotor angle oscillation in the base case against the WTG at Olorunsogo.

with sequential replacements at Olorunsogo and Geregu, confirming reduced stability due to higher oscillation amplitudes. It is noteworthy that the Ihovbor generator has a high participation factor in the dominant 0.67 Hz electromechanical oscillation, yet stability decreases. This observation does not agree with [24] which found that replacing the state significantly contributing to the electromechanical oscillation with a virtual synchronous generator improves stability. In fact, in our case, the stability deteriorates irrespective of generator replacement, thus emphasizing the context-dependent nature of RE studies.

C. Discussion and Contextual Comparison

The above study of the Nigerian grid demonstrates that DFIG-based wind integration can enhance transient stability at low penetration levels, but margins deteriorate once penetration exceeds relatively modest thresholds (≈7.5–20%, depending on the connection point). While integration at load buses shows these limits, replacing existing synchronous generators further exacerbates stability deterioration. This pattern arises from two coupled effects: (i) the limited reactive-power capability of DFIGs during faults, which aggravates voltage dips and short-term instability; and (ii) the displacement of synchronous generators, which reduces system inertia and weakens frequency and transient response. These outcomes are consistent with international experience, although the thresholds at which issues emerge vary with the system's strength and topology.

Akhmatov's Danish case study [36] highlighted similar short-term voltage stability challenges in a system with high wind and CHP contributions. Induction-machine turbines were shown to absorb significant reactive power during faults, deepening voltage sags and, in some cases, triggering cascaded disconnections. The study further distinguished between large offshore wind farms — required to ride through disturbances — and local units that often trip under undervoltage, and proposed mitigation measures such as dynamic reactive compensation and wind-turbine ramp-rate controls. These findings reinforce the conclusion that adequate reactive support and effective fault-ride-through capability are critical for secure DFIG integration.

In the UK context, Xia et al. [37] emphasized frequency-domain risks in a stronger, meshed grid. Their results show that higher DFIG shares increase ROCOF and reduce critical fault-clearance times (CFCT), with penetrations above 40–50% yielding CFCT values below Grid Code requirements. Stability could be preserved only through additional measures such as SVCs, HVDC reinforcements, enhanced primary reserves, or synthetic inertia. The UK network study illustrated that robust grids can tolerate higher non-synchronous penetration before instability arises, but only with extensive ancillary-service deployment.

The Algerian case [38] provided a distribution-level perspective in weak, radial systems. Simulations showed that DFIG farms are highly vulnerable to poor fault-ride-through and voltage collapse unless supported by D-FACTS devices. Both D-SVC and D-STATCOM improved stability, though with cost–performance trade-offs: D-STATCOM delivered stronger and faster support at higher costs, whereas D-SVC provided more economical but slower compensation. These findings highlighted the need to tailor remedies to the level of grid connection and economic feasibility.

More recently, Shabani et al. [10], instead of analyzing a national grid, employed a benchmark Single Machine Infinite Bus (SMIB) model to examine how equipment-level factors influence transient stability. Their results showed that the CCT improves with increasing wind penetration up to about 0.7 p.u. but declines thereafter, which is consistent with our findings. They also demonstrated that reactive power support from DFIGs enhances stability but increases converter current stress, pointing to the need for external devices such as STATCOMs.

Taken together, the Nigerian, Danish, UK, and Algerian case studies reveal a consistent picture: the mechanisms driving stability degradation — loss of inertia, limited MVAr support, and altered power flows — are universal, but the penetration thresholds and mitigation strategies are system-dependent. Stronger grids such as in the UK can accommodate 40–60% penetration before serious risks emerge [37], while weaker or less meshed systems such as in Nigeria (as demonstrated in this study), Denmark [36], and Algeria [38] experience critical issues at much lower levels.

IV. CONCLUSION, RECOMMENDATIONS, AND LIMITATIONS

This paper studied wind energy integration's impact on the Nigerian grid's stability, focusing on WTGs supplementing or replacing GFGs. We have identified optimal connection points and quantified the stability impacts for each scenario. The key conclusions are as follows:

i) Optimal placement of supplementary WTGs, specifically at a strong load bus like Ajah, can improve system transient stability. A 20% wind energy penetration (626 MW) at this location extended the CCT by 9%, from 0.55 to 0.60 s.
ii) A trade-off exists between power loss minimization and stability enhancement. The optimal penetration level for stability (20%) was found to be lower than the level for maximum loss reduction (24%), indicating that stability is the more constraining factor.
iii) Replacing GFGs with equivalent WTG capacity universally reduces system stability due to the loss of synchronous inertia. The least disruptive replacements (Geregu and Olorunsongo) still resulted in a 9% stability decrease, underscoring the need for compensatory measures.

A. Practical Recommendations for System Operators

The findings and the contextual comparison point to the following priorities:

i) Enforce enhanced grid-support functions in WTGs, including synthetic inertia, fast frequency response, and reactive capability;
ii) Deploy targeted compensation (SVC/STATCOM or D-FACTS) at weak nodes; and
iii) Site large wind plants at strong connection points or reinforce weak networks. These combined measures — also advocated in the Danish [36], UK [37], and Algerian [38] case studies as well as in study [10] — are essential to balancing efficiency with stability as wind penetration grows.

B. Limitations and Future Work

This study assumed a constant wind speed, which simplifies analysis but may overestimate stability margins since real wind turbulence and wake effects introduce power fluctuations that reduce the critical clearing time (CCT). In addition, the standard DFIG model used did not include advanced features such as Low Voltage Ride Through (LVRT), which affect fault dynamics.

Future studies should therefore consider variable wind speed profiles, conduct sensitivity analyses of system parameters, and evaluate advanced inverter controls (e.g., grid-forming technologies) to better capture the impact of large-scale wind integration on Nigerian grid stability.

REFERENCES

[1] C. Liu, “Empirical analysis of the relationship between renewable energy consumption and economic growth based on the Grey Markov model,” *Journal of Mathematics*, vol. 2022, Art. no. 5679696, 2022.

[2] J. L. Holechek, H. M. E. Geli, M. N. Sawalhah, R. Valdez, “A global assessment: can renewable energy replace fossil fuels by 2050?,” *Sustainability*, vol. 14, no. 8, Art. no. 4792, 2022.

[3] D. O. Obada, M. Muhammad, S. B. Tajiri, M. O. Kekung, S. A. Abolade, S. B. Akinpelu, A. Akande, “A review of renewable energy resources in Nigeria for climate change mitigation,” *Case Studies in Chemical and Environmental Engineering*, vol. 9, Art. no. 100669, 2024.

[4] A. Q. Al-Shetwi, “Sustainable development of renewable energy integrated power sector: Trends, environmental impacts, and recent challenges,” *Science of The Total Environment*, vol. 822, Art. no. 153645, 2022.

[5] M. M. Islam, T. Yu, G. Giannoccaro, Y. Mi, M. L. Scala, M. R. Nasab, J. Wang, “Improving reliability and stability of the power systems: A comprehensive review on the role of energy storage systems to enhance flexibility,” *IEEE Access*, vol. 12, pp. 152738–152765, 2024. DOI: 10.1109/ACCESS.2024.3476959.

[6] M. Khalid, “Smart grids and renewable energy systems: Perspectives and grid integration challenges,” *Energy Strategy Reviews*, vol. 51, Art. no. 101299, 2024. DOI: 10.1016/j.esr.2024.101299.

[7] J. Wang, X. Chen, M. Zhuang, Y. Li, Z. Ruan, Y. Wang, N. Zhang, J. Song, K. He, X. Lu, “Accelerating exploitation and integration of global renewable energy,” *The Innovation*, vol. 6, Art. no. 100873, 2025. DOI: 10.1016/j.xinn.2025.100873.

[8] Erdiwansyah, Mahidin, H. Husin, Nasaruddin, M. Zaki, Muhibbuddin, “A critical review of the integration of renewable energy sources with various technologies,” *Protection and Control of Modern Power Systems*, vol. 6, no. 3, pp. 1–18, 2021. DOI: 10.1186/s41601-021-00181-3.

[9] S. Impram, S. V. Nese, B. Oral, “Challenges of renewable energy penetration on power system flexibility: A survey," *Energy Strategy Reviews*, vol. 31, Art. no. 100539, 2020.

[10] H. R. Shabani, A. Hajizadeh, M. Kalantar, M. Lashgari, M. Nozarian, “Transient stability analysis of DFIG-based wind farm-integrated power,” *Electrical Engineering*, vol. 105, no. 6, p. 3719–3735, 2023.

[11] B. B. Adetokun, C. M. Muriithi, “Impact of integrating large-scale DFIG-based wind energy conversion system on the voltage stability of weak national grids: A case study of the Nigerian power grid,” *Energy Reports*, vol. 7, no. 2021, pp. 654–666, 2021.

[12] O. Olanite, M. N. Nwohu, B. A. Adegboye, O. J. Tola, “Large scale penetration impact of PMS-WTGs on Voltage and power loss for 52-bus, 330kV system of the Nigerian grid,” *Nigerian Journal of Technology*, vol. 43, no. 1, pp. 115–122, 2024.

[13] A. Kuri, E. Brackenhammer, "Challenges for integration of renewable energy in public grid," in *21st Wind and Solar Integration Workshop (WIW 2022)*, Hybrid Conference, Netherlands, 2022.

[14] S. Islam, N. K. Roy, "Renewables integration into power systems through intelligent techniques: Implementation procedures, key features, and performance evaluation," *Energy Reports*, vol. 9, pp. 6063–6087, 2023. DOI: 10.1016/j.egyr.2023.05.063.

[15] P. Cholamuthu, B. Irusappan, S. K. Paramasivam, S. K. Ramu, S. Muthusamy, H. Panchal, R. S. S. Nuvvula, P. P. Kumar, B. Khan, "A grid-connected solar PV/wind turbine based hybrid energy system using ANFIS controller for hybrid series active power filter to improve the power quality," *International Transactions on Electrical Energy Systems*, pp. 1–14, 2022.

[16] I. O. Ozioko, N. S.Ugwuanyi, A. O. Ekwue, C. I. Odeh, "Wind energy penetration impact on active power flow in developing grids," *Scientific African*, vol. 18, Art. no. e01422, 2022.

[17] M. S. Mastoi, M. J. Tahir, M. Usman, D. Wang, S. Zhuang, M. Hassan, "*Research* on power system transient stability with wind generation integration under fault condition to achieve economic benefits," *IET Power Electronics*, vol. 15, no. 3, pp. 263–274, 2022.

[18] N. S. *Ugwuanyi*, I. O. Ozioko, U.M. Uma, O. A. Nwogu, N. C. Ugwuoke, N. Nwokocha, "Enhancing renewable energy-grid integration by optimally placed FACTS devices: The Nigeria case study," *Science Journal of Energy Engineering*, vol. 12, no. 2, pp. 16–25, 2024.

[19] J. Shair, H. Li, J. Hu, X. Xie, "Power system stability issues, classifications *and* research prospects in the context of high-penetration of renewables and power electronics," *Renewable and Sustainable Energy Reviews*, vol. 145, Art. no. 111111, 2021.

[20] B. Shakerighadi, N. Johansson, R. Eriksson P. Mitra, A. Bolzoni, "An overview of stability challenges for power-electronic-*dominated* power systems: The grid-forming approach," *IET Generation, Transmission, & Distribution*, vol. 17, no. 2, pp. 284–306, 2023.

[21] A. Pepiciello, J. L. Dominguez-Garcia, A. Vaccaro, "The impact of *frequency* support by wind turbines on the small-signal stability of power systems," *Energies*, vol. 15, Art. no. 8470, 2022.," *Energies*, vol. 15, no. 22, Art. no. 8470, 2022.

[22] T. He, S. Li, S. Wu, K. Li, "Small-signal stability analysis for power system *frequency* regulation with renewable energy participation," *Mathematical Problems in Engineering*, vol. 2021, no. 1, Art. no. 5556062, 2021.

[23] N. S. Ugwuanyi, N. C. Ugwuoke, P. I. Obi, "Impact of grid-scale solar photovoltaic integration on power system performance," *Vokasi Unesa Bull. Eng. Technol. and Appl. Sc.*, vol. 2, no. 2, pp. 189–198, 2025. https://doi.org/10.26740/vubeta.v2i2.35474, 2025.

[24] M. Chen, D. Zhou, F. Blaabjerg, "High penetration of inverter-based power sources with VSG control impact on electromechanical oscillation of power system," *International Journal of Electrical Power and Energy Systems*, vol. 142, part B, Art. no. 108370, 2022.

[25] U. Agrawal, R. Huang, Z. Huang, "Analysis of the impact of the increasing inverter-based resources on inter-area modes of the U.S.," *TechRxiv*, vol. 1, 2022.

[26] O. Bamisile, Q. Huang, X. Xu, W. Hu, W. Liu, Z. Liu, Z. Chen, "An approach for sustainable energy planning towards 100% electrification of Nigeria in 2030," *Energy*, vol. 197, Art. no. 117172, 2020.

[27] A. U. Adoghe, T. M. Adeyemi-Kayode, V. Oguntosin, I. I. Amahia, "Performance evaluation of the prospects and challenges of effective power generation and distribution in Nigeria," *Heliyon*, vol. 9, Art. no. e14416, 2023.

[28] O. A. Somoye, "Energy crises and renewable energy potentials in Nigeria: A review," *Renewable and Sustainable Energy Reviews*, vol. 188, Art. no. 113794, 2023.

[29] M. H. Haque, "incorporation of fixed speed wind farms in power flow analysis," in *2nd IET Renewable Power Generation Conference (RPG 2013)*, Beijing, 2013.

[30] A. E. Feijoo, J. Cidras, "Modeling of wind farms in the load flow analysis," *IEEE Transactions on Power Systems*, vol. 15, no. 1, pp. 110–115, 2000.

[31] U. C. Ben, A. E. Akpan, C. C. Mbonu, C. H. Ufuofuonye, "integrated technical analysis of wind speed data for wind energy potential assessment in parts of southern and central Nigeria," *Cleaner Engineering and Technology*, vol. 2, Art. no. 100049, 2021. DOI: 10.1016/j.clet.2021.100049.

[32] "Renewable energy roadmap: Nigeria," International Renewable Energy Agency (IRENA), Abu Dhabi, 2023, 126 p.

[33] N. S. Ugwuanyi, I. O. Ozioko, N. C. Ugwuoke, "Dataset for the Nigerian 50-bus 330 kV power grid," *Zenodo*, pp. 1–7, 2024. DOI: 10.5281/zenodo.12091189.

[34] N. S. Ugwuanyi, U. U. Uma, A. O. Ekwue, "Characterization of oscillation in developing power systems: The Nigeria case study," in *2021 IEEE/IAS Power Africa*, Kenya, 2021.

[35] N. S. Ugwuanyi, U. U. Uma, A. O. Ekwue, "Fundamental study of oscillations in the Nigerian power systems," *Nigeria Journal of Technology*, vol. 40, no. 5, pp. 913–926, 2021.

[36] V. Akhmatov, "System stability of large wind power networks: A Danish study case," *International Journal of Electrical Power and Energy Systems*, vol. 28, no. 1, pp. 48–57, 2006.

[37] J. Xia, A. Dysko, J. O'Reilly, "Future stability challenges for the UK network with high wind penetration levels," *IET Generation, Transmission and Distribution*, vol. 9, no. 11, pp. 1160–1167, 2015.

[38] L. Wang, K. D. E. Kerrouche, A. Mezouar, A. V. D. Bossche, A. Draou, L. Boumeddiene, "Feasibility study of wind farm grid-connected project in Algeria under grid fault conditions using D-FACTS devices," *Applied Science*, vol. 8, no. 11, Art. no. 2250, 2018.

Innocent Onyebuchi Ozioko earned his B. Eng. degree from Enugu State University of Science and Technology, Enugu. Subsequently he received his M. Eng. and Ph.D. degrees in Electrical Engineering from the University of Nigeria, Nsukka. He is a certified engineer recognized by the Council for the Regulation of Engineering in Nigeria (COREN). He is currently a postdoctoral research fellow at Tshwane University of Science and Technology (TUT), South Africa. His research interests include power system analysis, power system control and stability, renewable energy integration, and fuel cell technologies. Email: innocent.ozioko.pg01268@unn.edu.ng.

Nnaemeka Sunday Ugwuanyi earned his B.Eng. and M.Eng. degrees in Electrical Engineering from the University of Nigeria, Nsukka, in 2012 and 2016, respectively. He completed his Ph.D. with Highest Distinction — Félicitations du Jury at École Nationale Supérieure d'Arts et Métiers, France, in 2020, where he also received the Pierre Bézier Award for the best thesis. He is a Lecturer and Postgraduate Coordinator in the Department of Electrical and Electronic Engineering at Alex Ekwueme Federal University, Ndufu-Alike, Nigeria, and a 2024 Visiting Scholar at MIT. In 2025, he received the Séjours Scientifiques de Haut Niveau (SSHN) grant from the French Ministry for Europe and Foreign Affairs. His research interests include power system stability, renewable energy integration, the use of normal forms for nonlinear modal analysis, and FACTS devices. Email: ugwuanyi.nnaemeka@funai.edu.ng.

Arthur Ekwue is a Royal Academy of Engineering Visiting Professor at Brunel University of London, Middlesex, London. He is also a Fellow of the Nigerian Academy of Engineering. His research interests include power transmission and distribution systems, voltage stability, distributed generation. Email: arthur.ekwue@brunel.ac.uk

Power Quality Improvement in Hybrid E-Bicycles Using the Adaptive Reinforcement Current Tracking-based Super-Lift Converter

Shajini G Inba Kani[1], P. Elangovan[1,*]

[1] Department of EEE, B.S.Abdur Rahman Crescent Institute of Science and Technology, India

***Abstract* — Electric bicycles are becoming increasingly popular as green mobility solutions. However, problems of low mileage, a poor power factor, and unstable charging voltage still persist. This study proposes a novel power management system with a Super-Lift Converter (SLC), Field Programmable Gate Array (FPGA)-regulated active front-end circuitry, and a flexible solar panel to address the issues. The system's design uses a 350 W BLDC hub motor and a 36 V 10.4 Ah lithium-ion battery. A SLC is inserted between the charger and battery to achieve a high voltage transfer gain and voltage ripple of less than 1%. The incorporated FPGA runs an Adaptive Reinforcement-based Current Tracking (ARCT) algorithm to provide power factor correction by generating a synchronized reference inductor current with the input voltage waveform. A 60 W, 36 V flexible solar panel is attached to a secondary input of the SLC to provide solar-assisted charging and extend the vehicle range from 45 km to 50 km per charge. During charging of the 36–42 V lithium-ion battery, the system is powered from a 230 V AC grid, stepped down to 100 V AC using a transformer, along with the PV input. Experimental results attest to a dramatic reduction in total harmonic distortion and enhanced current tracking performance. The proposed system provides a sustainable and compact solution for electric bicycles and similar energy-efficient mobility platforms.**

***Index Terms* — Active front end, battery, electric bicycle, power factor correction, total harmonic distortion.**

I. INTRODUCTION

Electric bicycles (e-bicycles) are a future substitute for conventional vehicles and a cost-effective, green, and energy-efficient form of urban transportation. With the world focusing on sustainable transport, e-bicycles are gaining momentum in urban areas, particularly in short-distance trips. Range limitations due to inefficient charging and energy management systems are still a hindrance to their widespread adoption. Low battery life and low power quality during charging are serious issues [1]. Smart control techniques could improve autonomy and user experience, according to the evidence provided by an adaptive electric bicycle study [2].

The primary challenge is battery efficiency. Lithium-ion batteries typically used in e-bicycles are current- and voltage-ripple-sensitive during charging, and such ripples can accelerate degradation and decrease the cycle life. Conventional boost converters, although simple and inexpensive, tend to lack the high gain and low ripple in a single step. Inductive power transfer and wireless charging system solutions enabled new e-bicycle configurations [3]; however, these systems tend to add complexity and cost. Hybrid parallel topologies and optimized coil topologies for a stable current output in inductive charging systems were also investigated [4].

The performance of the charging system is directly related to energy usage and ride quality. For example, a

---

[*] Corresponding author.
E-mail: elangoeee2007@gmail.com

DOI: 10.25729/esr.2025.04.0009

Received July 13, 2025. Revised October 24, 2025. Accepted November 27, 2025. Available online December 29, 2025.

control-based hybrid bicycle test experiment verified the necessity of finding the optimal tradeoff between fuel economy and capacity loss [5].

More advanced power management strategies can optimize energy utilization. A reinforcement learning-based assisted power management system was proposed to enable real-time power sharing adaptation between motor and human inputs in e-bicycles [6]. These intelligent strategies are crucial for meeting the performance needs of users while respecting size, cost, and energy storage limitations. A double-wheel drive strategy to improve user experience in electrically assisted bicycles also showed the need for combined control [7].

Thus, an efficient and scalable charging infrastructure is critical for mass adoption. Extremely large inductive charging stations using hybrid topology switching and single inverters were studied to support a growing number of e-bicycles [8]. Hybrid topologies with configurable voltage and current outputs were reported to increase charging flexibility [9, 10]. Even cost-effective wireless charging systems were implemented to provide feasible solutions to customers [11]. These developments notwithstanding, challenges still exist as concerns the high power factor (PF), low total harmonic distortion (THD), and low ripple, particularly in compact systems.

FPGA-based control solutions are becoming increasingly prevalent in power electronics owing to their capability for real-time operation and reconfigurability. High-precision timing, real-time digital control for active power filters, and high-frequency GaN-based DC-DC converters were all improved through FPGA implementations [12–14]. Online inductance identification based on FPGA-based systems also underscored the platform's potential for power converter control in electric vehicle (EV) systems [15].

Super-lift converter (SLC) topologies [16] proved useful for the high-voltage gain in low-ripple applications. In EV applications, advanced designs with buck converters or positive output lift stages can deliver higher voltage conversion efficiency and output quality [17, 18]. For example, a combination of Luo and Cuk topologies simplified the circuit, enhanced the gain, and enabled low-ripple operations [19]. Control strategies, such as the sliding mode and adaptive estimation, offer robust performance even in converter environments with uncertainties [20].

Adaptive control methods are crucial for systems that encounter model uncertainties, disturbances, or dynamic changes. Adaptively tuned current-mode control techniques and window-based mode selectors with adaptation improved the converter’s response [21]. Adaptive perturbation rejection techniques and output feedback control also improved robust tracking and system stability [22]. These techniques became even more crucial in EV systems, where source and load conditions can change rapidly.

In recent years, there has also been increasing interest in reinforcement-learning (RL) driven controllers for power converters and EVs. RL-based controllers in power electronic applications were introduced with steady-state error compensation schemes [23], whereas deep RL were implemented for dynamic active and reactive power control of grid-connected EVs [24]. Predictive RL methods [25] and meta-RL current control schemes for motor drives [26] indicated the feasibility of RL under various converter conditions. Real-world applications include RL-driven buck converter control under time-delay conditions [27], smart MPPT controllers for renewables [28], and

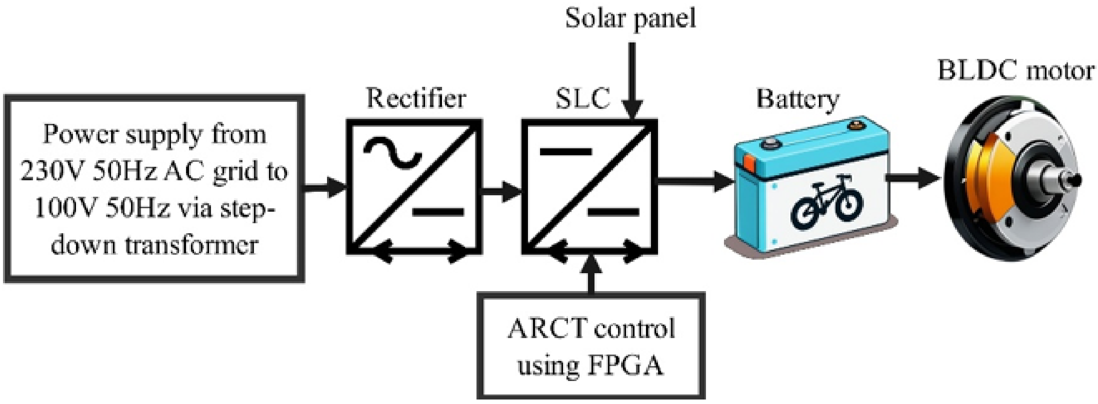

Fig. 1. Overall architecture of the proposed system.

stabilization of boost converters under CP loads through deep RL [29]. Most recently, safety-augmented and self-learning RL schemes were introduced for converter applications [30] and adaptive RL-driven PID controllers were used for multi-area power grids [31]. This demonstrates RL's capability for adaptability and application-performance optimization in power grids. Although these applications for the most part remain constrained by computational overhead, the lack of real-time FPGA-based implementation and limited optimization targets such as MPPT or converter stabilization give way to research evolution. Thus far no RL framework has been specifically adapted for e-bicycle platforms, which require compact implementation of hardware, converter gain, ripple, and simultaneous PF and THD compliance. Given this background, there is a pressing need for an FPGA-implemented adaptive RL approach capable of PF, THD, and ripple tradeoff under virtual AC–PV input and hybrid mode operations.

In addition, power quality problems [32] in battery charging from AC sources, such as PF degradation and high THD were reported. Various unidirectional non-isolated PFC converters offered exceptional size advantages, efficiency, and reduction in harmonic trade-offs [33]. It was suggested that high-current-density EV chargers employ modified PI controllers to enhance dynamic response [34, 35]. Second-harmonic current reduction methods were applied in two-stage PFC systems to eliminate distortions [36].

To address these challenges, the present study introduces a Super-Lift Converter (SLC) controlled by an FPGA-based Adaptive Reinforcement-Based Current Tracking (ARCT) algorithm. The major contributions of this work are summarized as follows:

- A first-of-its-kind FPGA-implemented ARCT for an on-board e-bicycle charger integrating grid and PV power.
- The experimentally proven near-unity power factor (0.99) and very low input current THD (2.23%).
- Stabilization of PV output voltage under varying irradiance using combined MPPT–ARCT interaction within the SLC topology.
- Reduction of battery terminal ripple (<1.5%) and improved charging smoothness, supporting reduced degradation and extended cycle life.
- Demonstration of a practical hybrid e-bicycle platform with a 15% improvement in battery-supported mileage, validating the proposed control strategy.

II. OVERALL E-BICYCLE SYSTEM ARCHITECTURE

The architecture of the hybrid charging and propulsion system of the e-bicycle proposed in this study is shown in Fig. 1. The system employs a stepped down single-phase 100 V, 50 Hz AC supply from a 230 V, 50 Hz AC grid using a step-down transformer, which is connected to a

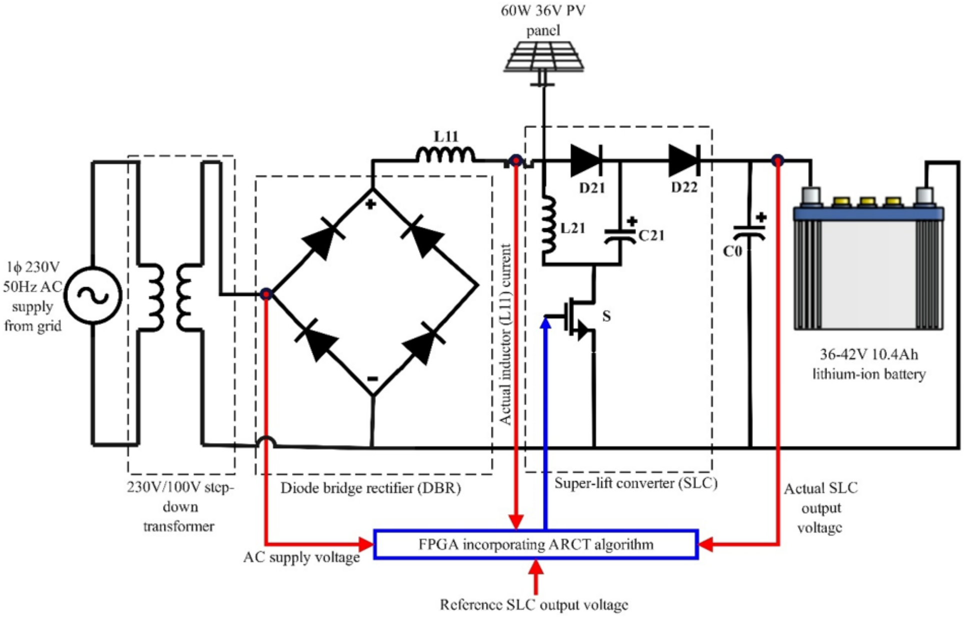

Fig. 2. Detailed diagram of the designed system.

TABLE 1. Nomenclature for the Proposed ARCT–SLC System

Variable	Description
V_{in}	Input AC voltage (after autotransformer)
V_R & I_R	Rectified AC input voltage & current
V_{PV} & I_{PV}	PV panel voltage & current
V_{SLC}	Average output voltage of SLC
v_o	Output/battery charging voltage
i_L	Inductor current
Δ	Duty ratio generated by the actor network
θ	Actor network weights
ω	Critic network weights
$r[k]$	Reward at iteration k
$\delta[k]$	Temporal-Difference (TD) error
γ	Discount factor
PF	Power factor
THD	Total harmonic distortion
V_{MPPT}	PV voltage at MPP
f_s	Switching frequency
T_s	Sampling period
N_{update}	Actor-critic update interval
α_a, α_c	Learning rates for the actor and the critic

rectifier for AC-to-DC conversion.

The rectified supply is connected to a Super-Lift Converter (SLC), which is tailored to provide a high voltage gain with low output ripple. The converter is driven in a three-port configuration to facilitate the hybrid energy input and output. Port 1 is supplied with DC from the grid and is energized for indoor or stationary charging, whereas port 2 is linked to a flexible solar panel that supplies power during outdoor cycling. The solar panel is a 36 V, 60 W module. The SLC charges a 36–42 V, 10.4 Ah lithium-ion battery pack. Port 3 supplies the regulated DC output to charge the lithium-ion battery, which supplies a Brushless DC (BLDC) motor for propulsion. An FPGA controller driven by an Adaptive Reinforcement-Based Current Tracking (ARCT) algorithm regulates the switching actions of the converter to provide voltage stability, enhance the power factor, and minimize harmonic distortion. The hybrid integrated configuration enhances energy efficiency, provides grid compatibility, and enhances the mileage of the e-bicycle.

A detailed schematic of the system implementation is shown in Fig. 2, where each functional block is represented by its corresponding electrical component. The AC supply is connected to a Diode Bridge Rectifier (DBR), and its output is filtered using an input inductor (*L11*).

The SLC stage includes a switching device (*S*), inductors (*L11* and *L21*), diodes (*D21* and *D22*), and capacitors (*C21* and *C0*), designed to have a multi-stage boost topology. A 60 W solar panel is implemented in the input path of the converter, enabling auxiliary energy harvesting. The SLC regulated output is supplied to a 10.4 Ah, 36–42 V lithium-ion battery. The FPGA is supplied with feedback signals such as the AC supply voltage, actual and reference SLC output voltages, and the current flowing through inductor *L11*. Based on this feedback, the ARCT algorithm dynamically controls the switching of *S* for an efficient operation under various load and input conditions. The figure provides the rationale behind the design by showing how the control and power stages communicate at the circuit level, enabling the high-efficiency and reliable operation of the hybrid e-bicycle charging system.

Passive components, such as inductor and capacitor values, are derived based on standard ripple constraints. The inductor is sized by

$$di_L = \frac{V_R \Delta}{L f_s}, \tag{1}$$

where, di_L is the ripple current in inductors *L11* and *L21*, V_R is the rectified AC input voltage, Δ is the switching duty cycle, and f_s is the switching frequency. Considering that the ripple current in the inductors is limited to 20% of the average inductor current at a switching frequency of 20 kHz, *L11* and *L21* can be chosen as 100 μH.

The capacitor is chosen by

$$dV_C = \frac{I_0 \Delta}{C f_s}, \tag{2}$$

where, dV_C is the ripple voltage in capacitor *C0* and I_0 is the current through capacitor *C0*. Considering that the ripple voltage in the capacitor is limited to less than 1% of the output voltage, *C0* can be set to 470 μF. Table 1 summarizes all mathematical symbols and parameter notations used in the ARCT-regulated SLC model to ensure clarity and consistency throughout the text.

III. SUPER-LIFT CONVERTER (SLC)

The SLC topology is derived from the Luo converter family, where voltage boosting is achieved through the sequential discharging and charging of multiple capacitors and inductors. A schematic of the SLC and its equivalent operating state are shown in Fig. 3. The illustration includes the entire circuit setup, as well as the two

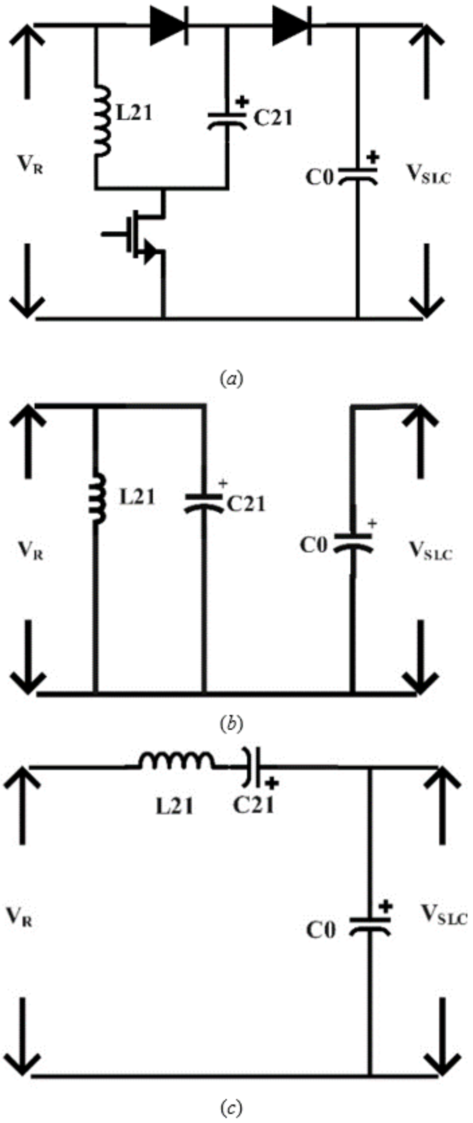

Fig. 3. (a) Overall circuit topology (b) Equivalent circuit when the switch is ON (c) Equivalent circuit when the switch is OFF.

prominent switching states, that is when the switch is ON and when the switch is OFF.

During the switch-ON interval, the DC link input energy of the switches is stored in inductor *L11* and capacitor *C21* is charged from the input voltage V_R, that is, the rectified voltage of a single-phase 100 V, 50 Hz AC source, by diode *D21*. The energy is stored for a very short time interval in the magnetic field *L11* and the electric field *C21* and no energy is transferred to the output. When the switch is OFF, diode *D21* is reverse-biased, diode *D22* is forward-biased, and the stored energies of *L11* and *C21* are transferred to the output side through *D22*, thereby boosting the voltage. The output capacitor *C0* filters this energy and provides a smooth DC output voltage V_{SLC} between battery terminals.

This two-step energy-transfer process allows the converter to superimpose the voltage across *C21* on top of the input voltage and generate a much higher output voltage. Not only does the operation increase the output, it also renders it low in ripple, which is a desirable characteristic for battery charging. Mathematical modeling of the voltage and current performance of the converter confirms this behavior. The average output voltage V_{SLC} of the SLC can be expressed as

$$V_{SLC} = \frac{2-\Delta}{1-\Delta} V_R \, , \tag{3}$$

where, V_R is the rectified AC input voltage, and V_{SLC} is the output voltage. Compared to the existing boost converter, which has a gain of $\frac{1}{2-\Delta}$, the SLC has improved gain characteristics for the same switching duty cycle.

Similarly, the converter output current I_{SLC} can be defined in terms of the input current I_R as

$$I_{SLC} = \frac{1-\Delta}{2-\Delta} I_R \,. \tag{4}$$

The front end of the SLC is a full wave diode bridge rectifier (DBR) and its average output voltage is given by

$$V_R = \frac{2V_p}{\pi}, \tag{5}$$

where, V_P is the peak value of supply AC voltage.

Substituting equation (5) in (3), we get

$$V_{SLC} = \frac{2-\Delta}{1-\Delta} . \frac{2V_p}{\pi} \,. \tag{6}$$

This expression ensures that the SLC effectively converts the voltage and current levels without disturbing the balance of energy and with minimal losses. The voltage transformation gain M is expressed as follows:

$$M = \frac{V_{SLC}}{V_R} = \frac{2-\Delta}{1-\Delta} \,. \tag{7}$$

The gain feature is much better than that of the conventional boost converter, especially for high duty cycle Δ values; therefore, the SLC is ideal for high-voltage, low-ripple battery charging.

The use of more than one lifting stage, along with a voltage boost provides seamless conduction on the input side, enabling an improved power factor and reduced harmonic distortion. Such characteristics are inherent in applications where the input supply is an AC grid and power quality needs to be guaranteed. Additionally, because of its mode of operation, the SLC inherently provides low electromagnetic interference (EMI) and reduced stress on the switch, thereby improving the system reliability and component life.

In the proposed system, the SLC is interfaced with an FPGA that implements an ARCT algorithm. The ARCT controller dynamically adjusts the duty cycle of switch S based on the real-time measurement of the inductor current and input voltage. The control causes the inductor current to follow a sinusoidal reference, essentially performing power factor correction at the input and stable charging at the output. The SLC with the ARCT algorithm achieves voltage step-up and intelligent control, resulting in a compact, adaptive, and grid-connected charging compliant system.

Thus, SLC simplifies the hardware and facilitates high-performance control integration. Its inherent high-gain characteristic, low output ripple, and compatibility with advanced digital control techniques, such as ARCT, make it a good choice for modern EV battery chargers. The next

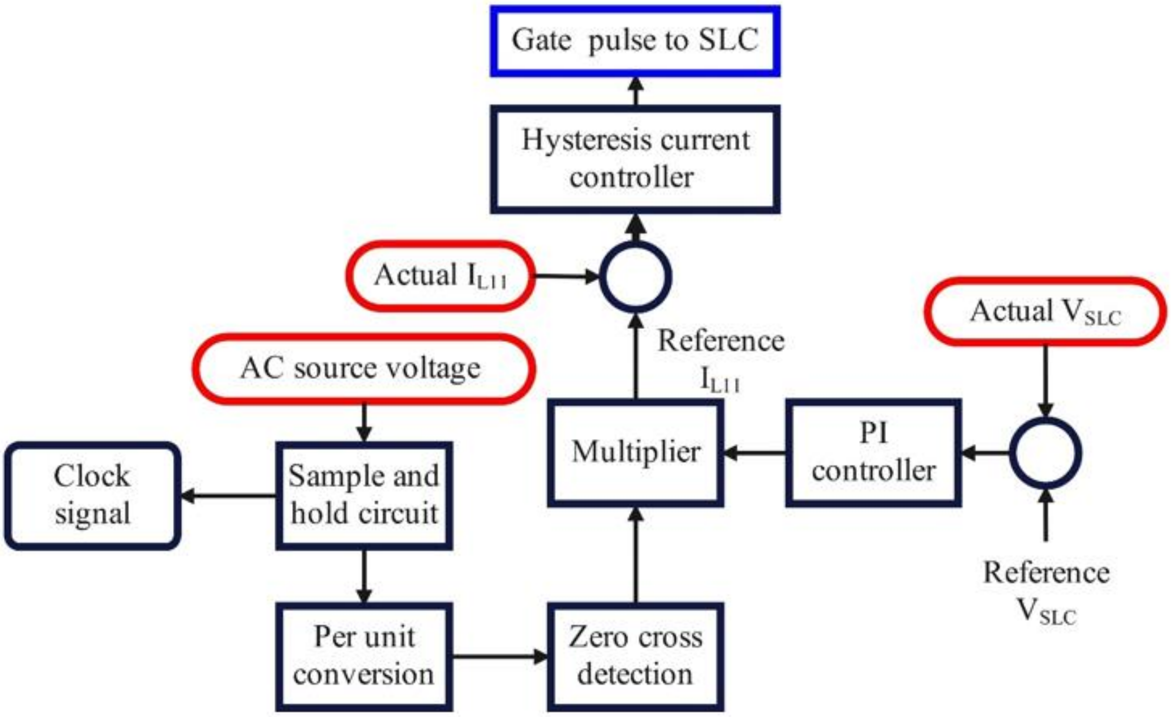

Fig. 4. Proposed ARCT architecture.

section discusses the ARCT algorithm, which controls the SLC operation to provide optimal current tracking and enhanced power quality.

IV. DESIGN FRAMEWORK OF THE ARCT ALGORITHM

The proposed ARCT configuration shown in Fig. 4 combines the high-voltage gain benefit of the Super-Lift Converter (SLC) with an adaptive reinforcement learning-based current tracking methodology to achieve improved power quality and battery charging stability.

The ARCT algorithm is based on the actor-critic reinforcement learning framework, which is defined by two primary components: the actor and the critic. The actor is responsible for selecting control actions (i.e., the switch duty cycle in the SLC), and the critic evaluates the quality of the action chosen by running a reward function based on the system response with special emphasis on inductor current tracking. The control objective is to condition the input current to follow a sinusoidal reference waveform in phase with the input voltage to achieve power factor correction and reduce the total harmonic distortion (THD).

The inductor current $i_L(t)$ is measured at each sampling instant and compared with the synthesized reference current $i_{L,ref}(t)$, which is generated as a scaled input rectified voltage.

The error is computed as follows:

$$e(t) = i_{L,ref}(t) - i_L(t)\,. \qquad (8)$$

The critic network approximates the estimated return using the estimate function $V(s_t)$, where s_t is the current state of the system.

The temporal-difference (TD) error signal is computed as

$$\delta(t) = r(t) + \gamma V(s_{t+1}) - V(s_t)\,, \qquad (9)$$

where, $\gamma \in (0,1]$ is the discount factor, and $s_t + 1$ is the next state considered as a consequence of applying the selected control action. The TD error is the error in the estimation of the reward and is what the actor and critic are updated with.

The actor network, responsible for generating the duty cycle $d(t)$, generates a control action based on a parameterized policy function $\pi_\theta(s_t)$, given by

$$d(t) = \pi_\theta(s_t) = \theta^M \phi(s_t)\,. \qquad (10)$$

Here, θ is the actor parameter vector, and $\phi(s_t)$ is the system state feature representation. The actor parameters are learned by the policy gradient method, which adjusts the control policy to maximize the expected reward:

$$\theta \leftarrow \theta + \alpha_a \delta(t) \nabla_\theta \log \pi_\theta(s_t)\,, \qquad (11)$$

where α_a is the actor's learning rate. Simultaneously, critic parameters ω, used for approximating $V(s_t)$, are updated to minimize the mean-squared TD error:

$$\omega \leftarrow \omega + \alpha_c \delta(t) \nabla_\omega V(s_t)\,, \qquad (12)$$

where α_c is the critical learning rate. Control action $d(t)$ is then converted into a gate signal for the power switch in the SLC. As the ARCT algorithm learns and adapts over time, the converter can dynamically switch the switching action to accurately follow the current, improve the input power factor, and minimize the harmonic distortions without system modeling or fixed control laws.

The strength of the ARCT approach is its generalization across the operating points. Unlike fixed-gain controllers that require re-design for different supply voltage or load levels, the actor-critic policy learns an optimal action across a wide range of conditions via reinforcement learning. Furthermore, the actor-critic architecture is a trade-off between learning stability and responsiveness and can be readily implemented at high speed in an embedded system on an FPGA platform.

The ARCT controller is implemented in discrete-time with the sampling time synchronized with the converter PWM switching frequency. It receives the sensed inductor current and supply voltage for each switching cycle, computes the control policy, updates the weights through gradient-based computations, and utilizes the updated duty cycle for the subsequent switching period. The reference current waveform $i_{L,ref}(t)$, is furnished by a zero-cross detection circuit and scaled in proportion to the instantaneous rectified AC input such that the input current is sinusoidal and in phase with the source voltage.

V. MATHEMATICAL MODELING AND THEORETICAL VALIDATION

The proposed Adaptive Reinforcement-Based Current Tracking (ARCT) algorithm employs an actor-critic reinforcement learning framework to regulate the SLC for lithium-ion battery charging from hybrid power sources. A thorough mathematical model of the system, where theoretical and experimental values are compared, such as power factor (PF), total harmonic distortion (THD), inductor current tracking, battery ripple voltage, and stable photovoltaic (PV) output is described below.

The total source current can be represented as

$$i_{in}(t) = i_L(t) + \sum_{n=2}^{\infty}\left(\frac{V_{in}}{nZ_n}\sin(n\omega t + \Phi_n)\right) = i_{L,ref}(t) + e(t)\,, \qquad (13)$$

where, $i_{in}(t)$ is the source current, $i_L(t)$ is the inductor current, V_{in} is the supply voltage, Z_n is the n-th harmonic impedance, ω is angular frequency, Φ_n is the phase angle of the n-th harmonic, $i_{L,ref}(t)$ is the reference inductor current, and $e(t)$ is the tracking error.

The dynamic voltage transfer gain of the SLC can be expressed as

$$M(t)=\frac{V_{SLC}}{V_R}=\frac{\left(2-\Delta(t)\right)^2+k_1e^2(t)}{\left(1-\Delta(t)\right)\left(1+k_2\dfrac{d\Delta(t)}{dt}\right)}, \tag{14}$$

where, $M(t)$ is the instantaneous gain, $\Delta(t)$ is the duty ratio, $e(t)$ is the tracking error, k_1 and k_2 are tuning constants.

The total harmonic distortion (THD) can be expressed by

$$\begin{aligned} I_{in,RMS}&=\sqrt{I_1{}^2+\sum_{n=2}^{N}I_n{}^2},\\ THD&=\left(\frac{I_{in,RMS}{}^2-I_1{}^2}{I_1{}^2}\right)^{\frac{1}{2}}\times 100\%, \end{aligned} \tag{15}$$

where, $I_{in,RMS}$ is the RMS input current and I_1 is the fundamental component.

The stabilized PV output current is derived from:

$$I_{PV}(t)=\frac{V_{MPPT}(t)}{R_{PV}}+\alpha_{pv}\sin(\omega_{sun}t)-\beta_{pv}e(t), \tag{16}$$

where, $I_{PV}(t)$ is the PV current, $V_{MPPT}(t)$ is the maximum power point voltage, R_{PV} is the panel resistance, ω_{sun} is the solar frequency component, α_{pv}, and β_{pv} are the control gains.

Ripple voltage at the battery terminal can be estimated by

$$\Delta V_{batt}(t)=\left[\frac{1}{C_{batt}}\int_0^T\left(I_{batt}(t)-\frac{V_{batt}(t)}{R_{\mathrm{int}}}\right)dt\right]+\gamma\frac{d\Delta(t)}{dt}, \tag{17}$$

where, $\Delta V_{batt}(t)$ is the ripple voltage, C_{batt} is the battery capacitance, $I_{batt}(t)$ is the battery charging current, $V_{batt}(t)$ is the terminal voltage, R_{int} is the internal battery resistance, and γ is the tuning constant.

The duty cycle generated by the actor network is

$$\Delta(t)=\sigma\left(W_a{}^T\Phi(s_t)+b\right)+\lambda\delta(t), \tag{18}$$

where, σ is the activation function, W_a is the actor weight vector, $\Phi(s_t)$ is the feature vector of state s_t, b is the bias, λ is the learning rate, and $\delta(t)$ is TD error.

The reward function used by the ARCT agent is given by

$$r(t)=-\left[\alpha_1e^2(t)+\alpha_2(1-PF)^2+\alpha_3THD^2\right], \tag{19}$$

where, α_1, α_2, and α_3 are weight constants, and PF and THD are the performance metrics. The long-term voltage stability of the battery output is ensured if

$$\lim_{T\to\infty}\frac{1}{T}\int_0^T\left|V_{batt}(t)-V_{ref}\right|dt\le 0.01V_{ref}, \tag{20}$$

where, V_{ref} is the reference terminal voltage.

The critic update includes PV regulation as

$$\nabla_\omega V(s_t)=\nabla_\omega\left(\sum_{j=1}^{n}\omega_j\Phi_j(s_t)+\xi\left|I_{PV}(t)-I_{PV,ref}\right|\right), \tag{21}$$

where, $V(s_t)$ is the critic value, ω_j are weights, $\Phi_j(s_t)$ are features, and ξ is the PV error penalty.

The net energy transferred to the battery is modeled by

$$E_{batt,total}=\int_0^T\left(\eta_{AC}P_{AC}(t)+\eta_{PV}P_{PV}(t)\right)dt-\int_0^T P_{loss}(t)dt, \tag{22}$$

where, η_{AC} and η_{PV} are the efficiencies of AC and PV paths, respectively, P_{AC} and P_{PV} are the input powers, and P_{loss} is the total converter loss. These equations provide theoretical backing to broadly explain the experimental results.

The proposed ARCT controller for SLC is implemented on an FPGA platform to ensure real-time operation and fast adaptability. The control process operates on a discrete-time scale synchronized with the switching frequency of the power converter. The switching stage is driven by the unipolar PWM at switching frequency $f_s = 20$ kHz. The triangular carrier for PWM has a frequency f_s and peak amplitude 1. The duty command $\Delta[k]$ (discrete-time index k) is translated to gate pulses by comparing $\Delta[k]$ with the carrier. The switch is ON when $\Delta[k] > carrier(t)$ and OFF otherwise. The control loop runs at the sampling frequency f_s and the sampling period is 50 μs. All sampled signals are filtered before digitization by a first-order anti-aliasing filter with the cutoff at f_c, which is one-fourth of f_s. Signals on the FPGA are represented in the fixed-point Q1.15 format (16-bit signed) to satisfy the timing and resource constraints.

A. TD Error Formulation

To make the ARCT algorithm explicit, the discrete-time temporal-difference error (TD error) used by the critic is implemented as

$$\delta(k)=r[k]+\gamma V_{\omega(s[k+1])}-V_{\omega(s[k])}, \tag{23}$$

where $\delta[k]$ is the TD error at sample k, $r[k]$ is the scalar reward at sample k, γ is the discount factor, $V_{\omega\,(\cdot)}$ is the critic value function parameterized by weight vector ω, and $s[k]$ is the system state vector at time-step k. The state vector is chosen as follows:

$$s[k] = [i_{L[k]}, V_{R[k]}, V_{SLC[k]}, i_{PV[k]}]^T , \tag{24}$$

where i_L is the measured inductor current, V_R is the rectified DC input (per unit), V_{SLC} is the SLC output/battery terminal voltage, and i_{PV} is the PV current.

B. Reward Function

The actor outputs a continuous duty command from a lightweight neural policy (one hidden layer) and is updated online using the policy-gradient style rule:

$$\theta[k+1] = \theta[k] + \alpha_a \delta(k) \nabla_\theta \pi_\theta (s[k]) , \tag{25}$$

where $\theta[k]$ is the actor parameter vector at the k^{th} step, α_a is the actor learning rate, $\delta[k]$ is the temporal difference (TD) error, $\pi_\theta(s[k])$ is the policy function parameterized by θ, evaluated at state $s[k]$, ∇_θ denotes the gradient with respect to actor parameters.

C. Critic Update

The actor output is saturated to enforce safe switching,

$$\Delta[k] = saturate(\pi_{\theta(s[k]}, \Delta_{\min}, \Delta_{\max}) , \tag{26}$$

where $\Delta_{\min} = 0.15$ and $\Delta_{\max} = 0.85$ in our implementation. The critic is updated using a semi-gradient TD (0) update implemented as follows:

$$\omega[k+1] = \omega[k] + \alpha_c \times \delta(k) \times \nabla_\omega V_{\omega(s[k])} , \tag{27}$$

where α_c is the critic learning rate and $\nabla_\omega V_\omega$ is the gradient of the critic value function.

D. Actor Update

The reward used for online learning is a normalized negative quadratic that balances the current tracking, power quality, and output regulation:

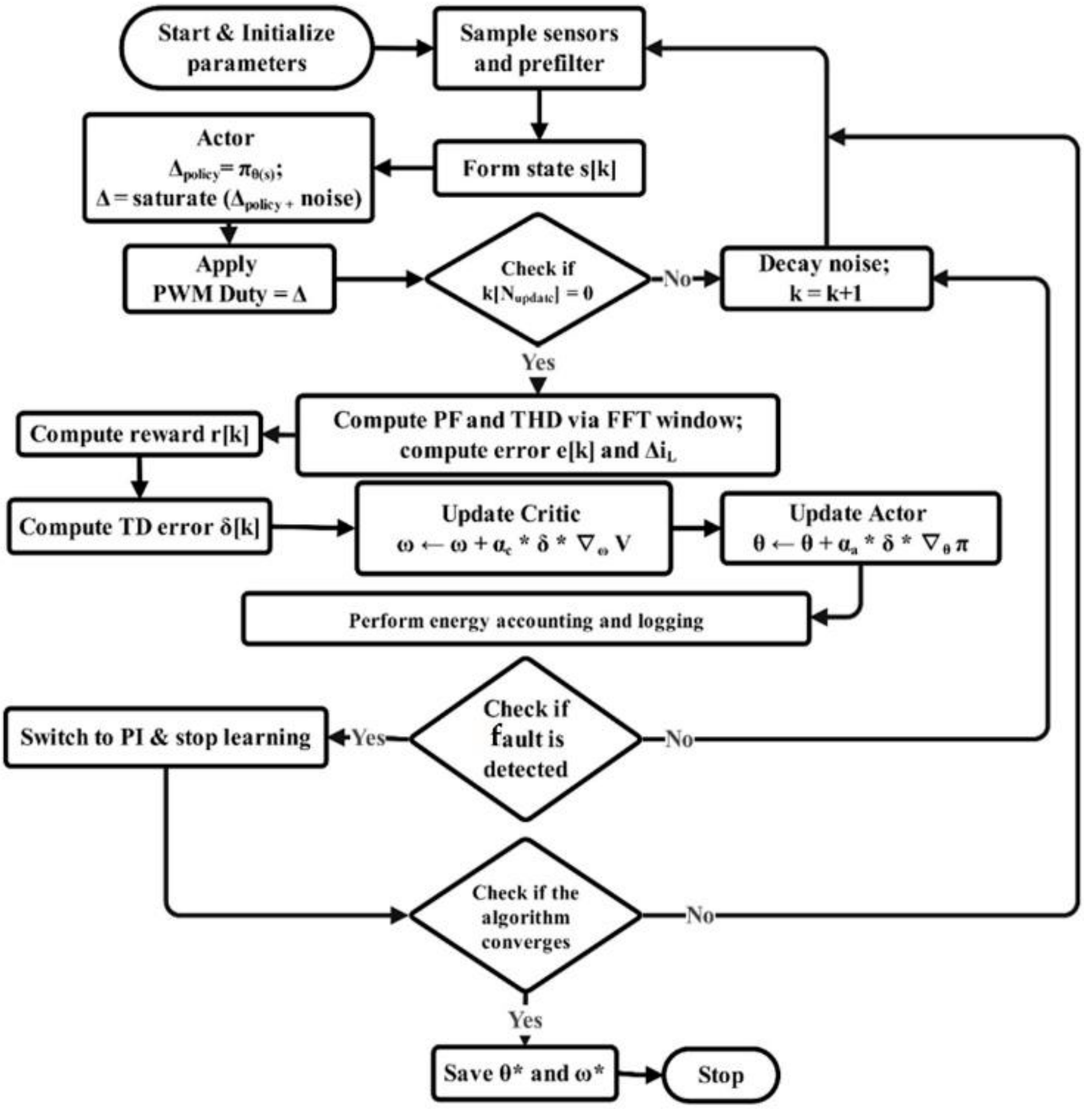

Fig.5. Adaptive reinforcement-based current tracking (ARCT) learning mechanism.

$$r[k] = -[\alpha_1 e^2[k] + \alpha_2(1 - PF[k])^2 + \alpha_3 THD[k]^2 - \\ -\alpha_4 (V_{SLC}[k] - V_{ref})^2 + \alpha_5 \Delta i_{L[k]}{}^2, \quad (28)$$

where $e[k] = i_{L,ref}[k] - i_L[k]$ is the inductor current tracking error, $PF[k]$ is the instantaneous power factor estimate (per unit), $THD[k]$ is the short-time THD estimate (per unit) computed over the last M samples, V_{ref} is the target battery charge voltage, $\Delta i_L[k]$ is the inductor ripple estimate, and $\alpha_1 - \alpha_5$ are scalar reward weights. Short-time THD and PF are computed using an N-sample sliding window FFT on the FPGA host (or on a connected controller) as follows:

$$THD[k] = \frac{\sqrt{\sum_{n=2}^{N_h} I_n{}^2}}{I_1}, \quad (29)$$

$$PF[k] = \frac{\frac{1}{T_\omega} \sum_{t=k-T_\omega+1}^{k} V_R(t) i_R(t)}{\sqrt{\frac{1}{T_\omega} \sum_{t=k-T_\omega+1}^{k} V_R(t)^2} \sqrt{\frac{1}{T_\omega} \sum_{t=k-T_\omega+1}^{k} i_R(t)^2}}, \quad (30)$$

where I_n are harmonic magnitudes of the input current computed from the short window FFT (N_h harmonics used; we use $N_h = 40$), I_1 is the fundamental, and T_ω is the window length in samples. The FFT window uses a Hanning window and energy is computed up to the 40th harmonic to match the IEEE harmonics standard. To limit online computation on the FPGA, the actor is evaluated every control cycle, while the critic weight updates and RMS/FFT-based PF/THD calculations are performed every N_{update} cycles. This reduces resource usage while preserving control responsiveness.

TABLE 2. Learning Hyper-Parameters

Component/Parameter	Specification
Switching frequency (*fs*)	20 kHz
Sampling period (*Ts*)	50 μs
Discount factor (γ)	0.95
Actor learning rate (α_a)	0.01
Critic learning rate (α_c)	0.005
Reward weights	0.5, 0.3, 0.2
PV penalty factor (ξ)	0.1
Duty ratio limits (Δmin, Δmax)	0.1, 0.9

The learning process of the ARCT controller is shown in Fig. 5. The actor network generates the control duty ratio $\Delta(k)$ based on the observed converter state $s(k)$. The critic network evaluates the temporal-difference (TD) error $\delta(k)$.

Fig. 6. View of the designed e-bicycle.

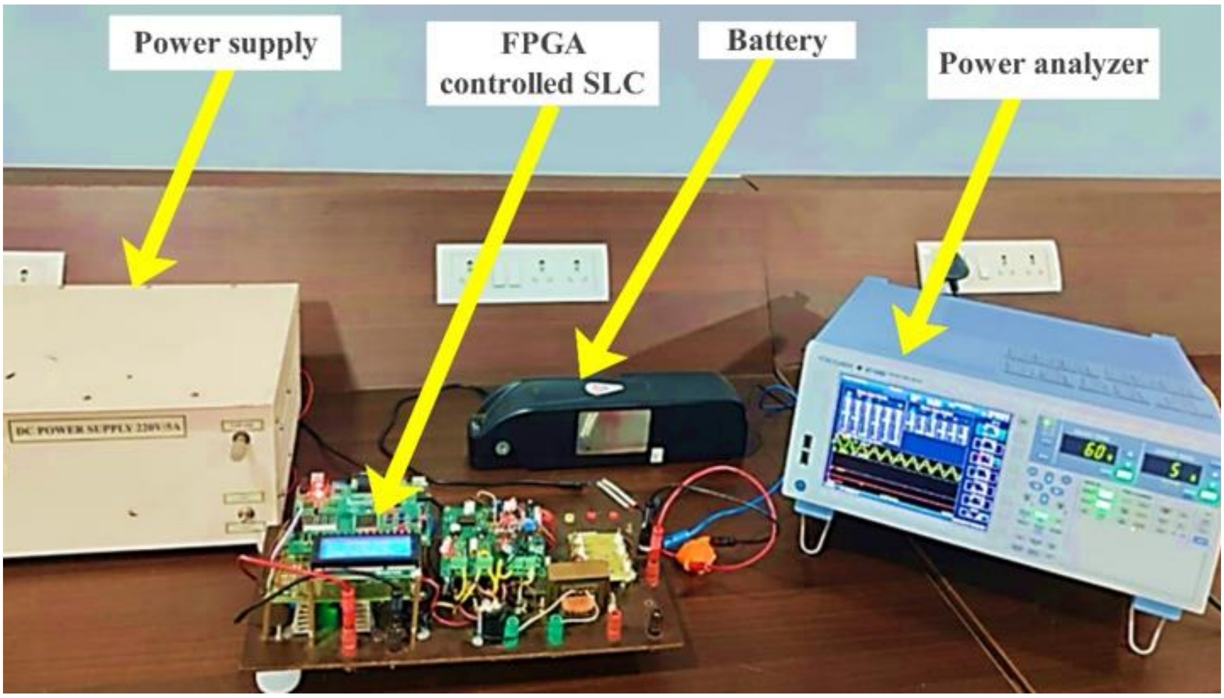

Fig. 7. Test bed of the incorporated super-lift converter.

Both networks update their parameters in real time according to the weight-update rule of Eq. (27) and Eq. (28).

The actor weights θ are adjusted to minimize the error between the reference inductor current and the measured value, while the critic weights ω estimate the long-term performance value.

This cooperative interaction enables adaptive duty-cycle regulation that yields ripple-free current tracking and improved PF correction under varying load and irradiance conditions. The learning hyper-parameters used in our experiments are summarized in Table 2.

VI. EXPERIMENTAL VALIDATION

To validate the performance of the proposed battery charging system using the SLC regulated by the ARCT algorithm, a hardware prototype was developed and tested. Figure 6 shows the designed e-bicycle with a hybrid charging system. The 10.4 Ah lithium-ion battery is placed on the middle frame to obtain the weight distribution balance. A solar panel is placed on the rear carrier with a cabinet design and flexible openings. The SLC and FPGA-based control circuitry are placed inside the solar panel cabinet for compactness. The BLDC hub motor is placed on the rear wheel to ensure smooth and efficient propulsion.

The test bed of the proposed ARCT-based FPGA-controlled SLC is shown in Figure 7. The experimental parameters for the proposed system are listed in Table 3.

The power factor (PF) and total harmonic distortion (THD) of the proposed hybrid e-bicycle charging system were experimentally evaluated using a Yokogawa WT1800E precision power analyzer, which complies with

TABLE 3. Experimental Parameters

Component/Parameter	Specification
AC input voltage	230 V RMS, 50 Hz
Input rectifier	Single-phase full-bridge diode rectifier
Battery capacity	10.4 Ah, 36–42 V lithium-ion battery
SLC inductor *L11 ,L21*	100 µH each
Capacitor *C21, C0*	470 µF / 63 V low-ESR electrolytic capacitors
Power switch	IRF540N MOSFET (100 V, 33 A, RDS(on)_{DS(on)} = 0.044 Ω)
Diodes *D21, D22*	Fast recovery diodes (UF4007 or MUR460 equivalents)
Control platform	FPGA-based custom controller
Sensor interfaces	Hall-effect voltage and current sensors

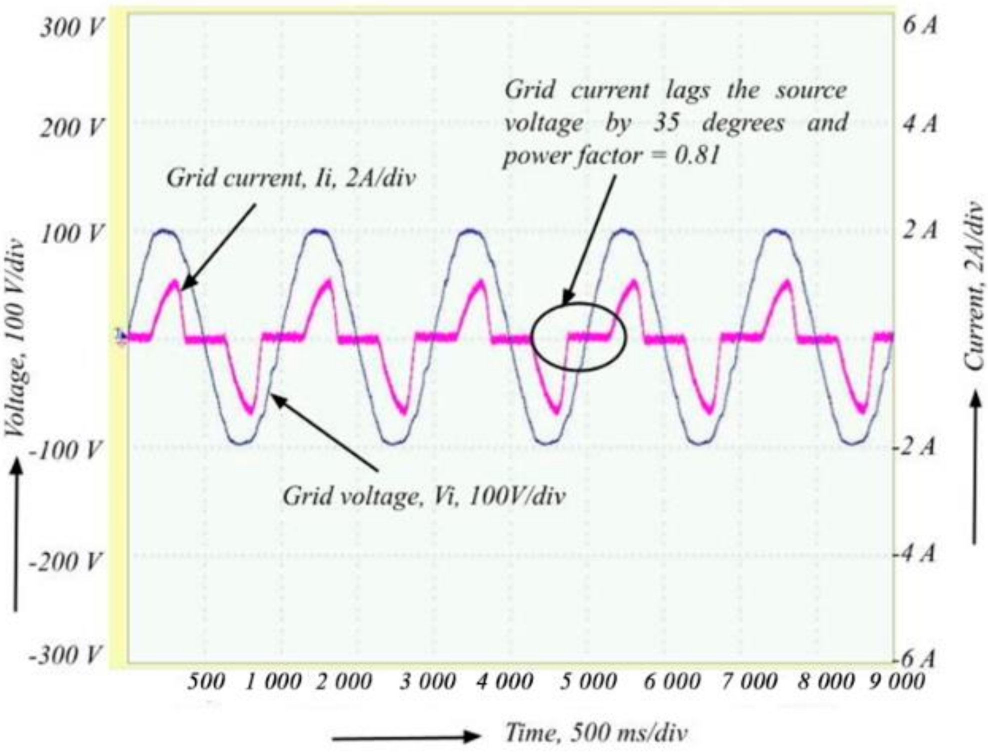

Fig. 8. Supply voltage and current without ARCT.

IEC/IEEE measurement standards. The analyzer was configured with a sampling frequency of 200 kHz and a measurement window synchronized with the fundamental grid frequency (50 Hz). For THD estimation, the Fast Fourier Transform (FFT) method was applied with a Hanning window, and harmonics up to the 40th were

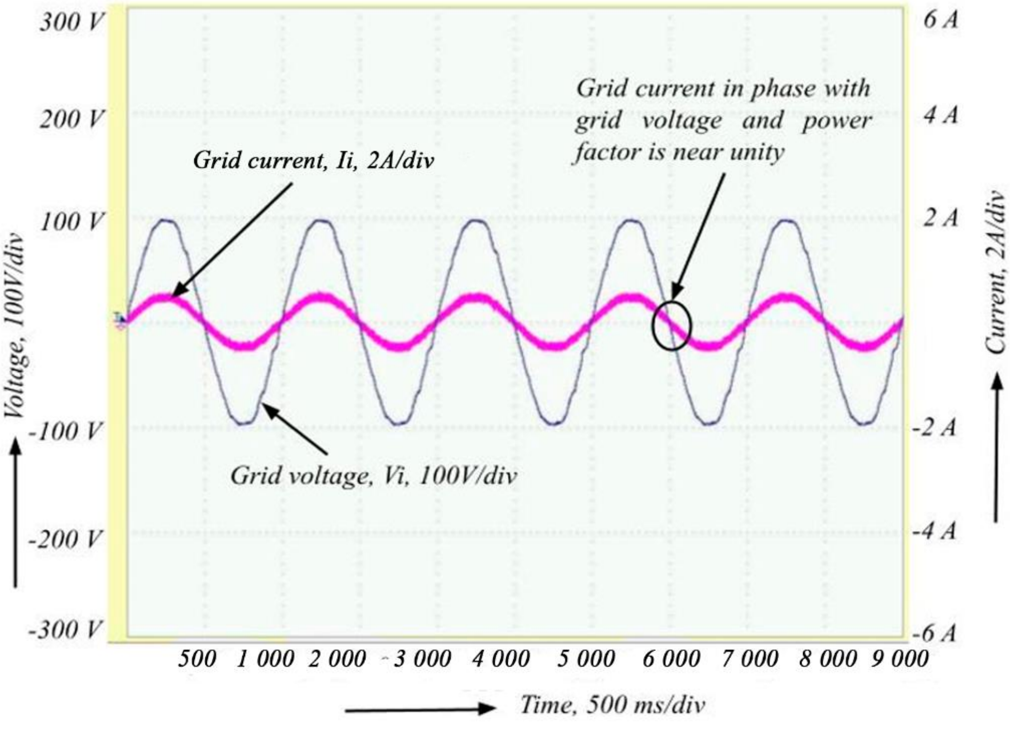

Fig. 9. Supply voltage and current with ARCT.

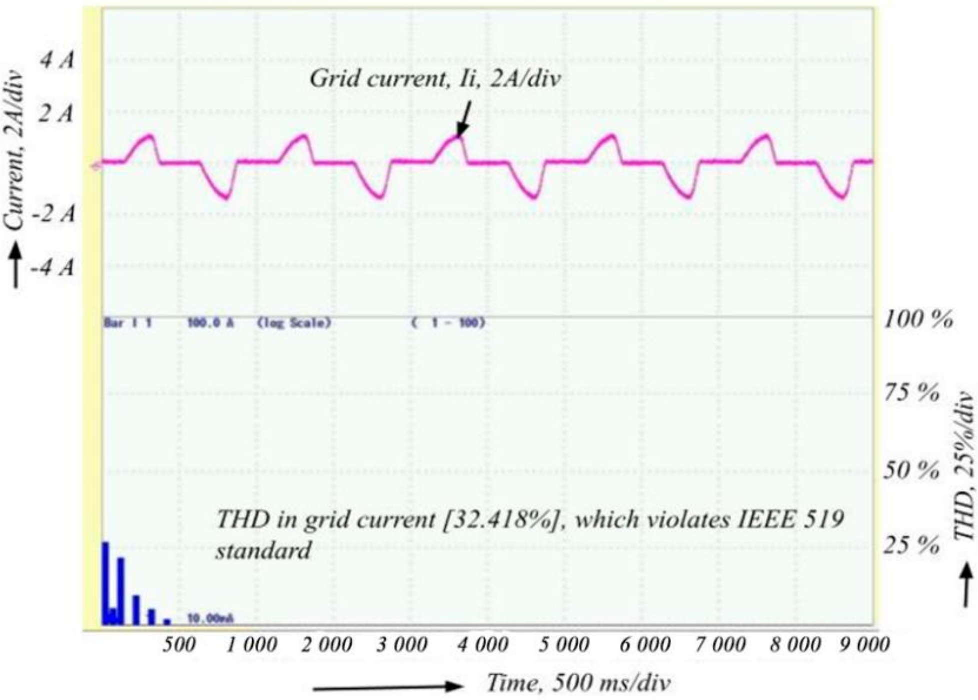

Fig. 10. THD in supply current without ARCT.

TABLE 4. THD Order and Current Without ARCT

Harmonic order	1	3	5	7	9	11	13
Grid current, A	0.2146	0.0565	0.0085	0.0027	0.0009	0.0003	0.0002

considered, as recommended by IEEE Std. 519-2014. The experimental results shown in Fig. 8–20 reveal significant improvements achieved with the aid of the proposed system. Figure 8 represents the supply voltage and current

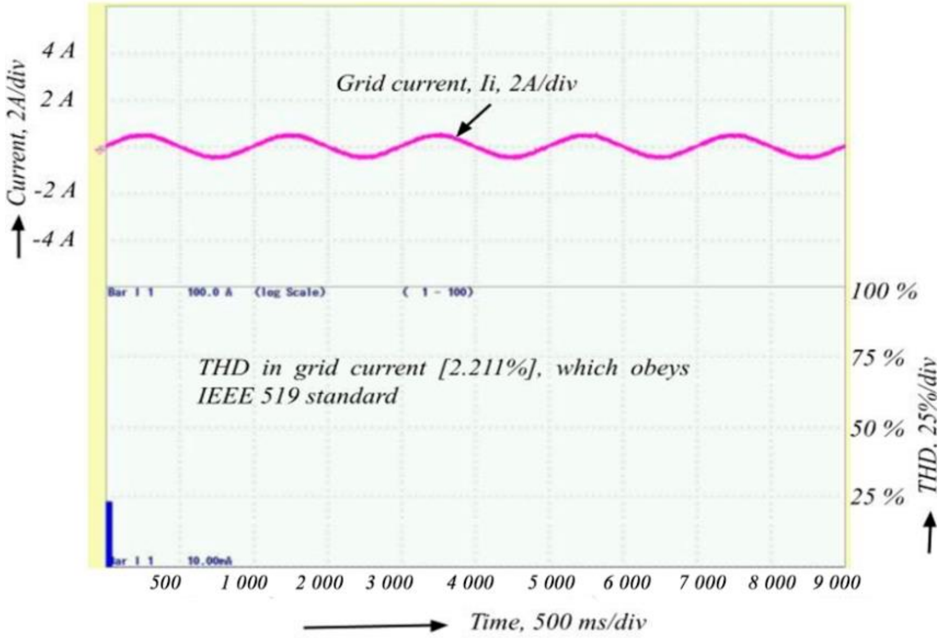

Fig. 11. THD in supply current with ARCT.

TABLE 5. THD Order and Current with ARCT

Harmonic order	1	3	5	7
Grid current, A	0.205	0.0002	0.001	0.001

waveforms during the charging of the battery without ARCT control. Without ARCT, there was a noticeable phase displacement between the current and voltage, indicating a poor power factor.

On the other hand, the waveforms were nearly in phase with the incorporation of ARCT control as shown in Fig. 9. This synchronization effectively enhanced the power factor and reduced the reactive power loss.

Figure 10 shows the Total Harmonic Distortion (THD) of the supply current in the absence of the proposed ARCT control. The harmonic order and the corresponding harmonic current values are summarized in Table 4. The current values up to the 13th harmonic, were measured and presented because the harmonics current was zero for harmonics above the 13th. The THD without ARCT control was 32.418%, which exceeded the acceptable limits set by the IEEE 519 standard.

According to IEEE 519-2014, the allowable current THD limit is 5% at the Point of Common Coupling (PCC). The high THD in the absence of ARCT indicates reduced equipment life and increased power loss. When the proposed ARCT control is implemented, the THD is significantly reduced to 2.211% (as shown in Fig. 11), which complies with the IEEE 519 standard and ensures a better power quality. The harmonic order and the corresponding harmonic current values are summarized in Table 5. The current values up to the 7th harmonic were measured and presented because the harmonics current was zero for harmonics above the 7th. This ensures the proper

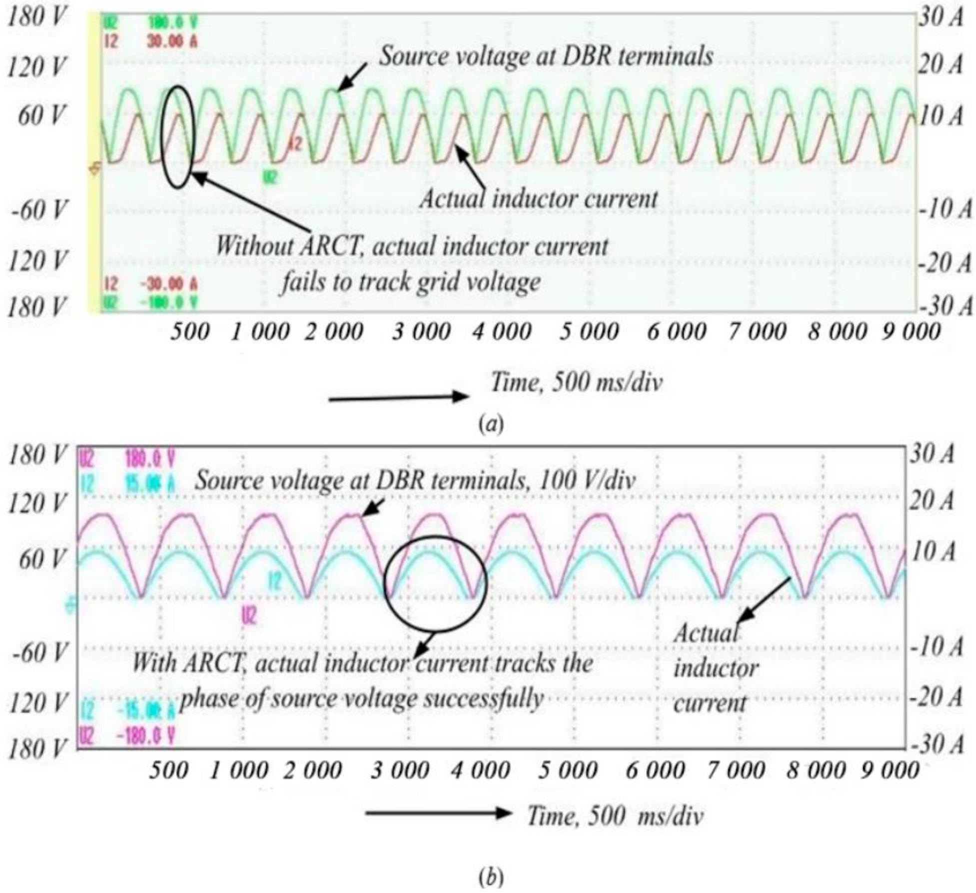

Fig. 12. Actual inductor current and source voltage at DBR terminals (a) without ARCT (b) with ARCT.

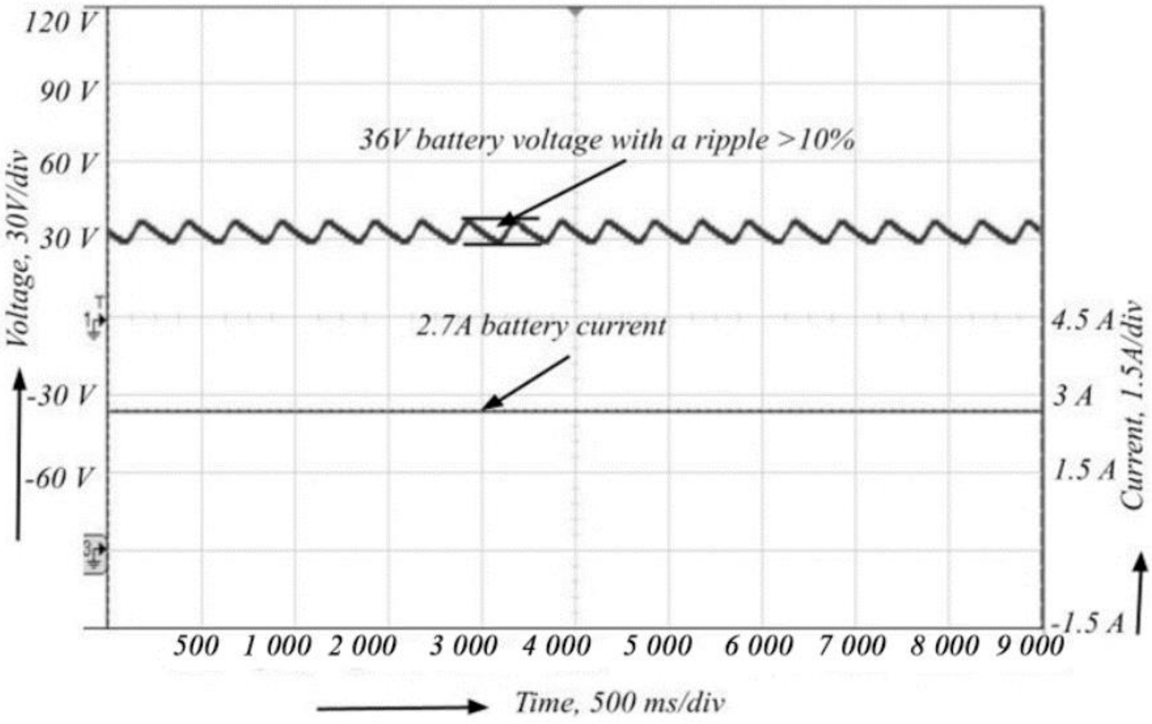

Fig. 13. Voltage and current in battery terminals without ARCT.

alignment of the supply current with the voltage waveform and minimizes harmonic distortions.

Figure 12 presents the waveforms of the source voltage at DBR terminals and actual inductor currents. Without ARCT control, there is a clear deviation of the actual inductor current from the voltage signal, resulting in inefficient current tracking and higher ripples. By contrast, with ARCT control, the actual inductor current closely aligns with the source voltage at DBR terminals, which validates the implementation of the ARCT algorithm leading to improved stability and reduced ripple.

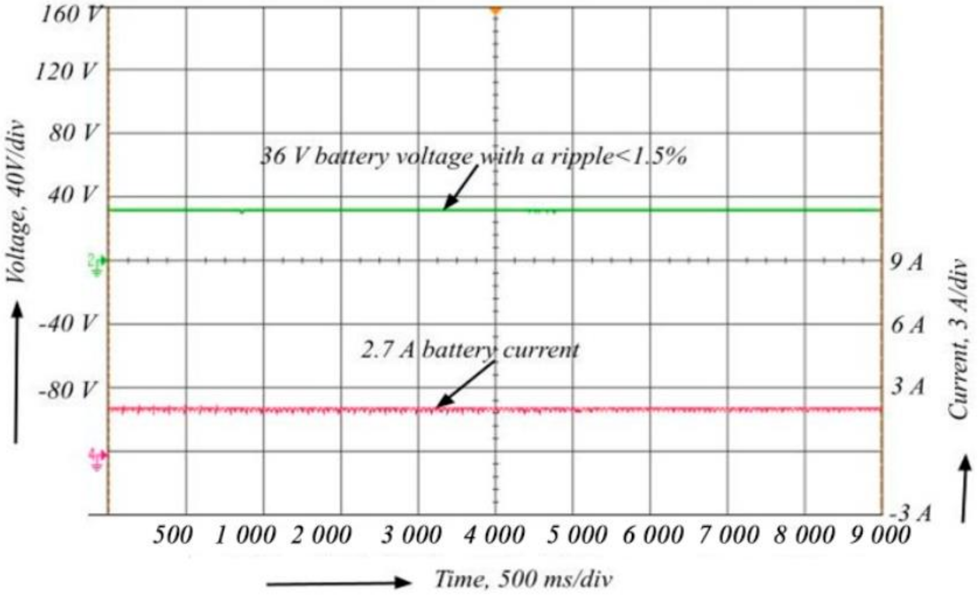

Fig. 14. Voltage and current in battery terminals with ARCT.

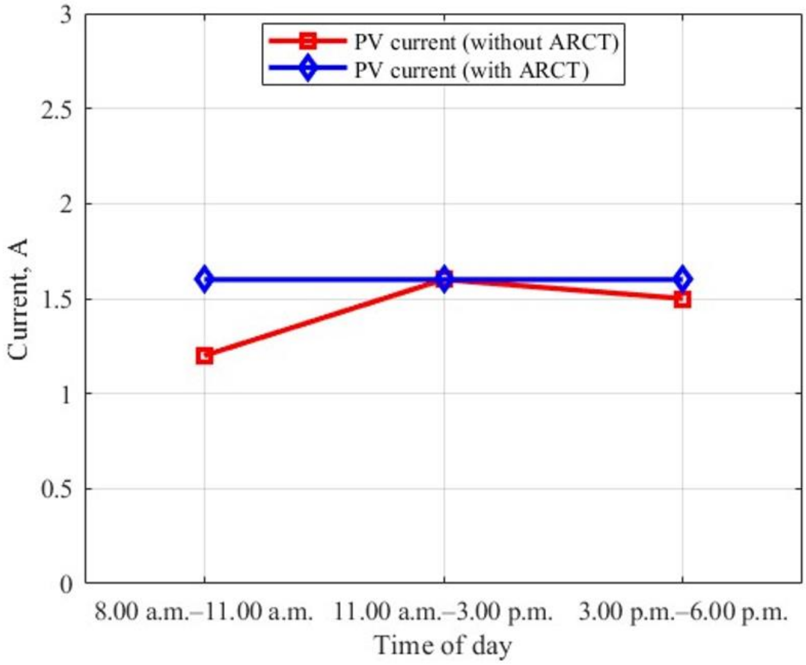

Fig. 16. PV output current with and without ARCT control.

Fig. 13 illustrates the voltage and current profiles at the battery terminals without ARCT control.

In the absence of ARCT control, the voltage at the battery terminals exhibited a ripple exceeding 10%, which compromised the charging process by introducing inefficiencies and potentially degrading the battery over time. The current profile also shows significant fluctuations owing to the high ripple voltage, resulting in uneven charging and reduced battery life. Conversely, with the implementation of ARCT control (Fig. 14), the ripple voltage was significantly reduced to less than 1%, thus emphasizing that harmonic distortion was limited.

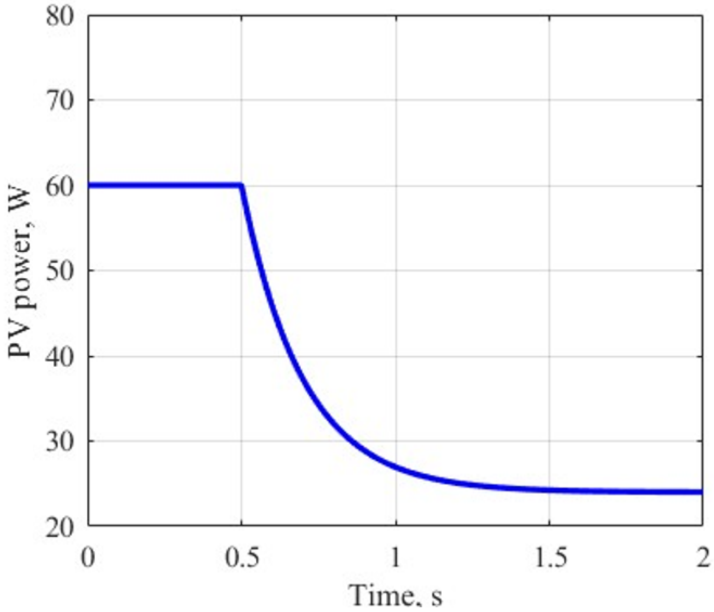

Fig. 17. MPPT dynamic response (1000→400 W/m^2).

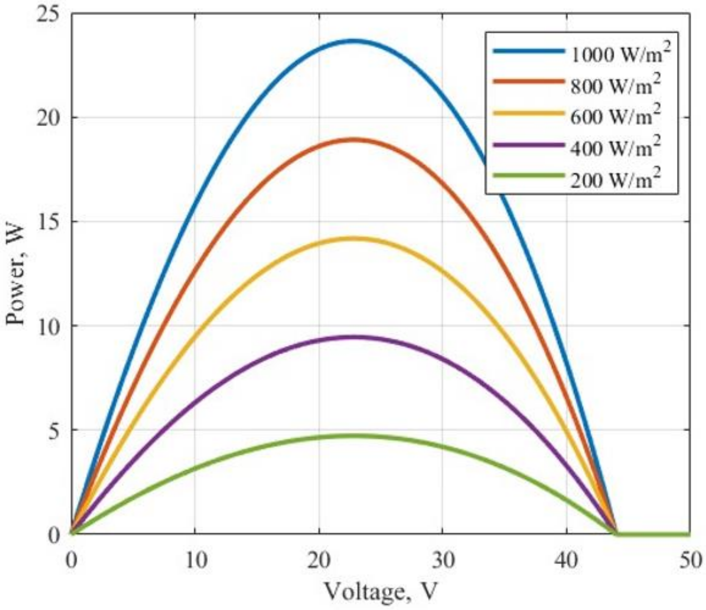

Fig. 18. P-V curves at 25°C.

Figure 15 shows the variability of the PV output voltage over different time ranges of the day, with and without ARCT control.

In the absence of the ARCT, the current oscillated with solar irradiance changes — 1.2 A in the morning (8:00–11:00 a.m.), 1.6 A at noon (11:00 a.m.–3:00 p.m.), and 1.5 A in the late afternoon (3:00–6:00 p.m.). These small oscillations demonstrate a lack of voltage control, with suboptimal current generation under changing sunlight conditions. With the ARCT algorithm, the output current is maintained at 1.6 A over all periods. This stability demonstrates the ARCT's capability to control the duty cycle of the converter and keep the operating point close to optimal, even with changing solar input. The regulated current improves the battery charging profile by providing constant energy, boosting efficiency and charging reliability under realistic outdoor conditions.

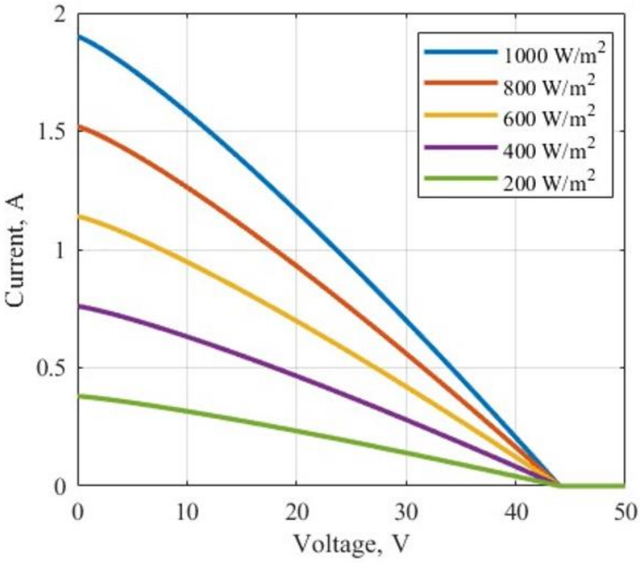

Fig. 19. I-V curves at 25°C.

A 60 W flexible PV module was tested under varying irradiance (200–1000 W/m²) and cell temperature (15°C, 25°C, 45°C). The FPGA implemented an MPPT algorithm with 500 Hz sampling, perturbation step $\Delta V = 0.2$ V, and convergence threshold $|\Delta P|/P < 0.5\%$. In the implemented solar interface, the MPPT is carried out using the Perturb-and-Observe (P&O) algorithm, chosen for its simplicity, fast convergence under slowly varying irradiance, and suitability for FPGA-based real-time execution. At STC (1 000 W/m², 25°C), $V_{mp} = 36.0$ V, $I_{mp} = 1.67$ A, $P_{mp} = 60.1$ W, and $V_{oc} = 44.0$ V. Tracking efficiency remained ≥ 97.8% across all test points, with convergence times < 0.45 s, validating robust real-time operation. At elevated temperature (45°C), V_{mp} dropped to 32.8 V with $P_{mp} = 55.3$ W, while at low temperature (15°C) the maximum output rose to 62.5 W. Dynamic MPPT tests with irradiance step 1000→400 W/m² achieved stable convergence within 0.32 s. The stabilized PV contribution (~1.6 A, ≈ 58 W) consistently extended the e-bicycle mileage by ~15%. The transient response of the PV power under a sudden irradiance drop from 1 000 W/m^2 to 400 W/m² is shown in Fig. 17. The FPGA-based MPPT converges smoothly within 0.32 s, maintaining high stability. This demonstrates the fast adaptability and tracking efficiency of the proposed controller.

Figure 18 illustrates P–V characteristics at 25°C for irradiance ranges of 200–1000 W/m². The pronounced peaks indicate accurate maximum power point recognition across conditions. The proposed MPPT reliably aligns with the true $P_{\max}$, supporting the reported ≥ 97.8%.

The I–V characteristics for different irradiance ranges are shown in Fig. 19. The observed curves displayed the expected current scaling with irradiance and stable open circuit voltage, V_{oc}. These results attest to the realistic PV modeling and the system maintains reliable energy harvesting under variable solar input.

A comparative analysis of the mileage and efficiency of the established e-bicycle under four different working

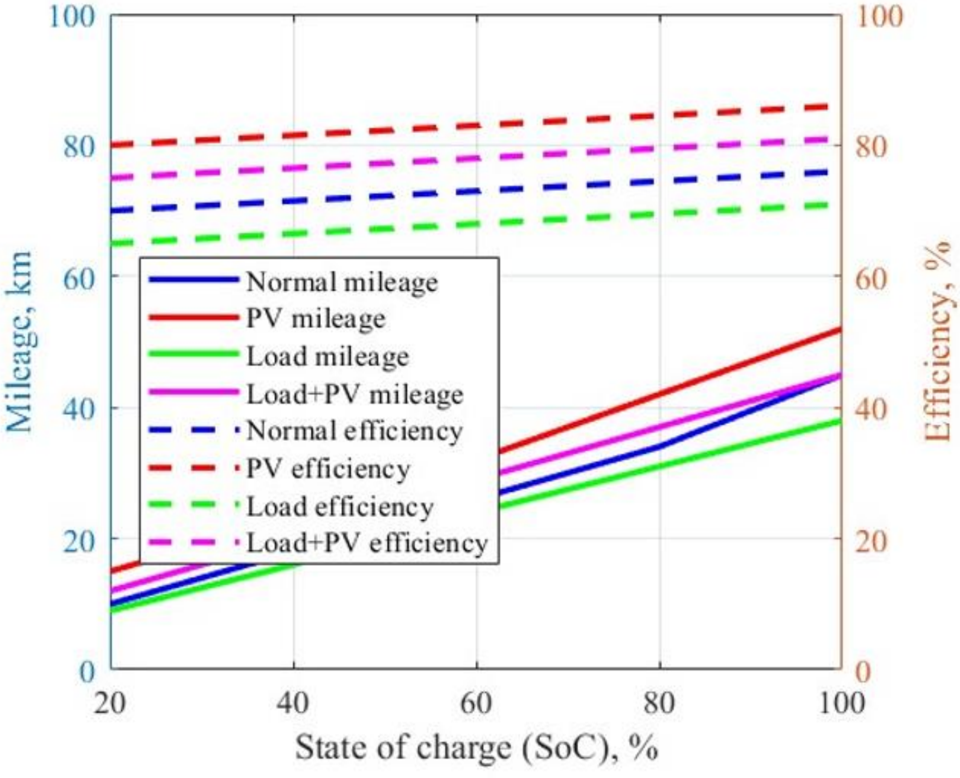

Fig. 20. Mileage and efficiency analysis of e-bicycle.

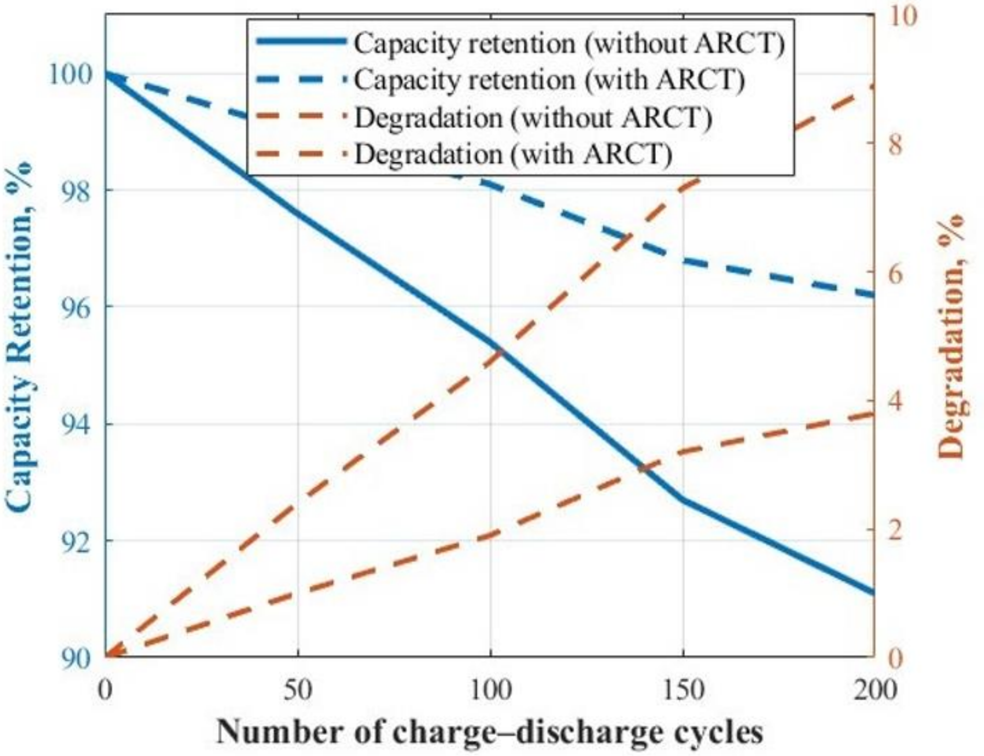

Fig. 21. Battery degradation analysis with and without ARCT control.

conditions, namely, normal operation (battery only), with PV support, loaded with 40 kg, and loaded with PV support, is shown in Fig. 20.

Under normal conditions, the bicycle attained a maximum mileage of 45 km at a 100% SoC. However, the addition of the PV panel increased the mileage to 52 km, authenticating an improvement of nearly 15% in travel range. During the application of 40 kg load, the mileage decreased due to increased power demand, but the presence of PV support partially compensated for this reduction, thus improving overall performance. A similar trend was detected in efficiency, where the PV-assisted modes consistently outperformed the battery-only cases, while the loaded conditions experienced a slight drop due to the increased torque demand. These results suggest that the proposed ARCT and PV integration not only enhances mileage but also withstands higher charging and discharging efficiency, thereby confirming the effectiveness of the designed hybrid e-bicycle system. The design is prone to uncertainties due to sensor tolerance, passive component variations, and environmental variations impacting PV panel output. Small timing delays during FPGA switching and FFT-based THD measurement also cause modest deviations in measured results. The above uncertainties are likely to cause modest effects on the reported results in mileage estimation and power quality indices but do not offset the measured performance enhancements. Future research should address these issues through the implementation of high-grade sensor calibration, adaptive robust control, and real-time uncertainty modeling to further elevate the level of reliability of the design.

To assess the long-term impact of the proposed ARCT-based charging, a battery degradation analysis was performed over 200 charge–discharge cycles of the e-bicycle’s 10-series (10S) NMC lithium-ion pack. Charge–discharge cycling was carried out between 100% and 20% SoC at a discharge current of 3.5 A under controlled ambient conditions of 27°C ± 2 °C. Three individual cells from the pack were additionally monitored to examine stress patterns under conventional charging and ARCT-controlled charging with ripple suppressed below 1.5%. Battery voltage, current, and temperature were recorded using a Keysight digital multimeter, a data logger, and an

TABLE 6. Comparative analysis of the proposed work with the existing works

Parameter	Hysteresis-based control [34]	Average current-mode control [35]	This study
Converter topology	High-gain DC–DC	Integrated 3-phase AC–DC	Super-lift converter (SLC)
Control schema	Modified PI	DSP-based digital PFC control	Adaptive reinforcement-based current tracking (ARCT) using FPGA
Implementation platform	DSP-based controller	Microcontroller	FPGA-based real-time control
Power factor (PF)	0.90	0.998	0.99
Total harmonic distortion (THD)	3.46%	2.87%	2.2%
Ripple in output voltage	~3.5%	~2.87%	< 1.5%
Dynamic response to load variation	Fast but unstable beyond high ripple	Moderate, requires parameter tuning	Fast and adaptive with minimal overshoot
Real-time adaptability	Limited (fixed threshold)	Limited (re-tuning needed)	Self-learning across operating points
Input source	Grid only	Grid only	Grid + flexible solar panel (hybrid source)
Energy backup	None	None	Solar panel backup
Battery charging application	General EV charger	EV on-board charging	E-bicycle (Lightweight mobile application)
Implementation complexity	Simple	Moderate	Higher (but FPGA allows compact execution)

INA219 precision current sensor. The degradation metric was defined as the percentage loss in usable capacity. Figure 21 compares the degradation rates for conventional charging and ARCT-based charging. It is evident that the ARCT-based system kept a more stable charging profile, reducing current ripple and thermal stress on the lithium-ion cells. Subsequently, the cumulative capacity loss after 200 cycles was limited to 3.8%, whereas conventional charging exhibited 8.9% degradation. We attribute this enhancement to the adaptive current tracking and reinforcement-based optimization, which continuously minimized the inductor current error and ensured near-ideal power flow into the battery. The observed difference translated to approximately a 57% reduction in degradation rate, confirming the benefits of the proposed ARCT control in extending battery lifespan.

The comparative analysis in Table 6 shows the improved operation and novelty of the proposed battery charging system in comparison to the two earlier studies.

The comparative analysis highlights that while hysteresis-based control [34] achieved a PF of 0.90 with a higher THD (3.46%) and ripple (~3.5%), and average current-mode control [35] improved the PF to 0.998 with reduced THD (2.87%) and ripple (~2.87%), both remain limited to the grid-only input and lack adaptability. In contrast, the proposed FPGA-based ARCT control on the SLC attained a near-unity PF (0.99), significantly reduced THD (2.2%), and minimal output ripple (<1.5%) with superior dynamic response and self-learning adaptability. Furthermore, by integrating a flexible solar panel input, the system uniquely provides hybrid energy support and mileage extension for lightweight e-bicycle applications, setting it apart from the conventional grid-only EV charger implementations.

VII. CONCLUSION

This study presents the design and experimental validation of a hybrid charging and propulsion system for an electric bicycle that integrates a Super-Lift Converter (SLC) controlled by an FPGA-based Adaptive Reinforcement-Based Current Tracking (ARCT) algorithm. The novelty of this study lies in the first reported application of the ARCT control for an e-bicycle on-board charger. The proposed approach effectively unifies solar and grid-based charging, ensuring uninterrupted operation under stationery and mobility conditions. Without the ARCT, the system had a poor power factor of 0.85 and a total harmonic distortion (THD) of 32.418%. With the ARCT control, the power factor was as high as 0.99 and the input current THD was reduced to 2.211%. The output ripple voltage was maintained within 1.5% peak-to-peak, making the battery safe for charging. The proposed FPGA-based implementation enabled real-time control of the SLC, with the actor-critic algorithm dynamically varying the duty cycle to reduce the current tracking error. Furthermore, the regulated photovoltaic output enabled consistent solar-assisted charging, contributing to a 15% increase in battery-supported mileage. The system successfully charged the battery while providing the grid compliance and ripple-free output, establishing the suitability of ARCT-controlled SLCs for compact and smart electric vehicle charging stations. Although the proposed hybrid charging system delivers optimized performance, certain practical limitations remain. The FPGA experiences computational loads at high sampling rates, while sensor tolerances and temperature-dependent passive component variations can affect learning stability. Moreover, scalability to higher-power electric vehicles will require thermal redesign and enhanced switch ratings, providing clear directions for future work.

ACKNOWLEDGMENT

This work was supported by Centre for Sustainable Development, B.S.Abdur Rahman Crescent Institute of Science and Technology, Chennai, India under Crescent Seed Money Project Scheme (Grant No. CSD/SMPS/2023/P1/04).

REFERENCES

[1] T. Myateg, V. Lyubchenko, O. Atamanova, S. Yurkov, E. Mogilenko, “The Influence of electric vehicle charging stations on the quality of power supply to the consumer in Novosibirsk 10/0.4 KV electrical networks,” *Energy Syst. Res.*, vol. 6, no. 2, pp. 62–74, 2023. DOI: 10.25729/esr.2023.02.0007.

[2] L. Stilo, H. Lugo, D. S. Velandia, P. P. Conway, A. A. West, “Personalised controller strategies for next generation intelligent adaptive electric bicycles,” *IEEE Trans. Intell. Transp. Syst.*, vol. 22, no. 12, pp. 7814–7825, 2021. DOI: 10.1109/TITS.2020.3009400.

[3] Y. Li, J. Hu, F. Chen, S. Liu, Z. Yan, Z. He, “A new-variable-coil-structure-based IPT system with load-independent constant output current or voltage for charging electric bicycles,” *IEEE Trans. Power Electron.*, vol. 33, no. 10, pp. 8226–8230, 2018. DOI: 10.1109/TPEL.2018.2812716.

[4] M. Corno, D. Berretta, P. Spagnol, S. M. Savaresi, “Design, control, and validation of a charge-sustaining parallel hybrid bicycle,” *IEEE Trans. Control Syst. Technol.*, vol. 24, no. 3, pp. 817–829, 2016. DOI: 10.1109/TCST.2015.2473821.

[5] G. Suri, S. Onori, “A control-oriented cycle-life model for hybrid electric vehicle lithium-ion batteries,” *Energy*, vol. 96, pp. 644–653, 2016. DOI: 10.1016/j.energy.2015.11.075.

[6] R. C. Hsu, C. T. Liu, D. Y. Chan, “A reinforcement-learning-based assisted power management with QoR provisioning for human-electric hybrid bicycle,” *IEEE Trans. Ind. Electron.*, vol. 59, no. 8, pp. 3350–3359, 2012. DOI: 10.1109/TIE.2011.2141092.

[7] M. Guarisco, F. Gao, D. Paire, “Autonomy and user experience enhancement control of an electrically assisted bicycle with dual-wheel drive,” *IEEE Trans. Ind. Appl.*, vol. 53, no. 2, pp. 1476–1484, 2017. DOI: 10.1109/TIA.2016.2617299.

[8] R. Mai, Y. Chen, Y. Li, Y. Zhang, G. Cao, Z. He, “Inductive power transfer for massive electric bicycles charging based on hybrid topology switching with a single inverter,” *IEEE Trans. Power Electron.*, vol. 32, no. 8, pp. 5897–5906, 2017. DOI: 10.1109/TPEL.2017.2654360.

[9] S. Kuznetsova, V. V. Khanaev, “Alternative possibilities of using electric cars in Siberia,” *Energy Syst. Res.*, vol. 5, no. 3, pp. 50–56, 2022. DOI: 10.38028/esr.2022.03.0007.

[10] Y. Chen, Z. Kou, Y. Zhang, Z. He, R. Mai, G. Cao, “Hybrid topology with configurable charge current and charge voltage output-based WPT charger for massive electric bicycles,” *IEEE J. Emerg. Sel. Top. Power Electron.*, vol. 6, no. 3, pp. 1581–1594, 2018. DOI: 10.1109/JESTPE.2017.2782269.

[11] A. Triviño-Cabrera, J. M. Gonzalez-Gonzalez, J. A. Aguado, “Design and implementation of a cost-effective wireless charger for an electric bicycle,” *IEEE Access*, vol. 9, pp. 85277–85288, 2021. DOI: 10.1109/ACCESS.2021.3084802.

[12] A. A. Patoli, G. Fortino, “FPGA-based system implementation of IEEE 1588 precision time protocol: A review,” *IEEE Sens.J.*, vol. 25, no. 11, pp. 18624–18642, 2025. DOI: 10.1109/JSEN.2025.3557277.

[13] Y. Zhou et al., “Online inductance identification and FPGA-based real-time digital control design for APF,” *IEEE Trans. Power Electron.*, vol. 38, no. 2, pp. 1549–1561, 2023. DOI: 10.1109/TPEL.2022.3209893.

[14] R. N. Tripathi, “Dead-time evaluation with switching frequency for GaN-based non-inverting buck-boost DC–DC converter using FPGA-based high-frequency control,” *IEEE J. Emerg. Sel. Top. Power Electron.*, vol. 12, no. 1, pp. 496–504, 2024. DOI: 10.1109/JESTPE.2023.3344458.

[15] Z. Li, J. Xu, K. Wang, P. Wu, G. Li, “FPGA-based real-time simulation for EV station with multiple high-frequency chargers based on C-EMTP algorithm,” *Prot. Control Mod. Power Syst*., vol. 5, no. 1, 2020. DOI: 10.1186/s41601-020-00171-x.

[16] F. L. Luo, H. Ye, *Advanced DC/DC converters*. New York, USA: CRC Press, 2003. DOI: 10.1201/9780203492925.

[17] B. Faridpak, M. Farrokhifar, M. Nasiri, A. Alahyari, N. Sadoogi, “Developing a super-lift Luo-converter with integration of buck converters for electric vehicle applications,” *CSEE J. Power Energy Syst*., vol. 7, no. 4, pp. 811–820, 2020. DOI: https://doi.org/10.17775/CSEEJPES.2020.01880.

[18] S. Mahdizadeh, H. Gholizadeh, S. A. Gorji, “A power converter based on the combination of Cuk and positive output super lift Lou converters: Circuit analysis, simulation and experimental validation,” *IEEE Access*, vol. 10, pp. 52899–52911, 2022. DOI: 10.1109/ACCESS.2022.3175892.

[19] F. Ghasemi, M. R. Yazdani, M. Delshad, “Step-up DC-DC switching converter with single switch and multi-outputs based on Luo topology,” *IEEE Access*, vol. 10, pp. 16871–16882, 2022. DOI: 10.1109/ACCESS.2022.3150316.

[20] M. Mahdavi, M. Shahriari-Kahkeshi, N. R. Abjadi, “An adaptive estimator-based sliding mode control scheme for uncertain POESLL converter,” *IEEE Trans. Aerosp. Electron. Syst*., vol. 55, no. 6, pp. 3551–3560, 2019. DOI: 10.1109/TAES.2019.2908272.

[21] C. Y. Chan, “Adaptive modified current-mode control of a hybrid high voltage gain converter,” *IEEE Trans. Circuits Syst. II Express Briefs*, vol. 71, no. 1, pp. 360–364, 2024. DOI: 10.1109/TCSII.2023.3303467.

[22] X. Jin, J. Qin, S. Member, “Adaptive perturbation rejection control for a class of converter systems with circuit realization,” *IEEE Trans. Syst. Man, Cybern. Syst*., vol. 52, no. 1, pp. 4740–4750, 2022. DOI: 10.1109/TSMC.2021.3103066.

[23] D. Weber, M. Schenke, O. Wallscheid, “Steady-state error compensation for reinforcement learning-based control of power electronic systems,” *IEEE Access*, vol. 11, pp. 76524–76536, 2023. DOI: 10.1109/ACCESS.2023.3297274.

[24] A. Ahmadian, K. Sedghisigarchi, R. Gadh, “Empowering dynamic active and reactive power control: A deep reinforcement learning controller for three-phase grid-connected electric vehicles,” *IEEE Access*, vol. 12, pp. 66068–66084, 2024. DOI: 10.1109/ACCESS.2024.3396449.

[25] Y. Wan, Q. Xu, T. Dragicevic, “Reinforcement learning-based predictive control for power electronic converters,” *IEEE Trans. Ind. Electron*., vol. 72, no. 5, pp. 5353–5364, 2025. DOI: 10.1109/TIE.2024.3472299.

[26] D. Jakobeit, M. Schenke, O. Wallscheid, “Meta-reinforcement-learning-based current control of permanent magnet synchronous motor drives for a wide range of power classes,” *IEEE Trans. Power Electron*., vol. 38, no. 7, pp. 8062–8074, 2023. DOI: 10.1109/TPEL.2023.3256424.

[27] D. Lee, B. Kim, S. Kwon, N. D. Nguyen, M. Kyu Sim, Y. Il Lee, “Reinforcement learning-based control of DC-DC buck converter considering controller time delay,” *IEEE Access*, vol. 12, pp. 118442–118452, 2024. DOI: 10.1109/ACCESS.2024.3448535.

[28] C. Wei, Z. Zhang, W. Qiao, L. Qu, “Reinforcement-learning-based intelligent maximum power point tracking control for wind energy conversion systems,” *IEEE Trans. Ind. Electron*., vol. 62, no. 10, pp. 6360–6370, 2015. DOI: 10.1109/TIE.2015.2420792.

[29] B. Huangfu, C. Cui, C. Zhang, L. Xu, “Learning-based optimal large-signal stabilization for DC/DC boost converters feeding CPLs via deep reinforcement learning,” *IEEE J. Emerg. Sel. Top. Power Electron*., vol. 11, no. 6, pp. 5592–5601, 2023. DOI: 10.1109/JESTPE.2022.3189078.

[30] Y. Wan, Q. Xu, T. Dragicevic, “Safety-enhanced self-learning for optimal power converter control,” *IEEE Trans. Ind. Electron*., vol. 71, no. 11, pp. 15229–15234, 2024. DOI: 10.1109/TIE.2024.3363759.

[31] R. Muduli, D. Jena, T. Moger, “Application of reinforcement learning-based adaptive PID controller for automatic generation control of multi-area power system,” *IEEE Trans. Autom. Sci. Eng*., vol. 22, pp. 1057–1068, 2025. DOI: 10.1109/TASE.2024.3359219.

[32] G. M. Mustafa, S. I. Gusev, “Active filters for standard-compliant power quality in electrical networks,” *Energy Syst. Res*., vol. 7, no. 1, pp. 51–65, 2024. DOI: 10.25729/esr.2024.01.0006.

[33] S. S. Sayed, A. M. Massoud, “Review on state-of-the-art unidirectional non-isolated power factor correction converters for short-/long-distance electric vehicles,” *IEEE Access*, vol. 10, pp. 11308–11340, 2022. DOI: 10.1109/ACCESS.2022.3146410.

[34] M. R. Haque, K. M. A. Salam, M. A. Razzak, “A modified PI-controller based high current density DC-DC converter for EV charging applications,” *IEEE Access*, vol. 11, pp. 27246–27266, 2023. DOI: 10.1109/ACCESS.2023.3258181.

[35] J. Liu, C. S. Wong, Z. Li, X. Jiang, K. H. Loo, “An integrated three-phase AC-DC wireless-power-transfer converter with active power factor correction using three transmitter coils,” *IEEE Trans. Power Electron*., vol. 38, no. 6, pp. 7821–7835, 2023. DOI: 10.1109/TPEL.2023.3238877.

[36] X. Huang, X. Ruan, L. Zhang, F. Liu, “Second harmonic current reduction schemes for DC-DC converter in two-stage PFC converters,” *IEEE Trans. Power Electron*., vol. 37, no. 1, pp. 332–343, 2022. DOI: 10.1109/TPEL.2021.3099170.

Shajini G Inba Kani is currently a Research Scholar at B.S. Abdur Rahman Crescent Institute of Science and Technology, Chennai, and serves as an Assistant Professor with the Department of Electrical and Electronics Engineering at Dhaanish Ahmed College of Engineering, Chennai. She obtained her Bachelor of Engineering (B.E.) degree in 2008 and Master of Engineering (M.E.) degree in 2011 from Anna University. With a strong academic background and over a decade of teaching experience, her research interests focus on power electronics and electric vehicle technology, particularly in the areas of energy management and converter design for sustainable mobility solutions.

P. Elangovan is currently an Assistant Professor with the Department of Electrical and Electronics Engineering at B.S. Abdur Rahman Crescent Institute of Science and Technology, Chennai. He received all his academic degrees from Anna University, including the B.E. in Electrical and Electronics Engineering (2007), the M.E. in Power Electronics and Drives (2011), and the Ph.D. in Electrical Engineering (2017). With over 15 years of academic and research experience, he specializes in power electronics, electric vehicles, and embedded systems. He has guided several postgraduate and doctoral scholars, with research interests focusing on advanced DC-DC converter topologies, high-gain converters, predictive control strategies for power factor correction, and sustainable energy management systems for electric mobility. Dr. Elangovan has published extensively in leading international journals and conferences and is an active member of IEEE. He also plays a key role in organizing technical events, mentoring students, and facilitating industry-academia collaborations. His contributions extend to curriculum development, consultancy, and innovation in engineering education. Through his continued commitment to research excellence and academic leadership, he is a major contributor to the advancement of power electronics and sustainable mobility technologies in India.

Drone Cargo Airships for Energy Supply (on the Example of the Irkutsk Region)

S.P. Popov[1,*], D.V. Maksakova[1]

[1] Melentiev Energy Systems Institute of Siberian Branch of Russian Academy of Sciences, Irkutsk, Russia

***Abstract* — The communities along the shores of Lake Baikal currently rely on firewood, coal, and petroleum products to generate thermal and electric energy. However, a large proportion of inefficient and outdated electric and thermal energy generation equipment compounds the negative environmental impact of energy facilities in the area. The study explores the possibility of improving the environmental situation through the use of liquefied natural gas. Given the inaccessibility of these territories, the potential for using airships to deliver fuel is examined. A comparative analysis of several logistics schemes for the delivery of liquefied natural gas is carried out. The findings reveal that the use of airships for power supply to new settlements in isolated and hard-to-reach areas of the Central Ecological Zone of the Baikal Natural Territory is preferable to the organization of multimodal transportation. In conclusion, we recommend considering the possibility of creating a pilot industrial test site in the Irkutsk region to accelerate the commercialization of unmanned cargo airship technologies.**

***Index Terms* — drone cargo airship, liquefied natural gas, isolated and hard-to-reach areas.**

I. INTRODUCTION

Lake Baikal is a natural site of global significance. To protect this invaluable resource, Federal Law No. 94-FZ “On Protection of Lake Baikal” was enacted on May 1, 1999. This legislation defines the ecological zoning of the Baikal Natural Territory (BNT), which is confined solely to the territory of the Russian Federation [1, 2]. Around 2.5 million people live in this area.

The Central Ecological Zone of the Baikal Natural Territory (CEZ BNT) is a coastal area of Lake Baikal with special conditions for ecological, social, and economic development. The CEZ BNT covers almost 90 thousand km^2 (including more than 31 thousand km^2 of lake water area), or 23% of the entire BNT. Table 1 shows, that the specially protected natural areas, including nature reserves, wildlife sanctuaries, and national parks, encompass 27 percent of the CEZ territory. The rest of the area is populated and economically engaged, featuring a tourism industry that is swiftly on the rise.

The World Natural Heritage Site “Lake Baikal” [4, 5] represents the core of the CEZ. Its total area is 88 thousand km^2, of which 31.5 thousand km^2 represents the water surface of Lake Baikal, and 19 thousand km^2 is the territory of three nature reserves (Baikalo-Lensky, Baikalsky, and Barguzinsky) and three national parks (Pribaikalsky,

TABLE 1. Structure of the CEZ BNT, %

Categories	Subject of the Russian Federation		Total CEZ BNT
	Irkutsk region	Republic of Buryatia	
Reserves	7	6	13
Wildlife sanctuaries	0.1	4	5
National parks	5	4	9
Other areas, including the water area of Lake Baikal	23.5	49.7	73

Note: Compiled from [3].

---

[*] Corresponding author.
E-mail: popovsp@isem.irk.ru

DOI: 10.25729/esr.2025.04.0010

Received September 17, 2025. Revised November 5, 2025. Accepted November 10, 2025. Available online December 29, 2025.

Zabaikalsky, and partly Tunkinsky). Five urbanized areas were excluded from the Lake Baikal World Natural Heritage Area. These are the towns of Baikalsk, Slyudyanka, and Kultuk in the Irkutsk Region; the towns of Babushkin and Severobaikalsk in the Republic of Buryatia [6].

Reserves and sanctuaries need a system for monitoring the health of the biosphere, observing weather phenomena, as well as for analyzing the quality and composition of the atmospheric and aquatic environments. Today's scientific activities require reliable power supply for buildings and for delivery of cargo, while ensuring that the environmental footprint on the protected area remains minimal.

"The main function of the CEZ BNT is to preserve the unique ecological system of Lake Baikal and to prevent negative impacts of economic and other activities on its health." At the same time, "within the boundaries of the zone ***it is prohibited to carry out*** *harmful types of industrial production, industrial extraction of natural resources, as well as the* ***construction activities not related to the functioning of existing*** *residential and other social* ***facilities****, national parks, and special economic zones." In addition,* ***the ban is also imposed on*** *"...the movement and parking of vehicles outside roads with a hard surface, the* ***establishment of*** *petrol stations,* ***fuel and lubricant depots****..."* [7].

In fact, the legislators prohibit the development of research and tourism infrastructure in the CEZ BNT outside existing settlements, and even more, they outlaw the establishment of new points for scientific, aesthetic, and educational observations of the natural environment of Lake Baikal.

The analysis of the interaction between man and nature at Lake Baikal is essential not only to improve the living conditions of people inhabiting its shores but also to reduce the anthropogenic impact, with the energy industry being one of its major contributors. At the same time, it is crucial to recognize that prohibiting tourists from visiting Lake Baikal, as well as hindering the socio-economic development of existing communities is simply impossible.

It is vital to create and maintain decent living, working, and recreational conditions for people to study and contemplate the majesty of this miracle of nature, to educate humanity about the most effective methods and approaches to preserve our common home, the ecosystem of the Earth. The local population, visitors, temporary residents, businesses, authorities in the Irkutsk Region and the Republic of Buryatia, as well as the Government of the Russian Federation share a collective responsibility for minimizing human impact on the ecosystem of Lake Baikal, especially its CEZ, limited only to the current technological level of civilization development.

A. Energy Supply to Isolated and Hard-to-Reach Areas

Monitoring the ecosystem of CEZ BNT [8, 9] aims to find ways of sustainable development of humanity and requires creating new communities and scientific observation stations on this territory. Meeting modern standards of living and working in these communities, including the availability of transportation services, requires the establishment of so-called "green" energy supply infrastructure in isolated and hard-to-reach areas (IHRA). The IHRA within the Central Ecological Zone of the Baikal Natural Territory (IHRA CEZ BNT) should become a world-class model for minimizing the impact of the energy services consumed (energy supply to buildings and fuel supply for vehicles) on the natural environment of Lake Baikal.

Currently, the settlements located within the CEZ BNT utilize firewood, coal, and petroleum products as fuels for heat and electricity generation. Petroleum products (including motor fuels) are widely used for all types of transportation across Lake Baikal and its catchment area, leading to detrimental effects on human health and the environment. This negative impact of energy facilities, including vehicles, is aggravated by numerous inefficient and outdated electricity and heat generation facilities still in operation.

The transportation (logistics) system is the basis for establishing energy infrastructure, as it ensures the supply of energy resources and other vital cargoes necessary for daily life and research activities in the CEZ BNT, benefiting both the residents (permanent and/or temporary) and the researchers. In particular, some of the "green" energy resources – natural gas (methane) and electricity – can be delivered by specialized forms of energy transportation (pipelines and power lines). The construction of linear transportation infrastructure, however, raises serious concerns regarding its unacceptable impact on the ecosystem [10].

Local renewable energy resources, such as biomass, energy from watercourses, wind, and solar radiation offer a promising alternative to conventional energy carriers that require delivery. However, the construction of facilities for power generation from Renewable Energy Sources (RES) and its transmission, i.e., cables and overhead power lines, disrupts ecosystem, due to considerable distances between the locations of settlements (energy consumption centers) and the optimal sites for RES.

B. Necessity and Feasibility of Airship LNG and Cargo Transportation

Previously, some researchers came to the conclusion that the most radical solution to reduce the energy-related environmental pollution in remote and inaccessible areas in the eastern and Arctic regions of Russia, including the CEZ BNT, in the case of the lack of renewable energy, is the introduction of gaseous fuel into the energy mix [11–22].

The modern energy supply system for stationary and mobile consumers of energy services in the CEZ BNT should be based on the most “environmentally friendly” or “green” energy carriers. At present, these are electricity and gaseous fuels.

The IHRA definition implies that electricity is generated at the location of final energy consumption.

Given the construction cost and the environmental impact of transmission lines in the CEZ BNT, a reliable, environmentally friendly, and cost-effective energy supply in IHRA could be developed using imported liquefied natural gas (LNG).

The cargo delivery to the settlements in the territory under consideration is complicated by the lack of motorways and equipped berths. The challenges of multimodal transportation of passengers and cargo are aggravated by the factor of sharply continental climate, which determines the seasonal nature of water transportation. It is obvious that the construction of motorways in inaccessible areas is impossible under the stringent regulations established for the CEZ BNT by the legislative bodies of the country.

The transportation infrastructure should be able to ensure the delivery of sufficiently large (in terms of weight and dimensions) energy equipment and a large number of building materials (including the materials for RES and for the operation of energy facilities), i.e., year-round availability of fuel, spare parts, and materials. At the same time, the negative environmental impact should be minimized at all stages of their life cycle.

Air freight is extremely expensive, but in the virtually unpopulated mountainous landscape of the western shore of Lake Baikal, it may be the only mode of transportation that can ensure the construction and fuel delivery with minimal impact on Lake Baikal's unique ecosystem [23, 24].

An in-depth analysis of problems related to IHRA energy supply revealed a strong correlation between the lack of qualified personnel to operate high-tech energy equipment and the necessity to replace physically and morally obsolete energy infrastructure facilities with new, environmentally “clean” ones. The creation of high-skilled jobs in the IHRA energy industry will become not only a driving force for the socioeconomic development of these territories but also a favorable condition for the adoption of innovative technological solutions in other sectors of life support, including the operation of transportation and engineering systems, their monitoring and maintenance.

Earlier, in their significant publications, A. A. Konoplyanik and V. V. Voroshilov indicated the prospects for the application of Drone Cargo Airship (DCA) to develop gas supply systems and the effect of this nascent sub-sector of air transportation on the socioeconomic growth of Russia [25–30].

C. Subject of the Study

A significant hurdle in organizing modern energy supply to the communities in the IHRA CEZ BNT, i.e., providing “green” energy for them, is transportation infrastructure, which is indispensable in the stages of construction and operation of energy facilities. At the same time, both transportation infrastructure and vehicles themselves must meet very high requirements in order to minimize their environmental impact.

To provide energy services to the population living in the IHRA CEZ BNT, we propose adopting the technologies for autonomous (decentralized) gas supply based on LNG and introducing an innovative type of air transportation, the Drone Cargo Airship (DCA) with a payload capacity of up to 60 tonnes, to ensure the construction and operation of gas infrastructure.

The object of this study is a possible set of autonomous gas supply systems for several settlements in the IHRA CEZ BNT in the Irkutsk region. The fuel source for these systems is assumed to be a small-scale LNG (SLNG) plant, located at the site of Kovykta gas & condensate field (Kovykta GCF) [31]. According to Gazprom Helium Service LLC estimates, the ex-works price of LNG will be no less than RUB 27.6 thousand per tonne (excluding VAT).

The subject of the study is a comparative assessment of the efficiency of different logistics schemes to ensure the construction of regasification facilities and, at the operational stage, their year-round fuel supply. The logistics schemes considered should include both traditional modes of transportation and innovative ones, using DCA.

Several settlements in the CEZ BNT were identified, and their prospective LNG demand was assessed. LNG storage facilities include sites for cryogenic LNG tank containers (CTC) or LNG storage tanks for seasonal fuel storage, regasifiers, heat exchangers, and gas distribution networks. The fuel supply to these systems relies on round trips. Each trip consists of delivery of filled CTCs from the SLNG plant to the consumers' LNG storage facilities, followed by the return of empty CTCs for refilling.

Three logistics schemes are examined. The first logistics scheme (LS) is based on the use of DCAs, while the other two represent multimodal routes using traditional modes of freight transportation. Their main difference is the use of a northern (Severobaikalsk) or southern (Kultuk settlement) CTC transshipment point for water transportation.

II. METHODOLOGY

A. Evaluation Methods

The total cost of transporting LNG to all the considered settlements was estimated based on their annual demand for each of the proposed LSs.

In addition, the cost of the transportation and energy infrastructure required for the phases of construction and operation of regasification plants is estimated for each LS. A production and financial model was developed for the economic evaluation of transportation services utilizing DCA, a currently non-existent class of unmanned airships capable of carrying heavy loads of up to 60 tonnes. This model was employed to explore the sensitivity of the operating cost of DCA to variations in its main technical and economic indicators.

Cash flows were compared for all LSs at a price that would allow LS1 to achieve a 10-year payback.

All estimations derived within this study were based solely on publicly available information.

B. Logistics Schemes for Fuel Delivery

Consumers

A modern energy supply system for the CEZ BNT, based on autonomous gas supply using LNG, will require a transportation system for cargo delivery that will ensure the most efficient development and operation of all essential energy infrastructure facilities. Efficiency should be understood as both minimizing the anthropogenic impact on the ecosystem and optimizing the costs to meet

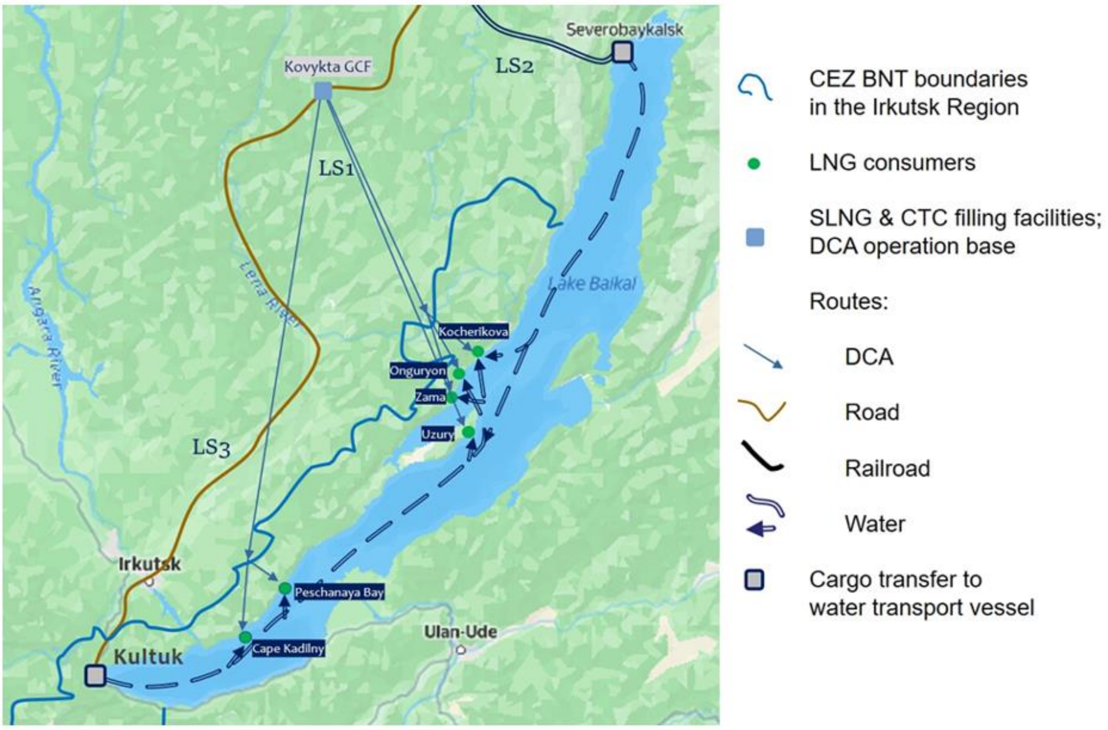

Fig. 1. Logistics scheme of LNG supply.

TABLE 2. Parameters for Estimating the LNG Delivery Costs

Settlement	Number of people, persons	LNG demand†, tonnes per year	Straight line distance from SLNG plant, km
Onguryon village	407	750 (500)	213
Kocherikova village	38	70 (45)	208
Zama village and Zama recreation center	76	160 (95)	229, 225 (227)*
Uzury village on Olkhon Island	9	20 (12)	249
Kadilny cape	up to 35	80 (30)	390
Peshchanaya Bay recreation center	up to 100	420 (18)	348

Note: † in parentheses - for wintertime
* for Zama location, 227 km are assumed.

energy demand. The latter includes the energy consumption of buildings and vehicles used for living, working, and recreation of both residents and visitors.

The settlements considered as potential consumers of autonomous gas supply on the basis of LNG in IHRA CEZ BNT in the Irkutsk region are as follows: Onguryon village, Kocherikova village, Zama village and the Zama recreation center, Uzury settlement on Olkhon Island, Kadilny cape, and the recreation centers of Baikal Dunes and Peshchanaya Bay (Fig. 1). To supply these consumers with fuel, it is proposed to build an SLNG plant at the site of PJSC Gazprom's Kovykta GCF. The DCA operational site is assumed to be located close to the SLNG plant.

The prospective demand for LNG in the settlements at issue was assessed assuming that LNG would be used for electricity and heat generation, as well as a fuel for motor, air, and water vehicles. The estimation of the LNG demand factored in the following indicators: the number of inhabitants (permanent and temporary), the specific consumption of electricity and heat, the specific LNG consumption for electricity and heat generation, and the specific LNG consumption for mobile energy units (including transport). The winter fuel demand was estimated based on accounting not only temperature factor, but also the ratio of the permanent to the temporary population. The annual LNG demand of six settlements was estimated at 1 500 tonnes, including 700 tonnes for the winter period.

With a known shipment point, the key input data for all logistics schemes are the destination locations and seasonally adjusted LNG consumption levels. Table 2 shows the fuel demand of the considered settlements, which are located in IHRA CEZ BNT in the Irkutsk region.

The distances (for LS1) from the estimated location of the SLNG plant to consumers shown in Table 2 were calculated using the interactive service [32], and represent, to a first approximation, LNG transport routes using DCA and CTC.

The Routes

The choice of a logistics scheme for LNG delivery from the point of production to the consumer is of primary importance for the development of autonomous gas supply systems [33]. The main method of estimating the cost of LNG transportation involves calculating the costs of each mode in the multimodal transportation chain on a round trip basis, including the delivery of LNG and the return of empty containers. The calculations rely on the financial and production model for each transportation mode explored, considering normative documents, as well as technical and economic indicators for the given transportation subsector. It is crucial to examine various organizational schemes of transportation service, which may significantly affect the results.

Logistics systems using traditional modes of freight transportation are concentrated in two favorable locations for water transportation infrastructure: Severobaikalsk in the north of Lake Baikal and Kultuk in the south. The main transportation option is the use of LNG-filled CTC for direct delivery of LNG from the LNG plant to the consumers' LNG storage facilities. Hereinafter, the logistics scheme using DCA is referred to as LS1, the scheme with transfer to water transport at Severobaikalsk is designated as LS2, and that at Kultuk is labeled as LS3.

Figure 2 shows all the logistics schemes for each route, explaining the chains of transportation operations. The points of origin and destination are the same for all the logistics schemes – LNG-filled CTCs are loaded onto vehicles at the SLNG plant and their final destination is the consumer's LNG storage facility.

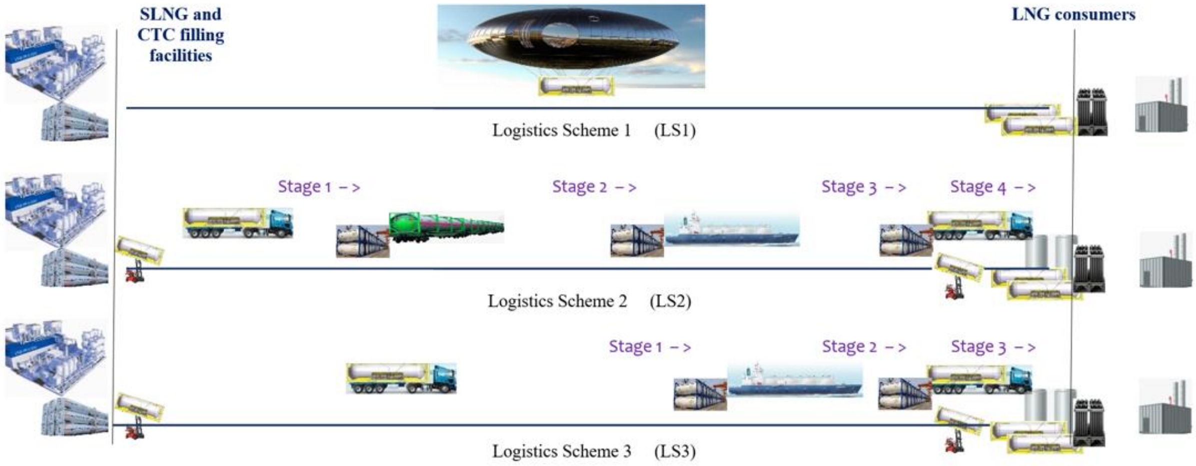

Fig. 2. Logistics schemes of LNG delivery routes.

The structure of the regasification systems at the customer's site is the same for LS2 and LS3 but differs for LS1. As there is no possibility of fuel delivery outside the navigation period, it is vital to stock up on fuel for the winter period in advance. In the context of small settlements, storing LNG directly in the CTC may be seen as a viable option. In this case, it may be necessary to design an LNG storage facility with CTCs of a smaller capacity in order to reduce LNG evaporation losses. When large seasonal storage is required, a more cost-effective solution may be to construct large stationary seismic-resistant storage facilities [34]. LS2 and LS3 necessitate storage areas with specialized loading and unloading equipment at CTC shipping, handling, and receiving points.

LS1 employs CTCs as the LNG storage within the regasification system. When the DCA reaches its destination, the empty CTC is replaced with a filled one, using the aircraft's flying crane capabilities. Similarly, DCAs receive and release cargo at the SLNG plant’s site.

It is assumed that KC.T75-45/0.8 tank containers manufactured by the Russian company UralKrioMash will be used for all logistics schemes. The storage time of LNG in such a CTC (when the tank is 86% full) is more than 80 days. The CTC is equipped with an evaporator to increase the pressure inside the tank. It can be operated outdoors at ambient temperatures ranging from – 40°C to + 50°C. The maximum weight of the CTC is 30–34 tonnes, the tare weight does not exceed 13.4 tonnes, and the weight of the transported LNG can reach 17–21 tonnes [35].

The water transportation routes, which are key to LS2 and LS3, encounter the problem of nearly complete absence of freight transportation in the Lake Baikal water area. This situation is compounded by the deterioration of previously built mooring facilities. As a result, to ensure the transportation of fuel and other cargoes by water, it is crucial to build new cargo berths and equip them with loading and unloading facilities.

C. Criteria for the Comparison of Logistics Schemes

The cost of services to transport the annual volume of LNG demand from SLNG plant to consumers is proposed as the main quantitative indicator to compare the efficiency of logistics schemes. A stronger justification of the options requires an additional assessment. The cargo delivery must be factored in at the construction stage of the autonomous gas supply and transportation infrastructure, especially if it is vital to the operation of the LS in question. To this end, we propose using the total cost of construction and development of CTC transshipment facilities for multimodal routes, alongside the subsystems for seasonal storage of LNG (if required). The latter is essential for ensuring a year-round supply to consumers.

The cost of transportation services for any logistics system can be determined in three ways, namely by: a) calculating the price at which an investment project achieves a payback (levelized cost), based on regulatory, methodological, and reporting information corresponding to the given type of transportation (or transportation service); b) using publicly available information on the services of commercial logistics companies; c) analyzing similar studies. Combinations of all these methods can also be employed.

Method of Calculating the Levelized Price of an Investment Project

Levelized cost is the price of products at which the sum of discounted costs equals the sum of discounted revenues for period T for which such a price is determined. It is assumed that costs are paid at the beginning of each period t and revenues are received at the end of each period t. This definition is expressed mathematically by equation

$$\sum_{t=1}^{T}\frac{C_t}{(1+r)^{t-1}}=\sum_{t=1}^{T}\frac{Ps_tV_t}{(1+r)^{t}}, \qquad (1)$$

where T is the number of the investment project implementation years; t is the ordinal number of the investment project implementation year; r is the discount rate; C_t is all costs of the project in year t; V_t is the quantity of products sold in year t; Ps_t is the product price in year t.

Since the price is assumed to be the same (i.e. the so called "constant prices") for all for all periods t, the transformation results in equation

$$Ps=\frac{\sum_{t=1}^{T}\frac{C_t}{(1+r)^{t-1}}}{\sum_{t=1}^{T}\frac{V_t}{(1+r)^{t}}}, \qquad (2)$$

which allows us to calculate the levelized cost of project Ps for period T at a given value of the exogenous parameter r, which characterizes the discount rate.

Extensive work is currently underway worldwide to identify promising designs and optimize the technical and economic parameters for the design, construction, and pilot operation of DCAs [36–39]. The information available in the public domain allows for aggregated calculations to estimate the cost of cargo transportation services in financial models and to analyze their sensitivity to the values of some crucial technical and economic parameters involved in DCA construction and operation. In our study, the numerical values of such parameters are assumed using the information from trustworthy experts. In the absence of a prototype DCA, only preliminary estimates are possible, with a high degree of uncertainty of technical and economic indicators and the environmental conditions required for transportation and assembly operations. Therefore, such estimates were made through expert analysis, based on informed justifications. Given the natural and climatic conditions of the BNT, the number of flight days was assumed to reach 270, with an average speed of 110 km/h and an expected cruising speed of 150

TABLE 3. Values of the Technical and Economic Indicators Used in the DCA Production-Financial Model

Indicators	Unit of measurement	Value
Technical		
Number of flight days per year	day/year	270
Average speed with load	kilometers per hour	110
Average loading/unloading time	hour	1,5
Maximum load weight	tonnes	60
LNG consumption (average)	kg LNG/hour	100
Staffing (per 1 DCA)	person	1.5
Financial and economic		
Discount rate	%	18
Payback period	years	27
LNG price (at the SLNG plant site)	rubles/kg	30
Cost of DCA	million rubles	3 000
DCA life (straight-line depreciation)	years	20
End-of-life renovation cost (% of the cost of a new DCA)	%	80
Maintenance costs, per cent of capital expenditures	%	18
DCA taxes, per cent of fixed assets	%	1,5
Accruals for labor remuneration fund	%	36
Headcount	person	1.5
Average salary (per month)	thousand rubles/person	100
Estimated value		
Levelized cost of transportation services	thousand rubles/hour	206

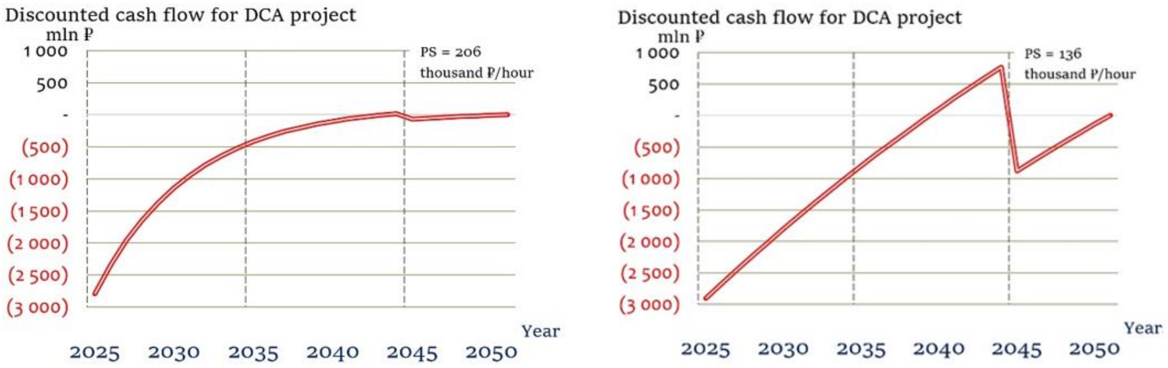

(*a*) Timeframe for evaluation – 27 years, *r* = 18%   (*b*) Timeframe for evaluation – 27 years, *r* = 2%

Fig. 3. Project profile of commercial application of DCA at different values of the r parameter.

km/h.

A production-financial model of DCA was developed as a research tool to estimate the costs of LS1 transportation. Table 3 summarizes the values of inputs and outputs of this model for the baseline conditions. Figure 3 shows the project profile corresponding to the values of the indicators in Table 3, but obtained for two values of the discount rate r: 18% and 2%. This shows the significance of this indicator in the calculation of the project's levelized cost.

After 20 years of operation, the DCA is depreciated and renovated. Project lifetime includes 20 years of DCA services before renovation and 7 years after renovation. When the value of the *r* parameter is high, the renovation of the aircraft at the end of its designated service life has virtually no effect on the hourly present value of DCA services, whereas when the value of the *r* parameter is low, this effect is significant, see Fig.3a and Fig.3b respectively.

CTC Transportation Cost Model Estimates

A mathematical model was developed to estimate the average annual cost of LNG transportation in the CTC, given the demand for LNG for all logistics schemes and for all consumers considered. This model takes the cost per flight hour as the main parameter characterizing the cost of freight transportation for LS1. Multimodal logistics schemes (LS2 and LS3) assume the price per tonne-kilometer of the respective mode of transportation. The distances to be travelled by the vehicles along the respective routes were calculated based on cartographic information and public services [32, 43–45]. The empty CTCs return along the same route. Due to the limited navigation time on Lake Baikal, which does not provide for winter transportation, it is essential to factor in the need for seasonal LNG storage at consumer sites. Table 4 shows the indicators characterizing the transportation process within

TABLE 4. Estimation of the Annual Number of LNG-Related Transportation Operations

Indicators	Measurement unit	Logistics scheme		
		LS1	LS2	LS3
CTC transportation distance (in one direction),	kilometers	208–390	587–879	742–1 035
including that for the following modes of transportation:				
By road	- " -	0	165†	643†
By rail	- " -	0	175	0
By water	- " -	0	255–550	110–400
By air (DCA)	- " -	208–390	0	0
The number of cargo transshipments (round trip)	units	0	8	6
Minimum total round trip time with CTCs	hour	6–9	53–92	50–89
Total transportation:				
Construction phase, one-off	million tonnes	0.2	14.3	14.3
Operational phase, annually	- " -	67.0	166.5	228.1

Note: † including roads between berth and consumer's regasification terminal.

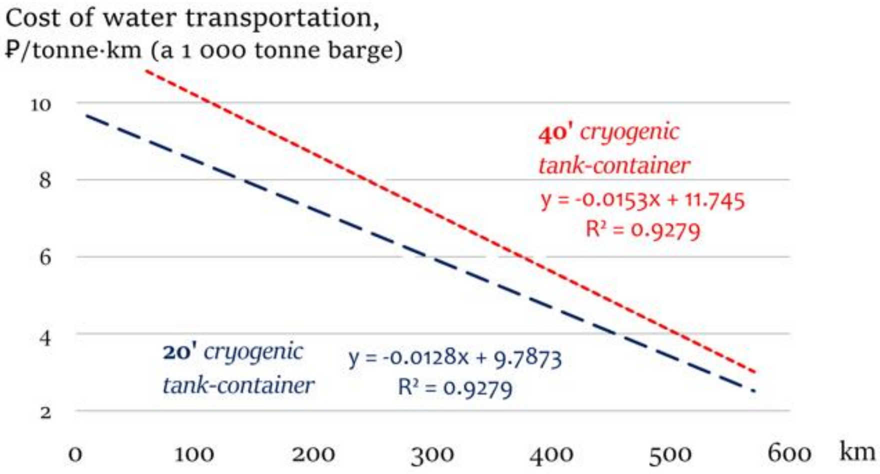

Fig. 4. Estimates of the cost of transporting cargo by a 1 000 tonne deadweight barge for 20' and 40' CTCs.

the LNG delivery to consumers, estimates of technical indicators of fuel transportation at the stage of energy system operation and cargo transportation at the stage of construction for the considered LSs.

Estimates of the volumes and weights of materials and equipment for the regasification terminals, berths, and roads from them to the terminals are essential to calculate the costs of transportation during the construction phase. These estimates were derived by analyzing similar studies that describe the methodology for such estimates and the data used.

D. The Analysis of Similar Studies

This method was used to justify three indicators of the CTC transportation cost calculation model for LS2 and LS3: the ratio of road-to-water freight costs per tonne-kilometer; the cost of container operations to transfer cargo from one transportation mode to another; and the cost of road construction from the berth to the consumer's LNG terminal.

The study [33] on multimodal LNG transportation cost analysis outlines a methodology for a universal approach to estimating the cost of transporting LNG from small-scale production plants. The authors of this paper developed technical and economic models for calculating the unit cost of LNG transportation by road and water, using data from the “TMkarta” service for rail transportation. The paper proposes an approach for estimating the cost of LNG transshipment. These results were used in our study to estimate the ratio of road-to-rail freight unit costs, as well as the cost of container operations for cargo handling.

Based on the generalization of information on several construction projects, the Ministry of Construction, Housing, and Utilities of the Russian Federation has established consolidated price standards for the construction of water transportation facilities [40]. The cost of river infrastructure (berths), including sheet pile walls up to 5 meters deep in weak soils, was estimated at RUB 1.562 million per meter, given all correction factors for the Irkutsk region.

The number of berths for LS2 and LS3 is equal to the number of customer locations plus one for transshipment of CTC (or construction cargo and equipment) from rail or road to water. Such berths should allow for the temporary storage of CTC, its transfer to the ship and back, using equipment with a lifting capacity of up to 60 tonnes. The total cost of building seven berths, each 70 meters long, is estimated at RUB 765 million.

Our study also relies on an investigation conducted by the Ministry of Transport of the Russian Federation [41], where the average cost of building 1 km of a single-lane category IV road in 2022 is estimated at RUB 27.1 million. The cost of category IV roads from the berth to the regasification terminal is estimated at RUB 340 million, and the annual cost of their maintenance (excluding the application of protective layers, wearing courses, and surface treatments) for six locations stands at RUB 2.7 million.

As already mentioned, the main obstacle to the estimation of the cost of water transportation on Lake Baikal is the lack of such transportation, along with the non-existence of equipped berthing facilities. Fruitful contacts with the Way Group transportation and logistics company made it possible to establish the fact of such a state of affairs and to obtain some information that would contribute to the estimation of the CTC water freight costs [42]. The specialists of this company calculated the prices for the transportation of a 20' CTC on a 1 000-tonne barge to possible transhipment points for all six LNG consumer locations and pointed out on numerous necessary conditions for the cargo transportation on Lake Baikal.

The information received from Way Group was utilized to construct linear tariff functions for the transportation of 20' and 40' containers on a 1 000 tonne barge (30 and 25 pieces, respectively, arranged in a single layer) for a distance of up to 600 km, see Fig. 4.

The distances along the routes were calculated using the following services:

- "Plot routes on the map" and "Plot a route" [43, 44] for road and water transportation, the road from the location suitable for berth construction to the location proposed for the regasification terminal for each consumer;
- "Calculation of tariff distance between railway stations" [45];
- "Geographic coordinates distance service" to find the shortest distance between locations for air transportation [32].

The cost of transportation infrastructure was calculated using the information provided by industrial equipment search services, but the cost of a wheeled stacker for handling CTC was expertly estimated at RUB 15 million [46]. Similarly, the total cost of construction of six seismic-resistant LNG storage tanks for seasonal storage with a total capacity of 1 700 m^3 was estimated at RUB 290 million (required only for LS2 and LS3), and the cost of regasification plants themselves (without the LNG storage tanks incorporated in them) for all logistics schemes was assumed to be RUB 210 million.

E. Additional Assumptions

The branch of the air transportation industry represented by DCAs is assumed to be a universal type of cargo transportation similar to road, rail, and water transportation. Its specific feature is the flying crane capabilities of the DCA, which means that it is equipped with special mechanisms for picking up and dropping off cargo. The use of DCAs in the installation of building contractures in IHRA has already been mentioned.

The specific features of the infrastructure for this type of transportation are the absence of linear structures and the high autonomy in transportation operations, achieved through establishing a network of aircraft basing and maintenance. For LS1, it is essential to factor in the infrastructure designed to serve the transportation of general-purpose cargoes of DCA in the transportation tariffs.

The study assumes that the cost of receiving, transporting, and installing the CTC at the delivery point is included in the cost of transportation services and that the DCA operational base is situated in the proximity to the SLNG plant site.

It is worth noting that in the LS1 calculation, the total round trip time of the CTC is obtained assuming that one CTC is delivered to one LNG consumer location. At the same time, with a maximum payload of 60 tonnes and a rigging weight of 5 tonnes, the LNG carrier can lift two 82% filled CTCs (a gross weight of 27 tonnes), allowing for restocking two locations in one round trip on a complex route. Thus, the total flight time required to meet the annual LNG demand will be reduced. It is assumed that the annual flight time saved will be used to transport other cargoes, ensuring that the total revenue of the transportation company remains steady. In this way, the levelized cost calculated with the production and financial model presented earlier, at maximum utilization of flight days per year, remains constant.

III. RESULTS

The basic technical and economic assumptions presented in Tables 2–4 for the three considered logistics schemes were applied to estimate the gas prices for consumers and unit one-off costs associated with the construction of regasification terminals and transportation infrastructure facilities. Table 5 presents these results and the cost structure, enabling the assessment of the comparative performance of different logistics schemes for establishing and operating autonomous gas systems in several settlements within the CEZ BNT under the constraints imposed by the Federal Law No. 94-FZ "On Protection of Lake Baikal."

The estimates obtained indicate that LNG delivery to the IHRA CEZ BNT in the Irkutsk region based on the use of modern unmanned cargo airships can be acceptable for commercial consumers in these settlements, and, if subsidized, for the population.

While the cost of annual fuel transportation for LS2 and LS3 is lower than for LS1, the construction costs for

TABLE 5. Estimates of the LNG Delivery Cost

Indicators	Measurement unit	Logistics scheme		
		LS1	LS2	LS3
Financial and economic				
Cost of LNG procurement	million rubles	45	45	45
Cost of LNG transportation, *including:*	- " -	105	34	96
By road	- " -	0	22	88
By rail	- " -	0	4	0
By water	- " -	0	8	8
By air (DCA)	- " -	105	0	0
CTC transshipment	- " -	0	0.4	0.3
Construction costs of regasification systems,	- " -	210	664	664
including seasonal LNG storages (6 units with a total capacity of 1 700 m^3)	- " -	0	490	490
delivery of materials and equipment*	- " -	36	139	139
Cost of a logistics scheme,	- " -	0	1 184	1 169
including berths (7 pcs., 70 m each)	- " -	0	765	765
regasification terminal – berth roads (6 pcs.)	- " -	0	344	344
transshipment facilities (6+3 pcs. for LS2 and 6+2 pcs. for LS3)	- " -	0	75	60
*Reference: *estimated weight of construction materials and equipment*	thousand tonnes	2.2	55	55
Estimated				
Consumer gas prices (at regasification terminal) for the settlements in the IHRA CEZ BNT	rubles per m^3	66–88	38–43	64–84
Specific one-off costs of the regasification terminal (and transportation infrastructure for LNG consumers for LS2 and LS3)	- " -	100	880	873

regasification terminals and route development (one-off costs) for LS2 and LS3 are significantly higher than for LS1. For a comparative analysis of the financial efficiency of the considered LNG projects, the profiles of the respective projects were calculated (under the constant prices), as shown in Fig. 5.

As these projects are to be financed mainly by government budgets at various levels, once the project payback is achieved, the levelized cost (converted into a transportation tariff) should offset a minimum level of

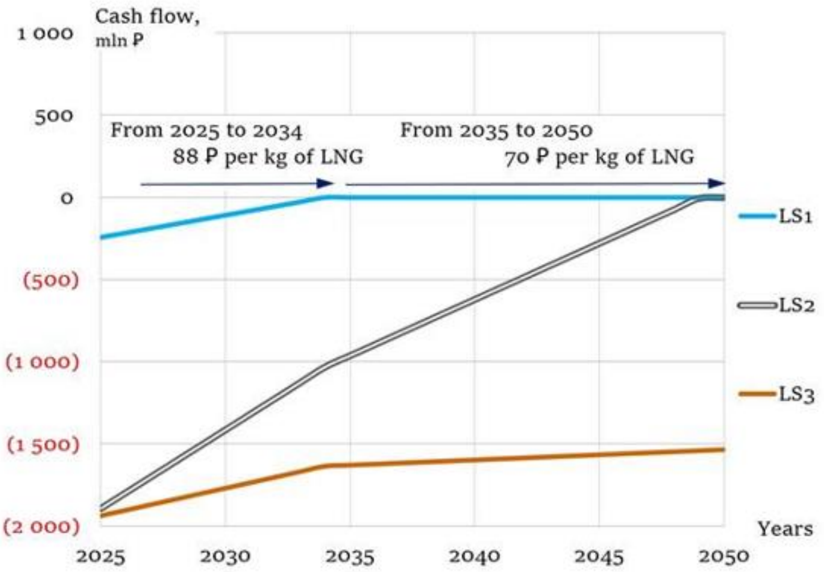

Fig. 5. Cash flows for all considered logistics schemes of energy supply to consumers.

budget subsidies for energy supply rather than ensure the profit of transportation companies.

The obtained results indicate that DCAs are more preferable for energy supply of settlements in the IHRA CEZ BNT than the multimodal transportation routes. In this case, at least the Irkutsk region is interested in the early establishment of DCAs with a carrying capacity of up to 60 tonnes. Furthermore, the Irkutsk region has a favorable combination of natural-climatic and industrial-economic factors for the operation of DCAs, which can attract developers and potential users of DCAs to organize their pilot operation on the territory of the region.

The prerequisites for the establishment of a pilot test site in the Irkutsk region to accelerate the commercialization of DCA technologies (with a lifting capacity of up to 60 tonnes) are as follows.

- The south of the Irkutsk region, including CEZ BNT, has favorable climatic conditions for the establishment of a DCA pilot test site. These conditions are much better than in the northern and arctic areas of the Asian part of the Russian Federation, where large and extra-large DCAs are designed to improve transportation links.
- The Irkutsk region has significant industrial potential for the production of materials and equipment required for the development and operation of next-generation aircraft prototypes (Irkutsk aircraft plant; factories for producing aluminium, polymers; plants for manufacturing cables; petrochemical and chemical industries).
- The Irkutsk region has a well-developed system for training workers and engineers in the aerospace industry. In particular, the Irkutsk National Research Technical University has founded an advanced engineering school for aircraft construction technologies.
- There is a logistics hub of all modes of land and air transportation in the south of the Irkutsk region, which facilitates the establishment and operation of the proposed DCA pilot site.
- The Irkutsk region has significant hydrocarbon resources and operating fields that produce natural gas with a high helium content. A small-scale LNG production facility and a helium separation unit were tested at the Kovykta gas condensate field. Helium is already produced in the region's north by the Irkutsk Oil Company.

IV. SENSITIVITY ANALYSIS

The production-financial model of a 60-tonne LNG tanker was used to analyze the sensitivity of the cost per flight hour to the values of such markedly uncertain parameters at this stage of the research as the price of LNG (since LNG is to be used as fuel for DCA) and the discount rate *r*.

The technical and economic indicators given in Table 3

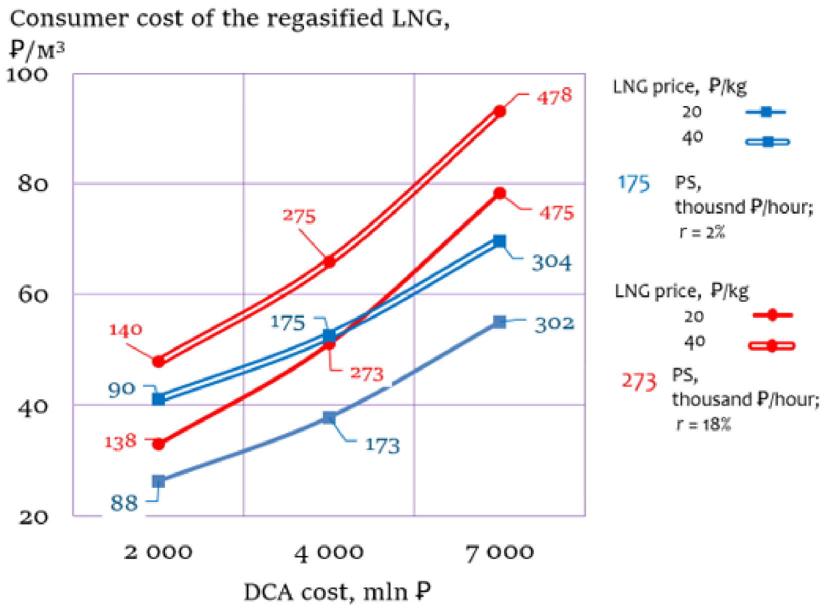

Fig. 6. Sensitivity analysis of flight hour cost (price of the DCA services) and consumer cost of the regasified LNG.

were employed to determine the price per flight hour (the cost of DCA services) for the maximum average annual freight traffic over a distance of 350 km using two CTCs with a gross weight of 27 tonnes (a net LNG weight of 13.5 tonnes). The varied financial and economic parameters of the model included a DCA price assumed to be RUB 2, 4, and 7 billion; a discount rate of 2% and 18%; and an LNG price at the SLNG plant of RUB 20 and RUB 40 per kg. The results obtained for all combinations of variable parameters are presented with graphs demonstrated in Fig. 6.

The analysis of the obtained dependencies indicates a strong influence of the DCA price (reflecting the technology readiness level, TRL) and the discount rate (reflecting the investment climate) on the price of an aircraft flight hour. Less significant is the dependence of the cost of DCA services on the price of purchased fuel, which in this example can be interpreted as a change in the specific consumption of LNG by the propulsion system at a constant price of this fuel.

V. CONCLUSIONS AND SUGGESTIONS

The Irkutsk region faces serious problems in supplying energy and fuel to settlements in the IHRA CEZ BNT. In particular, it is challenging to protect the ecosystem in the CEZ BNT, while providing a modern level of energy services to the population (to both those who live and work permanently in the area and those who stay there temporarily, including tourists).

At the current stage of transportation and energy technology development, the optimal approach to the enhancement of energy supply to such settlements is a combination of innovative technologies of autonomous energy systems powered by LNG and using unmanned airships, to ensure such energy systems and fuel delivery to them.

The Irkutsk region has ample opportunities for LNG production, from both the unique Kovykta gas condensate field and other numerous hydrocarbon fields on the Siberian platform.

The Irkutsk region has favorable conditions conducive to the establishment of a pilot industrial site aimed at accelerating the commercialization of unmanned cargo airship technologies.

Given the need to create modern energy systems based on LNG for the settlements within the IHRA CEZ BNT and the availability of favorable opportunities to organize pilot operation of unmanned cargo airships, we recommend the authorities of the Irkutsk region to create public-private partnership institutions to balance the interests of businesses, developers of new airships, and other stakeholders.

DISTRIBUTION OF AUTHORS' CONTRIBUTIONS

S.P. Popov – idea, structure and content of the paper; D.V. Maksakova – development of the production-financial model for road transportation and calculations using it.

ACKNOWLEDGMENT

The research was carried out under State Assignment Project (no. FWEU-2021-0004) of the Fundamental Research Program of Russian Federation 2021–2030 using the resources of the High-Temperature Circuit Multi-Access Research Center (Ministry of Science and Higher Education of the Russian Federation, project no. 13.CKP.21.0038).

We would like to express our gratitude to the personnel of the Way Group Transportation and Logistics Company, as well as to A. V. Ivanchenko, the Chief Engineer of the SK Irkut-Allians, Ltd, for their helpful expert estimations and assistance in gathering information on non-existing water transportation routes and construction costs for port infrastructure on Lake Baikal.

REFERENCES

[1] Schemes of ecological zones of the Baikal natural territory [Online]. Available: http://geol.irk.ru/baikal/terr/mterreczond/terrshemezBNT. Accessed on: Sep. 5, 2025. (In Russian)

[2] Detailed Map of the Baikal Natural Territory, Ministry of Natural Resources and Environment of the Russian Federation, 2012. [Online]. Available: https://baikal-1.ru/4sitedoc/181121-baikal-nature-territory.pdf. Accessed on: Sep. 5, 2025. (In Russian)

[3] IAS “Nature of Buryatia,” Data Banks on Natural Resources and Natural Sites of the Republic of Buryatia, Territories of World Natural Heritage Sites. [Online]. Available: https://ias.burpriroda.ru/BNT/ovpn.php?arrFilter_3485_397352289=Y&arrFilter_3487_3532402574=Y&arrFilter_3487_1163851270=Y&set_filter=%CF%EE%EA%E0%E7%E0%F2%FC. Accessed on: Sep. 5, 2025. (In Russian)

[4] Lake Baikal – UNESCO World Heritage Site [Online]. Available: http://bic.iwlearn.org/en/documents/state-of-the-environment-report-the-lake-baikal-basin-1/general-conditions-of-the-baikal-lake-basin/1-6-lake-baikal-2013-unesco-world-heritage-site. Accessed on: Sep. 5, 2025.

[5] Lake Baikal, Natural Heritage Protection Fund [Online]. Available: http://www.nhpfund.org/nominations/baikal.html. Accessed on: Sep. 5, 2025.

[6] Protection of Lake Baikal. World Natural Heritage Site Status. [Online]. Available: http://irkipedia.ru/content/ohrana_baykala_status_obekta_vsemirnogo_prirodnogo_naslediya. Accessed on: Sep. 5, 2025. (In Russian)

[7] Resolution of the Government of the Russian Federation (2020, Dec. 31). *No. 2399, On Approving the List of Activities Prohibited in the Central Ecological Zone of the Baikal Natural Territory (as amended on Jan. 26, 2023)*. [Online]. Available: https://base.garant.ru/400167820/. Accessed on: Sep. 5, 2025. (In Russian)

[8] Resolution of the Government of the Russian Federation (2023, Feb. 18). *No. 260, On Approval of the Regulations on State Environmental Monitoring of the Unique Ecological System of Lake Baikal and Declaring null and void Resolution of the Government of the Russian Federation No. 85 of 2 February 2015*. [Online]. Available: http://static.government.ru/media/files/bdI32hM6mlJZJMuDulkZNtGqOzrmvH7k.pdf. Accessed on: Sep. 5, 2025. (In Russian)

[9] Environmental monitoring of Lake Baikal [Online]. Available: https://baikalake.ru/en/. Accessed on: Sep. 5, 2025.

[10] L. M. Korytny, *Echoes of ecological and economic scandals*. Novosibirsk, Russia: Publishing House of SB RAS, 2011, 328 p. ISBN 978-5-7692-1206-2. (In Russian)

[11] A. A. Koshelev, "Concept of energy supply of Baikal natural territory," *Bulletin of Irkutsk State Economics Academy*, no. 6, Art. no. 64, 2010. (In Russian)

[12] A. A. Koshelev, "Power supply of the Baikal ecological zone," in *Eastern vector of the energy policy of Russia: current state, a look into the future*, N. I. Voropai, B. G. Saneev, Eds. Novosibirsk, Russia: Academic Publishing House GEO, 2011, pp. 331–333. (In Russian)

[13] A. A. Koshelev, "Fuel and energy sector," in V. M. Plusnin, I. N. Vladimirov, *Territorial planning of Central Ecological Zone of Baikal Natural Territory*. Novosibirsk, Russia: Academic Publishing House GEO, 2013, pp. 158–165. (In Russian)

[14] A. A. Koshelev, "Principles of shaping feasible energy supply within the Baikal natural territory," *Fuel and energy complex of the Baikal region: current state and development prospects*, B. G. Saneev, Ed. Novosibirsk, Russia: Academic Publishing House GEO, 2015, pp. 143–157. (In Russian)

[15] I. Yu. Ivanova, B. G. Saneev, E. V. Gubiy, E. P. Maysyuk, T. F. Tuguzova, "Specific features of the decarbonization measures in the energy sector in off-grid remote territories of Russia's eastern regions," *E3S Web of Conferences*, vol. 470, Art. no. 01049, 2023.

[16] B. G. Saneev, I. Yu. Ivanova, A. K. Izhbuldin, T. F. Tuguzova, "The impact of the development of resources in the Eastern Arctic on energy and fuel supply to consumers," *Energy Policy*, no. 7. pp. 86–95, 2021. DOI: 10.46920/2409-5516_2021_7161_86.

[17] E. P. Maysyuk, I. Yu. Ivanova, "Ecological assessment of different fuel types for energy production in the Arctic regions in the Far East of Russia," *Arctic: Ecology and Economics*, no. 1 (37), pp. 26–36, 2020. DOI: 10.25283/2223-4594-2020-1-26-36. (In Russian)

[18] I. Yu. Ivanova, T. F. Tuguzova, A. K. Izhbuldin, "Justification of feasible options of energy supply to consumers in the eastern zone of the Russian Arctic: methodological approaches and their practical application," in *Proc. All-Russian Scientific and Practical Conference with international participation "Thermophysics and Energy of Arctic and Subarctic Territories," devoted to the 80th anniversary of Dr. Rev Ivanovich Gavriliev*, Yakutsk, Russia, Jun. 24–27, 2019, pp. 187–192. (In Russian)

[19] B. G. Saneev, I. Yu. Ivanova, E. P. Maisyuk, A. K. Izhbuldin, "Main directions of solving environmental problems of the energy sector in the Central Ecological Zone of the Baikal Natural Territory," in *Proc. International Scientific and Practical Conference "Geographical Foundations and Ecological Principles of Regional Policy of Nature Management," dedicated to the memory of corresponding member of RAS A. N. Antipov*, Irkutsk, Russia, Sep. 23–27, 2019, pp. 607–611. (In Russian)

[20] B. G. Saneev, I. Yu. Ivanova, E. P. Maisyuk, T. F. Tuguzova, "Implementation of environmental protection measures in the heat power industry in the Central Ecological Zone of the Baikal Natural Territory," *Ecology and Industry of Russia*, vol. 22, no. 7, pp. 20–25, 2018. DOI: 10.18412/1816-0395-2018-7-20-25. (In Russian)

[21] B. G. Saneev, I. Yu. Ivanova, E. P. Maisyuk, A. K. Izhbuldin, T. F. Tuguzova, "Transition to gas of boiler houses operating in the Central Ecological Zone of the Baikal Natural Territory: prerequisites, effects, barriers," *Geography and Natural Resources*, no. S6, pp. 27–31, 2016. (In Russian)

[22] I. Yu. Ivanova, T. F. Tuguzova, A. K. Izhbuldin, "Comparative efficiency of natural gas when used for heat supply to consumers within the Baikal natural territory," in *Proc. the 8th International Scientific and Technical Conference "Energy: Management, Quality and Efficiency of Energy Resources Use,"* Blagoveshchensk, Russia, May 27-29, 2015, pp. 330–334. (In Russian)

[23] Russia's Aerosmena will build huge airships in the shape of a "flying saucer." [Online]. Available: https://www.techcult.ru/technics/13068-aerosmena-letayushie-tarelki. Accessed on: Sep. 5, 2025. (In Russian)

[24] Aerosmena hybrid thermal airships, [Online]. Available: https://lynceans.org/wp-content/uploads/2021/04/Aerosmena_hybrid-thermal-airships-converted.pdf. Accessed on: Sep. 5, 2025.

[25] A. A. Konoplyanik, V. V. Voroshilov, “Decentralized off-grid gasification of the Russian Arctic: small tonnage LNG and cargo airships (problem statement and possible solutions). Challenges for Russian equipment manufacturers: opportunities for production of modular gas power plants, cryo-fueling stations,” *Regionalnaya Energetika i Energosberezhenie,* no. 3, pp. 54–61 (part 1); no. 4, pp. 77–81 (part 2), 2021. (In Russian)

[26] V. V. Voroshilov, A. A. Konoplyanik, “How do we develop Russia’s East of the Urals? One of the options is the use of small tonnage LNG and cargo airships,” *Neftegazovaya Vertikal*, no. 17–18, pp. 16–24 (part 1); no. 19–20, pp. 24–35 (part 2), 2021. (In Russian)

[27] A. A. Konoplyanik, “Who will replace the northern importation? Unmanned airships are not included in the unmanned aviation development strategy,” *Vedomosti*, Dec. 29, 2023. [Online]. Available: https://www.vedomosti.ru/business/columns/2023/12/28/1013520-severnii-zavoz. Accessed on: Sep. 5, 2025. (In Russian)

[28] “Why does Russia not consider the use of unmanned cargo airships? Innovative aviation equipment will enable transportations under severe meteorological conditions,” *Nezavisimaya Gazeta – monthly supplement "NG-Energy"*, Jan. 16, 2024, pp. 12. (In Russian)

[29] V. V. Voroshilov, A. A. Konoplyanik, F”rom transition to gas in the Russian Trans-Urals and Arctic zone to energy consolidation of Eurasia (part 1),” *ECO*, no. 2, pp. 236–260, 2024. DOI: 10.30680/ECO0131-7652-2024-2-236-260. (In Russian)

[30] V. V. Voroshilov, A. A. Konoplyanik, “From transition to gas in the Russian Trans-Urals and Arctic Zone to energy. consolidation of Eurasia (part 2),” *ECO*, no. 2, pp. 205-233, 2024. DOI: 10.30680/ECO0131-7652-2024-3-205-233. (In Russian

[31] Y. Fursova, “Natural gas liquefaction facility planned to be built by Gazprom's subsidiary in Irkutsk region,” *Siberian Economist*, Nov. 15, 2023. [Online]. Available: https://sibmix.com/?p=9757. Accessed on: Sep. 5, 2025. (In Russian

[32] Geographic coordinates distance service. [Online]. Available: https://addressextractor.ru/. Accessed on: Sep. 5, 2025. (In Russian)

[33] O. V. Tarovik, O. M. Mudrova, “Estimation of the cost of transporting low-tonnage LNG,” *World of Transport and Transportation*, vol. 17, no. 5, pp. 130–163, 2019. DOI: 10.30932/1992-3252-2019-17-5-130-163.

[34] A fragment of the general seismic zoning map. [Online]. Available: https://seis-bykl.ru/modules.php?name=Seismo_r. Accessed on: Sep. 5, 2025. (In Russian)

[35] Technical Gas Supply Systems LLC, Cryogenic ISO Tank 40ft container. [Online]. Available: https://sptg.ru/product/kriogennye-iso-tanki/kriogennyy-iso-tank-konteyner-40-futov/. Accessed on: Dec. 24, 2025. (In Russian)

[36] Novosibirsk proposes using airships for cargo transportation in the energy sector. [Online]. Available: https://www.itp.nsc.ru/news/v_novosibirske_predlozhili_ispolzovat_dirizhabli_d.html. Accessed on: Sep. 5, 2025. (In Russian)

[37] Russia tests an airship that does no need a mooring mast [Online]. Available: https://www.itp.nsc.ru/news/v_rossii_ispytali_vysokomanevrennyy_dirizhabl_s_dv.html. Accessed on: Sep. 5, 2025. (In Russian)

[38] A drone airship will be demonstrated at the Technoprom-2024 forum [Online]. Available: https://www.itp.nsc.ru/news/dirizhabl-bespilotnik_prodemonstriruyut_na_forume_.html. Accessed on: Sep. 5, 2025. (In Russian)

[39] A drone airship will be demonstrated at the Technoprom-2024 forum [Online]. Available: https://www.itp.nsc.ru/news/dirizhabl-bespilotnik_prodemonstriruyut_na_forume_.html. Accessed on: Sep. 5, 2025. (In Russian)

[40] Development of airship infrastructure is discussed at Technoprom. [Online]. Available: https://www.sbras.info/articles/nauka-dlya-obschestva/na-tekhnoprome-obsudili-razvitie-dirizhabelnoy-infrastruktury. Accessed on: Sep. 5, 2025. (In Russian)

[41] Order of the Ministry of Construction of Russia (2024, Feb. 16). *No. 121/4, On Approval of Consolidated Construction Price Standards, NCC 81-02-29-2024 (Collection No. 20), focusing on marine and river transport facilities*. (In Russian)

[42] “Report on the Cost of Construction, Reconstruction, Overhaul, Repair and Maintenance of 1 km of Public Roads in the Russian Federation (2022),” Ministry of Transport of the Russian Federation. [Online]. Available: https://mintrans.gov.ru/documents/7/13010. Accessed on: Sep. 5, 2025. (In Russian) Way Group Transport and logistics company. [Online]. Available: https://www.wayg.ru/en. Accessed on: Sep. 5, 2025.

[43] Building routes on the map [Online]. Available: https://yandex.ru/maps/. Accessed on: Sep. 5, 2025. (In Russian)

[44] Route information. [Online]. Available: https://all-routes.ru/rasstoyanie-kachug-magistralnyy. Accessed on: Sep. 5, 2025. (In Russian)

[45] Calculation of tariff distance between stations. [Online]. Available: https://online.freicon.ru/info/tariff-distance-calculation. Accessed on: Sep. 5, 2025. (In Russian)

[46] Heavy-duty skid steer loader model YDM-01. [Online]. Available: https://russian.alibaba.com/product-detail/Heavy-duty-rotate-flip-overturn-turn-1600688015204.html?spm=a2700.7724857.0.0.430544a63prpGq. Accessed on: Sep. 5, 2025. (In Russian)

Sergei Popov, Ph.D. in Energy Systems Modeling, serves as a Senior Researcher at the Melentiev Energy Systems Institute of the Siberian Branch of the Russian Academy of Sciences (ESI SB RAS). He conducts in-depth analyses of energy markets in East Asia and Asia-Pacific region. In 2004–2011, he worked at the Asia Pacific Energy Research Center, Japan. His research interests include energy systems modeling, development of regional energy policies, and international energy cooperation.

Darya Maksakova, Ph.D. in Energy Systems, serves as a Researcher at the ESI SB RAS, where she has been contributing since 2016, after graduating with the Bachelor's degree in International Economics from Baikal State University, Russia. She earned her Master's degree in Finance from the same university in 2018. Her research interests include energy economics and energy modeling tools.

Enhancing Reliability of Fuel Gas System at Combined Cycle Power Plant

P.A. Batrakov[1], A.A. Batrakova[1], E.A. Ryzhnikova[1,2]

[1]Nizhnevartovsk State University, Nizhnevartovsk, Russia
[2]Siberian Federal University, Krasnoyarsk, Russia

***Abstract* — This paper presents a methodology to boost the reliability of a combined natural gas and associated petroleum gas system (fuel gas system, FGS) for a gas turbine unit in a combined cycle power plant. The use of failure mode, effects, and diagnostic analysis (FMEDA) is proposed to avoid unplanned shutdowns of the power plant. This method identifies and evaluates potential types of failures, develops measures to reduce them, and establishes a new protection system. The system includes a gas analysis system (GAS), a shut-off valve system (SVS), a fuel gas controller (FGC), and workstations for an engineer and operator. The gas analysis system has two automatic subsystems with different measurement methods. One of them includes three gas chromatograph analyzers that operate according to the 2-out-of-3 voting. The results of gas chromatography and the diagnostic archive of alarms serve as the basis for analyzing the causes of possible failures. Reliability models were developed to confirm the effectiveness of using diagnostic data from gas analyzers within the gas subsystem. They employ a gas chromatography and a common fuel gas controller. The FMEDA findings demonstrate that a new safety interlock can be implemented without any additional financial outlay for software and hardware.**

***Index Terms* — Combined cycle power plant, diagnostic alarm, failure detection, associated petroleum gas supply, safety interlock, gas chromatography, reliability.**

I. INTRODUCTION

There is a growing interest in using reliability theory to enhance the availability, profitability, and safety of power generation. This is due to the unexpected production shutdowns caused by equipment failures at power plants leading to adverse events and their negative consequences for all stakeholders.

Combined cycle power plants (CCPPs) powered by gas and steam turbines are gaining significant traction. In regions with active oil production, associated petroleum gas (APG) is a byproduct, making its utilization particularly challenging. A viable solution to this problem is to use the CCPP running on APG.

Flaring gas is an inefficient utilization method, while burning it in gas turbine engines is a more environmentally friendly and cost-effective approach. This process involves cleaning the gas and connecting it to the system. In this paper, we consider the Brayton cycle, where associated petroleum gas is used in conjunction with a traditional fuel such as natural gas. The gas mixture is fed into the combustion chamber. APG is the primary fuel in this system, while natural gas plays a crucial role in stabilizing operational parameters when the APG composition fluctuates. This is essential, as compositional instability is the key challenge when using APG. In this method, the amount of APG and natural gas can be varied depending on demand. The basic operating principle was previously presented in [1].

The use of this mixture as a fuel, however, poses a number of challenges related to the quality of the gas supplied from different sources. The composition of APG, unlike that of natural gas, varies significantly depending on

---

[*] Corresponding author.
E-mail: peter_1cool@mail.ru

DOI: 10.25729/esr.2025.04.0011

Received November 5, 2025. Revised December 3, 2025. Accepted December 10, 2025. Available online December 29, 2025.

the field. The production process also influences the quality.

Therefore, gas analyzers are essential to monitor impurities in APG and prevent potential component failures in the gas turbine, which could negatively impact operational safety. This paper proposes a method for enhancing the reliability of a fuel gas system with gas chromatograph analyzers that enable failure diagnosis.

The method relies on diagnostic data obtained from gas analyzers, including gas chromatographs, and the history of alarms. The protection system, using FMEDA, prevents the unplanned equipment and plant shutdowns.

II. LITERATURE REVIEW

Enhancing the reliability of fuel gas systems at thermal power plants is critical for ensuring uninterrupted equipment operation, minimizing emergency situations, and extending service life.

Studies on automated control, preventive maintenance, and system redundancy made a significant contribution to the development of this field. A primary emphasis is placed on the implementation of automatic monitoring systems for gas pipelines and equipment.

According to [2], the use of intelligent diagnostic systems enables the early detection of failures and reduces the risk of emergency situations. Particular attention is also paid to the advanced materials and sealing technologies to ensure tightness and corrosion resistance, as confirmed by scientific studies.

In reliability management, predictive analytics algorithms and risk assessment models play a pivotal role, enabling the early detection of potential failures and the implementation of corrective measures [3, 4].

Of particular importance is the automation of the pressure and fuel flow monitoring systems, contributing to the stabilization of system operating parameters [5, 6]. Redundancy and automated system recovery significantly enhance overall resilience [7]. The implementation of backup components and automatic gas re-feeding helps prevent downtime and reduce the energy losses.

A number of studies emphasize the importance of integrated solutions that include the modernization of technical equipment, implementation of the automatic control systems, and the predictive maintenance [2, 6]. The modeling and artificial intelligence methods in the predicting system are instrumental in increasing the reliability and operational efficiency [8].

III. PROPOSED RELIABILITY IMPROVEMENT BASED ON FAILURE MODE, EFFECTS, AND DIAGNOSTIC ANALYSIS

Failure mode and effects analysis (FMEA); failure mode, effects, and criticality analysis (FMECA); and failure mode, effects, and diagnostic analysis (FMEDA) are important tools for analyzing the reliability and safety of systems, processes, and products. Each of them is considered in more detail in [9].

1. FMEA is a systematic method used to identify potential failure modes in a system, process, or product and to evaluate their consequences [10].

The main steps of FMEA include:

– identifying the possible scenarios (modes) through which the system could fail;

– assessing the consequences of each failure mode for the system and users;

– identifying the causes that could lead to each failure mode;

– assessing the risk levels using criteria such as the probability of failure, the severity of its consequences, and the possibility of its detection.

2. FMECA is a more complex method that incorporates all the steps of FMEA, as well as a criticality assessment of each failure mode [10]. Criticality is determined based on the probability of failure, its consequences, and the ability to detect it.

FMECA is an extended version of FMEA that includes the criticality analysis. This method complements the FMEA process with a step evaluating the importance of each failure mode in terms of its impact on the system or process. This evaluation enables the identification of the most critical failure modes that require special attention.

3. FMEDA is another extension of FMEA [10]. This method includes an analysis of the system diagnostic capabilities, including its capacity to detect and diagnose failures. This analysis enables the assessment of the system's response effectiveness regarding potential failures and the mitigation of their consequences.

FMEA, FMECA, and FMEDA are widely used in managing risk and ensuring operation reliability. These methods enable the identification of potential problems early in the development and implementation of products or processes, which, in turn, contributes to improved quality and safety.

To validate the methodology, FMEDA was additionally conducted. This analysis is a key tool for assessing functional safety and reliability in power systems, particularly in the critical areas.

Leading global power equipment suppliers such as Siemens, ABB, and General Electric (GE) actively use FMEDA to ensure compliance with stringent industry standards such as IEC 61508 [11, 12].

FMEDA is applicable to a wide range of power equipment and systems. It is used to analyze sensors and transmitters, such as pressure and temperature sensors, which play a pivotal role in the control and protection systems. FMEDA is also applied to actuators, valves, control systems, and controllers, as well as high-voltage equipment, including switchgear and transformers. Furthermore, FMEDA is in demand in the realm of process automation, embracing automated process control systems (APCS) and programmable logic controllers (PLC), particularly within the nuclear and thermal power industries [13].

The leading manufacturers widely use this method. In particular, ABB employs this method to assess the functional safety of its devices, certifying them according to the IEC 61508 standard [13].

Based on FMEDA, the company calculates safety metrics such as the safe failure rate and the probability of failure on demand. Specifically, for pressure transmitters used in critical systems, FMEDA determines the failure rate, failure modes (safe or dangerous, detected or undetected), and the capability for self-diagnosis.

Siemens, in turn, develops automated FMEDA processes to reduce the time and effort required for analysis. The company applies this method to assess the safety of chips, boards, and integrated circuits, enhancing the reliability of control systems, particularly in automotive applications according to the ISO 26262 standard [12]. In the context of larger-scale solutions, FMEDA serves as an integral component of verification and validation procedures, ensuring operational safety throughout the product lifecycle.

While industrial giant GE does not publicly disclose detailed information about its FMEDA reports, the company is known to employ similar methods to improve the reliability of equipment such as turbines and generators. Specifically, GE uses advanced analytics and software tools to predict and prevent failures directly related to FMEDA concepts. By analyzing potential failures and their consequences, GE optimizes the maintenance strategies and minimizes the unexpected downtime.

The FMEDA process in the energy sector involves the collection of component data from a variety of sources, including failure rate databases such as OREDA, supplier inputs, and operational metrics. Then a failure mode is analyzed, identifying all potential causes of failure, such as short circuits or open circuits. The effects of each failure on the overall system operation are subsequently assessed.

FMEDA is therefore an integral component of the power equipment design and operation lifecycle, particularly at leading companies such as Siemens, ABB, and GE. This tool ensures a high level of safety and reliability, minimizing the risk of failures and ensuring compliance with stringent safety standards in this critical area.

Based on the methods studied, we selected FMEDA to calculate the failure rate for end systems, including single devices or a group of devices that perform a more complex function.

FMEDA was originally developed to analyze electronic devices. Currently, it is applied to the mechanical and electromechanical systems.

The main steps in calculating mean time between failures (*MTBF*), safety integrity level (*SIL*), and availability using FMEDA involve creating a FMEDA table. This table contains the data on effect, criticality, diagnosis, alongside warning, and is compiled for each system component.

First, the failure rate (λ) of a component is categorized based on consequences and diagnostics: λ^{DUC} is the detected unavoidable critical failure; λ^{DUN} is the detected unavoidable non-critical failure; λ^{DDC} is the detected dangerous critical failure; λ^{DDN} is the detected dangerous non-critical failure.

The overall failure rates for each category for the entire system are calculated by summing the corresponding failure rates for all components:

$$\lambda_{total}^{DUC} = \sum \lambda_i^{DUC}, \tag{1}$$

$$\lambda_{total}^{DUN} = \sum \lambda_i^{DUN}, \tag{2}$$

$$\lambda_{total}^{DDC} = \sum \lambda_i^{DDC}, \tag{3}$$

$$\lambda_{total}^{DDN} = \sum \lambda_i^{DDN}. \tag{4}$$

The *MTBF* for a system is calculated using formula (5):

$$MTBF = \frac{1}{\lambda_{total}} = \frac{1}{\sum \lambda_i}, \tag{5}$$

The safe failure fraction (SFF) is the proportion of safe and diagnosable dangerous failures relative to all failures that affect safety. It is calculated as follows:

$$SFF = \frac{\sum \lambda^{DUN} + \sum \lambda^{DDN} + \sum \lambda^{DDC}}{\sum \lambda^{DUC} + \sum \lambda^{DUN} + \sum \lambda^{DDC} + \sum \lambda^{DDN}}. \tag{6}$$

The probability of demand average failure (PFD_{avg}) is the average probability of failure on demand for systems that operate under low demand. It is calculated as follows:

$$PFD_{avg} = \lambda^{DUC}\left(\frac{T_1}{2}\right) + \lambda^{DDC}\left(\frac{MTTR + T_{nc}}{T_1}\right), \qquad (7)$$

where T_1 is the interval between regular tests, $MTTR$ is the mean time to recovery, T_{nc} is the time spent in an inoperative state due to a failure.

The calculated SFF and PFD_{avg} values are used to determine the achievable SIL, which depends on the system architecture and its operating mode.

The system is designed to operate using a Brayton cycle configuration and utilizes a dual-fuel combustion process that blends associated petroleum gas (APG) and natural gas.

The gas turbine unit (GTU) parameters are based on the specifications of a SIEMENS SGT-1000F gas turbine. In the nominal operating mode, the inlet temperature is 1583 K, the outlet temperature is 856 K, and the pressure rise is 15.8.

Several operating modes are considered by varying the gas flow rate, with the exhaust gas temperature ranging between 700 and 873 K. Efficient gas mixing depends on the uniform levels of temperature and pressure, which is why natural gas is additionally supplied by a compressor.

Full utilization of APG (1.48 kg/s) eliminates the need for natural gas. If the thermal parameters exceed the normal level, natural gas is supplied and regulated according to the parameters monitored by the Wobbe index sensor.

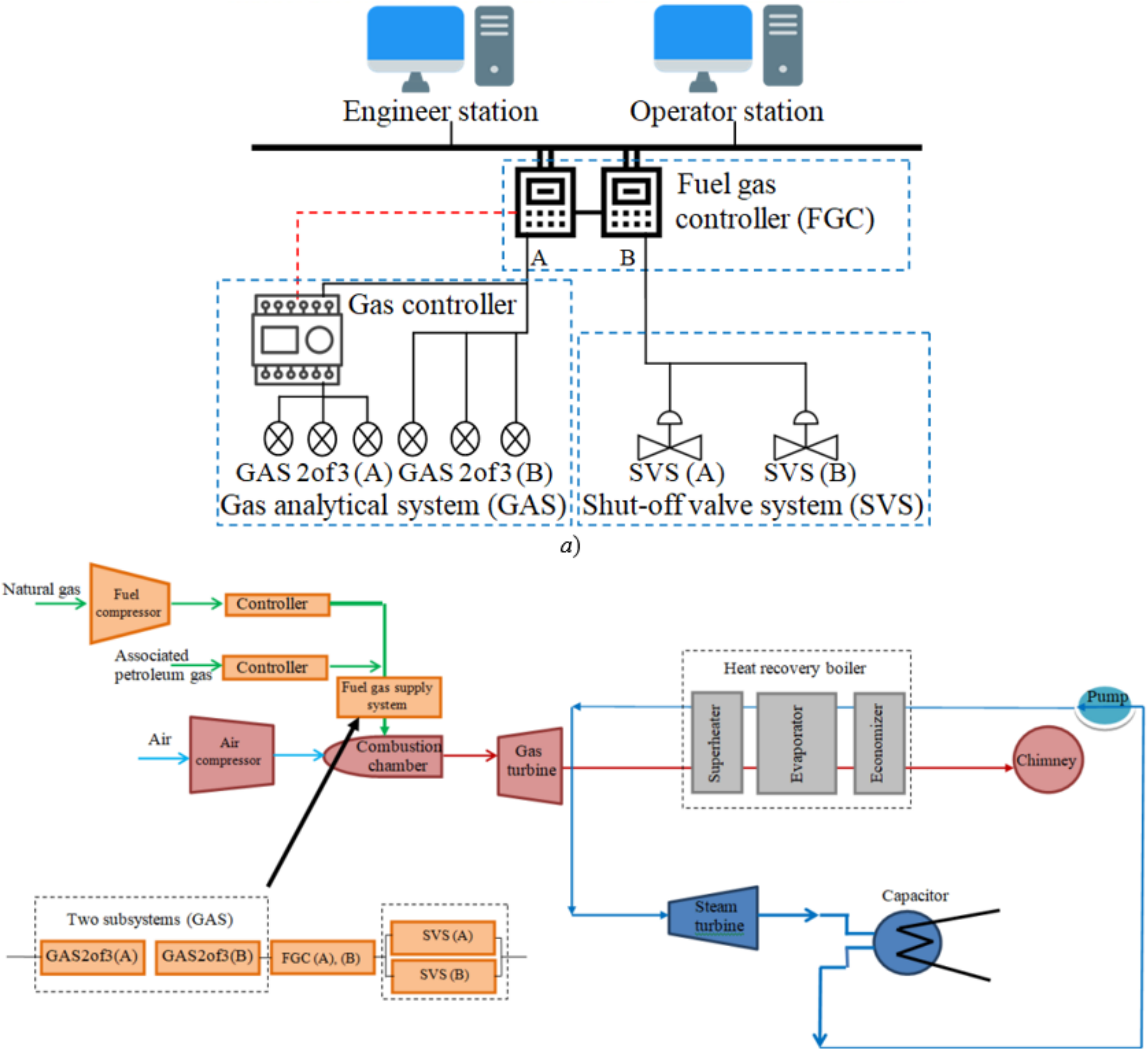

a)

b)

Fig. 1. Diagrams of the structural reliability (a) and the gas turbine system architecture (b) for the studied FGS.

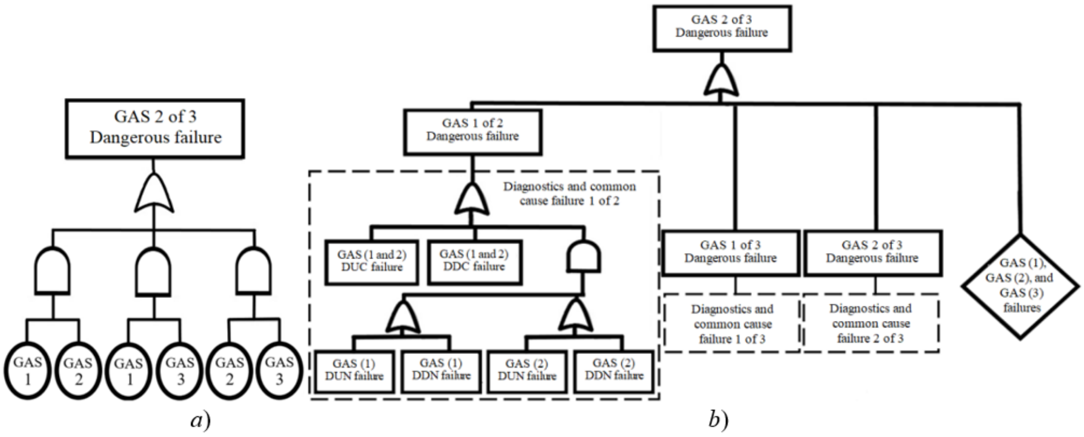

Fig. 2. Fault tree of the GAS subsystems in the 2-out-of-3 voting algorithm without failure diagnostics (a) and with failure diagnostics (b).

The air flow rate is up to 188 kg/s, ensuring the system operability in various modes. As gas volumes increase to 1.46 and 1.48 kg/s, respectively, and at an air flow rate of 150 kg/s, the inlet temperature remains below the permissible limits [1].

Based on the initial data, we investigate the system architecture presented in Fig. 1(a). It includes a gas analysis system (GAS), a shut-off valve system (SVS), a fuel gas controller (FGC), and engineer/operator stations.

The system has two GAS subsystems operating based on a 2-out-of-3 voting algorithm. The first subsystem, the 2-out-of-3 GAS (A), uses three remote gas analyzers of the gas chromatograph. The second subsystem, the 2-out-of-3 GAS (B), utilizes integrated gas analyzers operating with non-dispersive infrared (NDIR) sensors [14].

Gas chromatograph analyzers provide failure diagnostics, while NDIR gas analyzers do not. A reliability block diagram for the system under study is presented in Fig. 1(b) for the purpose of reliability analysis. Implementation of the fuel gas system primarily requires monitoring the system load and mandatory coordination of supply parameters for both natural and fuel gas at the point where both fuels are already mixed. The probability of success for the studied FGS ($P(t)_{\mathrm{FGS}}$) can be expressed using an exponential distribution as follows:

$$P(t)_{\mathrm{FGS}} = P(t)_{\mathrm{GAS}} P(t)_{\mathrm{FGC}} P(t)_{\mathrm{SVS}}, \qquad (8)$$

$$P(t)_{\mathrm{GAS}} = P(t)_{\mathrm{GAS}(2 of 3)(\mathrm{A})} P(t)_{\mathrm{GAS}(2 of 3)(\mathrm{B})}, \qquad (9)$$

$$P(t)_{\mathrm{FGC}} = P(t)_{\mathrm{FGC(A)}} P(t)_{\mathrm{FGC(B)}}, \qquad (10)$$

$$P(t)_{\mathrm{SVS}} = P(t)_{\mathrm{SVS(A)}} + P(t)_{\mathrm{SVS(B)}} - P(t)_{\mathrm{SVS(A)}} P(t)_{\mathrm{SVS(B)}}, \qquad (11)$$

$P(t)_{\mathrm{GAS}}$, $P(t)_{\mathrm{FGC}}$, and $P(t)_{\mathrm{SVS}}$ represent the probabilities of successful execution of the failure diagnostic functions for the GAS, FGC, and SVS, respectively.

The capacity of the GAS subsystem to effectively detect component failures is a key factor in improving system availability and safety.

In the 2-out-of-3 voting, there are two main types of fault trees for the GAS subsystem: with failure diagnosis and without it. These diagrams in Fig. 2(a) and 2(b) are true representations of reality.

Reliability models of the GAS subsystem with failure diagnostics must consider two key aspects: common cause failures (CCF) in the 2-out-of-3 voting lists and failures of automatic diagnostic functions.

Since any component can be either successful or unsuccessful, $P(t)$ is the complement of $F(t)$ to unity. The analytical reliability estimate $P(t)$ for the system and the probability distribution of random time-to-failure variables are assumed to be exponential.

The success probabilities for the GAS subsystem without failure diagnosis, the fuel gas controller, and the shut-off valve system are formulated as follows [15]:

$$P(t)_{GAS(2 of 3)(\mathrm{A}),w/0,\mathrm{Diag}} = 3e^{-2\lambda^{D} t_{ti}} - 2e^{-3\lambda^{D} t_{ti}}, \qquad (12)$$

$$P(t)_{GAS(2 of 3)(\mathrm{A}),w,\mathrm{Diag}} = 1 - 3\Big[(1 - e^{-\lambda^{DUC} t_{ti}}) + (1 - e^{-\lambda^{DDC} t_{at}}) + \\ + ((1 - e^{-\lambda^{DUC} t_{ti}}) + (1 - e^{-\lambda^{DDC} t_{at}}))^2\Big], \qquad (13)$$

$$P(t)_{FGC(A)} = P(t)_{FGC(\mathrm{B})} = e^{-2\lambda^{D} t_{ti}}, \qquad (14)$$

$$P(t)_{SVS(A)} = P(t)_{SVS(\mathrm{B})} = e^{-2\lambda^{D} t_{ti}}, \qquad (15)$$

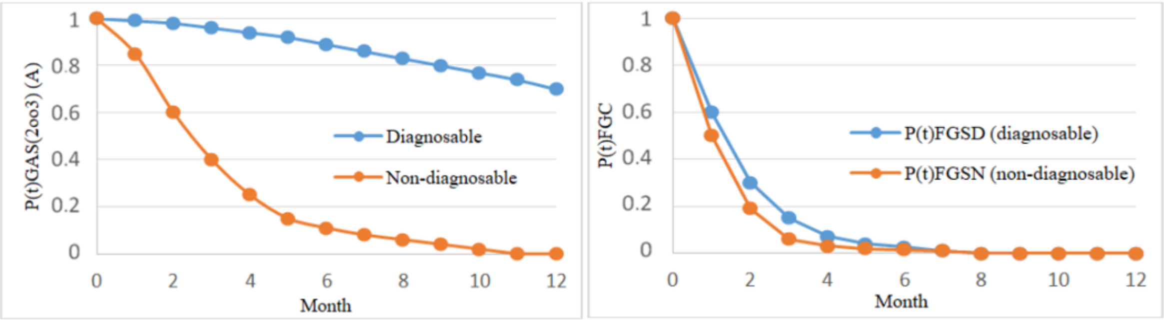

a) *b)*

Fig. 3. Reliability models (a) for the GAS subsystem with/without failure diagnostics; (b) for the FGC with/without failure diagnostics.

where t_{ti} is the time interval between tests or checks of the system or component condition. It can be established for regular reliability monitoring and the identification of potential problems before failures; t_{at} is the mean time required to repair a system or component after its failure. This indicator is important for assessing system availability and planning its maintenance [16].

These parameters are often used in reliability analysis and maintenance management to optimize diagnostics and repair processes, while minimizing equipment downtime.

This study examined reliability models of the GAS subsystem, as well as the FGS, operating with and without failure diagnostics. Graphs illustrating these models are presented for clarity.

Figure 3(a) shows the graphs corresponding to the reliability models of the GAS subsystem with and without failure diagnostics.

Substituting equations (12), (14), and (15) into equation (8), as well as equations (13), (14), and (15) into equation (8), we can obtain the reliability models for the FGS with and without failure diagnostics.

The results show that the failure diagnostic information provided by the gas chromatograph analyzers enhances the reliability of both the 2-out-of-3 GAS (A) and the FGC.

Design optimization relying on the FMEDA results enables the estimation of the initial *MTBF* based on statistical data and operating experience. Following the FMEDA, critical failure points were identified, facilitating modifications, the use of more reliable components, or the incorporation of redundancy.

The calculations demonstrated a 20% increase in *MTBF* and the system's upgrade from *SIL*2 to *SIL*3, exhibiting higher safety and reliability. Increased diagnostic coverage was achieved through the development of new diagnostic algorithms that detect a greater number of potentially dangerous failures, thereby reducing the frequency of undetected dangerous failures.

Optimization of maintenance is a key factor in ensuring the reliability and efficiency of systems. Before the integration of FMEDA, maintenance followed prescriptive regulations rather than actual operational state of the equipment. However, after conducting FMEDA and investigating the most probable failure modes and their possible origins, more effective maintenance strategies were formulated considering the equipment condition. This approach reduced the mean time to restore (*MTTR*) and

TABLE 1. FMEDA for the Studied Fuel Gas System

Case	Gas analysis system		Fuel gas composition		Gas turbine effect	Criticality	Diagnosis	Remark
	Normal	Error	Normal	Abnormal				
1	O	–	O	–	Normal state	–	Detectability	Correct state
					Triggering	Safe	Detectability	Impossible state
2	O	–	–	O	Normal state	Dangerous	Detectability	Impossible state
					Triggering	Safe	Detectability	Correct state
3	–	O	O	–	Normal state	Safe	Detectability	Diagnosis usage
					Triggering	Safe	Detectability	Correct state
4	–	O	–	O	Normal state	Dangerous	Detectability	Impossible state
					Triggering	Safe	Detectability	Correct state

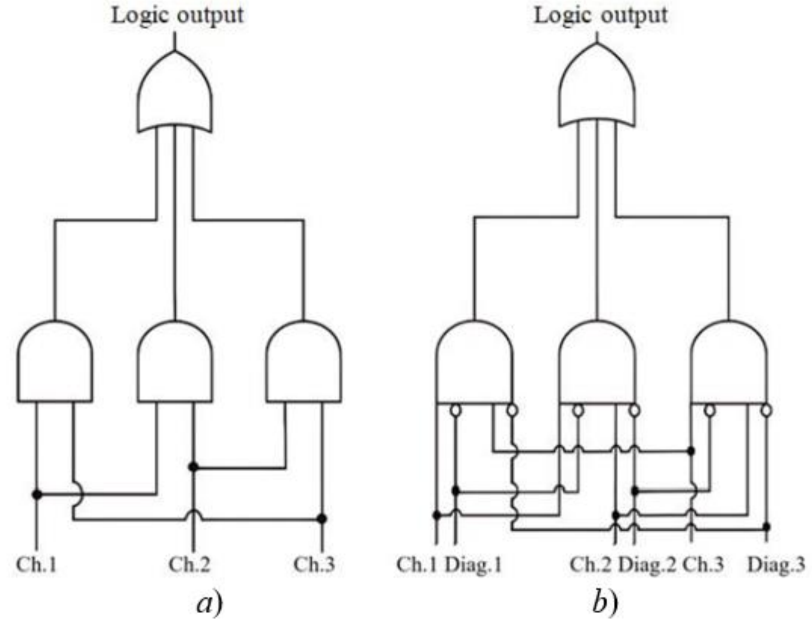

Fig. 4. Logic schemes of the existing safety interlock (a) and newly designed safety interlock (b). Ch.1, Ch.2, and Ch.3 are FGC input channels for the primary signals from the three gas analyzers. Diag. 1, Diag. 2, and Diag. 3 represent the FGC input channels designed to receive diagnostic information from the three gas analyzers.

increased the system availability.

System availability is defined as the ratio of the *MTBF* to the sum of the mean time between failures and the *MTTR*. The obtained results of FMEDA are presented in Table 1.

The analysis revealed the potential to improve the reliability of GAS and ensure the normal operation of the fuel gas composition in case 3. However, the standard protection system of the existing FGS would fail to activate in the absence of adequate failure diagnostics.

During project implementation, this model undergoes validation, a multi-stage process confirming that the model's reliability metrics correspond to actual operational data. This enables the model to be used for safety assessment.

At this stage, the model is verified by comparison with existing FMEDA systems (e.g., the project conducted by United Electric Controls in Watertown, MA, USA, under contract no. Q20/06-041). The project report, prepared by Brad Hitchcock, is available under UEC 20/06-041 R001, version V1, revision R1, November 20, 2020. This report confirms that the system has become more reliable due to the inclusion of factors that minimize the likelihood of overlooking errors that could lead to undetectable, dangerous failures [17–19]. To prevent an unwanted shutdown, a new protection system was developed without

TABLE 2. Results of Checking the Logic Operation of the Existing FGS Safety Interlock without Failure Diagnostics

Situation	Ch.1	Diag. 1	Ch.2	Diag. 2	Ch.3	Diag. 3	Logic Output
Operating	0	–	0	–	0	–	Normal
Ch. 1 error	1	–	0	–	0	–	Normal
Ch.1 and Ch. 2 error	1	–	1	–	0	–	Shutdown

*Operating = 0, Error = 1

TABLE 3. Results of Testing the Logic Operation of the Newly Designed FGS Safety Interlock with Failure Diagnostics

Situation	Ch.1	Diag. 1	Ch.2	Diag. 2	Ch.3	Diag. 3	Logic Output
Operating	0	0	0	0	0	0	Normal
Ch.1 error	1	1	0	0	0	0	Normal
Ch.1 and Ch.2 error	1	1	1	1	0	0	Normal

*Operating = 0, Error = 1

additional software and hardware modifications for the LNG plant with a failure diagnostic system (Fig. 4) [20].

IV. RESULTS

Table 2 presents the results of testing the logic operation of the existing FGS safety interlock without failure diagnostics. Table 3 shows the results of testing the logic operation of the newly developed FGS safety interlock using failure diagnostics.

Channels 1-3 (Ch. 1, Ch.2, and Ch.3) represent the FGC input channels designed to receive output signals from the three gas analyzers of the GAS subsystem. The FGC input channels designed to receive diagnostic information from the three gas analyzers are denoted by Diag. 1, Diag. 2, and Diag. 3.

The developed protection system successfully adapts to the operating conditions of the GAS subsystem in a 2-out-of-3 configuration, providing reliable protection against potential failures. Therefore, the new safety interlock based on the failure diagnostic capabilities of the gas chromatograph analyzers enhances the reliability of the tested FGS.

V. CONCLUSION

The study revealed the importance of FMEDA for the reliability analysis of complex systems, such as gas analysis and fuel gas control systems in power systems.

The use of a mixture of associated petroleum gas and natural gas in combined cycle gas turbines is instrumental in boosting the efficiency, environmental safety, and fuel diversification, while facilitating flexible fuel management, cost reduction, and enhancement of operational efficiency. The utilization of APG reduces oil production waste, lowers emissions, and contributes to sustainable development. Technologies for controlling the mixture composition are essential for stabilizing operation of turbines, extending their service life, and mitigating risks. The use of APG is also conducive to the expansion of the domestic fuel market and reduces dependence on imports, especially in the oil-producing regions of Russia. Overall, combining natural and associated petroleum gas boosts the efficiency, safety, and eco-friendliness of power plants.

This methodology allows for both the assessment of component failure rate and the identification of key aspects affecting the overall reliability of the system. The analysis shows that the implementation of diagnostic functions using gas analyzers significantly enhances failure detection efficiency, as well as availability and safety of the entire system.

The developed protection system, based on failure diagnostic capabilities, is an important step toward minimizing unplanned downtime and improving the reliability of the power plants. A comparative analysis of the existing and new safety interlocks confirmed the advantages of the diagnostic functions, creating promising avenues for optimizing maintenance and reliability management processes.

Thus, the findings from the study demonstrate the necessity of integrating advanced diagnostic methods into design and operation of complex technical systems to enhance their reliability and safety.

ACKNOWLEDGMENT

This study was funded by the Yugra Scientific and Technological Development Fund (Agreement no. 2024-518-09).

REFERENCES

[1] P. A. Batrakov, E. A. Ryzhnikova, A. A. Batrakova, “The use of associated petroleum gas by burning it in a mixture with natural gas in a combined cycle gas plant to generate mechanical energy and electricity,” in 2024 *Dynamics of Systems, Mechanisms and Machines (Dynamics 2024)*, vol. 1, Omsk, Russian Federation, Nov. 12–14, 2024, pp. 1–8, 2024.

[2] S. Khalid, et al, “Advances in fault detection and diagnosis for thermal power plants: A review of intelligent techniques,” *Mathematics*, vol. 11, no. 8, Art. no. 1767, 2023.

[3] C. Pengchao, “Advancements and future outlook of safety monitoring, inspection and assessment technologies for oil and gas pipeline networks,” *Journal of Pipeline Science and Engineering*, vol. 5, pp. 100–267, 2025.

[4] R. P. Bam, R. S. P. Gaonkar, C. P. George, “Machine learning-based predictive maintenance for diagnostics and prognostics of engineering systems,” in *Intelligent Prognostics for Engineering Systems with Machine Learning Techniques*. Boca Raton, USA: CRC Press, 2023, pp. 211–243.

[5] S. Liu, et al, “ECoalVis: Visual analysis of control strategies in coal-fired power plants,” *IEEE transactions on visualization and computer graphics*, vol. 29, no. 1, pp. 1091–1101, 2022.

[6] D. I. Candra, C. A. W. Tamayo, “Optimization for biogas power plants using automatic control of gas pressures,” *Journal of Mechatronics, Electrical Power, and Vehicular Technology*, vol. 4, no. 1, pp. 9–16, 2013.

[7] M. H. Sahraei, et al, “A survey on current advanced IGCC power plant technologies, sensors and control systems,” *Fuel*, vol. 137, pp. 245–259, 2014.

[8] A. A. Kapansky, “Modern strategies for using artificial intelligence to prevent accidents in technical resource supply systems,” *Bulletin of Kazan State Power Engineering University*, vol. 16, no. 1 (61), pp. 38–51, 2024. (In Russian)

[9] S. N. Kharlap, et al, “Features of methods for analyzing the types and consequences of failures of harvester devices,” in *Proc. Problems of transport safety materials of the XII International Scientific and Practical Conference dedicated to the 160th anniversary of the Belarusian Railway*, Gomel, Belarus, 2022, pp. 227–230. (In Russian)

[10] “Analysis of types and consequences (criticality, diagnosability) of failures (FMEA/FMECA/FMEDA).” [Online]. Available: http://www.kconsult-cis.com/fmea-fmeca.html. Accessed on: Oct. 15, 2025. (In Russian)

[11] L. Wang, F. Zhang, “Transmitter fault diagnosis technology for high-risk complex scenario,” in *Proc. 2024 6th International Conference on System Reliability and Safety Engineering (SRSE)*, Hangzhou, China, 2024, pp. 378–381.

[12] O. Ivasiuk, V. Kharchenko, “Using the FMEDA/FIT verification method to assess the cybersecurity of a programable logic controller: a new interpretation of the SIS principle,” *Aerospace Technic and Technology*, no. 1, pp. 76–90, 2024.

[13] M. Catelani, L. Ciani, G. Patrizi, “Logic solver diagnostics in safety instrumented systems for oil and gas applications,” *Safety*, vol. 8, no. 1, Art. no. 15, 2022.

[14] M. Catelani, L. Ciani, V. Luongo, “The FMEDA approach to improve the safety assessment according to the IEC61508,” *Microelectronics Reliability*, vol. 50, no. 9–11, pp. 1230–1235, 2010.

[15] B. Hitchcock, “Failure Modes, Effects and Diagnostic Analysis,” Series 12 Switch. United Electric Controls, Watertown, MA, USA. Contract Number: Q20/06-041. Rep. No.: UEC 20/06-041 R001. Version V1, Revision R1, Nov. 20, 2020.

[16] M. Chaari, et al, “A model-based and simulation-assisted FMEDA approach for safety-relevant E/E systems,” in *Proc. the 52nd Annual Design Automation Conference*, San Francisco, USA, 2015, pp. 1–6.

[17] D. K. Kostrin, “Modern electronic gas sensors: an overview of the basic physical principles of operation and promising developments,” *Physics*, vol. 17, no. 4, pp. 5–20, 2024. (In Russian)

[18] A. I. Kostogryzov, “On models and methods of probabilistic analysis of information security in standardized processes of system engineering,” *Cybersecurity Issues*, no. 6 (52), pp. 71–82, 2022. (In Russian)

[19] A. Julsereewong, T. Thepmanee, “Design and implementation of functional safety for repairable systems,” in *Proc. the SICE annual conference*, Nara, Japan, 2018. pp. 1638–1643.

[20] A. P. Durakovsky, S. V. Ponomarev, “A model of a system for countering software tools for studying code,” *Information Technology Security*, vol. 22, no. 1, pp. 22–24, 2015. (In Russian)

Petr A. Batrakov, Ph. D. in Engineering, serves as an Associate Professor in the Research Laboratory of Energy-Saving Engineering and Technology at Nizhnevartovsk State University. He is the author of 110 scientific papers. His research interests include burning processes, kinetic models, transformation of combustion products, and environmental safety.

Anastasia A. Batrakova is a second–year Master’s student in Thermal Power Engineering and Thermal Technology, specifically Industrial Thermal Power Engineering and Thermal Technology. She was awarded a scholarship from the Government of the Russian Federation in 2025. She is the author of four scientific papers. Her research interests include the studies of organic fuels and ways to convert them into advanced fuel types.

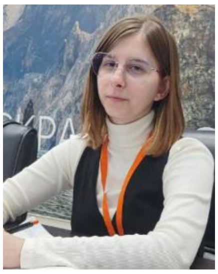

Ekaterina A. Ryzhnikova, a postgraduate student pursuing a Ph. D. in Theoretical and Applied Heat Engineering at the Siberian Federal University, is currently an assistant at the Research Laboratory of Energy-Saving Engineering and Technology at Nizhnevartovsk State University. She is the author of 14 scientific papers. Her scientific interests include burning processes, kinetic models, transformation of combustion products, and environmental safety.

Prospects for the Development of the Gas Motor Fuel Market in Russia

I.V. Provornaya[1], I.V. Filimonova[1,*], V.A. Vakhnova[2], A.A. Dolganov[1,2]

[1] Trofimuk Institute of Petroleum Geology and Geophysics of the Siberian Branch of the Russian Academy of Sciences, Novosibirsk, Russia
[2] Novosibirsk State University, Novosibirsk, Russia

***Abstract* — The study focuses on a gas motor fuel market, assessing its level of expansion across Russia's federal districts in the context of their specific economic situation and infrastructure capabilities. A unique set of key factors influencing the expansion of the vehicle fleet that uses natural gas as fuel is identified for each federal district. The current availability of the necessary compressed natural gas refueling infrastructure across different regions is analyzed in detail. The effectiveness of government support measures aimed at stimulating both demand and supply in the gas motor fuel market is evaluated. The paper also reviews forward-looking projects intended to further expand the market both in individual constituent entities of the Russian Federation and nationwide. The findings suggest that for the market to thrive, it is vital to enhance the regulatory and legal framework that governs interaction between the federal center and the regions, expand the network of refueling stations, promote innovative projects through private investment, and cultivate a positive public image of gas motor fuel.**

***Index Terms* — Natural gas, alternative fuel, gas motor fuel, GMF infrastructure, government support.**

---

[*] Corresponding author.
E-mail: filimonovaiv@list.ru

DOI: 10.25729/esr.2025.04.0012

Received September 15, 2025. Revised November 5, 2025. Accepted December 10, 2025. Available online December 29, 2025.

I. INTRODUCTION

There is a persistent global trend toward the adoption of alternative fuels in many countries. Gas motor fuel (GMF), which is based on natural gas rather than petroleum products, offers a number of significant advantages: it is economically beneficial, environmentally clean, and features a high level of safety. The most common types of gas motor fuel are liquefied natural gas (LNG), compressed natural gas (CNG), and liquefied petroleum gas (LPG).

Each of these fuel types is characterized by specific physical properties, transportation methods, and areas of application. LPG, a mixture of propane and butane, while relatively inexpensive and environmentally friendly, it nevertheless remains mostly a petroleum-refining product and poses explosion risks at certain atmospheric concentrations. Since government support programs for the development of gas-powered transport do not include this type of fuel, its impact on the market will not be considered in this study.

Possessing the world's largest natural gas reserves, Russia has substantial prospects for the development of the market for natural gas as a motor fuel [1]. This position underpins energy security and independence, while stimulating the production of gas equipment and the creation of new jobs in servicing and operating gas-powered transport. The shift to methane will likewise help reduce fuel costs, i.e., provide more affordable fuel for the public and businesses [2]. Consequently, the state policy is aimed at increasing domestic consumption of natural gas through the advancement of GMF infrastructure [3].

In 2021, the Government of the Russian Federation approved the "Transport Strategy of the Russian Federation to 2030 with a Forecast up to 2035," which envisions an increase in natural gas consumption by a factor of 15–19 by 2035 relative to 2021. According to the

Strategy, the key prerequisites for introducing new types of transport fuels encompass the development of fuel production, fuel cells, and engines; the establishment of a distribution system for new fuels, and the build-out of infrastructure. In addition, the state program for Energy Development 2024 was aimed at stimulating the adoption of natural gas-powered vehicles and increasing domestic consumption. Similar objectives were set out in the "Energy Strategy of the Russian Federation until 2050," published on April 12, 2025, which envisions a tenfold increase in methane consumption compared to 2023 levels.

The uneven development of the gas motor fuel (GMF) market across Russia's regions is heavily influenced by economic conditions, regional policy, and the suspension of government support programs, which limits the availability of statistics. This study aims to assess the level of natural gas development as a motor fuel in various regions of Russia.

II. LITERATURE REVIEW

The development of the gas-motor fuel market is relevant due to the strategic importance of converting transport to natural gas. The analysis of literature reveals a wide range of studies conducted to assess the gas motor fuel market. Methodological approaches utilized by researchers can be grouped into several most common areas: econometric modeling, economic efficiency assessment methods, life cycle assessment methods, and rating analysis.

Econometric modeling provides an important tool for analyzing and forecasting the gas motor fuel market. "Motor fuel choice: An econometric analysis" is a classic study that uses econometric models of multiple logistic regression to analyze consumer behavior when choosing motor fuels, including GMF [4]. The authors provide a quantitative framework for assessing the demand elasticity and consumer preferences for fuel. The study [5] uses Bayesian VAR models to estimate the elasticity of demand for automotive fuels and thoroughly examines the demand sensitivity to prices and external factors for the Italian market. Some papers forecast natural gas consumption in the transportation sector. A multi-hybrid model used in [6] combines statistical and deep learning models to predict natural gas consumption in the transport sector. A similar problem is solved in [7] for Pakistan's market. The advantages of econometric modeling include the ability to quantify the demand elasticity, while taking account of consumer behavior, the impact of competition and political factors. At the same time, there are disadvantages such as the need for extensive and reliable data, the models' sensitivity to the selection of variables and assumptions, challenges in interpreting the results under multidimensional influences, and limited data on the GMF market.

The methodology for assessing the economic efficiency of GMF is an important tool for making informed decisions on the introduction and development of the GMF market. In [8], an investment project for the creation of a network of compressed natural gas (CNG) filling stations in Romania is analyzed based on the cost-benefit analysis methodology. Some studies analyze the transition of freight transportation from diesel fuel to LNG [9, 10]. The greenhouse gas emissions from various types of motor fuels are assessed in [11, 12]. The disadvantages of methodological approaches to assessing the economic effectiveness of using GMF include the difficulty of adapting models to regional conditions; complexity of integrating technical, economic, and environmental parameters; and a high dependence on the quality and completeness of data.

The Well-to-Wheel (WTW) method is often used as a life cycle assessment approach for both fuels and vehicles. It is also employed to assess the energy efficiency and greenhouse gas emissions of vehicles throughout the entire lifecycle of fuel or energy. This approach is considered both for individual vehicles [13–15] and for the entire fleet [16–18]. Nevertheless, the Well-to-Wheel (WTW) method has a number of significant drawbacks that are important to consider when conducting analysis and making decisions. It offers limited life cycle coverage, ignores some environmental impacts, exhibits strong dependence on generalized and averaged data, and leaves out of consideration economic and social aspects.

The methods of rating the development of the gas motor fuel market are based on a variety of factors. The study [19] proposes a methodology for ranking vehicles using different types of fuels, including renewable and non-renewable. Data on the territorial ranking of the GMF market are often found in specialized industry reports and market research, which are difficult to analyze in detail.

Despite the variety of existing approaches to analyzing the gas motor fuel market, there are some disadvantages associated with the inaccessibility of the methodological approach and the statistical database, which does not allow us to thoroughly analyze the research results.

III. METHODOLOGY

The selection of factors plays an important role in constructing a regression model. According to the published research, the model's factors must satisfy certain requirements: they should be quantitatively measurable and independent of one another, since high correlation among factors may lead to inconsistent estimates. In theory, the model can include an unlimited number of factors that meet these conditions; in practice, however, a large number of explanatory variables does not yield the desired results. The introduction of superfluous indicators into the model will neither increase the coefficient of determination nor reduce the residual variance.

Accordingly, after selecting variables based on the research problem, a correlation analysis is needed to exclude redundant factors. A correlation matrix is employed to identify relationships between factors and a dependent variable, while examining pairwise correlations between independent variables. Correlation coefficients above 0.6 indicate interdependence of factors. In this case, one of the factors, the one demonstrating lower correlation with the dependent variable, should be excluded, as they duplicate each other.

There are also cases where two or more factors influence each other. This phenomenon is referred to as multicollinearity, which prevents assessing the effect of each factor separately. Multicollinearity leads to a loss of economic meaning for the regression parameters and their unreliable estimates. Testing for multicollinearity is carried out using the determinant of the factors' correlation matrix: if the determinant is zero or close to zero, the factors are highly dependent. The solution to multicollinearity reduces to excluding factors or incorporating their interaction terms into the model. In the latter case, the statistical significance of the interaction is verified using Fisher's F-test.

In the literature, the regression equation is commonly constructed using one of the following factor-selection procedures: backward elimination, forward selection, and stepwise regression analysis. The first method removes factors from the full set; the second adds factors to an empty model one by one; and the third combines the previous two, checking at each step the significance of the factors included in the model and removing those that are not significant.

This study involves examining the correlation matrix of the regressors, which allows for the removal of highly correlated variables at the first step. All remaining regressors are selected using a stepwise elimination procedure.

TABLE 1. Factors and Their Conventional Designations Used in the Model

Factor	Conventional Designation
Fixed Capital Investment	*Inv*
Gross Regional Product	*GRP*
Per Capita Income	*PCI*
Population	*Pop*
Number of Natural Gas station (automobile gas-filling compressor stations and cryogenic refueling stations)	*NGst*
Paved Road Density	*PRD*
Average Annual Methane Price	*AMP*
Harmful (Pollutant) Emission into Atmospheric from Motor Vehicles	*HEA*

To carry out the panel-data analysis, we formed a balanced panel dataset based on the databases of the websites of federal state statistical services (EMISS, Rosstat) and the State Traffic Safety Inspectorate (GIBDD), as well as the annual reports of Gazprom Gas Motor Fuel LLC. The analysis covered 66 regions selected by the volume of methane consumption in transport sector. Regions with zero values for this indicator were excluded from the analysis. In light of the lack of official statistics beyond 2022, particularly regarding the critical indicator of "the number of gas stations on highways," the data is confined to the period from 2015 to 2022. For convenience, all candidate factors considered for inclusion in the model were assigned designations, as shown in Table 1.

The panel datasets are compiled for each federal district. These panel data are used to build the regression models, including a pooled regression:

$$\begin{aligned} Ngt_{it} &= \alpha + \beta_1 NGst_{it} + \beta_2 Inv_{it} + \beta_3 GRP_{it} + \beta_4 PCI_{it} + \\ &+ \beta_5 PRD_{it} + \beta_6 AMP_{it} + \beta_7 HEA_{it} + \beta_8 Pop_{it} + \varepsilon_{it}, \end{aligned} \qquad (1)$$

where α and β_n are the model coefficients, i is the region index, t is the year (time) index, and ε_{it} is the error term;

a fixed-effects model:

$$\begin{aligned} Ngt_{it} &= i\mu_i + \beta_1 NGst_{it} + \beta_2 Inv_{it} + \beta_3 GRP_{it} + \beta_4 PCI_{it} + \\ &+ \beta_5 PRD_{it} + \beta_6 AMP_{it} + \beta_7 HEA_{it} + \beta_8 Pop_{it} + \vartheta_{it}, \end{aligned} \qquad (2)$$

where i is the region index, t is the year (time) index, β is the vector of regression coefficients, μ_i is the regional effects (fixed unknown parameters), ϑ_{it} is the error term, normally distributed with parameters $(0, \sigma_\vartheta^2)$; and a random-effects model:

$$\begin{aligned} Ngt_{it} &= \alpha + \delta_i + \beta_1 NGst_{it} + \beta_2 Inv_{it} + \beta_3 GRP_{it} + \beta_4 PCI_{it} + \\ &+ \beta_5 PRD_{it} + \beta_6 AMP_{it} + \beta_7 HEA_{it} + \beta_8 Pop_{it} + \lambda_{it}, \end{aligned} \qquad (3)$$

TABLE 2. Sample of Regions by Federal District

Federal District	Regions
Central	Regions: Belgorod, Bryansk, Vladimir, Voronezh, Ivanovo, Kaluga, Kostroma, Kursk, Lipetsk, Moscow, Oryol, Ryazan, Smolensk, Tambov, Tver, Tula, Yaroslavl; City of Moscow
Southern	Regions: Astrakhan, Volgograd, Rostov; Republics: Adygea, Crimea; Krasnodar Territory; City of Sevastopol
Northwestern	Regions: Arkhangelsk, Vologda, Kaliningrad, Leningrad, Novgorod, Pskov; Republic of Komi; City of Saint Petersburg
Siberian	Regions: Irkutsk, Kemerovo, Novosibirsk, Omsk, Tomsk; Altai Republic; Altai Territory
Ural	Regions: Kurgan, Sverdlovsk, Tyumen, Chelyabinsk; Khanty-Mansi Autonomous Area-Yugra; Yamalo-Nenets Autonomous Area
Volga	Regions: Kirov, Nizhny Novgorod, Orenburg, Penza, Samara, Saratov, Ulyanovsk; Republics: Bashkortostan, Tatarstan, Udmurt Republic, Chuvash Republic; Perm Territory
North Caucasian	Republics: Dagestan, Ingushetia, Kabardino-Balkaria, Karachay-Cherkessia, North Ossetia–Alania; Stavropol Territory
Far Eastern	Republic of Sakha (Yakutia), Sakhalin region

where i is the region index, t is the year (time) index, β is the vector of regression coefficients, δ_i is the regional effects, normally distributed with parameters $(0, \sigma_{\vartheta}^2)$, α is the intercept, λ_{it} is error term, normally distributed with parameters $(0, \sigma_{\lambda}^2)$.

All models were estimated by ordinary least squares (OLS) and subsequently tested for autocorrelation and heteroskedasticity of the errors. Where necessary, the OLS estimator was replaced with a generalized least squares (GLS) estimator. The most appropriate model was chosen using the Wald, Wooldridge, and Hausman tests. Based on the test results, the significant factors for each federal district were then identified.

IV. RESULTS AND DISCUSSION

The level of development of natural gas as a motor fuel for vehicles was analyzed separately for each federal district (Table 2 shows the regions considered).

The Far Eastern federal district includes only two regions, as only they demonstrate a positive value for the indicator of the "number of gas stations along highways." However, according to the statistical information available after 2022 on other factors, the market for natural gas as a motor fuel is burgeoning in the Far Eastern federal district, as well as throughout the country. The escalation of the geopolitical situation significantly affected the gas motor fuel market in Russia after 2022, resulting in the stimulation of import substitution policy, improvement in energy security, and adaptation to the instability of global energy markets. In the face of sanctions and limited access to international petroleum market, Russia has intensified the development of its domestic natural gas market as an alternative to traditional fuels. As a result, the Government of the Russian Federation has approved a Concept for the development of the gas motor fuel market in the Russian Federation until 2035, considering external geopolitical challenges.

The dependent variable is the number of motor vehicles running on natural gas. This indicator is chosen because it reflects consumer demand (i.e. it is more mass-market in nature than trucks and buses), demonstrating infrastructure accessibility for the population. Based on the findings in paper [7] along with the reports of Gazprom Gas Motor Fuel [20, 21], we identified the factors presented in Table 3.

The results of the regression analysis of the natural gas market in the Central federal district enable tests to determine whether individual effects are present (Table 4).

The first two tests confirmed the presence of individual effects, while the Hausman test helped select a model with random effects. Next, the residuals obtained in the selected model were checked for autocorrelation and

TABLE 3. Model Factors

Socio-economic	Industry-specific	Environmental
Fixed capital investment per capita (thousand rubles)	Number of refueling stations (units)	Emissions of harmful (pollutant) substances from transport (thousand tonnes)
Gross regional product per capita (thousand rubles)	Density of paved public roads (km per 1 000 km² of territory)	
Average per capita monetary income (rubles per month)	Average annual methane price (rubles)	
Population (thousand people)		

TABLE 4. Statistical Tests for Choosing the Best Model for the Central Federal District

Test	Calculated statistics	P-value	Output
Wald test	16.948	<2.2e-16	Reject the null hypothesis
Breusch-Pagan test	2.422	0.015	Reject the null hypothesis
Hausman test	8.017	0.155	Accept the null hypothesis

TABLE 5. FGLS Model with Fixed Effects for the Central Federal District

Indicator	Value	Standard deviation	P-value
Number of gas stations	-0.129	0.116	0.261
Investments in fixed assets per capita	-0.005	0.303	0.987
Average annual methane cost	-0.271	0.547	0.62
Paved-road density	6.503	2.297	0.004
Emissions into the atmosphere	-0.07	0.107	0.512
Multiple R^2		0.708	

heteroscedasticity. The Breusch-Godfrey test was used to test the hypothesis about the absence of first-order autocorrelation, since the p-value took the value 5.322e-08, it was rejected. The Breusch-Pagan test for heteroscedasticity was also performed, we obtained a p-value equal to 0.001, therefore, the null hypothesis about the absence of heteroscedasticity was rejected.

The next step is to eliminate the consequences of heteroscedasticity. A feasible generalized least squares (FGLS) model was built for both fixed and random effect regression, and then the best of the two models was selected using the Hausman test (Table 5).

The coefficient of determination in this model shows that the selected factors describe the dependent variable by 70%, which indicates the high quality of the model. At the same time, the p-value for each individual factor does not meet the accepted significance level of 0.1. The factors are eliminated step by step, starting with the regressor showing the largest p-value (Table 6).

Thus, the number of passenger vehicles that can run on methane in the Central Federal District is affected by the number of gas filling stations and the paved-road density. Both factors belong to the group of industrial factors, indicating that infrastructure plays a crucial role in the expansion of the market for natural gas as a fuel in the Central federal district. The negative coefficient for the number of CNG stations is attributed to the presence of multi-fuel filling stations in the regions of the Central federal district. Consequently, in the regions with a larger fleet, it may be more profitable to deploy these facilities.

In all districts, the “population size” factor is strongly correlated with other variables, therefore we exclude it from the analysis at the selection stage. GRP and fixed asset investments are strongly correlated, which is explained by Keynesian theory suggesting that investments are integral to aggregate demand, which fosters the growth of GRP. In each federal district, only one of these factors is included in the model. In most districts, the average monthly per capita income strongly correlates with other regressors, but it has a lesser effect on the number of methane-fueled vehicles. Consequently, we opted to exclude it at the selection stage in five out of eight districts.

Analysis of the models using the R software enabled us to identify the most significant factors for each federal district from those initially selected (Table 7).

TABLE 6. Total Coefficients for the Central Federal District

Regressors	Value	P-value
The number of gas stations	-0.169	0.069
Paved-road density	3.758	0.013

TABLE 7. Significant Factors by Federal District

Federal district	The number of CNG/LNG stations	Methane price	Fixed capital investment	Paved-road density	Pollutant emissions	Model
Central	1			1		GLS “within”
Southern	1	1	1	1		GLS “within”
Northwestern	1	1	1			GLS “within”
Siberian	1	1	1		1	GLS “within”
Ural	1		1		1	GLS “within”
Volga	1	1				GLS “random”
North Caucasian		1	1	1	1	GLS “within”
Far Eastern	1		1			GLS “within
All regions		1	1	1		GLS “random”

Moreover, the same factors entered the models with different signs across districts, indicating regional specificities in the development level of the gas motor fuel (GMF) market. The sets of significant factors also differ; therefore, to generalize the results at the national level, four of the most frequently occurring factors were highlighted: the number of CNG stations, paved-road density, the average annual methane price, and fixed capital investment per capita.

The number of vehicles running on GMF is strongly influenced by infrastructure, i.e., by the number of refueling stations. Accordingly, developing the infrastructure will drive the expansion of the vehicle fleet, which will positively affect methane consumption. Another important factor for Russia’s GMF market is the price of methane itself. It is therefore important to take measures to support both vehicle owners and entrepreneurs in this market for the equilibrium price to be acceptable for both the demand and supply sides. The last significant factor – fixed capital investment – underscores the need to attract investors to the developing natural gas market.

Note that in three districts –Siberian, Ural, and North Caucasian – there is a negative relationship between the number of methane-fueled vehicles and atmospheric pollutant emissions, which points to the environmental effect of this fuel type.

Table 7 also presents the final models selected. All of them take account for unobserved effects. These effects include government support measures at both the federal and regional levels. Essential measures to foster the growth of the methane market encompass providing subsidies for converting vehicles to methane; funding the construction of gas refueling infrastructure; reducing transport tax on methane-powered vehicles; and granting access to land for CNG stations without competitive bidding.

The calculations indicate that the level of GMF market development is influenced by different factors across the federal districts. This is due to the historically established spatial distribution of production, population, and infrastructure. In this context, federal GMF development policy should be differentiated for each district, aiming at addressing its specific barriers (for example, supporting LNG projects in the Siberian and Far Eastern federal districts, expanding the CNG network in the Central and Volga federal districts).

Since 2022, the gas motor fuel market has experienced the dynamic growth despite the current economic challenges and instability in global markets. The growth is ensured by an active government policy (in 2025, the Government of the Russian Federation approved the Concept for the development of the gas motor fuel market in the Russian Federation until 2035). This policy is driven by the economic benefits of using GMF compared to petroleum products, striving to bolster energy security and reduce the environmental burden. The share of GMF in the total fuel balance is currently modest, yet it holds a potential for a substantial growth in the future.

V. CONCLUSION

The development of the gas motor fuel (GMF) market in Russia varies significantly by region, which is associated with the differences in the level of government support, the political and economic landscape, and the availability of infrastructure.

Econometric analysis reveals that the significant factors for most federal districts are the number of CNG stations, paved-road density, the average annual methane price, and fixed capital investment per capita. The models selected based on statistical tests that feature fixed or random effects underscore the individual differences among regions within each federal district. Many models contain negative coefficients for certain factors, which can be explained by specific characteristics of the district or region. The primary apparent contradictions in the findings are a negative relationship between the number of vehicles and the infrastructure serving them, as well as a positive relationship between the price of methane and the number of vehicles using it as fuel.

For example, in the Northwestern federal district, a 1% expansion of infrastructure for methane-fueled vehicles leads to a 0.05% decrease in the number of such vehicles. In Saint Petersburg, methane sales per CNG station exceed the level observed in other constituent entities of the Russian Federation. Therefore, in this case, construction of new refueling stations is required solely to meet the demand of the existing vehicle fleet. The expansion of infrastructure is not the cause for the decrease in the number of vehicles, but rather an ineffective attempt to stimulate them, leading to the opposite result due to a complex imbalance in the market. Addressing this contradiction requires simultaneous stimulation of both supply (infrastructure) and demand (vehicles).

Furthermore, the Northwestern federal district can be used as an example of an individual region to explain the evident violation of the law of demand. In the Vologda region, growth in per capita income is proportional to growth in methane prices, therefore when consumers choose a vehicle, the cost of fuel has little influence on the purchase decision, while other characteristics, such as environmental performance, become more important. Thus, one of the individual unobserved effects may be vehicle owners' preferences. The positive relationship between the cost of methane and the number of vehicles using it as fuel may reflect a situation where the price of methane is in a favorable range for attracting investors and users, justifying the improvement in infrastructure, and providing environmental benefits.

The further dynamic development of the GMF market in Russia requires continuous refinement of the regulatory and legal frameworks, expansion of the refueling-station infrastructure, and support of innovative projects, while incentivizing demand for GMF vehicles. The following recommendations can be applied to ensure the successful advancement of the natural gas fuel market:

1. Adopt a comprehensive approach: ensuring active coordination between the federal center and the regions, incorporating tax incentives, subsidies for vehicle conversion to methane, and other incentives.
2. Attract investment: supporting domestic manufacturers of equipment and technologies, creating appealing conditions for private investors.
3. Enhance infrastructure: expanding the network of gas refueling stations and improving the quality of service for gas-fueled vehicles.
4. Cultivate a positive image: raising awareness about the benefits and environmental advantages of gas motor fuel through the mass media and social campaigns.

ACKNOWLEDGMENT

This research was supported by the Russian Science Foundation (RSF), Grant No. 23-78-10156, https://rscf.ru/project/23-78-10156/

REFERENCES

[1] A. E. Kontorovich, L. V. Eder, I. V. Filimonova, S. M. Nikitenko, "Key problems in the development of the power of Siberia project," *Regional Research of Russia*, vol. 8, no. 1, pp. 92–100, 2018.

[2] A. V. Komarova, I. V. Filimonova, A. Yu. Novikov, A. A. Kartashevich, "Greenhouse gas emissions from the oil and gas and coal industry of the Novosibirsk region," *Geology and Mineral resources of Siberia*, no. 4–1 (60), pp. 101–108, 2024. (In Russian).

[3] I. V. Provornaya, I. V. Filimonova, A. D. Krutilina, "Assessment of the influence of various factors on the change in the carbon intensity of the economies of the world," *Proceedings of Tomsk Polytechnic University. Georesource engineering*, vol. 335, no. 5, pp. 107–117, 2024. (In Russian)

[4] D. L. Greene, "Motor fuel choice: An econometric analysis," *Transportation Research Part A: General*, vol. 23, no. 3, pp. 243–253, 1989.

[5] A. Marabucci, L. Marchetti, "Price elasticity of fuel demand. An econometric approach," *European transport\Trasporti Europei*, no. 93, pp. 1–16, 2023.

[6] Z. Pala, "Comparative study on monthly natural gas vehicle fuel consumption and industrial consumption using multi-hybrid forecast models," *Energy*, vol. 263, Art. no. 125826, 2023.

[7] M. A. Khan, "Modelling and forecasting the demand for natural gas in Pakistan," *Renewable and Sustainable Energy Reviews*, vol. 49, pp. 1145–1159, 2015.

[8] E. Mitrică, "Economic analysis of the initial investment for intermediary introduction of compressed natural gas in Romania," *Energy for Sustainable Development*, vol. 76, Art. no. 101270, 2023.

[9] L. Langshaw et al., "Environmental and economic analysis of liquefied natural gas (LNG) for heavy goods vehicles in the UK: A Well-to-Wheel and total cost of ownership evaluation," *Energy Policy*, vol. 137, Art. no. 111161, 2020.

[10] M. Mohammad, M. Ehsani, "An investigation of natural gas as a substitute for diesel in heavy duty trucks and associated considerations," *arXiv preprint*, arXiv:1512.01421, 2015.

[11] S. Cheon et al., “Finding the most suitable vehicle type for projected years using analytic hierarchy process integrated with economic and environmental aspects,” *Journal of Cleaner Production*, vol. 426, Art. no. 139075, 2023.

[12] D. A. Hagos, E. O. Ahlgren, “Well-to-wheel assessment of natural gas vehicles and their fuel supply infrastructures–Perspectives on gas in transport in Denmark,” *Transportation Research Part D: Transport and Environment*, vol. 65, pp. 14–35, 2018.

[13] D.C. Rosenfeld et al., “Comparison of advanced fuels - which technology can win from the life cycle perspective?” *Journal of Cleaner Production*, vol. 238, Art. no. 117879, 2019.

[14] W. Choi, et al., “Greenhouse gas emissions of conventional and alternative vehicles: predictions based on energy policy analysis in South Korea,” *Appl. Energy*, vol. 265, Art. no. 114754, 2020.

[15] S. Ramachandran, U. Stimming, “Well to wheel analysis of low carbon alternatives for road traffic,” *Energy Environ. Sci*, vol. 8, pp. 3313–3324, 2015.

[16] A. Watabe, et al., “Impact of low emissions vehicles on reducing greenhouse gas emissions in Japan,” *Energy Pol*, vol. 130, pp. 227–242, 2019.

[17] M. Rüdisüli, et al., “Prospective life-cycle assessment of greenhouse gas emissions of electricity-based mobility options,” *Appl. Energy*, vol. 306, Art. no. 118065, 2022.

[18] I. Kim, J. Kim, J. Lee, “Dynamic analysis of well-to-wheel electric and hydrogen vehicles greenhouse gas emissions: focusing on consumer preferences and power mix changes in South Korea,” *Appl. Energy*, vol. 260, Art. no. 114281, 2020.

[19] H. S. Mohamadabadi, G. Tichkowsky, A. Kumar, “Development of a multi-criteria assessment model for ranking of renewable and non-renewable transportation fuel vehicles,” *Energy*, vol. 34, no. 1, pp. 112–125, 2009.

[20] Gazprom Gas Motor Fuel. Ranking of Russian Regions by the Level of Gas Motor Fuel Market Development. 2024 [Online]. Available: https://gmt.gazprom.ru/d/textpage/73/115/rejting-regionov-2024.pdf. Accessed on: Mar. 11, 2025. (In Russian)

[21] Gazprom Gas Motor Fuel. Ranking of Russian Regions by the Level of Gas Motor Fuel Market Development. 2023 [Online]. Available: https://gmt.gazprom.ru/d/textpage/73/115/reiting-regionov-2023.pdf. Accessed on: Mar. 11, 2025. (In Russian)

Irina V. Provornaya, Ph.D. in Economics, is a Senior Researcher at the Trofimuk Institute of Petroleum Geology and Geophysics of the Siberian Branch of the Russian Academy of Sciences, Novosibirsk, Russia. She is also an Associate professor in Novosibirsk National Research State University. Her scientific interests include analysis of the current state and forecast of the oil and gas market expansion in Russia and the world.

Irina V. Filimonova, D. Sc. in Economics, Professor, currently holds the position of Head of Laboratory at the Trofimuk Institute of Petroleum Geology and Geophysics of the Siberian Branch of the Russian Academy of Sciences, Novosibirsk, Russia. She also leads the Political Economy Chair in Novosibirsk National Research State University. Her scientific interests include strategic planning of the oil and gas industry development in Russia and the regions of Eastern Siberia and the Far East.

Victoria A. Vakhnova is a student at Novosibirsk National Research State University, Novosibirsk, Russia. Her scientific interests include forecasting the development of the gas market in Russia and globally.

Alexey A. Dolganov is a Master's student at Novosibirsk National Research State University, Novosibirsk, Russia. He also serves as an engineer at the Trofimuk Institute of Petroleum Geology and Geophysics of the Siberian Branch of the Russian Academy of Sciences, Novosibirsk, Russia. His scientific interests include forecasting the development of the oil and gas market in Russia and across the globe.

A System of Models for Studying the Impact of Hydropower Plants Planned in Mongolia on the Hydrological Regime of the Russian Part of the Selenga River Basin

V.M. Nikitin[1], N.V. Abasov[1], E.N. Osipchuk[1*], V.M. Berdnikov[1], V.S. Gasan[1]

[1] Melentiev Energy Systems Institute of Siberian Branch of Russian Academy of Sciences, Irkutsk, Russia

***Abstract* — The paper describes models designed to study the impact of hydropower plants (HPPs) planned in Mongolia on the hydrological regime of the Russian part of the Selenga river and Lake Baikal, considering various hydrological conditions and utilizing available technical information on the HPP projects. The developed models include software components for selecting an optimal dam site when precise coordinates are unavailable; constructing reservoir configurations and bathymetric curves demonstrating the reservoir water level-volume-area relationships; preparing hydrological statistics of water inflow into the planned reservoir by correlating meteorological indicators with flow; modeling HPP operating conditions based on different criteria. The primary object of this study is the Egiin Gol HPP on the Eg river, a left tributary of the Selenga river. Mongolia is planning to begin its construction in the coming years. The produced models assess the potential impact of the Egiin Gol HPP reservoir filling and operation on hydrological regimes across various water periods in the downstream pool, along its entire length from the HPP dam to the Selenga river inflow into Lake Baikal. The findings from the modeling serve as the basis for further research into the possible impact of the HPPs planned in Mongolia on the ecosystems of the Selenga river and Lake Baikal.**

***Index Terms* – Reservoir design, modeling of hydropower plant operating conditions, hydrological studies, flow management, transboundary basin, the Selenga river, Egiin Gol hydropower plant.**

I. INTRODUCTION

The development of Mongolia's hydropower industry began in the 1960s, when the Soviet Institute of Hydroproject and the Mongolian Ministry of Agriculture conducted joint preliminary studies of the Selenga, Egiin Gol, Orkhon, Tuul, and Khovd rivers, alongside other tributaries of the Selenga [1–3]. As a result, the potential hydropower capacity of the Selenga river basin was estimated at 1.5 GW, allowing for the annual electricity generation of 7.5 billion kWh. The total theoretical hydropower potential of all Mongolian rivers is even higher. According to research conducted by the Institute of Meteorology of Mongolia in the 1960s–1970s, the average annual flow of 3 800 small and large rivers in the west and north of the country is 34.6 km^3 per year with a potential capacity of 6.3 GW. The most significant resources, almost three quarters of all potential, are concentrated in the northern Mongolia (the basins of the Selenga, Onon, and Kerulen rivers). The remaining potential is found in the western part of the country, within the basins of the Khovd and Zavkhan rivers.

In 1973–1976, the Leningrad Branch of the "Hydroproject" Institute (Gidroproekt) developed a scheme for the placement of potential hydropower plants in the Selenga river basin, identifying future sites for their location and estimating the main parameters (head, installed capacity, and electricity generation) for 22 potential HPPs [3].

In the early 1990s, after the collapse of the USSR, Mongolia began to cooperate more actively with

---

[*] Corresponding author.
E-mail: osipchuk@isem.irk.ru

DOI: 10.25729/esr.2025.04.0013

Received September 15, 2025. Revised November 5, 2025. Accepted December 18, 2025. Available online December 29, 2025.

international hydropower companies on the design of hydropower plants [4–9]. Companies from Switzerland, Italy, and Mongolia carried out the first feasibility study and an Environmental Impact Assessment (EIA) for the Egiin Gol hydropower plant project between 1991 and 1994. The project was not developed further for various reasons. A new stage in the evolution of hydropower in Mongolia started in 2012. By this time, the demand for electricity had increased significantly, and there was a shortage of maneuvering capacities in the energy system due to the rapid growth of Mongolia's economy. The Government of Mongolia decided to implement the Shuren hydropower plant, the Egiin Gol hydropower plant, and the Orkhon-Gobi projects [9]. The World Bank was involved in the feasibility studies for these projects between 2013 and 2015.

In 2016–2017, commissioned by the Ministry of Natural Resources and Environment of the Russian Federation, the Irkutsk Scientific Center and several institutes of the Siberian Branch of the Russian Academy of Sciences (SB RAS), including the Melentiev Energy Systems Institute (ESI SB RAS), conducted a study titled “Assessment of the impact of planned construction of hydropower plants in Mongolia on the transboundary Selenga river basin within the borders of the Russian Federation.” The findings from the study indicated that future Mongolian hydropower plants, including the Egiin Gol HPP, could potentially have a significant impact on the ecosystem of the Russian part of the Selenga river basin, the primary tributary of Lake Baikal.

The Government of Mongolia included the construction of the Egiin Gol Hydropower plant in the list of priority projects for implementation in 2023. A joint meeting on this issue between the Ministers of Natural Resources of the Russian Federation and Mongolia, as well as the Presidents of the Russian and Mongolian Academies of Sciences, was held in Moscow in October 2024. Following the meeting, Russia and Mongolia agreed on an Action Plan for a collaborative study to assess the possible impact of the Egiin Gol HPP project on Lake Baikal and the Selenga river and decided to establish a Russian-Mongolian Expert Group. This assessment will involve investigating possible changes in the hydrological regimes of the Selenga river, relative to natural conditions, within the borders of the Russian Federation, due to the future construction of the Egiin Gol HPP in Mongolia. This analysis will also focus on the potential effects of the Egiin Gol HPP construction on the ecosystem of the Selenga river basin and Lake Baikal, highlighting the environmental and social aspects according to the internationally accepted frameworks of environmental impact assessment of hydraulic structures, and adhering to the UNESCO standards. ESI SB RAS is one of the participants in these studies.

Since 2013, ESI SB RAS has developed various models for energy, water management, hydrological, hydraulic, and environmental studies on operating hydropower plants and those under planning and design [10–15].

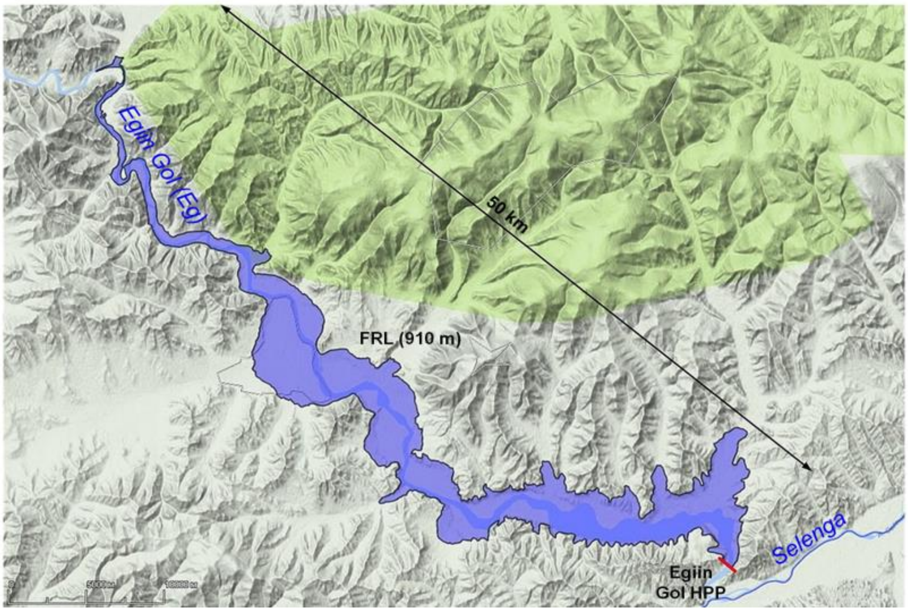

Fig. 1. Configuration of the Egiin Gol hydropower plant.

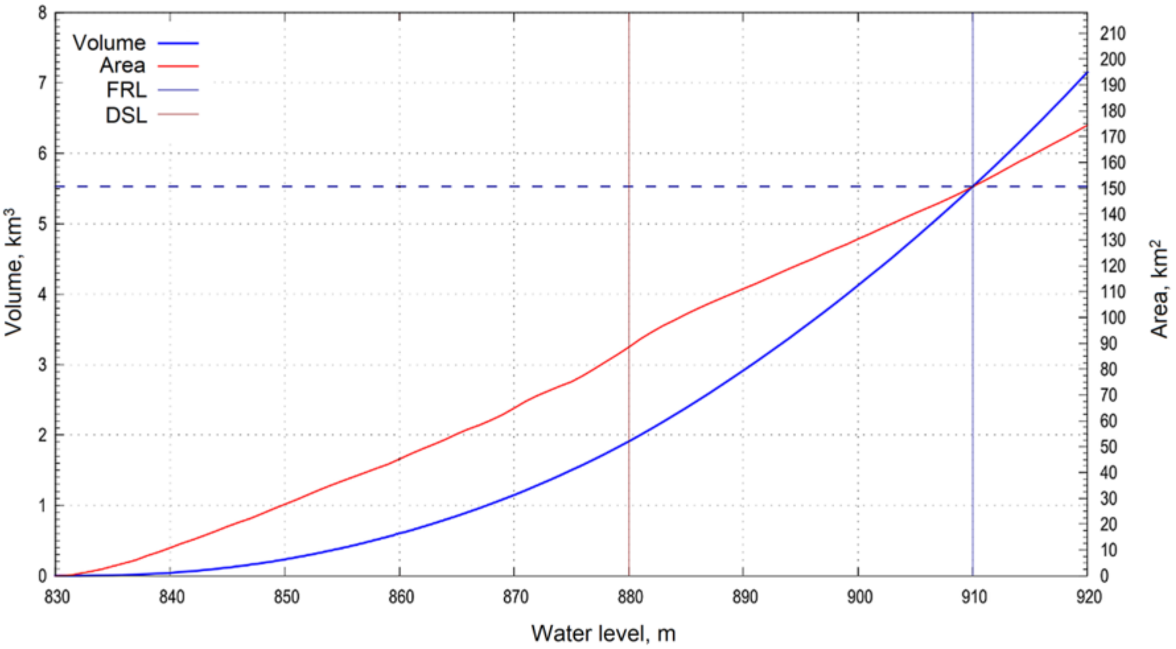

Fig. 2. The Egiin Gol HPP reservoir water level-volume-area relationships.

II. STRUCTURE OF MODELS OF HYDROPOWER PLANTS UNDER DESIGN (METHODOLOGY)

The study and analysis of the future operating conditions of the planned (potential) power plants require various pre-design engineering surveys, including modeling.

The choice of a dam site is based on three main criteria: 1) the minimum length (for economic reasons); 2) the optimal live storage of the reservoir (for various flow rates); 3) the maximum inflow of water into the reservoir (based on hydrological surveys). Geophysical, geological, water management, socio-economic, and environmental surveys are additionally required for the selected dam site and height. Modern GIS data of the digital relief (1 arcsecond or less) enable the creation of various algorithms for selecting the dam site. For example, one can select the dam with a specified interval from the center of the river, rotating it around the central point to find the minimum length at a given height of the dam on the digital relief. Figure 1 shows the reservoir configuration of the Egiin Gol hydropower plant. Figure 2 demonstrates the reservoir contour and its bathymetric curves of the water level-volume-area relationships, obtained by modeling.

The bathymetric curves, which show the reservoir water level-volume relationship, are successively determined by increasing the water level at specified intervals and identifying the configuration of the waterline through the construction of isolines. This process involves calculating the area for each water level elevation. If the specified interval is small, the volume (V) can be calculated using formula

$$V(h) = V(h - \Delta h) + \big(S(h) + S(h - \Delta h)\big)\Delta h / 2\,, \quad (1)$$

where S is the area; h is the water level; Δh is the specified interval of the water level change (sampling accuracy).

Reservoir live storage refers to the volume of water between the Dead Storage Level (DSL) and the Full Reservoir Level (FRL). The volume between the FRL and the Maximum Water Level (MWL) is used exclusively to manage excess flow and protect the hydropower plant from potential destruction.

There are no reliable statistics on average monthly and ten-day flow rates for the poorly studied river basins in Mongolia. When statistical data are unavailable for the selected site, the flow rates are normally determined by precipitation over the drainage area, surface temperatures, relative humidity, wind speed, and the average gradient of individual river segments. The runoff parameters can be estimated using average meteorological values for the basin. Since meteorological data are much more representative (e.g., average monthly GPCC precipitation values with a resolution of 1°×1° for the period since 1901 and average daily NOAA temperatures since the last century [16–19]) and highly correlated with known flow rates in certain sites, the runoff of the Selenga river basin in the Mongolian part can be approximately estimated using the following procedure.

The average annual flow rate of the river Q^y for year y is estimated using formula

$$Q^y = \bar{Q} + k_1 \sum_{t\in M_1} \Delta S_t^y - k_2 \sum_{t\in M_2} \Delta S_t^y \Delta T_t^y, \qquad (2)$$

where $\bar{Q}$ is the long-term average annual flow rate; ΔS_t^y, ΔT_t^y are deviation of average monthly precipitation and temperatures from the norm for year y and month t; $M_1 = \{10, 11, 12, 1, \ldots, 9\}$ is the set of months of the hydrological year (from the 10th month of the previous year to the 9th month of the current year); $M_2 = \{6, \ldots, 9\}$ is the summer and autumn months; k_1, k_2 are coefficients that take into account the proportions of precipitation and evaporation depending on the temperature deviation from the norm.

Using the known actual flow data Q_{act}^y for year y, we find the unknown coefficients k_1, k_2 by applying least squares method:

$$\sum_{y\in Y} \left(Q_{act}^y - Q^y\right)^2 \to \min_{k_1, k_2}, \qquad (3)$$

where Y is the set of years of flow data.

The estimations of the flow during the summer-autumn months should consider the flow of the previous month through the following formula:

$$Q_t^y = \bar{Q}_t + r_1 \sum_{t\in M_1} \Delta S_t^y - r_2 \sum_{t\in M_2} \Delta S_t^y \Delta T_t^y + r_3 Q_{t-1}^y, \qquad (4)$$

where $\bar{Q}_t$ is the average annual flow for month t; Q_{t-1}^y is flow of the previous month; r_1, r_2, r_3 are empirical coefficients that take into account precipitation for the year, evaporation in the summer, and flow of the previous month.

The flow during the winter months is negligible and can be estimated based on that of the previous month and the winter temperature deviation.

Evaporation plays an important role in the water balance in the Mongolian part of the Selenga river basin, which is attributed to high air temperatures, winds, and low relative humidity. According to the simplified methodology developed by the State Hydrological Institute, evaporation can be determined using following formula [20–23]:

$$I(t,\tau) = 0.14\Big(1 + 0.72V(t,\tau)\big(e_w(t,\tau) - e_a(t,\tau)\big)\Big), \qquad (5)$$

where $I(t,\tau)$ is the evaporation depth from the water surface over period $[t, t+\tau]$, mm/ km^2; τ is the calculation period in days; $V(t,\tau)$ is the average wind velocity at 2 m height above ground level over period τ, m/s; $e_w(t,\tau)$ is the average water vapor pressure of saturated air depending on the water temperature over period τ, hPa or mbar; $e_a(t,\tau)$ is the average water vapor pressure in the air over period τ, hPa.

Empirical formulas for average water and air

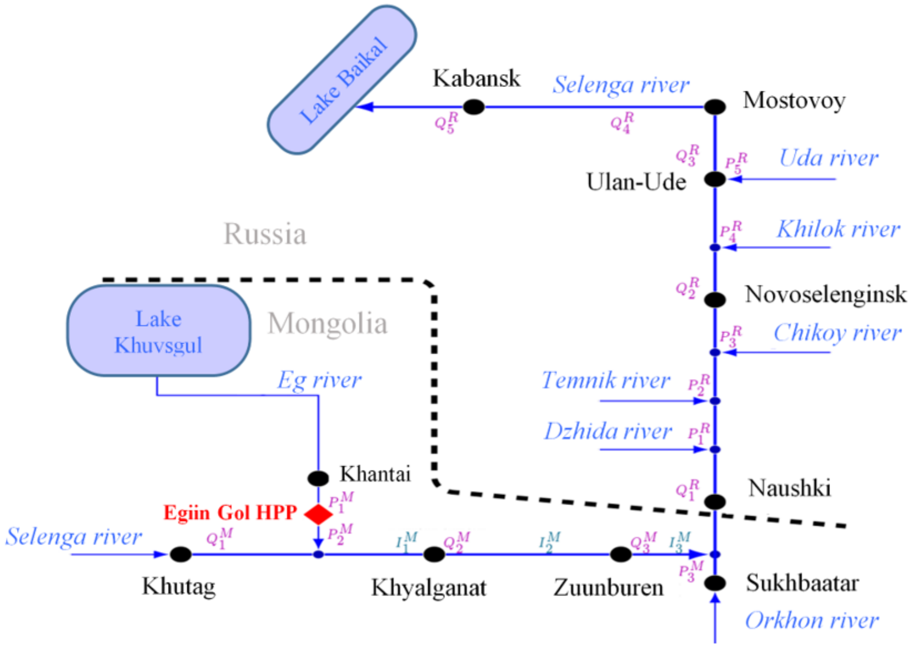

Fig. 3. Hydrologic map of the Selenga river designed to assess the potential impact of the regulated regime of the Eg river on the Russian part of the Selenga river and Lake Baikal.

temperatures over period τ, and average relative air humidity $f(t,\tau)$ are used to calculate $e_w(t,\tau)$, $e_a(t,\tau)$:

$$e_w(t,\tau) = \lambda_w \cdot 10^{\lambda_1 \frac{T_w(t,\tau)}{\lambda_2 + T_w(t,\tau)}}, \tag{6}$$

$$e_a(t,\tau) = \lambda_a f(t,\tau) \cdot 10^{\lambda_1 \frac{T_a(t,\tau)}{\lambda_2 + T_a(t,\tau)}}, \tag{7}$$

where λ_w, λ_a, λ_1, λ_2 are some numerical empirical coefficients; $T_w(t,\tau)$, $T_a(t,\tau)$ are temperature of water and air at time t over period τ.

Figure 3 shows a hydrologic map of the Selenga river, created to analyze the impact of the planned Egiin Gol HPP. The map reflects the main tributaries and assessment sites used to model the impact of changes in hydrological regimes after the commissioning of the HPP and during the reservoir filling period.

The map highlights the following gauging stations:

– Khutag, Khyalganat, Zuunburen, Khantai, Sukhbaatar in Mongolia;

– Naushki, Novoselenginsk, Ulan-Ude, Mostovoy, Kabansk in Russia.

Flow rates for the main bed of the Selenga River at the gauging stations are indicated by Q_i^M, Q_j^R (the M index for Mongolian i^{th} station and the R index for Russian j^{th} station). Flow rates for the tributaries are indicated by P_i^M, P_j^R. The indicators I_i^M, ω_i^M, ω_j^R relate to evaporation (and dispersion), as well as discrepancies for Mongolian and Russian parts.

The flow rate balance relations are given below (time indicators are omitted for clarity):

$$\begin{gathered}
Q_2^M = Q_1^M + P_2^M - I_1^M \pm \omega_2^M, \\
P_2^M = P_1^M \text{ for natural conditions of the Eg river,} \\
P_2^M \neq P_1^M \text{ for regulated conditions of the Eg river,} \\
Q_3^M = Q_2^M - I_2^M \pm \omega_3^M, \\
Q_1^R = Q_3^M + P_3^M - I_3^M \pm \omega_1^R, \\
Q_2^R = Q_1^R + P_1^R + P_2^R + P_3^R \pm \omega_2^R, \\
Q_3^R = Q_2^R + P_4^R + P_5^R \pm \omega_3^R, \\
Q_4^R = Q_3^R \pm \omega_4^R, \\
Q_5^R = Q_4^R \pm \omega_5^R.
\end{gathered} \tag{8}$$

The flow rate of the Selenga River into Lake Baikal is $Q_5^R(t,\tau)$ for any time t and the aggregation (averaging) period τ. The main hydrological model sections that necessitate flow rate balance check are: 1) Khutag–Khyalganat; 2) Khyalganat–Zuunburen; 3) Zuunburen–Naushki; 4) Naushki–Novoselenginsk; 5) Novoselenginsk–Mostovoy; 6) Mostovoy–Kabansk.

The regulated flow is modeled using the following main parameters of planned HPPs and reservoirs:

$Q = q + q^{spill}$ is the flow rate passing through HPP site, m^3/s;

q is the flow rate through turbines of HPP, m^3/s;

q^{spill} is the flow rate over spillway, m^3/s;

h^{UP}, h^{DOWN} are the upstream and downstream pool elevations, m;

$H = h^{UP} - h^{DOWN}$ is the water head, m, defined as the upstream pool elevation less the downstream pool elevation (in this paper, the gross head is used neglecting head loss);

W is the HPP capacity, kW, calculated by formula

$$W(t) = 9.81\eta H(t) q(t), \tag{9}$$

where η is the efficiency of hydropower equipment;

W^{inst} is the installed capacity, representing the maximum power output of HPP;

W^{firm} is the firm capacity, i.e. the minimum power output, provided by the HPP to meet the power system load;

E is the power output of HPP, kW·h, over period T, calculated by following formula:

$$E(t_0,T) = \int_{t_0}^{t_0+T} W(t)\,dt; \tag{10}$$

h^{DSL}, V^{DSL} are the Dead Storage Level (DSL) and its corresponding volume, representing the portion of the reservoir capacity not used under normal operating conditions;

h^{FRL}, V^{FRL} are the Full Reservoir Level (FRL) and its corresponding volume, representing the maximum water level maintained by the hydraulic structure under normal operating conditions;

h^{MWL}, V^{MWL} are the Maximum Water Level (MWL) and its corresponding volume, used for additional flood flow transformation (moderation);

V^{live} is the live storage of the reservoir used for active flow regulation;

$V^{total} = V^{DSL} + V^{live}$ is the total storage of the reservoir, comprising dead and live storage.

The primary indicator for HPP management is the flow rate passing through the dam $Q(t)$, which affects the storage volume of the reservoir $V(t)$, as well as the levels of upstream $h^{UP}(t)$ and downstream $h^{DOWN}(t)$ pools. The HPP capacity $W(t)$ depends on the water head $H(t)$ and is determined by changes in the flow rate passing through the turbines $q(t)$.

Given the complexity of the inflow structure, this study analyzes the net inflow $P(t)$, which includes filtration, evaporation, and groundwater flow in accordance with the water balance.

A model for HPP management [14] is presented as a mathematical programming problem, incorporating averaged HPP operating parameters for various time periods (ten-day, monthly, quarterly, and annual).

We consider the HPP management problem for a given vector of net inflow. The specified time interval $t \in [t_0, T]$ is divided into N equal periods of duration τ with constant values of variables within each interval.

The change in the reservoir storage volume depends on the net inflow and the flow rate passing through the HPP. These characteristics determine the water balance equation, which has the following form:

$$\frac{dV}{dt} = P(t) - Q(t),\ t \in [t_0, T]. \tag{11}$$

Equation (11) can be represented in a finite-difference form for the j^{th} period:

$$V_j = V_{j-1} + (P_j - Q_j)\tau,\ \ j = \overline{1, N}, \tag{12}$$

where P_j and Q_j are time-averaged indicators, V_{j-1} and V_j are the characteristics at the beginning of the intervals.

The input data include:

$P = (P_1, \ldots, P_N)$ – the vector of the averaged values of net inflow into the reservoir;

$h^{UP}(t_0) = h_0^{UP}$, $h^{DOWN}(t_0) = h_0^{DOWN}$ – the initial levels of upstream and downstream pools;

$h^{UP} = f^{DOWN}(V)$ – the upstream pool level-volume curve;

$h^{UP} = f^{DOWN}(Q)$ – the curve of relationship between the downstream pool level and the flow rate passing through HPP.

The variables are:

$Q = (Q_1, \ldots, Q_N)$ – the vector of the averaged flow rates passing through HPP;

$V = (V_1, \ldots, V_N)$ – the vector of the storage volumes;

$h^{UP} = (h_0^{UP}, \ldots, h_N^{UP})$, $h^{DOWN} = (h_0^{DOWN}, \ldots, h_N^{DOWN})$ – the vectors of the upstream and downstream pool levels.

Based on equation (12) and unique relationships $h^{UP} = f^{UP}(V)$, $h^{DOWN} = f^{DOWN}(Q)$ known for the reservoir, we can use the vector of averaged flow rates Q to express the vectors of V, h^{UP}, h^{DOWN} and the indicators for periods $j = \overline{1, N}$ that include:

$E_j = k^E \tau W_j$ – the electricity generation over period τ, where k^E is numerical coefficient for converting dimensions;

$W_j = 9.81\eta q_j (H_j + H_{j-1})/2$ – the average power output of HPP;

$H_j = h_j^{UP} - h_j^{DOWN}$ – the water head;

$q_j = Q_j - q_j^{spill}$ – the flow rate through the HPP turbine, where q^{spill} is the flow rate over spillway, which depends on the operational characteristics of the turbines and constraints of installed capacity of HPP.

The mathematical programming problem for HPP management is formulated as follows: for a given vector P, optimization criterion, equality constraints B, and inequality constraints G, it is necessary to find the optimal vector $X = \{Q, q, q^{spill}, h^{UP}, h^{DOWN}, V, E, W, H\}$, defined as follows:

$$F(P, X) \to \min_X, \tag{13}$$

$$B = \left\{ b_k(X) = 0 : k = \overline{1, N^B} \right\}, \tag{14}$$

$$G = \left\{ g_k(X) \geq 0 : k = \overline{1, N^G} \right\}, \tag{15}$$

where F is a given function; b_k is a set of equality constraints; g_k is a set of inequality constraints; N^B, N^G are the numbers of components in B and G.

The optimal vector X obtained from problem (13–15) is employed to determine the above-described HPP and reservoir management indicators.

Function F can take various forms depending on the reservoir filling or drawdown conditions. The primary optimization criteria include: maximum firm capacity of the HPP during the winter period; maximum HPP electricity output value (in monetary terms), reflecting the total electricity output from the HPP across periods, taking into account penalties for deviations from planned targets, as well as penalties from the flow rate over spillway in summer period.

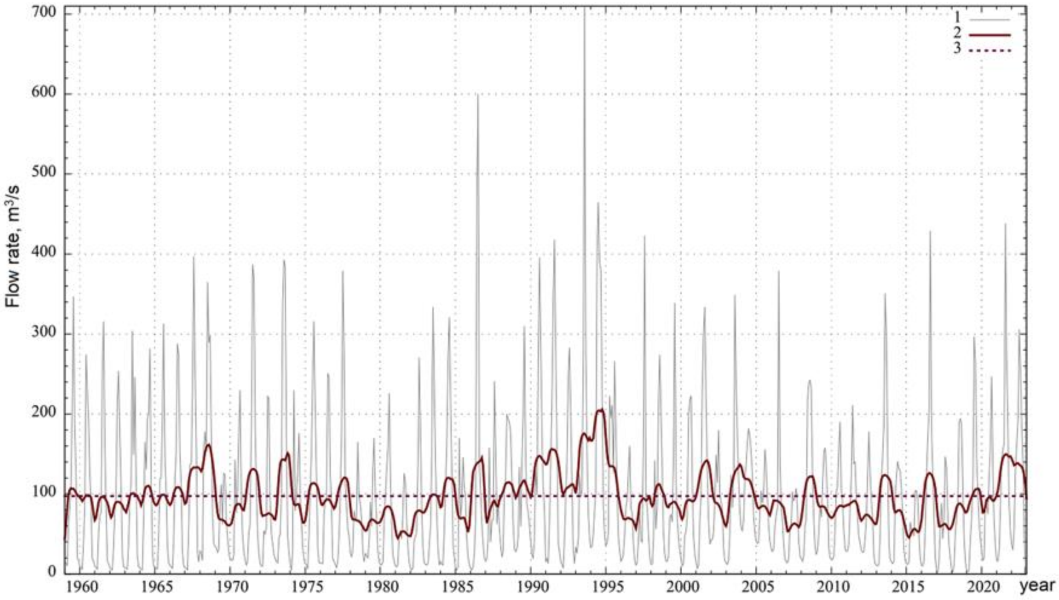

Fig. 4. Dynamics of changes in the monthly average flow rate of the Eg river (Khantai) between 1959 and 2022 (1 – average monthly flow rate, 2 – average moving annual flow rate, 3 – average annual flow rate).

The equality constraints (14) of the model include the water balance equation (12) and various empirical relationships between parameters.

The inequality constraints (15) include groups of constraints for periods $j=\overline{1,N}$, based on the following classification:

1) Technical constraints, which are defined by the characteristics of the hydroelectric facility:

$Q_j \le Q^{max}$ – flow capacity through HPP;

$q_j \le q^{max}$, $q_j^{spill} \le q^{spill\,max}$ – maximum flow rates passing through the HPP turbines and the spillway;

$h^{DSL} \le h_j^{UP} \le h^{MWL}$ – operating range of the reservoir;

$H^{min} \le H_j \le H^{max}$ – permissible change of the water head;

$W_j \le W_j^{inst}$ – installed capacity of HPP;

2) Energy constraints, which are defined by the capacity of HPP:

$W_j \ge W_j^{firm}$ – firm capacity of HPP;

$\hat{W}_j^{min} \le W_j \le \hat{W}_j^{max}$ – dispatching constraints of minimum and maximum capacity of HPP;

3) Environmental constraints, which are defined by flow rates passing through HPP and reservoir levels:

$Q_j \ge Q_j^{min}$ – environmental flow requirements;

$\left|Q_j - Q_{j-1}\right| \le \Delta Q_j$ – constraint on changes in flow through HPP.

4) Water management constraints, which encompass various additional requirements for water users and consumers (for example, water transport, water intakes).

In the process of feasibility studies on the hydropower plants in the Selenga River basin, technical parameters of these plants, including planned electricity output and capacity, alongside the parameters of their reservoirs varied constantly. For example, the Shuren hydropower plant, according to the estimates of the Lengidroproekt Institute in 1976 [3], had various options for installed capacity: 1) 300 MW with a reservoir volume of 4.8 km^3; 2) 268 MW with a volume of 4.2 km^3; 3) 240 MW with a volume of 3.3 km^3.

The river flow at the proposed locations for the HPPs shows high intra-annual variability, therefore, it is crucial to estimate the required live storage of the reservoirs that would smooth out flow irregularities and ensure the target electricity and power output. The live storage has a significant impact on the firm capacity, which requires considering the reliability of average daily power outputs based on long-term flow data, particularly during the winter period.

III. Results and Discussion

Modeling the hydropower plant operation requires representative statistics of the monthly average indicators. Figure 4 shows the dynamics of the Eg river flow rate for 1959–2022.

Figure 4 demonstrates the average monthly and moving annual flow rates, as well as the average annual flow rate (97 m^3/s) for the time span from 1959 to 2022. The maximum average monthly flow rate of 709 m^3/s was recorded once in August 1993, while minimum values (below 4 m^3/s) were observed several times during various winter months. Using the 63-year average monthly statistics shown in the Figure, we can generate various rule curves based on specified criteria for the operation of the hydropower plant.

The study focuses solely on the case with a set maximum power output during peak load hours in the Mongolian energy system. We have developed a model for managing the Egiin Gol HPP, taking into account the specific characteristics of the hydropower facility and its structures. The steps for modeling the Egiin Gol HPP and its reservoir are as follows:

1. Collect and analyze hydrological data on the Selenga river basin and its lateral tributaries, building inflow scenarios for different reliability levels at the Egiin Gol HPP dam site;
2. Model the Egiin Gol HPP reservoir and its characteristics;
3. Establish the relationship between changes in the downstream pool level and the flow rate of the Egiin Gol HPP to determine the water head;
4. Assess the reservoir filling time of the Egiin Gol HPP under various parameters of environmental flow requirements and inflow availability;
5. Set the scenario parameters (operational rules) for regulating the Egiin Gol HPP;
6. Model daily (hourly) operating conditions of the Egiin Gol HPP depending on regulation scenarios;
7. Model long-term operating conditions of the Egiin Gol HPP depending on water conditions and constraints;
8. Determine indicators for possible changes in the natural flow of the Selenga river at both the border of the Russian Federation and the gauging stations across the country.

The system of models developed at the ESI SB RAS allows for modeling the Egiin Gol HPP reservoir, while defining its characteristics. It also models various operating conditions of the Egiin Gol HPP, examining limitations and establishing rules for managing the hydropower plant flow rates.

Modeling the hydropower plant relies on three power output scenarios built using an hourly time step: *Scenario 1* for average water conditions, *Scenario 2* for high water conditions, and *Scenario 3* for low water conditions.

Scenario 1 describes the primary increase in power output (158–315 MW) from November to February during

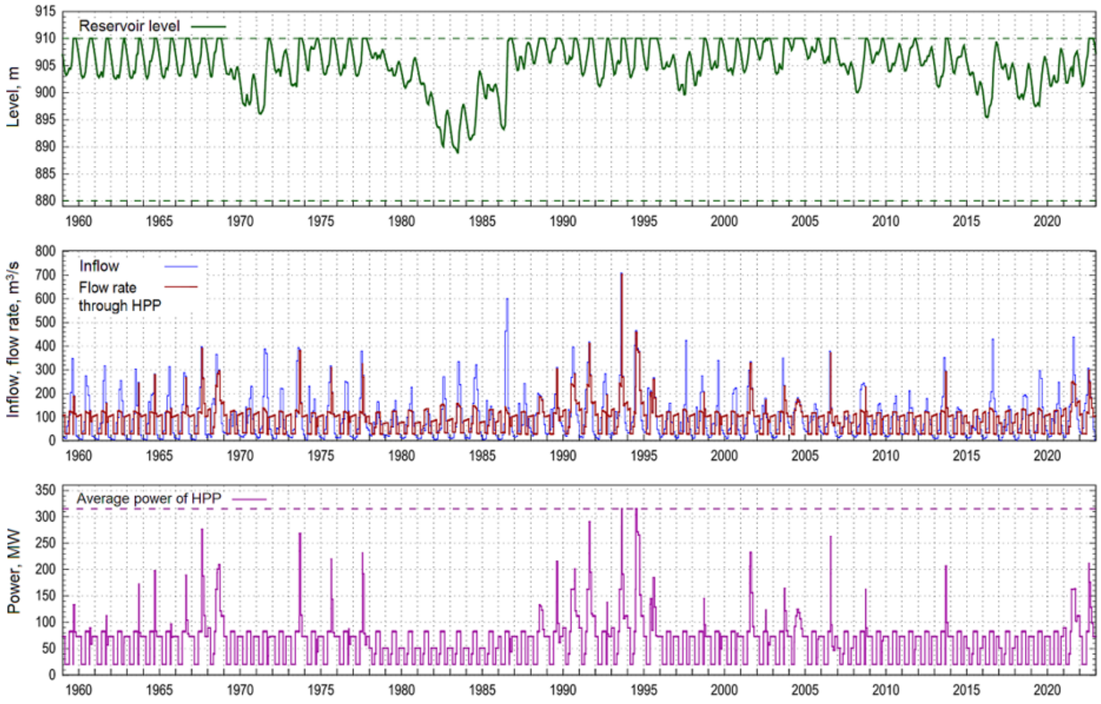

Fig. 5. Operating conditions of the Egiin Gol HPP in 1959–2022.

peak load hours (5 pm to 9 pm), with the HPP operating at its installed capacity of 315 MW from 6 pm to 8 pm. During the summer months (June to August), the output reaches 100 MW during the daytime (7 am to midnight).

Scenario 2 suggests the increase in power output both from November to February and from July to October, with the highest level occurring between 6 pm and 9 pm. From November to December, the output rises to 158, 206, and 315 MW from 3 pm to midnight, while during January and February, it reaches 158–315 MW from 4 pm to 10 pm. From July through September, after the reservoir is filled, the HPP operates around the clock with an output ranging from 109 to 315 MW.

Scenario 3 is similar to Scenario 1, yet it features a narrower power output range of 138 to 275 MW during the winter months.

Modeling of the Egiin Gol HPP during its normal operating conditions rested on the above-described power output scenarios (the main one for an average-water year, and those for high-water and low-water periods). The developed simulation model calculates the required hourly turbine flow rate based on the needed HPP power output, considering changes in upstream and downstream pool levels, and the operating head. Next, all operational parameters are calculated for the current hour before transitioning to the next interval. The hourly results are then averaged to establish daily operating conditions and identify peak indicators.

Due to the high intra-daily variability of power output and water flow rates, the Egiin Gol HPP project includes a buffer dam and a reregulation reservoir, which would smooth out the fluctuations in the intra-daily flow into the downstream pool.

Figure 5 shows the results of modeling the Egiin Gol HPP based on a continuous inflow series for the timespan from 1959 to 2022. Under normal water conditions, the reservoir level ranges between 900 and 910 m. In summer, the average HPP output is 82.5 MW, with flow rates of 115–130 m³/s, while in winter, it averages 73 MW, with flow rates of 100–110 m³/s (Scenario 1). Two periods are observed in the low-water years. These are 1978–1983, when the reservoir level drops to 889 m, and 2014–2017, when it decreases to 895 m. During these periods, the average winter HPP power output is reduced to 51 MW, at flow rates of 70–90 m³/s (Scenario 3). In high-water years (1968, 1990, 1991, 1993, 1994, 2021), the summer power output reaches 82.5–163 MW, at flow rates of 115–230 m³/s. The winter power output ranges from 89 to 112 MW, with flow rates of 130–170 m³/s (Scenario 2). After the reservoir is filled to the Full Reservoir Level (FRL) in high-water years, the average daily HPP output can rise up to the installed capacity of 315 MW, with a maximum turbine flow rate of 445 m³/s.

To assess the impact of reservoir filling on downstream pool flows, three flow scenarios (average, low, and high) and three environmental (minimum) flow scenarios were

TABLE 1. Changes in Average Monthly Flow Rate at Naushki Gauge Station According to the Egiin Gol HPP Reservoir Filling Scenario During Average Water Years (1999–2002)

Year	Month	Natural flow rate, m^3/s	Deviation (regulated), m^3/s			Exceedance probability (regulated), %			Exceedance probability (natural), %
			Scenario 1	Scenario 2	Scenario 3	Scenario 1	Scenario 2	Scenario 3	
1999	8	609	–299	–244	–239	96.1	91.6	91.1	59.6
2000	7	279	–160	–155	–130	98.9	98.7	97.7	88.1
2000	8	276	–178	–123	–118	99.9	99.9	99.9	97.9
2000	9	329	–183	–143	–133	99.1	97.4	96.9	83.4
2000	10	220	–73	–68	–53	99.2	99.0	98.1	92.2
2001	7	443	–258	–253	–228	95.9	95.7	93.9	68.2
2001	8	442	–294	–239	–234	99.9	99.8	99.7	82.6
2001	9	339	–183	–143	–133	98.7	96.9	96.2	82.1
2001	10	263	0	–85	–70	83.2	97.4	96.0	83.2
2002	5	313	0	0	–99	0	0	97.5	80.3
2002	7	272	0	0	–110	0	0	97.2	88.8
2002	8	217	0	0	0	0	0	99.7	99.7
2002	9	210	0	0	0	0	0	96.0	96.0
2002	10	202	0	0	0	0	0	95.0	95.0

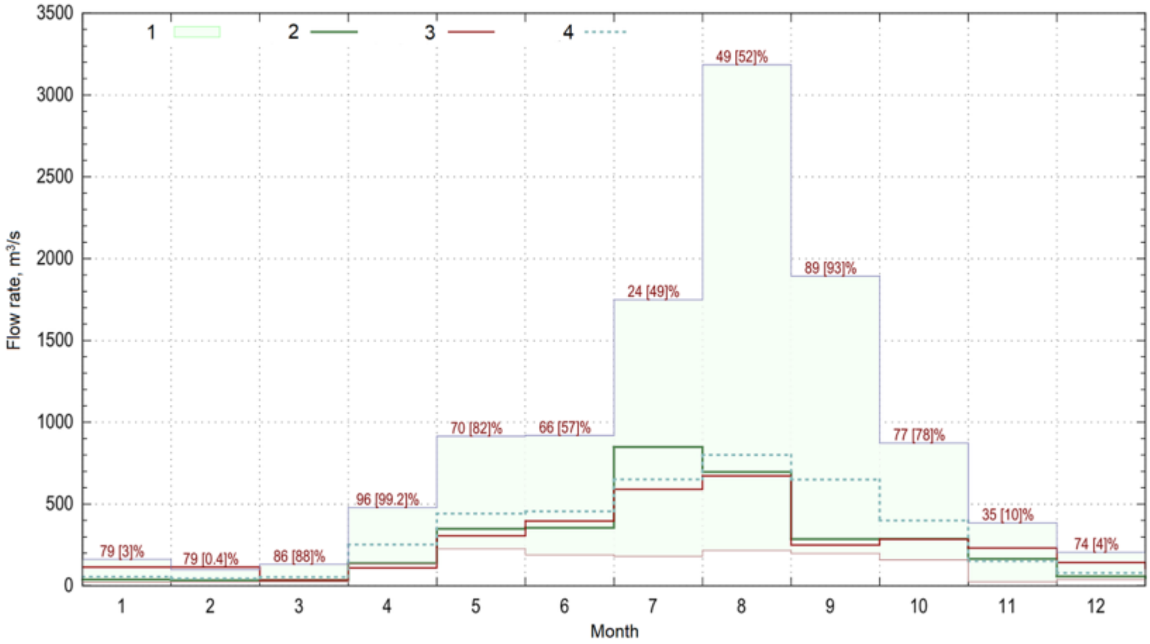

Fig. 6. Flow rate variation chart for the Selenga river (Naushki gauging station) for 2006, showing the 50% annual inflow exceedance probability for the HPP reservoir (1 – boundaries of natural flow, 2 – actual flow for 2006, 3 – regulated HPP flow, 4 – average natural flow).

used: 1) a baseline scenario with a constant design flow rate of 40 m^3/s (except for months when inflows are below 40 m^3/s); 2) a flow rate with at least 99% exceedance probability for each month; 3) a flow rate with at least 95% exceedance probability for each month.

The period between 1999 and 2002 was selected to represent an average flow year. For this period, the operating conditions were modeled using three reservoir filling scenarios, identifying months with critical exceedance probabilities (above 95%, Table 1). As seen in the Table, the third filling scenario is the closest to the natural conditions, having minimal impact on the change in the hydrological regime at the Naushki gauging station. Under natural conditions, the exceedance probability of average monthly flow rates exceeded 95% only four times during the observation period: in May 1998, August 2000,

TABLE 2. Changes in the Average Monthly Flow Rates of the Selenga River (Naushki) with the 50% Exceedance Probability of Annual Inflow into Hydropower Plant Reservoir in 2006

Month	Flow rate, м^3/s		Deviation		Exceedance probability, %	
	Natural	Regulated	m^3/s	%	Natural	Regulated
1	39	114	75	192.3	78.7	2.6
2	33	114	81	245.5	78.6	0.4
3	35	34	–1	–2.9	86.2	88.3
4	138	110	–28	–20.3	96.3	99.2
5	348	305	–43	–12.4	70.4	82.2
6	355	396	41	11.5	66.1	56.8
7	849	590	–259	–30.5	24.3	49.5
8	696	672	–24	–3.4	48.8	51.6
9	286	250	–36	–12.6	88.8	92.5
10	287	285	–2	–0.7	77.2	77.8
11	165	231	66	40	34.7	9.5
12	58	143	85	146.6	73.8	4.0

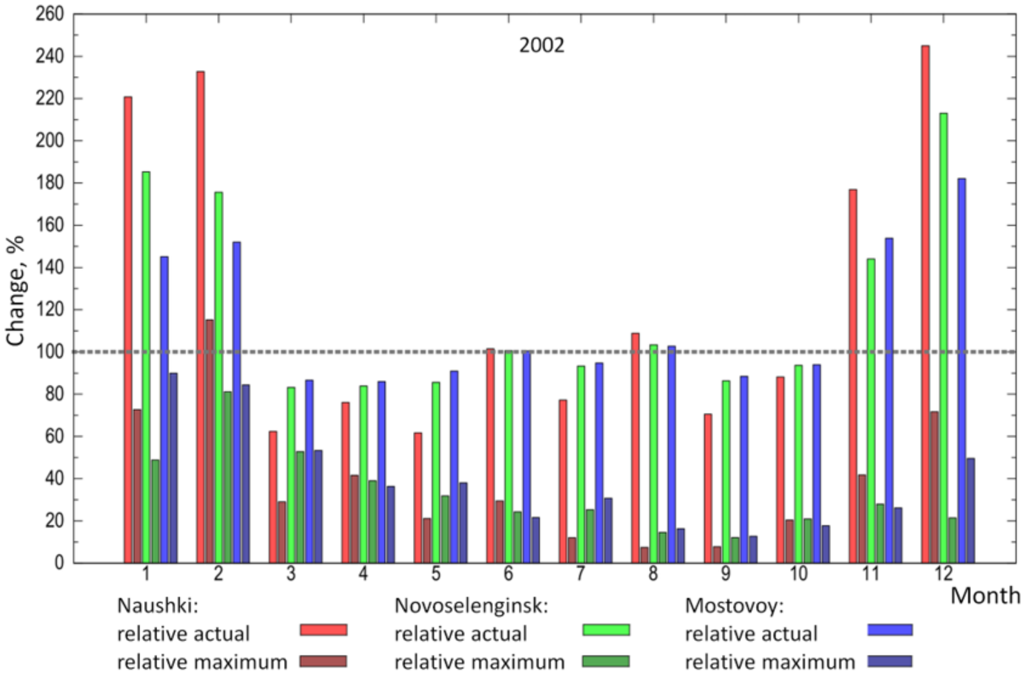

Fig. 7. Changes in hydrological regimes for three Russian gauging stations for 2002 (in % of actual and maximum average monthly values).

August 2002, and September 2002. For all considered scenarios, the exceedance occurs in 8 or more months.

The exceedances partially persist for the Novoselenginsk and Mostovoy gauging stations. The flow rate at the Mostovoy station determines the inflow into Lake Baikal, which could potentially conflict with its environmental requirements.

The primary role of the Egiin Gol HPP in the power system is to cover intraday load variations. Varying hydrological conditions must be factored in by modeling for various Eg River flow rate exceedance probabilities, ranging from 99% to 1%.

Figure 6 illustrates flow rate deviations in the regulated regime compared to natural conditions at the Naushki gauging station under average water conditions. The Figure highlights the range of natural flow rate variations based on accumulated statistics, along with actual and regulated average monthly indicators.

The chart shows that the winter months are critical, particularly February, when the average monthly exceedance probability drops from 79% to 0.4% (the flow rate exceeds the maximum recorded historical indicator for February). Table 2 presents the changes in flow rates, the difference in absolute and relative indicators, and the exceedance probability for both natural and regulated conditions.

The exceedance probability surpasses 95% in April, when the flow rate declines from 96.3% to 99.2%. The violations of exceedance probability below 5% are observed during the winter months: January (a decrease from 78.7% to 2.6%), February (a drop from 78.6% to 0.4%), and December (a decline from 73.8% to 4%). These winter months show an increase in flow rates by 192.3%, 245.5%, and 146%, respectively. Overall, the exceedance probability violations occur at the Naushki gauging station during the winter months, characterized by a significant increase in flow rates, and in certain summer months.

Figure 7 shows the regulated flow deviations from natural conditions across all months for the low-water year 2002.

Winter flow rates vary significantly for all gauging stations, which underscores the necessity of special environmental research. The charts are generated automatically after modeling the regimes with the specified parameters. Particular attention should be paid to flow rates that exceed the recorded maximum average monthly indicators. For example, at the Naushki gauging station, the flow rate increases by 120% in a low-water year and by 180% in an average year relative to the maximum indicator recorded in February based on statistics accumulated for the timespan from 1955 to 2023.

IV. CONCLUSION

The system of models designed to assess the impact of HPPs planned in Mongolia on hydrological regimes makes it possible to conduct comprehensive studies on the selection of optimal dam sites and construct bathymetric curves of reservoirs for identifying the hydropower and water management scenarios that enable the assessment of the impact of regulated operations on the downstream hydrological regime. The models built were employed to preliminarily assess the impact of the planned Egiin Gol HPP on the hydrological regime of the Russian part of the Selenga river. The findings indicate significant potential changes in flow rates during the winter months. These changes create potential threats to the health of the ecosystems of both the Selenga river and Lake Baikal. Furthermore, during low and average water years, risks of reduced flow rates arise, which may also negatively affect the river and lake ecosystems.

The developed models and software are fully adaptable to the new operational management requirements of the planned Egiin Gol HPP and can also facilitate the exploration of other hydropower projects.

ACKNOWLEDGMENT

The study was carried out within the state assignment for the Matrosov Institute for System Dynamics and Control Theory SB RAS under the project “Comprehensive Environmental Assessment of the Impact of the Mongolian Egiin Gol Hydropower Project on the Territory of the Russian Federation, Lake Baikal” (Scientific project code: FWEW-2025-0001, Registration number: 125091110246-2).

REFERENCES

[1] *Technical and economic report on the possibility of using the hydro resources of the rivers within the Selenga and Khovd river basins (Mongolian People's Republic).* Moscow, USSR: All-Union State Institute “Hydroenergoproekt,” 1960, 127 p. (In Russian)

[2] N. T. Kuznetsov, *Basic regularities of the river regime of the Mongolian People's Republic*. Moscow, USSR: USSR Academy of Sciences Publishing House, 1955, 104 p. (In Russian)

[3] *Shuren hydroelectric complex on the Selenga river (Mongolian People's Republic). Technical report on priority surveys of 1975-76, Book 2. Topographic and geodetic surveys*. Leningrad, USSR: Zhuk All-Union Research Institute “Gidroproekt,” 1976, 121 p. (In Russian)

[4] N. K. Davi, G. C. Jacoby, A. E. Curtis, N. Baatarbileg, “Selenge River, Mongolia Streamflow Reconstruction,” *World Data Service for Paleoclimatology*. Boulder CO, USA, vol. 19, pp. 288–299, 2006.

[5] M. G. Grechushnikova, K. K. Edelstein, “Rapid Assessment of the Consequences of Hydraulic Engineering Construction in the Selenga River Basin,” *Water Management in Russia*, no. 1, pp. 66–82, 2016. (In Russian)

[6] E. Simonov, S. Zabelin, et al, “Hydropower Development of the Selenga River: Prospects and Consequences,” Technical Report, 2017, 25 p. DOI: 10.13140/RG.2.2.15703.57765. (In Russian)

[7] D. Dagvadorj, L. Natsagdorj, J.Dorjpurev, B.Namkhainyam, et al, *Mongolia: Assessment Report on Climate Change 2009*. Ulaanbaatar, Mongolia: Ministry of Nature, Environment, and Tourism of Mongolia, 2010, 228 p.

[8] *In-Depth Review of Energy Efficiency Policies and Programs: Mongolia*. Brussels, Belgium: Energy Charter Secretariat, 2011, 126 p.

[9] G. Dolgorsuren, et al, *Integrated Water Management Plan of Mongolia*. Ulaanbaatar, Mongolia: Government of Mongolia, Ministry of environment and green development, 2013, 341 p.

[10] N. V. Abasov, V. M. Nikitin, T. V. Berezhnykh, E. N. Osipchuk, “Monitoring and Predictive Estimations of Atmospheric Parameters in the Catchment Area of Lake Baikal,” *Atmosphere*, vol. 13, no. 49, 2022.

[11] V. M. Nikitin, N. V. Abasov, M. V. Bolgov, E. N. Osipchuk, “The Stability of the Water Management System in the Angara River Basin in Different Water Level Conditions,” *Geography and Natural Resources*, vol. 42, no. 2, pp. 139–147, 2021. DOI: 10.1134/S1875372821020104.

[12] V. M. Nikitin, N. V. Abasov, E. N. Osipchuk, “Modeling of Long-term Operating Regimes of Hydro Power Plants as Part of Energy and Water Systems in the Context of Uncertainty,” *E3S Web of Conf.*, vol. 209, Art. no. 05014, 2020 DOI: 10.1051/e3sconf/202020905014.

[13] E. N. Osipchuk, V. M. Nikitin, N. V. Abasov, “Possibilities of Enhancing the Efficiency of the Angara Cascade of Hydroelectric Power Plants,” *Journal of Physics: Conference Series*, vol. 1652, Art. no. 012022, 2020.DOI: 10.1088/1742-6596/1652/1/012022.

[14] N. V. Abasov, V. M. Nikitin, E. N. Osipchuk, “A System of Models to Study Long-Term Operation of Hydropower Plants in the Angara Cascade,” *Energy Systems Research*, vol. 2, no. 2, pp. 5–18, 2019. DOI: 10.25729/esr.2019.02.0001.

[15] V. M. Nikitin, N. V. Abasov, E. N. Osipchuk, T. V. Berezhnykh, “An Assessment of Environmental Flow for Modelling the Operating Conditions of Mongolian Hydropower Plants in the Transboundary Basin of the Selenga River,” *IOP Conference Series: Earth and Environmental Science*, vol. 381, Art. no. 012069, 2019. DOI: 10.1088/1755-1315/381/1/012069.

[16] F. Hourdin, T. Mauritsen, A. Gettelman, J. C. Golaz, et al, “The art and science of climate model tuning*,” Bulletin of the American Meteorology Society*, vol. 98, no. 3, pp. 589–602, 2017.

[17] A. Becker, P. Finger, A. Meyer-Christoffer, B. Rudolf, et al, “A description of the global land-surface precipitation data products of the global precipitation climatology centre

with sample applications including centennial (trend) analysis from 1901–present," *Earth System Science Data*, vol. 5, pp. 71–99, 2013.

[18] K. Schamm, M. Ziese, A. Becker, P. Finger, et al, "Global gridded precipitation over land: A description of the new GPCC First Guess Daily product," *Earth System Science Data*, vol. 6, pp. 49–60, 2014.

[19] U. Schneider, P. Finger, A. Meyer-Christoffer, E. Rustemeier, et al, "Evaluating the hydrological cycle over land using the newly-corrected precipitation climatology from the global precipitation climatology centre (GPCC)," *Atmosphere*, vol. 8, no. 3, Art. no. 52, 2017. DOI: 10.3390/atmos8030052.

[20] B. D. Zaykov, *Evaporation from the water surface of ponds and small reservoirs in the USSR*, Ser. Proceedings of the State Hydrological Institute, vol. 21(75). Leningrad, USSR: Gidrometeoizdat, 1949, 54 p. (In Russian)

[21] A. I. Chebotarev, *General hydrology*. Leningrad, USSR: Gidrometeoizdat, 1975, 544 p. (In Russian)

[22] K. E. Ivanov, *Water exchange in mire landscapes*. Leningrad, USSR: Gidrometeoizdat, 1975, 280 p. (In Russian)

[23] V. N. Mikhailov, A. D. Dobrovolsky, S. A. Dobrolyubov, *Hydrology*. Moscow: Vysshaya Shkola Publishing House, 2008, 463 p. (In Russian)

Vyacheslav M. Nikitin, Dr. Sci. in Engineering (1992), is the Head of Hydropower and Water Management Systems Laboratory at the Melentiev Energy Systems Institute of the Siberian Branch of the Russian Academy of Sciences (ESI SB RAS). His research interests include management of large-scale energy and water systems, including hydropower plants and their cascades; development of methodologies for water resource management rules.

Nikolai V. Abasov, Ph. D. in Engineering (1999), is a Senior Researcher in the Hydropower and Water Management Systems Laboratory at the ESI SB RAS. His research interests include development of new techniques and methodologies for enhancing the efficiency of hydropower systems in the context of a changing climate, as well as research into water balance and flow changes.

Evgeny N. Osipchuk, Ph. D. in Engineering (2014), is a Senior Researcher in the Hydropower and Water Management Systems Laboratory at the ESI SB RAS. His research interests include development of methodological support and software to improve the efficiency and reliability of hydropower plants, considering probabilistic predictive inflow scenarios, various optimization criteria and constraints.

Vladislav M. Berdnikov is a Research Engineer in the Hydropower and Water Management Systems Laboratory at the ESI SB RAS. V. Berdnikov is a postgraduate student in the Ph.D. program for Energy Systems and Complexes. His research interests include the development of algorithms and software systems that employ AI methods for exploring hydropower plants.

Viktor S. Gasan is a Research Engineer in the Hydropower and Water Management Systems Laboratory at the ESI SB RAS. V. Gasan is a postgraduate student in the Ph.D. program for Mathematical Modeling, Numerical Methods and Software Complexes. His research interests include development of GIS support algorithms, analysis of geoclimatic data, and forecasting methods.